ABSTRACT

Title of dissertation: VISUALIZING QUANTUM REACTIVE SCATTERING DYNAMICS

Michael R. Warehime,
Doctor of Philosophy, 2015

Dissertation directed by: Professor Millard H. Alexander
Department of Chemistry

The Born-Oppenheimer approximation, which allows a decoupling of electronic and nuclear motion, underlies the investigation of molecular dynamics. In some cases this decoupling is not possible, so that nuclear motion can induce changes in electronic state. It is then necessary to account for collision-induced transitions between multiple potential energy surfaces. This is an inherently quantum phenomena. In this dissertation we present a new way to visualize these non-adiabatic transitions in chemical reactions of open-shell atoms. Toward this end, we have developed new algorithms and developed a MATLAB-based software suite for simulating non-adiabatic reactions. We have also determined new molecular potential energy surfaces and their couplings required to simulate the reactive dynamics.

VISUALIZING QUANTUM REACTIVE SCATTERING DYNAMICS

by

Michael R. Warehime

Dissertation submitted to the Faculty of the Graduate School of the
University of Maryland, College Park in partial fulfillment
of the requirements for the degree of
Doctor of Philosophy
2015

Advisory Committee:
Professor Millard H. Alexander, Chair/Advisor
Professor Christopher Jarzynski
Professor Garegin Papoian
Professor Paul Dagdigian
Professor Dianne P. O'Leary

To my parents

Acknowledgments

I would like to express my sincere gratitude to my advisor Millard Henry Alexander for providing the opportunity and openness to pursue the research projects contained herein and for his unending support, understanding and guidance, both personally and professionally, as these projects have evolved over the years. I would also like to thank many of my peers at the University of Maryland for their thoughtful conversation, rewarding personal interactions and, at times, for much needed distraction. I especially thank Dvir Kafri and Jacek Kłos who have been indispensable resources and both possess a seemingly infinite supply of patience. Finally, I thank my family, my parents Brad and Cyndy, and my siblings, Matt, Ness and Nan, who have provided a lifetime of loving support and encouragement.

Table of Contents

List of Abbreviations

BO	Born-Oppenheimer
PES	Potential Energy Surface
FE(M)	Finite Element (Method)
DFT	Density Functional Theory
JCP	Journal of Chemical Physics
MSJ	Mass-Scaled Jacobi
SO	Spin-Orbit
BVP	Boundary Value Problem
LHS	Left Hand Side
FD	Finite Difference
MEP	Minimum Energy Path
CRESU	Cinétique de Réaction en Éclement Supersonique Uniforme, (reaction kinetics in uniform supersonic flow)
SA-CASSCF	State-Averaged Complete Active Space Configurational Self-Consistent Field
ic-MRCISD	Multi-Reference Configuration Interaction Calculations including explicitly Single and Double excitations
RHF	Restricted Hartree-Fock
CCSD(T)	Coupled Cluster Method with inclusion of Single, Double, and (perturbatively) Triple Excitations
UHFBR	Post-Hartree-Fock scheme with corrections for dispersion interactions
XDM	eXchange-hole Dipole Moment
RCCSD(T)	Restricted CCSD(T)
CEPA	Coupled Electron PAir method
CC	Close-Coupling
CD	Centrifugal Decoupled
AB	Adiabatic Bender
DCS	Differential Cross-Section
ICS	Integral Cross-Section
NN	Neural Network
MLP	Multilayer Perceptron Network
BMLP	Bridged Multilayer Perceptron Network
FCC	Forward Cascade Network
DBN	Deep Belief Network
RMSE	Root-Mean-Squared-Error
PIP	Permutation Invariant Polynomial
LM	Levenberg-Marquardt
PIP	Permutation Invariant Polynomial

List of Tables

List of Figures

Chapter 1: Introduction and Overview

The subject of this work is the identification and visualization of quantum effects in the dynamics of electronically open-shell, atom-diatom systems.

Since the development of molecular beam techniques [1] to investigate chemical reaction dynamics some 60 years ago, chemical physicists have developed a panoply of theoretical methods to interpret and model these experiments. The Born-Oppenheimer (BO) approximation [2] has proved most useful in this endeavor and is an essential underpinning in modern studies in theoretical and computational chemistry.

Within this approximation the motion of the electrons in a molecule is decoupled from the motion of the nuclei. The forces on the nuclei are defined by the gradient of the electronic potential energy. Physically one can understand this approximation as follows; because electrons are so much lighter than nuclei (even the lightest nucleus – the proton – is 1840 times heavier than an electron) electrons react much faster to external perturbations. Accordingly, the electrons will adjust instantaneously to the motion of nuclei and their respective dynamics can be decoupled.

In quantum mechanical terms the BO approximation allows one to write the

total molecular wave function as the product of an electronic wave function and nuclear wave function. In practice one solves the electronic problem first, which depends only parametrically on the nuclear coordinates. The dependence of the electronic energies on the position of the nuclei is (along with the repulsion between the nuclei) the potential energy of the latter. This potential energy surface allows for the simulation of the nuclear dynamics. There exist many software packages for both accurate electronic structure calculations [3–5] and nuclear dynamics simulations [6–9].

For systems where the BO approximation predicts the nuclear dynamics correctly, we say that the nuclei move adiabatically, i.e. their motion is confined to a single electronic potential energy surface (one eigenstate of the electronic problem). In the case of adiabatic dynamics, classical, semiclassical methods such as ring-polymer methods models [10], classical [11] and Monte Carlo [12] trajectory methods, and transition-state methods [13] work well to model the nuclear dynamics of reactive scattering. Because exact quantum scattering software packages are limited to a few atoms (though recently there has been advances in treatable system size [14]) these classical and quasi-classical methods are the only option for larger systems.

In this thesis we are interested in nonadiabatic – non-BO – dynamics, where the motion of the electrons and nuclei cannot be decoupled, and the nuclear motion evolves on multiple, coupled electronic potential energy surfaces. The essentially quantum nature of coupling and interference between molecular potential energy surfaces can't be described by classical mechanics. As a consequence, an *ad hoc* method

must be used to account for non-BO behavior in classical and semi-classical simulations. Many such methods exist including surface hopping, [15], time-dependent self-consistent fields [16] and linear approximations of the initial value problem [17]. Ultimately, though, an accurate description of the reaction dynamics of nonadiabatic systems demands an exact quantum treatment based on *ab initio* potential surfaces. Very little software exists to simulate the general case of nonadiabatic reaction dynamics. What software that does exist [6] must be extended anew for each nonadiabatic system, which is time consuming and restricts its use to all but a few experts in the field. The lack of available nonadiabatic reactive scattering software has motivated the majority of the work contained in this dissertation.

This dissertation is organized into six chapters. The following chapter, Chapter 2, is an introduction to the nonadiabatic dynamics of collisions between open-shell atoms and closed-shell diatomic molecules. We start this discussion with a brief theoretical treatment of the BO approximation and its breakdown. We identify the common sources of nonadiabaticity in reactive scattering, namely coupling near conical intersections, spin-orbit coupling and Coriolis coupling. We then define our system of interest, i.e. the quantum reactive scattering dynamics of an open-shell atom with a closed shell diatomic molecule. We focus on the coordinate system and physical scattering boundary conditions used throughout this work.

After defining the system of interest, we turn to dynamical studies of atom-diatom reactions in Chapter 3. Scattering software packages available today are generally based on finite difference propagation of the wave function and are, in general, difficult to use, not easily generalized to new systems, and do not readily

provide the scattering wave function. These concerns combined with the noted lack of general purpose nonadiabatic software has inspired our development of a novel extension of the finite element (FE) method for approximating reactive scattering dynamics. We have implemented this FE approach to quantum reactive scattering in MATLAB.

In Chapter 3 we work through many applications of the FE method to approximate the Schrödinger equation for atom-diatom systems beginning with bound state systems. Once we have introduced the finite element method and its application to Schrödinger's equation, we apply the algorithm to adiabatic, reactive scattering. It is here, we derive our novel modifications to the way boundary conditions are handled in the FE scattering algorithm of Askar and Rabitz [18]. We use the exemplary hydrogen exchange reactions such as H+H_2, F+H_2, F+HCl and their isotopic variants to test our new algorithm.

Subsequently, in Chapter 3 we generalize the results of the FE adiabatic scattering algorithm to nonadiabatic systems. We focus on the formulation of the boundary condition for coupled reactive scattering. We introduce the topic of the fluid-dynamical picture of quantum reactive scattering, studied in detail in the literature [19–26]. We show how this fluid-flow picture of quantum mechanics can extend our intuition of the nonadiabatic, quantum reactive scattering. We test the nonadiabatic FE scattering algorithm with the F+HCl and F+H_2 reactions.

In the last section of Chapter 3, motivated by modern laser-cooling experimental methods that can resolve hyperfine structure [27], we apply our nonadiabatic dynamics method to the Li+CaH system, which is a potential candidate for the

preparation of ultra-cold molecular systems.

In Chapter 4 we describe in more detail the potential energy surfaces of atom-diatom reactions. We have analyzed the potential energy surfaces of many reactive, atom-diatom systems that exhibit similar nonadiabatic character, such as $F+H_2$, F+HCl, $O+H_2$. In this chapter we discuss the technical details of these potential surfaces and describe our new, highly accurate, *ab initio* calculations for the $O+H_2$ system.

Accurate *ab initio* potential surface calculations are computationally expensive. Even in the era of distributed computation, these calculations can takes weeks and sometimes months. Density Functional Theory (DFT) has been successfully used in a wide range of chemical applications and in Chapter 5 we analyze its use as a computationally cheaper alternative for the determination of potential energy surfaces for atom-diatom systems. Specifically this chapter analyzes the ability of DFT to model long-range dispersion forces in open-shell systems, which has historically proven difficult for DFT [28].

Finally, after the technical discussion, Chapter 6 presents a concise summary of the work presented in this dissertation. We also comment on projects that could be inspired by this work.

The exciting developments of our ongoing work, involving the use of statistical learning models to fit potential energy surfaces, are described in Appendix A.

1.0.1 Published Works

Much of the work presented in the following chapters has been previously published in peer reviewed journals. This section identifies which works have been cross-referenced and provides the references to the respective articles.

Chapter 3 is largely contained in the following series of works which have previously been published in *the Journal of Chemical Physics* (JCP). Chapter 3 also borrows from another work, on the nonadiabatic dynamics of Li+CaH, which is currently in draft form (*see below*).

[1] M. Warehime, M. H. Alexander, *A MATLAB-based finite-element visualization of quantum reactive scattering. I. Collinear atom-diatom reactions.* J. Chem. Phys. **141**, 024118 (2014) [29].

[2] M. Warehime, M. H. Alexander, *A MATLAB-based finite-element visualization of quantum reactive scattering. II. nonadiabaticity in the F+HCl and F+H_2 reactions on coupled potential energy surfaces.* J. Chem. Phys. **142**, 034108 (2015) [30].

The study presented in Chapter 5 involving new potential energy surfaces of the ground state Ar+NO($X^2\Pi$) system has been published JCP.

[3] M. Warehime, J. Kłos and E. Johnson, *New XDM-corrected potential energy surfaces for* Ar-NO($X^2\Pi$): *A comparison with CCSD(T) calculations and experiments.*, J. Chem. Phys. **142** 024302 (2015) [31].

1.0.2 Manuscripts in Progress

At the time of the presentation of this thesis to the committee there were several projects contained herein that have yet to be published:

Chapter 3 contains a new study on the nonadiabatic dynamics of the Li(^{2}S) + CaH($^2\Sigma^+$) system in the ultra-cold regime. We have drafted a manuscript to be submitted to Chemical Physics Letters based on this work.

[4] M. Warehime, J. Kłos, *Collisions between* Li(^{2}S) *and* CaH($^2\Sigma^+$) *on the lowest triplet and singlet potentials: Two-dimensional finite element studies on coupled potential surfaces.*

The study presented in Chapter 4 on the potential energy surfaces of O(^3P) + H_2 is in preparation for publication in JCP.

[5] M. Warehime, J. Kłos and M. H. Alexander, *Time reversal invariant basis for nonadiabatic reactive scattering of* F(^2P)+H_2 *and* O(^3P)+H_2.

Appendix A contains new work on a project using neural networks to model molecular potential energy surfaces. This is the subject of a forthcoming paper, which will likely be submitted to the Journal of Computational Chemistry.

[6] M. Warehime and M. H. Alexander, *Identifying optimal neural network topology for fitting molecular potential surfaces.*

Chapter 2: Nonadiabatic Dynamics of Open-Shell Atom+Diatom Systems

2.1 Nonadiabatic Chemistry

The accurate dynamical modeling of nonadiabaticity in molecular collisions has implications in a variety of fields including solar energy [32], photosynthesis [33,34], human vision [35], combustion dynamics [36], fuel cells [33, 34], and interstellar and atmospheric chemistry [37, 38], to name a few. In this work we investigate nonadiabatic dynamics in the simplest class of chemical reactions: collisions between an atom and a diatomic molecule. Understanding nonadiabaticity in this class of reactions will refine our understanding of this effect in more complex systems.

Nonadiabatic dynamics has been studied near conical intersections [45–49], as well as induced by spin-orbit [50–55] or Coriolis coupling [56,57]. A panoply of methods and mathematical tools have been developed to investigate this phenomenon. These include exact time-dependent [58–60] and time-independent [50–54, 61–64] quantum scattering, as well as extensions of classical trajectory methods [15,65–71].

2.1.1 Born-Oppenheimer Approximation

In this section we briefly recapitulate the theoretical framework for nonadiabatic chemistry provided by Jasper and coworkers [72]. The Hamiltonian of a molecular system can be written

$$H(Q,q) = T(Q) + H_e(q;Q)$$

where Q refer to the nuclear degrees of freedom, q refers to the electronic degrees of freedom, $T(Q)$ is the nuclear kinetic energy and $H_e(q;Q)$ is the electronic Hamiltonian, which includes the nuclear repulsion. Systems that are accurately modeled within the BO approximation are those whose dynamics evolve on a single electronic potential surface, in which case we can write the total molecular wave function, $\Psi(Q,q)$, as

$$\Psi(Q,q) = \Psi^{\eta}(Q)|\eta\rangle$$

where $|\eta\rangle$ is an eigenstate of the electronic Hamiltonian, which also depends parametrically on the nuclear degrees of freedom, Q. This wave function solves Schrödinger's equation, namely

$$\left[T(Q) + H_e(q;Q) - E\right]\Psi(Q,q) = 0$$

where E is the total energy of the system. Substituting the BO wave function, premultiplying by $\langle\eta|$, and integrating over the electronic degrees of freedom yields

$$\left[T(Q) + V^{\eta,\eta}(Q) - E\right]\Psi^{\eta}(Q) = 0$$

where $V^{\eta,\eta}(Q) = \langle\eta|H_e(q;Q)|\eta\rangle_q$ is the electronically-adiabatic potential energy surface (PES) associated with electronic state η, and the subscript q denotes integration over the electronic degrees of freedom.

2.1.2 Beyond the Born-Oppenheimer Approximation

Many chemical systems require more than one electronic PES to accurately describe the nuclear dynamics. In such cases we expand the nuclear wave function in the set of electronic wave functions

$$\Psi(Q,q) = \sum_{\eta} \Psi^{\eta}(Q)|\eta\rangle.$$

Substituting this expression for the wave function into Schrödinger's equation we have

$$[T + H_e(q;Q) - E]\left(\sum_{\eta} \Psi^{\eta}(Q)|\eta\rangle\right) = 0.$$

For now, let us remember that the kinetic energy operator is proportional to the Laplacian, so that we can write for simplicity

$$T \propto \frac{\partial^2}{\partial Q^2}.$$

Premultiplying by the electronic wave functions and integrating over the electronic degrees of freedom we obtain the following set of coupled equations

$$\sum_{\eta,\eta'} \left[T + T_1^{\eta',\eta} + T_2^{\eta',\eta} + V^{\eta,\eta}(Q) - E\right] \Psi^{\eta}(Q) = 0 \tag{2.1}$$

where terms $T_1^{\eta',\eta}$ and $T_2^{\eta',\eta}$ result from the product rule and are defined as

$$T_1^{\eta',\eta} = 2\langle\eta'|\frac{\partial}{\partial Q}|\eta\rangle\frac{\partial}{\partial Q}$$

and

$$T_2^{\eta',\eta} = \langle \eta' | \frac{\partial^2}{\partial^2 Q} | \eta \rangle.$$

Here $V^{\eta,\eta}$ is the matrix element of the electronic Hamiltonian, which is diagonal in the electronic state index. The kinetic energy terms, however, are not diagonal in the electronic state index. Note that we have assumed the Cartesian expression for the Laplacian. In other coordinate systems T is more complicated but still involves second derivatives with respect to the coordinates. But we see, even in the simplest Cartesian form, that the kinetic energy operator couples the electronically adiabatic states.

In some applications it is more convenient to transform this system of equations to a basis in which the kinetic energy terms are diagonal and the potential energy terms are not diagonal, the so-called diabatic basis. It should be noted, however, that this is not always possible, and the term quasi-diabatic basis is used for the basis which minimizes the off-diagonal coupling in the kinetic energy operator. For our purposes we will use the term diabatic, with the knowledge that we are using only approximately diabatic states.

2.1.3 Conical Intersections

Conical intersections occur when two states of different symmetry mix as the system moves to a lower symmetry configuration. If these two states cross in the high-symmetry geometry, then at nearby lower-symmetry geometries the degeneracy of the adiabatic states is lifted forming a cone of intersection. In a system with n

degrees of freedom the conical intersection forms a seam of dimension $n-2$ [73]. In the vicinity of the seam of conical intersection, because the two states are degenerate, the nonadiabatic couplings T_1 and T_2, no matter how small, can lead to a significant mixing. Thus, along the seam of conical intersections the BO approximation breaks down. An accurate picture of the motion of the nuclei near conical intersections must therefore involve two (or more) coupled adiabatic PESs. Conical intersections appear in wide range of systems and are central to a discussion of nonadiabatic dynamics.

2.1.4 Spin-Orbit Interactions

Another source of nonadiabatic dynamics in molecular systems is the spin-orbit interaction. The spin-orbit Hamiltonian, which arises from the coupling of the electron's spin and orbital angular momentum, can be written as

$$H_{so}(Q) = A(Q)\mathbf{L}\cdot\mathbf{S},$$

where $\mathbf{L}$ is the orbital angular momentum operator, $\mathbf{S}$ is the spin angular momentum operator, and $A(Q)$ is the spin-orbit constant, which is geometry dependent. The spin-orbit interaction is not included in the electronic Hamiltonian, $H_e(Q,q)$, which contains only electrostatic interactions. The addition of $H_{so}(Q)$ can couple different adiabatic electronic states. This can be important in collisions of atomic and molecular radicals whenever both L and S are non-zero. The study of such systems is an important component in this dissertation.

2.1.5 Coriolis Coupling

Electronic Coriolis coupling occurs when an open-shell atom or molecule collides with another atom or molecule. As stated above the nuclear kinetic energy term, T, is the Laplacian operator. This operator contains terms that include the angular momentum of the nuclei. The coupling between the angular momentum of the nuclei and the electronic angular momentum can give rise to mixing between different electronic states. This is called electronic-rotational Coriolis coupling.

In many dynamical studies these terms are ignored, as they tend to be small, just as T_1 and T_2 are ignored. However, a complete description of the nonadiabatic dynamics of reactive collisions must account for the electronic Coriolis coupling. Schatz and Drukker provide an excellent study on the importance of electronic-rotational Coriolis coupling in nonadiabatic reactive collisions [178]. In the present work we do not include nonadiabatic effects that arise due to electronic Coriolis coupling.

2.1.6 Nonadiabatic Reactive Scattering

In this work we are interested in approximating the results to Eq. 2.1 for reactive collisions between an open-shell atom and closed-shell diatomic molecule. In the following sections we describe this system in detail including the choice of coordinate system and physical scattering boundary conditions.

2.2 Atom+Diatom Reactive Scattering

To begin the discussion of quantum reactive scattering dynamics we first define the system of interest. In particular, we are interested in the reactive collisions between a diatomic molecule, BC, and a lone atom, A, with a fixed amount of total energy in the system. Let m_a, m_b and m_c denote the atomic masses in the A + BC reaction. After a collision there are three possible arrangements, let γ designate the arrangement, with $\gamma = a$ the A+BC arrangement, $\gamma = b$ the B+AC arrangement, and $\gamma = c$ the C+AB arrangement. There is a fourth possibility, i.e. triatomic breakup, but we will not consider such high energy effects in this work. The main goal of reactive scattering calculations is to accurately calculate the probability of each of these possible outcomes as a function of the total energy of the system.

2.3 Collinear Atom-Diatom Reactive Scattering

In this section we start with a collinear model for the reaction dynamics in which all atoms are constrained to move along a single line. If the initial arrangement is A+BC, then only two possible outcomes can occur in a collinear reaction, namely γ = a and c. In the collinear model there are two degrees of freedom. Possible coordinate systems include bond coordinates, which are defined as the separation between AB, u_{ab}, and between BC, u_{bc}, or Jacobi coordinates to describe the system. The Jacobi coordinates are the most natural way to write the asymptotic behavior of the reactive system. The Jacobi coordinates are the following transformation of

the bond coordinates,

$$\begin{aligned} \bar{R}_a &= u_{ab} + \left(\frac{m_c}{m_b + m_c}\right) u_{bc} \\ \bar{r}_a &= u_{bc}. \end{aligned} \tag{2.2}$$

A similar expression holds for the Jacobi coordinates in the product arrangement, $\bar{R}_c$ and $\bar{r}_c$. Figure 2.1 shows a graphical representation between the Jacobi and bond coordinate systems.

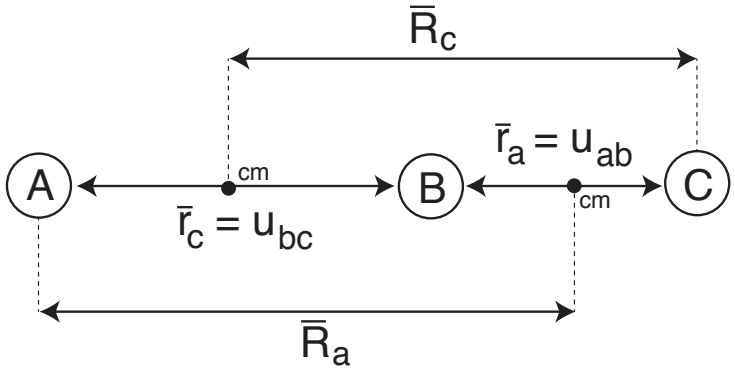

Figure 2.1: Representation of the bond coordinates, $(u_{\alpha\beta}, u_{\beta\gamma})$, and Jacobi Coordinates, $(\bar{R}_\alpha, \bar{r}_{\beta\gamma})$, for collinear reactive scattering. The 'cm' label denotes the center of mass of the diatomic molecule.

However, we elect to use a third set of coordinates in this work, the mass-scaled Jacobi coordinates (MSJ). [39–41] As we will see in Chapter 3 the reactive scattering problem is simpler in the MSJ coordinates. These MSJ coordinates are defined as (for arrangement a)

$$R_a = \lambda_a \bar{R}_a$$

$$r_a \;=\; \lambda_a^{-1}\,\bar{r}_a \tag{2.3}$$

where the scaling parameter, λ_a is defined as

$$\lambda_a = \left(\frac{\mu}{\mu_{bc}}\right)^{1/2} \tag{2.4}$$

with μ_{bc} defining the standard reduced mass of the BC diatomic moiety, and

$$\mu = \left[\frac{m_a m_b m_c}{m_a + m_b + m_c}\right]^{1/2} = \left[\frac{m_a m_b m_c}{M}\right]^{1/2},$$

where M is the total mass of the system. The relation between the Jacobi and mass-scaled Jacobi coordinates for the product arrangement is equivalent with

$$\lambda_c = \left(\frac{\mu}{\mu_{ab}}\right)^{1/2}. \tag{2.5}$$

The reactant and product MSJ coordinates are related by the orthogonal transformation [42]

$$\begin{bmatrix} R_c \\ \\ r_c \end{bmatrix} = \begin{bmatrix} \cos\alpha & \sin\alpha \\ \\ \sin\alpha & -\cos\alpha \end{bmatrix} \begin{bmatrix} R_a \\ \\ r_a \end{bmatrix}, \tag{2.6}$$

where the "skew" angle between $\vec{R}_a$ and $\vec{R}_c$ is

$$\alpha = \arctan\left[\left(\frac{m_b(m_a + m_b + m_c)}{m_a m_c}\right)^{1/2}.\right] \tag{2.7}$$

The collinear model restricts any rotational motion and therefore the total energy of the system is a function of the nuclear coordinates. When the free atom is asymptotically far from the diatomic molecule (large R limit), the total energy is the sum of the collisional energy (kinetic energy) of the free atom and the vibrational energy of the diatom. In MSJ coordinates we write this as follows

$$\lim_{R\to\infty} E_{tot}(R, r) = E_{col}(\mathrm{k}_\alpha) + E_{vib}(\mathrm{v}_\alpha) \tag{2.8}$$

where we assume the atom can be treated as a plane wave with wave vector, k, and v is the vibrational quantum number for the diatom and γ identifies the arrangement (A, B or C). Note we have set the zero of energy to be the minimum of the diatomic vibrational potential.

A typical reaction in this collinear model with fixed total energy, E_{tot}, can now be described. Atom A, with collisional energy proportional to k_a approaches diatom BC in the vibrational state v_a. With sufficient collisional energy the atom can reach the transition state (point of closest approach). From the transition state one of two outcomes is possible, either a) no reaction occurs and the reactant atom, with collisional energy proportional to k'_a, moves away from the diatomic molecule, in the vibrational state $\mathrm{v}_a{}'$, (note this may be inelastic) or b) a reaction occurs and the newly freed C atom, with collisional energy proportional to k'_c moves away from the newly formed AB diatom, in vibrational state v'_c. We denote the probability for starting in the reactant vibrational state v_α and ending up in the β exit channel in the v'_β vibrational state as $|S_{\mathrm{v}_\alpha,\mathrm{v}'_\beta}|^2$. Note the use of the $'$ denotes 'exit channel'. Figure 2.2 shows a diagrammatic representation of the collinear model.

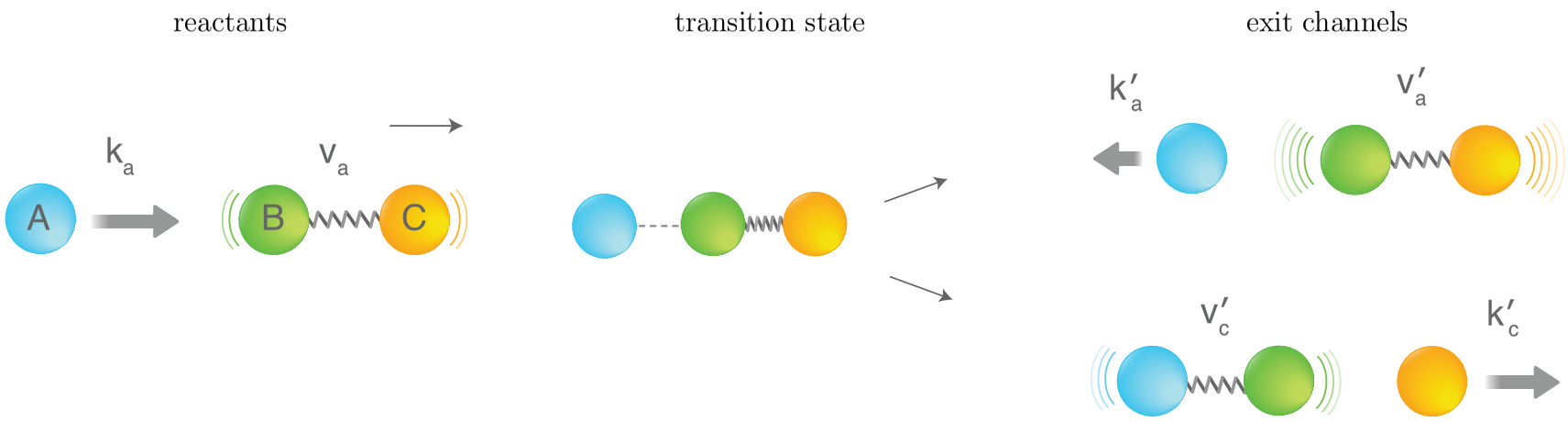

Figure 2.2: Possible energy exchange mechanisms in a collinear atom-diatom reaction. In the reactant arrangement (left) the A atom, with kinetic energy proportional to k_a, approaches the diatomic BC in the vibrational state v_a. The transition state (center) denotes the geometry of closest approach. From the transition state the system may end up in one of two exit channels; the inelastic a-channel (top right) in which the system can might rearrange the internal energy or the two reactive c-channel (bottom right). In both exit channels the energy of the system is described by the exiting atom with kinetic energy proportional to k'_γ and the diatomic in the vibrational state v'_γ.

2.3.1 Adiabatic Scattering

In the collinear model presented in the previous section all atoms are constrained to move along a line and, accordingly, the angular momentum terms vanish in the collinear model. Furthermore, in collinear geometries the interaction potential is simply a function of the magnitude of the MSJ coordinates. The collinear Hamiltonian can then be written simply as

$$H = \frac{-1}{2\mu}\nabla^2 + V^{\gamma}(R_\gamma, r_\gamma) + V_\gamma(r_\gamma) \qquad (\gamma = a, c), \tag{2.9}$$

where $\nabla^2 = \frac{1}{R_\gamma}\frac{\partial^2}{\partial R_\gamma^2}R_\gamma + \frac{1}{r_\gamma}\frac{\partial^2}{\partial r_\gamma^2}r_\gamma$. Note we will use atomic units, ($\hbar = 1$, $m_e = 1$), throughout this work, unless noted explicitly.

2.3.1.1 Potential Energy Surface

Within the Born-Oppenheimer approximation, the potential energy surface $V(R, r)$ is just the electronic energy of the ABC system as a function of the nuclear coordinates. Typically, [43, 44] we express this as a sum of two- and three-body terms, so that, in the reactant arrangement

$$V(R, r) = E_a + V_{bc}(r_a) + V_{abc}(R_a, r_a),$$

and, in the product arrangement

$$V(R, r) = E_c + V_{ab}(r_c) + V_{abc}(R_c, r_c).$$

Here V_{bc} and V_{ab} are the potential energy curves of the diatomic BC and AB molecules. We shall define the zero of energy to be the electronic energy of atom

A plus the electronic energy of the BC molecule at its equilibrium internuclear distance, $r_c = r_c^{(e)}$. Thus,

$$E_c = E_a + \Delta E_r = E_a + D_e(BC) - D_e(AB),$$

where ΔE_r is the energy of reaction, which is the difference in the bond dissociation energies of the BC and AB molecules.

2.3.1.2 Schrödinger's Equation

Using the collinear Hamiltonian from the previous section we are interested in solving the following time-independent formulation of Schrdinger's equation

$$\left[\frac{-1}{2\mu}\nabla^2 + V_{abc}(R_\gamma, r_\gamma) + V_{\alpha\beta}(r_\gamma)\right]\Psi_\gamma(R_\gamma, r_\gamma) = E_{tot}\Psi_\gamma(R_\gamma, r_\gamma) \tag{2.10}$$

We define the physical boundary of this problem as the geometries for which the lone atom is far away from the diatomic molecule, i.e. when $R_\gamma \gg 1$. We note a typical large R_γ limit is around 10-20 a_0. In the asymptotic regime of each channel the interaction potential is exactly zero, i.e.

$$\lim_{R_\gamma \to \infty} V_{abc}(R_\gamma, r_\gamma) = 0 \qquad (\gamma = a, c). \tag{2.11}$$

The Hamiltonian is separable in the asymptotic regime. We can write the asymptotic Hamiltonian in terms of kinetic and vibrational terms

$$\lim_{R_\gamma \to \infty} H = H_{kin}(R) + H_{vib}(r),$$

where

$$H_{kin}(R) = -\frac{1}{2\mu}\frac{\mathrm{d}^2}{\mathrm{d}R_\gamma^2},$$

and

$$H_{vib}(r) = -\frac{1}{2\mu}\frac{\mathrm{d}^2}{\mathrm{d}r_\gamma^2} + V_{\alpha\beta}(r).$$

This result is intuitive. When the atom is far away from the diatomic molecule the atomic degree of freedom, R_γ, is treated like a free particle, and the diatomic molecule degree of freedom is a vibrational Hamiltonian. We can write down the time-independent formulation of Schrödinger for both the kinetic and vibrational terms, namely

$$-\frac{1}{2\mu}\frac{\mathrm{d}^2}{\mathrm{d}R_\gamma^2}\Xi_\gamma(R_\gamma) = E_{col}\Xi_\gamma(R_\gamma), \tag{2.12}$$

and

$$\left[\frac{-1}{2\mu}\frac{\mathrm{d}^2}{\mathrm{d}r^2} + V_{\alpha\beta}(r_\gamma)\right]\chi_{\mathrm{v}_\gamma}(r_\gamma) = E_{vib}\chi_{\mathrm{v}_\gamma}(r_\gamma). \tag{2.13}$$

The solutions to Eq. (2.12) are plane-waves with wave vector $k_\gamma = \sqrt{2\mu E_{col}}$. The solutions to Eq. (2.13) are vibrational functions index by the vibrational quantum number and for the purposes of notation let v_γ designate the v^{th} vibrational level in arrangement γ ($\gamma = a$ or c). We note $E_{vib} = \varepsilon_{\mathrm{v}_\gamma}$ is the energy of the v^{th} vibrational level of the diatomic moiety in arrangement γ. In the following section we show how these asymptotic forms can be used to construct the physically meaningful boundary conditions.

2.3.1.3 Physical Boundary Conditions

The standard scattering boundary conditions correspond to collision of A with BC initially in a particular vibrational state v_a. In the reactant channel the wave function is a linear superposition of an incoming wave, with unit incoming flux, in

state v_a and outgoing waves, with amplitudes $S_{\mathrm{v}'_a,\mathrm{v}_a}$ in all the other energetically accessible (designated "open") BC vibrational levels. In the product channel the wave function will be a linear superposition of purely outgoing waves, with amplitudes $S_{\mathrm{v}'_c,\mathrm{v}_a}$ in all the energetically accessible AB vibrational levels. The amplitudes S form a column vector of length N_v, equal to the sum of the energetically accessible BC and AB vibrational levels.

There is an equivalent column of amplitudes, but with different values, corresponding to incoming waves in each open vibrational level of the reactant and the product states. The full $N_\mathrm{v} \times N_\mathrm{v}$ matrix of amplitudes is called the S-matrix. The modulus squared of any S-matrix element is the probability that the collision of A with BC in the vibrational level specified by the column index (remember, that "vibrational level" can refer to the vibrational motion of either BC or AB) will result in A+BC in the vibrational level corresponding to the row index. Then the general S-matrix element will be designated $S_{\mathrm{v}_\gamma',\mathrm{v}_\gamma}$, where the v_γ' denotes an outgoing term in the γ channel and v_a corresponds to the initial, incoming term in the reactant channel.

In the case where the lone atom, A, approaches the diatomic molecule, BC, in vibrational level v_a, we can write the scattering boundary conditions as (note that these are expressed in terms of unscaled, reactant and product Jacobi coordinates)

$$\lim_{R_\gamma \to \infty} \Psi(R_\gamma, r_\gamma) = \Psi_\Gamma(R_\gamma, r_\gamma) = \sum_\gamma^{a,c} \left[f^*_{\mathrm{v}_a}(\bar{R}_a, \bar{r}_a)\delta_{a,\gamma} + \sum_{\mathrm{v}_\gamma'=0}^{\mathcal{N}_\gamma} f_{\mathrm{v}_\gamma'}(\bar{R}_\gamma, \bar{r}_\gamma)\, S_{\mathrm{v}_\gamma',\mathrm{v}_a} \right] \tag{2.14}$$

where Γ is the boundary to the physically relevant domain (we cover more on the

scattering domain in Chapter 3). We use the Kronecker $\delta_{a,\gamma}$ to remind us that there is only an incoming term in the reactance ($\gamma = a$) arrangement. Here $\mathcal{N}_\gamma$ is the quantum number of the highest open vibrational level of the diatomic in the γ channel. The boundary basis functions, f_{v_γ}, with $\gamma = a$ or c, are defined as

$$f_{\mathrm{v}_\gamma} = k_{\mathrm{v}_\gamma}^{-1/2}\, \Xi_\gamma(\bar{R}_\gamma)\, \chi_{\mathrm{v}_\gamma}(\bar{r}_\gamma), \tag{2.15}$$

and $f^*_{\mathrm{v}_a}$, which implies an incoming plane wave, is the complex conjugate of f_{v_a}, an outgoing wave. Where $E_{col} = E - \varepsilon_{\mathrm{v}_\gamma}$, and μ_γ is the collision reduced mass in arrangement γ

$$\mu_a = m_a(m_b + m_c)/M$$

and similarly for the product arrangement ($\gamma = c$). Furthermore, these f functions are linear products of the solutions to Eqs. (2.12) and (2.13) so we are guaranteed to solve the asymptotically separable time independent Schrödingier equation.

By specifying the value of the solution along the boundary in Eq. (2.14), we are imposing Dirichlet boundary conditions. These boundary conditions, however, contain the $S_{\mathrm{v}'_\gamma,\mathrm{v}_a}$ amplitudes, which are not known *a priori*. As we will show in our application of the finite element method, we will simultaneously determine the wave function Ψ and the S-matrix.

2.3.2 Nonadiabatic Scattering

In the previous section we limited our scope to systems that evolve according to the BO approximation. We now turn our focus to systems where the BO approximation breaks down and we must explicitly include nonadiabatic effects. In

particular we are interested in systems with complex electronic structure. To include the effects of coupled electronic states we introduce the electronic state label η. We can then expand the Hamiltonian for the coupled system as follows

$$H(Q_\gamma, q) = \sum_{\eta,\eta'} |\eta'\rangle H^{\eta',\eta}(Q_\gamma)\langle\eta|. \tag{2.16}$$

Here Q designates the nuclear degrees of freedom $(R, r,)$ for a collinear reaction [or (R, r, θ) for a full three-dimensional description] and q designates the electronic degrees of freedom with Born-Oppenheimer electronic eigenfunctions $|\eta\rangle$. As in the adiabatic case, the nuclear coordinates, Q_γ, can be written in terms of any appropriate set of MSJ coordinates.

Explicitly including the kinetic and potential terms, as in Eq. (2.9), in the γ channel, we have

$$H(Q_\gamma, q) = -\frac{1}{2\mu}\sum_{\eta,\eta'} T^{\eta',\eta}(Q_\gamma)\delta_{\eta',\eta} + \sum_{\eta,\eta'} |\eta'\rangle V^{\eta',\eta}(Q_\gamma)\langle\eta|. \tag{2.17}$$

This is the so-called diabatic representation of the problem. The adiabatic representation of this problem is the one that diagonalizes the potential energy, $V(Q_\gamma)$, for all values of the nuclear coordinates, Q_γ. We see that the potential is coupled in the diabatic basis, and the kinetic energy is coupled in the adiabatic basis.

2.3.2.1 Potential Energy Surface

As before we can describe the potential as the sum of interaction terms and diatomic terms

$$\sum_{\eta,\eta'} |\eta'\rangle V^{\eta',\eta}(Q_\gamma)\langle\eta| = \sum_{\eta,\eta'} |\eta'\rangle V_{abc}^{\eta',\eta}(Q_\gamma)\langle\eta| + \sum_{\eta,\eta'} V_{\alpha\beta}^{\eta',\eta}(Q_\gamma)\delta_{\eta',\eta}, \tag{2.18}$$

where the diagonal nature of the diatomic potential is a requirement that the system be in a single electronic state asymptotically.

The diagonal $\eta' = \eta$ components of the potential energy $\hat{V}$ are the potential energy in state η which is a function of the nuclear degrees of freedom. The off-diagonal components of V will represent either the the mixing of two electronic states which belong to separate irreducible representations in high-symmetry geometries or coupling due to terms in the Hamiltonian (for example, spin-orbit coupling) not included in the construction of the diabatic states. We discuss the various coupling mechanisms in Section 2.1.

2.3.2.2 Schrödinger's Equation

Including the electronic state label, η, into the nuclear wave function, we see the dynamics for the electronically coupled system are governed by the following equation, namely

$$\left[-\frac{1}{2\mu}\sum_{\eta,\eta'}^{n} T^{\eta',\eta}(Q_\gamma)\delta_{\eta',\eta} + \sum_{\eta,\eta'}^{n} |\eta'\rangle V^{\eta',\eta}(Q_\gamma)\langle\eta|\right]\sum_{\eta}^{n}\Psi^{\eta}(Q_\gamma)|\eta\rangle = E_{tot}\sum_{\eta}^{n}\Psi^{\eta}(Q_\gamma)|\eta\rangle, \tag{2.19}$$

where we have assumed there are n electronic states. We represent the total molecular wave function in the coupled picture as

$$\Psi(Q_\gamma, q) = \sum_{\eta}^{n}\Psi^{\eta}(Q_\gamma)|\eta\rangle \tag{2.20}$$

This formulation of Schrödinger's equation is more easily represented in matrix form

$$\left[-\frac{1}{2\mu}\begin{bmatrix} T & 0 \\ 0 & T \end{bmatrix} + \begin{bmatrix} V^{11} & V^{12} \\ V^{12} & V^{22} \end{bmatrix}\right]\begin{bmatrix} \Psi^1 \\ \Psi^2 \end{bmatrix} = E_{tot} I \begin{bmatrix} \Psi^1 \\ \Psi^2 \end{bmatrix}, \tag{2.21}$$

where **I** is a 2x2 identity matrix. Here we have limited the system to two electronic states for simplicity. Most of this work is motivated by finding approximate solutions to Eq. (2.21).

2.3.2.3 Physical Boundary Conditions

The extension from Eq. 2.14 to multiple electronic states is straightforward. The electronic state index η can be added to the expansion coefficients and the wave function must satisfy boundary conditions appropriate to multi-state scattering.

$$\lim_{R_\gamma \to \infty} \Psi(R_\gamma, r_\gamma) = \Psi_\Gamma(R_\gamma, r_\gamma) = \sum_{\gamma}^{a,c} \left[f_{\mathrm{v}_a}^{\eta\ *}(\bar{R}_a, \bar{r}_a)|\eta\rangle \delta_{a,\gamma} + \sum_{\eta'} \sum_{\mathrm{v}_{\gamma'}} S_{\mathrm{v}_{\gamma'},\mathrm{v}_a}^{\eta',\eta} f_{\mathrm{v}_{\gamma'}}^{\eta'}(\bar{R}_\gamma, \bar{r}_\gamma)\,|\eta'\rangle \right] \tag{2.22}$$

where $f_{\mathrm{v}_\gamma}^{\eta}$ is the asymptotic (A+BC or AB+C) wavefunction (the product of a plane wave multiplied by a vibrational wave function for the diatomic in electronic state η in arrangement γ,

$$f_{\mathrm{v}_\gamma}^{\eta} = (k_\gamma^\eta)^{-1/2} \Xi_\gamma^\eta(R_\gamma) \chi_{\mathrm{v}_\gamma}^\eta(r_\gamma). \tag{2.23}$$

Inelastic or reactive scattering can occur to any energetically open, vibrational level associated with any electronic state. The S matrix is doubly-indexed in the electronic state, so that $S_{\mathrm{v}_{\gamma'},\mathrm{v}_a}^{\eta',\eta}$ is the amplitude for a transition from the BC vibrational state v_a in electronic state η to either the AB vibrational state $\mathrm{v_c}'$ in the ABC electronic state η' or BC vibrational state $\mathrm{v_a}'$ in the ABC electronic state η'.

With the equations of motion and boundary conditions well defined we are

now able to approximate the reaction dynamics for collinear reactive scattering. In Chapter 3 we derive a novel finite element algorithm to simultaneously determine the scattering amplitudes and the scattering wave function for both adiabatic and nonadiabatic systems.

2.4 3D Atom-Diatom Reactive Scattering

In reality the triatomic system is not constrained to motion along a line. While the collinear model of reactive scattering provides intuition to the nature of nonadiabatic dynamics, one needs to account for all degrees of freedom using a three dimensional model to achieve 'chemically accurate' results. Instead of a vibrational state, the diatomic molecule is most accurately describe by a rotational-vibrational (ro-vibrational) state. We use the notation (v,j) to identify the ro-vibrational state where v is the vibrational quantum number and j is the rotational quantum number. Figures 2.3 and 2.4 show the MSJ coordinates and a schematic representation of the possible energy exchanges in a fully three-dimensional atom-diatom reaction, respectively.

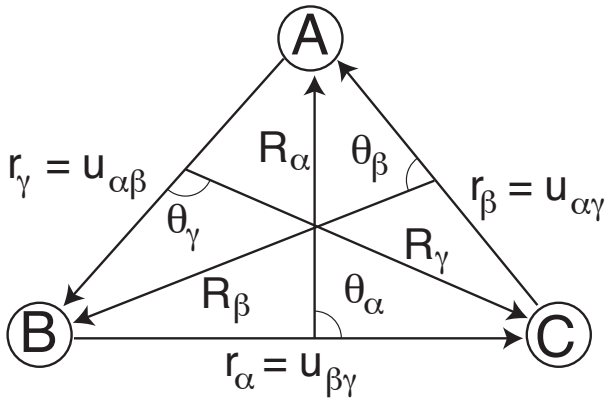

Figure 2.3: Representation of the bond coordinates, $(u_{\alpha\beta}, u_{\beta\gamma})$, and Jacobi Coordinates, $(\bar{R}_\alpha, \bar{r}_{\beta\gamma}, \theta_\alpha)$, for collinear reactive scattering.

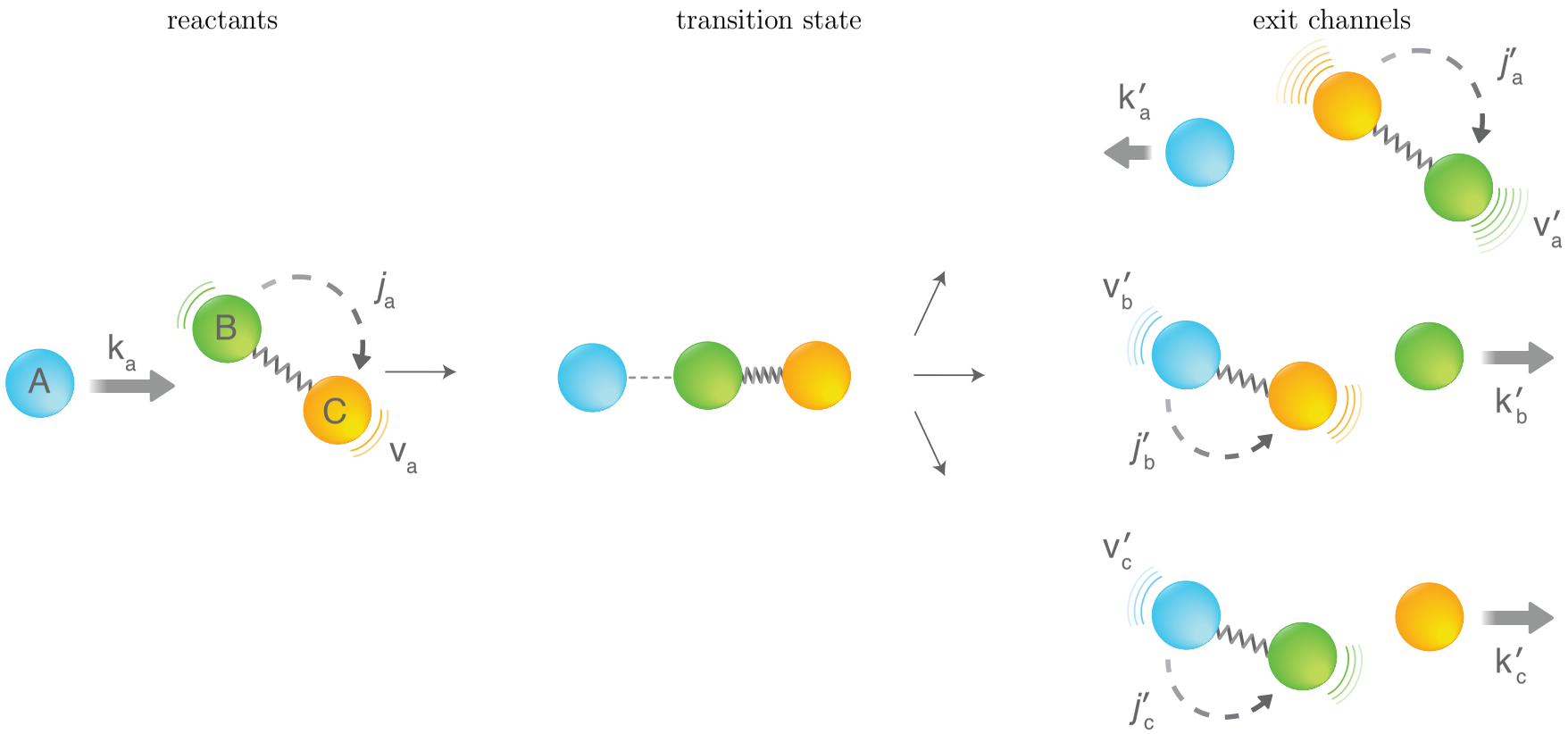

Figure 2.4: Possible energy exchange mechanisms in a fully 3D atom-diatom reaction. In the reactant arrangement (left) the A atom, with kinetic energy k_a, approaches the diatomic BC in the ro-vibrational state (v_a, j_a). The transition state (center) denotes the geometry of closest approach, in this case a collinear geometry. From the transition state the system may end up in any of three exit channels; the inelastic a-channel (top right) in which the system can only rearrange the internal energy or one of the two reactive channels 'b' (center right) or c (bottom right). In each exit channel the energy of the system is described by the exiting atom with kinetic energy k'_γ and the diatomic in the ro-vibrational state (v'_γ, j'_γ).

2.4.1 Adiabatic Scattering

In this section we extend the results from collinear atom and diatom dynamics to rotating systems. The Hamiltonian for the 3D problem can be written in terms of any of the three arrangement MSJ coordinates. From [42] we have

$$H = -\frac{1}{2\mu}\left[\frac{1}{R_\gamma}\frac{\partial^2}{\partial R_\gamma^2}R_\gamma + \frac{1}{r_\gamma}\frac{\partial^2}{\partial r_\gamma^2}r_\gamma + \frac{\mathbf{L}_\gamma^2}{R_\gamma^2} + \frac{\mathbf{j}_\gamma^2}{r_\gamma^2}\right] + V_{tot}^\gamma(R_\gamma, r_\gamma, \theta_\gamma) \qquad (\gamma = a, b, c). \tag{2.24}$$

The orbital angular momentum operator, $\mathbf{L}_\gamma$, is the kinetic energy corresponding to the lone atom orbiting the diatom, and the diatomic angular momentum operator, $\mathbf{j}_\gamma$, is associated with the kinetic energy of the rotating diatomic. The total angular momentum of the system is the sum of the orbital and angular momenta, $\mathbf{J} = \mathbf{L} + \mathbf{j}$.

2.4.1.1 Potential Energy Surface

In any arrangement we can write the potential energy surface from Eq. (2.24) as a sum of two and three body terms

$$V_{tot}^\gamma(R_\gamma, r_\gamma, \theta_\gamma) = E + V_\gamma(r_\gamma) + V^\gamma(R_\gamma, r_\gamma, \theta_\gamma)$$

At large values of R_γ we have

$$\lim_{R_\gamma \gg 1} V^\gamma(R_\gamma, r_\gamma, \theta_\gamma) = 0.$$

As in the collinear case, in the limit of $R_\gamma \gg 1$ the potential only depends on the diatomic coordinate and the Hamiltonian given in Eq. (2.24) is asymptotically separable.

2.4.1.2 Schrödinger's Equation

We limit the discussion in this section to cases with where the total angular momentum is set to zero, i.e. $J = 0$. The unrestricted case has been covered in detail in Ref [42]. Writing the time independent formulation of Schrödinger's equation for the 3 dimensional problem we have

$$H\Psi(R_\gamma, r_\gamma, \theta_\gamma) = E_{tot}\Psi(R_\gamma, r_\gamma, \theta_\gamma). \tag{2.25}$$

It is typical to expand the total wave function as a product of radial functions and angular functions

$$\Psi(R_\gamma, r_\gamma, \theta_\gamma) = \sum_{j=0} G_j(R_\gamma, r_\gamma)P_j = \sum_{j=0} \frac{g_j(R_\gamma, r_\gamma)}{Rr}P_{j'}, \tag{2.26}$$

where $P_j(\cos\theta_\gamma)$ is a Legendre polynomial associated with the j^{th} rotational state of the diatomic molecule in the γ arrangement. We can reduce the three dimensional problem to a set of coupled equations in two dimensions by integrating over the angular degrees of freedom,

$$\sum_{j,j'} \int P_{j'}[H - E]P_j g_j(R_\gamma, r_\gamma) = 0. \tag{2.27}$$

Evaluation of this integral yields the following set of equations coupled equations

$$\sum_{j,j'} \left[-\nabla^2\delta_{j,j'} + \frac{j(j+1)}{I(R_\gamma, r_\gamma)} + 2\mu\left[V_{j,j'}(R_\gamma, r_\gamma) - E\right]\right] g_j(R_\gamma, r_\gamma) = 0 \tag{2.28}$$

where $\nabla = \partial^2 R_\gamma + \partial^2 r_\gamma$, $I(R_\gamma, r_\gamma) = \left(\frac{1}{R_\gamma^2} + \frac{1}{r_\gamma^2}\right)$. The potential term will, in general, couple all values of j,

$$V_{j'j}(R_\gamma, r_\gamma) = \int P_{j'}V_{tot}^{\gamma}(R_\gamma, r_\gamma, \theta_\gamma)P_j \sin\theta_\gamma \, \mathrm{d}\theta_\gamma.$$

We have used $dV = {R_\gamma}^2 {r_\gamma}^2 \sin\theta_\gamma \mathrm{d}\theta_\gamma \mathrm{d}R_\gamma \mathrm{d}r_\gamma$ as the volume element associated with the Hamiltonian. We have also used the fact that the Legendre polynomials are eigenfunctions of the total angular momentum operator. In the case of $J = 0$, the angular momentum operators from Eq. (2.24) can be written as

$$\frac{\mathbf{L}^2}{R_\gamma^2} + \frac{\mathbf{j}^2}{r_\gamma^2} = \frac{(\mathbf{J} - \mathbf{j})^2}{R_\gamma^2} + \frac{\mathbf{j}^2}{r_\gamma^2} = \frac{\mathbf{j}^2}{I(R, r)} \tag{2.29}$$

and

$$\int P_{j'} \mathbf{j}^2 P_j \sin\theta_\gamma \, \mathrm{d}\theta_\gamma = j(j+1)\delta_{j,j'}. \tag{2.30}$$

In practice the summations over j are truncated at some j_{max} such that all rovibrational states have energy less than the total energy, E_{tot}.

2.4.1.3 Physical Boundary Conditions

When the lone atom is asymptotically far away from the diatomic molecule in a given arrangement, (large R_γ limit), we can separate the Hamiltonian (Eq. 2.24) into atomic and diatomic terms

$$\lim_{R_\gamma \gg 1} H = H(R_\gamma) + H(r_\gamma).$$

The R_γ dependent terms can be written as

$$H(R_\gamma) = -\frac{1}{2\mu}\left[\frac{\partial^2}{\partial R_\gamma^2} + \frac{j(j+1)}{R_\gamma^2}\right]. \tag{2.31}$$

The wave function describing the motion of the lone atom must satisfy the following formulation of Schrödinger's equation

$$\left[H(R_\gamma) - E_{col}\right] \rho_j(R_\gamma) = 0.$$

This can be rewritten as

$$\left[-\frac{\partial^2}{\partial R_\gamma^2} + \frac{j(j+1)}{R_\gamma^2} - k^2\right] \rho_j(R) = 0,$$

where $k = \sqrt{2\mu E_{col}}$. Using the change of variables $x = kR_\gamma$, we have

$$\left[x^2\partial^2 x - j(j+1) + x^2\right] \hat{\rho}_j(x) = 0.$$

The solutions to this differential equation are the Riccati-Bessel functions,

$$\hat{j}_n(x) = x j_n(x) = \sqrt{\pi x/2}\ J_{n+1/2}(x)$$

and

$$\hat{y}_n(x) = -x y_n(x) = -\sqrt{\pi x/2}\ Y_{n+1/2}(x).$$

We use the Ricatti-Hankel functions

$$\hat{h}_n^{(1,2)}(x) = xh = x[j_n(x) \pm i y_n(x)],$$

whose asymptotic behavior appropriately describes the free atom,

$$\lim_{x \gg 1} \hat{h}_n^{(1,2)}(x) = (\mp i)^{n+1} \exp[\pm ix]. \tag{2.32}$$

The r dependent Hamiltonian from Eq. 2.31 can be written

$$H(r_\gamma) = -\frac{1}{2\mu}\left[\frac{\partial^2}{\partial r_\gamma^2} + \frac{j(j+1)}{r_\gamma^2}\right] + V_\gamma(r_\gamma).$$

Asymptotically, the diatomic wave function in the γ arrangement must satisfy

$$\left[-\frac{1}{2\mu}\partial^2 r_\gamma + \frac{j(j+1)}{2\mu r_\gamma^2} + V_{\beta,\gamma}(r_\gamma)\right] \chi_{\mathrm{v}_\gamma,j}(r_\gamma) = \varepsilon_{\mathrm{v}_\gamma,j}\chi_{\mathrm{v}_\gamma,j}(r_\gamma). \tag{2.33}$$

The solutions to Eq. 2.33 are the rotational-vibrational vibrational states, $X_{\mathrm{v}_\gamma,j}(r_\gamma)$, in the γ arrangement with vibrational quantum number v_γ and rotational quantum number j_γ. In practice these are determined numerically.

We can are free to take the asymptotic solution to be a linear combination of products of Ricatti-Bessel functions and rovibrational states. Typically we set the total energy of the reaction and fix the diatomic molecule in some initial rovibrational state $(\mathrm{v}_\gamma, j_\gamma)$. We can then write $E_{col} = E - \varepsilon_{\mathrm{v}_\gamma, j_\gamma}$.

The reactant channel has both an incoming and outgoing term, while the other two channels have purely outgoing terms. For a system prepared with total energy E, and the reactant diatomic, BC, initially in the rovibrational state (v_a, j_a), the boundary conditions can be written in terms of S-matrix elements, $S^{\mathrm{v}_\gamma', j_\gamma'}_{\mathrm{v}_a, j_a}$ as

$$\Psi_\Gamma(R_\gamma, r_\gamma, \theta_\gamma) = \sum_{\gamma}^{\gamma=a,b,c} \left[\hat{h}^{(2)}_{j_a}(k_{\mathrm{v}_a, j_a} R_a) \chi_{\mathrm{v}_a, j_a}(r_a) \delta_{a,\gamma} + \sum_{j'_\gamma} \sum_{\mathrm{v}_{\gamma'}} \hat{h}^{(1)}_{j'_\gamma}(k_{\mathrm{v}_{\gamma'}, j'_\gamma} R_\gamma) \chi_{(\mathrm{v}_{\gamma'}, j'_\gamma)}(r_\gamma) S^{\mathrm{v}_\gamma', j_\gamma'}_{\mathrm{v}_a, j_a} \right]. \tag{2.34}$$

The physical interpretation of these scattering boundary conditions for the three dimensional problem correspond to the collision of A with BC in a particular rovibrational state, (v_a, j_a) with a fixed total energy, E. The collisions can redistribute the energy of the reactants (inelastic collisions) and produce a new rovibrational state in the reactant arrangement, (v_a', j_a'), with probability $|S^{\mathrm{v}_a', j_a'}_{\mathrm{v}_a, j_a}|^2$. The collisions may also induce a reaction to one of two product channels, b: B+AC in a product rovibrational state, (v_b', j_b') with probability $|S^{\mathrm{v}_b', j_b'}_{\mathrm{v}_a, j_a}|^2$ or c: C+AB in a product rovibrational state, (v_c', j_c') with probability $|S^{\mathrm{v}_c', j_c'}_{\mathrm{v}_a, j_a}|^2$. Extremely high energy collisions may induce a triatomic breakup, but we will not consider such high energy collisions here.

Ultimately, we are interested in chemically accurate predictions of the collision dynamics of open shell, atom-diatom reactions, especially those which violate the BO

approximation. The complexity of the equations of motion becomes less tractable as we add the electronic state index and remove the $J = 0$ restriction.

2.5 Conclusion

In this chapter we have defined our system of interest, namely nonadiabatic reactive collisions between an atom and diatomic molecule. We are interested in approximating the reactive scattering wave function and the state-to-state reaction probabilities as a function of the collisional energy. To this end, in the next chapter we derive a novel extension of the finite element method applied to quantum reactive scattering dynamics for nonadiabatic reactions.

Chapter 3: Reactive Atom-Diatom Systems and the Finite Element Method

3.1 Overview

Theoretical and computational advances have enabled the fully-quantum modeling of elementary chemical reactions at a state-to-state level [74]. Time-independent methods [6] can be used to investigate, in detail, quantum effects of reactive systems such as resonances [75] and nonadiabatic transitions [63] in triatomic (atom and diatomic molecule) reactions. Time-dependent methods [74, 76–78] have enabled the state-to-state study of four-atom reactions in all degrees of freedom [79–81] and, just recently, the study of a 6-atom reaction, [82] albeit in reduced dimensionality.

These sophisticated methods allow the determination of state-resolved differential and integral cross sections. This involves calculation of the S-matrix which arises in the imposition of physical scattering boundary conditions. Despite the vast attention given to the development of computational machinery for the determination of the S-matrix, there has been little attention devoted to developing a qualitative quantum picture of the mechanism of reactive scattering.

Most of our understanding of reaction dynamics is based on the standard

one-dimensional models of passage over, or through, a barrier. In two dimensions, qualitative pictures of chemical reactions are common, [83–85] but based on classical trajectories. Time-dependent treatments, in which the evolution of a wave packet is followed in time, can provide quantum insight into a reaction as it unfolds. A beautiful illustration for the $H+H_2$ reaction is presented in the review article by Althorpe and Clary, [74] although other examples are rare. One disadvantage of the time-dependent method is that the evolving wave packet is a convolution over a large number of energies so that watching the wave packet move in time gives little insight into the dynamics at a particular energy.

A time-independent approach can yield an energy-resolved picture, specifically within the hydrodynamic interpretation of quantum mechanics. Here, the probability density $|\Psi|^2$ is seen as an inhomogeneous fluid [86]. The flow of this fluid is described by the probability current density field $\mathbf{J}$.

$$\mathbf{J}(q) = \frac{-i\hbar}{2m}[\Psi(q)\boldsymbol{\nabla}\Psi^*(q) - [\boldsymbol{\nabla}\psi(q)]\psi^*(q)] \tag{3.1}$$

There are obvious analogies to the flow of fluids or electricity. Of course, due to the uncertainty principle, energy resolution is achieved only at the loss of temporal information.

In early work, Hirschfelder and co-workers explored the coordinate dependence of the probability current density field for model two-dimensional reactive potential energy surfaces [20, 87]. They identified, as might be expected in a hydrodynamic pictures, vortices and eddies, which varied as a function of the collision energy

and the curvature of the potential. Kuppermann and co-workers, in work largely unpublished, [21,88] determined the probability current density field for the collinear $H+H_2$ reaction. Wyatt and co-workers have investigated the probability current density field for the $H+H_2$ and $F+H_2$ reactions, using both time-dependent ($H+H_2$) and time-independent ($F+H_2$) methods. [22–24, 89]

Manolopoulos, Alexander and co-workers have presented techniques for the calculation of the probability current density field in inelastic scattering, [26, 90] and in molecular photodissociation [25, 91–94]. In their subsequent analysis of the photodissociation of the HBr molecule, Péoux and co-workers have compared the time-independent viewpoint, in which the evolution of the probability current density field is followed in space, with the time-dependent viewpoint, in which the evolution of the wave packet is followed in time [95].

The time-independent treatment of quantum reactive scattering dates back nearly 40 years [96–98]. The vast majority of these treatments [98–100] involve finite-difference based [101] numerical solutions of the Schrödinger equation for a given set of physical scattering boundary conditions. Because of numerical stability issues, one does not solve for the wave function directly, but rather for its logarithmic derivative [6, 102, 103] or, in the renormalized Numerov method, [104, 105] the ratio of the wave function at one point to its value at a previous point.

Consequently, to determine the probability and the probability current density field one must store the log-derivative matrix at each step (or, alternatively, the wave function ratio), determine the S-matrix, and, finally, extract the scattering wave function from the S-matrix and the stored set of log-derivative matrices. Similarly,

in a time-dependent treatment post-processing is required to obtain the scattering wave function at given collision energy by Fourier transform of the wave packet.

In contrast to propagation and time-dependent methods, basis set methods solve directly for the scattering wave function, and are thus an important tool for the dynamicist. Specifically, the S-matrix version of the Hulthén-Kohn variational principle of Miller and Zhang [106–108] has been the standard in variational scattering calculations. Jaquet and others [109, 109, 110] implemented this approach with a finite element (FE) basis.

Here we describe an alternative FE approach to determine simultaneously a piece-wise approximation to the scattering wave function and the S-matrix itself. In the FE treatment of Askar, Cakmak, and Rabitz [18] and Jaquet [111] the wave function on the reactant and product boundaries is fixed to a given vibrational state. One must solve an FE linear matrix problem for each of these pre-imposed boundary conditions, then taking linear combinations to correspond to the scattering boundary conditions. In our version we determine one or more columns of the S-matrix from a single calculation.

There have been relative few applications of the FE method to reactive scattering [18, 111–118]. In their initial paper, Askar, Cakmak and Rabitz [18] point out the advantages of the FE approach over the more widely used propagator methods [98–100]. First, one can use a single set of coordinates, which eliminates the need to match different coordinate systems asymptotically. Secondly, FE methods can easily handle the irregular angled domains of reactive scattering. Thirdly, the scattering wave function is generated directly, at no extra cost. Finally, compared

to traditional propagator methods, [98–100] the FE method involves larger, but extremely sparse matrices. This allows the use of extremely efficient sparse-matrix solvers, of which MATLAB takes complete advantage.

We have developed a MATLAB-based code, which takes advantage of the ease and sophistication of this widely-used computational package, as well as the availability of third-party scripts. Our code is available online [119]. This can be a tool to conceptualize the quantum character of chemical reactions in more than one dimension. Through plots of the probability current density field one can visualize quantum tunneling, recrossing of the transition state, and quantum vortices.

In Secion 3.2 we first work through the application of the finite element method to bound state, collinear atom-diatom systems. This is a natural starting place as the boundary conditions (that the wave function vanish asymptotically) are the easiest to enforce. We then derive our novel extension of the FE machinery to reactive collisions of collinear atom-diatom systems evolving on a single potential surface in Section 3.3. In this Section we also compare our algorithm with the FE algorithm developed previously [18] and provide evidence that our results match those from other methods for the well studied H+H_2, F+H_2 and F+HCl reactions. In Section 3.4 we remove the single surface constraint and extend our algorithm to nonadiabatic, collinear, atom-diatom systems. Finally, in Section 2.4 we focus on how this FE algorithm can be used for bound, 3D atom-diatom systems. We conclude this chapter with our thoughts on how one might apply this algorithm to reactive fully 3D, rotating, atom-diatom systems.

3.2 Collinear Bound Systems

In this section we outline the application of the finite element method to approximate the bound state wave functions and energies for collinear atom-diatom systems.

3.2.1 Weak Formulation of Schrödinger's Equation

We first outline a general variational approach to boundary value problems (BVP) before application to reactive scattering. The two-dimensional Schrödinger equation from Eq. (2.10), in atomic units we have

$$\left[-\nabla^2 + 2m(V - E)\right] \Psi = 0 \text{ on } \Omega \tag{3.2}$$

and

$$\Psi = 0 \text{ on } \Gamma, \tag{3.3}$$

where Ω is the relevant physical domain and Γ is the boundary to this domain. Note we have assumed the wave function vanishes along the boundary.

By premultiplying the differential Eq. (3.2) by any arbitrary function, ξ (this is conventionally labelled a "test" function), and integrating over the domain we obtain

$$\int_\Omega \xi \left[-\nabla^2 + 2m(V - E)\right] \Psi = 0 \tag{3.4}$$

We can now apply Green's formula – integration by parts in more than one dimension – to the first term in Eq. (3.4) to obtain

$$-\int_\Omega \xi \nabla^2 \Psi = \int_\Omega \nabla\xi \cdot \nabla\Psi - \int_\Gamma \xi(\hat{n} \cdot \nabla)\Psi \tag{3.5}$$

where $\hat{n} \cdot \nabla$ is the derivative normal to the boundary Γ. Substitution of Eq. (3.5) into Eq. (3.4) yields the variational formulation of Eq. (3.23), namely

$$\int_{\Omega} \nabla\xi \cdot \nabla\Psi + 2m\,\xi\,(V - E)\Psi = \int_{\Gamma} \xi\,(\hat{n} \cdot \nabla)\Psi_{\Gamma} \tag{3.6}$$

where we have explicitly used Eq. (3.24).

Borrowing notation from the finite element community, we introduce the bilinear form [101], or energy inner product [120],

$$a(\xi, \Psi) = \int_{\Omega} \nabla\xi \cdot \nabla\Psi + 2m\,\xi(V - E)\Psi \tag{3.7}$$

and defining the boundary integral

$$b(\xi, \Psi_{\Gamma}) = \int_{\Gamma} \xi(\hat{n} \cdot \nabla)\Psi_{\Gamma} \tag{3.8}$$

we can write the original BVP [Eq. (3.23)] more compactly as

$$a(\xi, \Psi) = b(\xi, \Psi_{\Gamma}). \tag{3.9}$$

Equation (3.9) is entirely general for any system that can be described by the time-independent Schrödinger equation. Note that this transformation underlies the Kohn (and other) variational methods [42, 121, 122].

3.2.2 Finite-Element Solution

To obtain an approximate solution of Eq. (3.9) we first discretize the domain into a finite, triangulated domain, Ω, defined by N nodes (vertices) and delimited by a polygonal boundary, Γ. The desired approximation is then typically represented as

a piece-wise function on this triangulation. In this work we use piece-wise Galerkin-type polynomials for simplicity. The triangulation procedure for the first three polynomial order, P, are shown in Fig. 3.1.

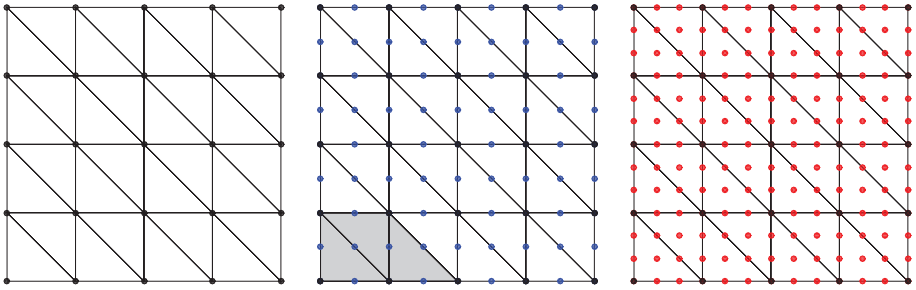

Figure 3.1: Model triangulations for the unit square [-1 1]x[-1 1] for the first three polynomial orders. (left) For unique piece-wise linear polynomials ($P = 1$) the triangulation must be defined at three points for every triangle. These three points are taken to be the nodes (vertices) of each triangle shown as black dots. (center) For unique piece-wise quadratic polynomials ($P = 2$) the triangulation must be defined at 6 points per triangle. It is typical to add the midpoint of each edge for every triangle, shown here in blue. The shaded region is used to model the Galerkin polynomials in Fig. 3.2. (right) Finally, for unique piece-wise cubic polynomials ($P = 3$) the triangulation must contain 10 points per triangle. The common placement of these nodes is shown in red.

We then expand the solution Ψ in a set of basis functions:

$$\Psi \approx \sum_{i=1}^{N} C_i \, \Phi_i, \tag{3.10}$$

where Φ_i is a piece-wise polynomial associated with the i^{th} node.

$$\Phi_i(R, r) = \sum_{j=1}^{n_i} \phi_{ij}(R, r) \tag{3.11}$$

Here $\{R, r\}$ designate two spatial coordinates and the j index refers to one of the n_i triangles associated with node i (in two dimensions usually $n_i = 6$). Above the j^{th} triangle, the function ϕ_{ij} is a bivariate polynomial of order P, which we can write as

$$\phi_{ij}(R, r) = \sum_{k,l}^{k+l \leq P} c_{ij,kl} \, R^k \, r^l. \tag{3.12}$$

These so-called "hat" functions have a value of unity at node i and are zero at all other nodes [120].

The simplest approximation involves limiting the polynomial order to $P = 1$, in which case the nodes are the vertices of the triangles. The functions $\phi_{ij}(R, r)$ are planes, so that the resulting polynomial basis function Φ_i [Eq. (3.11)] is a planar, polygonal (usually hexagonal) pyramid, which is unity at node i and vanishes at each of the nearest-neighbor nodes.

For $P = 2$ the nodes are defined by both the vertices of the triangles, and, in addition, the mid-points of each side of every triangle. This gives rise to two types of hat functions (illustrated in Fig. 3.2): those which are unity at a vertex and those which are unity at a mid-point. In the present description we focus on the P2 basis for clarity, but all of the following results hold for any polynomial order N. Furthermore, the provided software takes the polynomial order N as an input and automatically prepares the calculation allowing the user to efficiently tune the accuracy of a given calculation.

The $P = 2$ hat functions for triangle j are obtained by solution of the equation

$$\mathbf{XC} = \mathbf{1}, \tag{3.13}$$

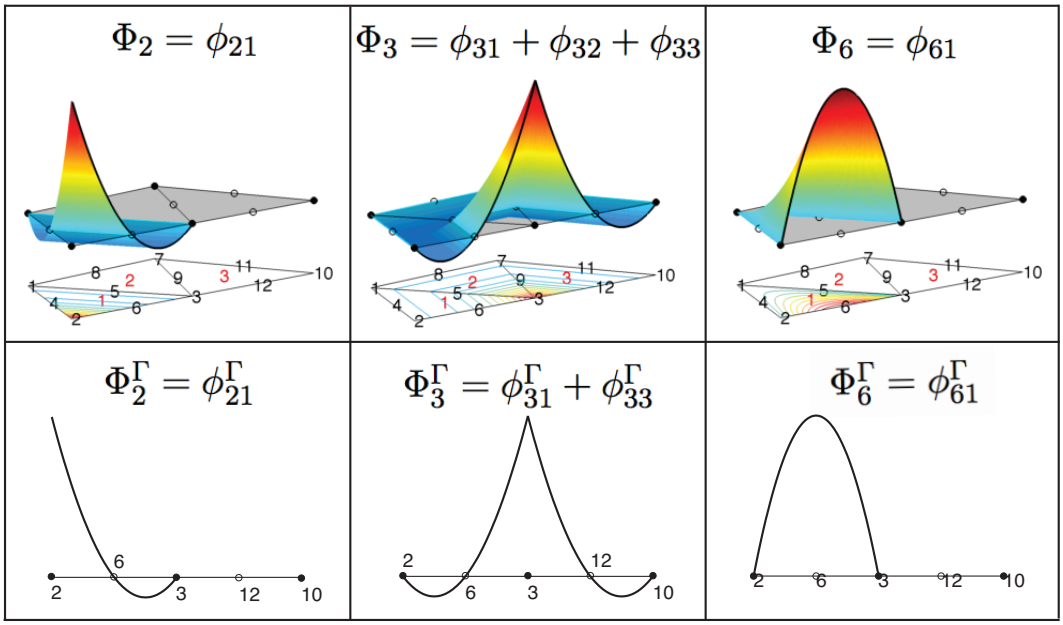

Figure 3.2: Polynomial basis functions along the boundary for the sample triangulation shown in Fig. 3.1. The red numbers denote the triangle numbering scheme, and the black numbers denote the nodal numbering scheme. The black lines in the upper panel are the projections of the Φ_i functions along the boundary. These 1D functions are shown separately in the lower panel. The filled dots indicate a vertex node, and the empty dots indicate a midpoint node. As the center panel reveals, not all ϕ_{ij} functions contribute to Φ_j^Γ.

where the dimension of the $\mathbf{X}$ matrix is 6×6, with the row indices corresponding to the points (vertices and mid-points) and the column indices corresponding to the double kl index in Eq. (3.12), so that

$$X_{i,m=1:6} = [R_i^2,\ R_i r_i,\ r_i^2,\ R_i,\ r_i,\ 1].$$

Thus the row index of the $\mathbf{C}$ matrix corresponds to the kl indices while the column

index corresponds to j.

The hat functions which are unity above the vertex nodes are a composite of, in general, $n_i = 6$ bivariate quadratic functions, from Eq. (3.11), one above each triangle. In contrast, any midpoint node is shared by at most two triangles. Thus the $P = 2$ hat functions which are unity at a midpoint node are a composite of at most two bivariate quadratic functions above the two triangles which share this midpoint, so that $n_i = 2$ in Eq. (3.11). In both cases the hat functions are piecewise continuous along the common sides of any two triangles which share either the vertex or the midpoint.

Obviously, one can adopt more sophisticated ways of choosing both the triangularization algorithm and the basis functions in Eq. (3.10) with the goal of maximizing accuracy for a given domain Ω while minimizing the number of nodes. (One choice which comes to mind is the use of Lobatto shape functions [123]). For the present two-dimensional application, the $P = 2$ basis functions defined above offer an excellent compromise between simplicity, accuracy, and computational speed.

By expanding the wave function in a sum of basis functions, we convert Eq. (3.9) into a matrix equation. We start by replacing the true wave function in the bilinear form with the basis function expansion, and replacing the test function, ξ, by a single basis function, Φ_j, which yields

$$a(\Phi_j, \sum_i C_i \Phi_i) = \sum_i C_i \, a(\Phi_j, \Phi_i) = b(\Phi_j, \Psi_\Gamma). \tag{3.14}$$

This can be cast as a matrix equation

$$\mathbf{A}C = 0. \tag{3.15}$$

Where we have assumed, that for a bound-state problem, the wave function vanishes along the boundary, Γ, so that Eq. (3.15) reduces to the standard set of homogeneous linear equations. In the following section we give the numerical details for how to compute the matrix elements of $\mathbf{A}$ using the bilinear form and the Galerkin polynomials.

3.2.3 FE Matrix Integrals

In this section we briefly outline the numerical evaluation of the integrals that constitute the elements of the $\mathbf{A}$ matrix in Eq. (3.15). We start with the bilinear form between two Φ basis functions, namely (written in MSJ coordinates)

$$\mathbf{A}_{ij} = a(\Phi_i, \Phi_j) = \int_\Omega \nabla\Phi_i \cdot \nabla\Phi_j \; dRdr + 2\mu \left[\int_\Omega \Phi_i \, V \, \Phi_j \; dRdr - \int_\Omega \Phi_i \, \Phi_j \; dRdr \right]. \tag{3.16}$$

The evaluation of these integrals is simplified using the bivariate polynomials from Eq. (3.12)

$$\begin{aligned} \mathbf{A}_{ij} &= \sum_{k,l} \int_\Omega \delta_{kl} \nabla\phi_{ik} \cdot \nabla\phi_{jl} \; dRdr + 2\mu \left[\int_\Omega \delta_{kl}\phi_{ik} \, V \, \phi_{jl} \; dRdr - E \int_\Omega \delta_{kl}\phi_{ik} \, \phi_{jl} \; dRdr \right] \\ &= \mathbf{T}_{ij} + 2\mu \left[\mathbf{V}_{ij} - E \, \mathbf{O}_{ij} \right]. \end{aligned} \tag{3.17}$$

The delta function, δ_{kl}, is the source of the sparsity in the FE calculation. The major advantage of the FE method is that any single basis function has a non-zero overlap with a tiny subset of the total set of functions in Ω, specifically only for nodes which share a common triangle, i.e. $k = l$. For $P = 2$ calculations, a typical node has non-zero overlap with 19 other nodes. As we shall see, this extreme sparseness dramatically reduces the required computational time.

Rather than use MSJ Jacobi coordinates to evaluate the elements of the **T**, **V**, and **O** matrices, we first transform to a "standard" triangle, with coordinates designated (x, y) and vertices (0,0), (0,1), and (1,0). To convert the integrals in Eq. (3.17) from MSJ coordinates to standard triangle coordinates we need to we need to define, in standard triangle coordinates, the basis functions $\phi_{ik}(R, r)$, the gradient operator and the area element $\mathrm{d}R\mathrm{d}r$.

For a given triangle k with vertices (R_1, r_1), (R_2, r_2), and (R_3, r_3) the transformation to the standard triangle is

$$\begin{bmatrix} R_k \\ \\ r_k \end{bmatrix} = \mathbf{M} \begin{bmatrix} x \\ \\ y \end{bmatrix} + \begin{bmatrix} R_1 \\ \\ r_1 \end{bmatrix}, \tag{3.18}$$

where

$$\mathbf{M} = \begin{bmatrix} R_2 - R_1 & R_3 - R_1 \\ \\ r_2 - r_1 & r_3 - r_1 \end{bmatrix}.$$

This transformation will allow us to express the basis functions in terms of the basis functions for the standard triangle. These are (for $P = 2$)

$$\phi_{ij}(x, y) = c_{20}x^2 + c_{11}xy + c_{02}y^2 + c_{10}x + c_{01}y + c_{00},$$

where we have suppressed the ij labels in Eq. (3.12) and the coefficients, obtained from Eq. (3.13), for nodes $i = 1 - 6$ are listed in Table 3.1. These functions are unity, successively, at the 6 nodes (vertices and edge mid-points) of the standard triangle, ordered as (0,0), (1,0), (0,1), (1/2,1/2), (1/2,0) and (0,1/2). It is easy to verify that these polynomials vanish at all other nodes.

Table 3.1: Expansion coefficients for the $P = 2$ (quadratic) basis functions, ϕ_{ij}, for the standard triangle.

j	non-zero node	c_{20}	c_{11}	c_{02}	c_{10}	c_{01}	c_{00}
1	(0,0)	2	4	2	–3	–3	1
2	(1,0)	2	0	0	–1	0	0
3	(0,1)	0	0	2	0	–1	0
4	(1/2,0)	–4	–4	0	4	0	0
5	(1/2,1/2)	0	4	0	0	0	0
6	(0,1/2)	0	–4	–4	0	4	0

The gradient operator transforms as

$$\boldsymbol{\nabla}_{Rr} = (\mathbf{M}^{-1})^T \boldsymbol{\nabla}_{xy}$$

and the unit area as

$$dRdr = \det(\mathbf{M})\, dxdy.$$

Over any given triangle we can also expand the potential in terms of the six $P = 2$ basis functions, with expansion coefficients equal to the value of the potential at the vertex or midpoint at which the particular basis function is non-vanishing. In other words, over triangle k

$$V_k(R, r) \cong \sum_{n=1}^{6} V(R_n, r_n)\phi_{nk}(R, r) = \sum_{n=1}^{6} V_n\, \phi_{nk}(R, r), \tag{3.19}$$

where $V(R_n, r_n) = V_n$ is the value of the potential at the n^{th} node. The elements of the $\mathbf{T}$, $\mathbf{V}$ and $\mathbf{O}$ matrices can now be computed by transformation to standard

triangle coordinates

$$T_{ij} = \sum_{k}^{N_{ij}} \det(\mathbf{M}_k) \int_{t_k} \left[(\mathbf{M}_k^{-1})^T \boldsymbol{\nabla}_{xy} \phi_{ik}(x,y)\right] \cdot \left[(\mathbf{M}_k^{-1})^T \boldsymbol{\nabla}_{xy} \phi_{jk}(x,y)\right] \, dxdy, \quad (3.20)$$

and

$$O_{ij} = \sum_{k}^{N_{ij}} \det(\mathbf{M}_k) \int_{t_k} \phi_{ik}(x,y)\, \phi_{jk}(x,y) \, dxdy, \quad (3.21)$$

and

$$V_{ij} = \sum_{k}^{N_{ij}} \sum_{n=1}^{6} V(R_n, r_n) \, \det(\mathbf{M}_k) \int_{t_k} \phi_{ik}(x,y)\, \phi_{nk}(x,y)\, \phi_{jk}(x,y)\, dxdy. \quad (3.22)$$

Here, the outer sum runs over all the N_{ij} triangles which contain both nodes i and j. For $P = 2$ there are 36 possible integrals (6^2) in the expressions for the matrix elements of $\mathbf{T}$ and $\mathbf{O}$ and 216 (6^3) possible integrals for the $\mathbf{V}$ matrix. For each matrix the number of distinct integrals is reduced by symmetry. Askar and co-workers [18] report the values of these integrals, which are identical to those calculated in the present work. Because Askar and co-workers use an oblique coordinate system to describe the standard triangle instead of cartesian coordinates, the gradient operator has a different transformation. Consequently, the elements of the $\mathbf{T}$ matrix in the work of Askar *et al.* must be transformed to match the values calculated in the present work.

The elements of the $\mathbf{T}$, $\mathbf{V}$ and $\mathbf{O}$ matrices need be computed only once, and can be stored and reused in scattering calculations at different total energies. The only input that is required to determine these matrices is the $N \times 2$ matrix containing the node locations in MSJ coordinates and the $N \times 1$ vector containing the values of the potential at these nodes. Furthermore, given MATLAB's native sparse matrix

handling and vectorization capabilities, these matrices to be built anew for each problem with little computational cost.

More details of these calculations are available in the software reference for COLSCAT available on the web [119]. With the numerical form of the $\mathbf{A}$ matrix in hand the bound state wave functions and their energies are trivial to compute. The system of equations $\mathbf{A}C = 0$ is solved by invoking the ‘(backslash) matrix operator in MATLAB. Given the sparse nature of the $\mathbf{A}$ matrix the bound states are found very quickly, even for very large ($N > 100$K) mesh sizes. In the following section we extend this result to systems with nonzero boundary conditions.

3.3 Collinear Adiabatic Scattering

The bound state problem is relatively easy because the molecular wave function must vanish asymptotically. The reactive scattering problem is less straightforward as the form of the molecular wave function must asymptotically match the physical scattering boundary conditions described in Chapter 2. In each case the physical boundary conditions contain a linear combination of the scattering amplitudes, which are not known *a priori*. In this section we derive our novel FE algorithm to solve the reactive scattering problem for collinear reactions. Unlike previous applications of the FE method to reactive scattering our algorithm solves for both the scattering amplitudes and scattering wave function simultaneously. We conclude this section with a discussion comparing our algorithm with the previous implementation.

3.3.1 Reactive Scattering Domain

The domain, Ω, for a reaction scattering problem is broken up into three sections; the reactant channel ($\gamma = a$) where atom A is far from diatom BC ($R_a \gg 1$), the product channel ($\gamma = c$) where atom C is far from diatom AB ($R_c \gg 1$) and the interaction region where the three atoms are close to one another. Figure 3.3 shows a representative reactive scattering domain of the H+H_2 reaction.

The scattering domain, Ω, is also defined by its boundary Γ. For a collinear reaction this boundary, like the domain, is also broken into three sections; the reactant boundary, Γ^a where the boundary conditions include an incoming term and outgoing terms, the product boundary, Γ^c where the boundary conditions only contain outgoing terms, and the remaining portion of the boundary where we assume the wave function is zero.

The assumption that the wave function is zero along all other boundaries to the scattering domain is a constraint on the value of the potential along the boundary. For values of small enough values of r_γ and R_γ this is naturally the case, the potential becomes exponentially large when atoms get 'too' close. When both r_γ and R_γ become large we enter the triatomic breakup regime. In this work we will not explicitly treat the triatomic breakup regime, instead we consider collision energies 'low enough' that the wave function does enter the region of triatomic breakup. There is a bit of art required to balance the number of nodal points and and the value of the potential along Γ when constructing the domain and triangulation for a given system.

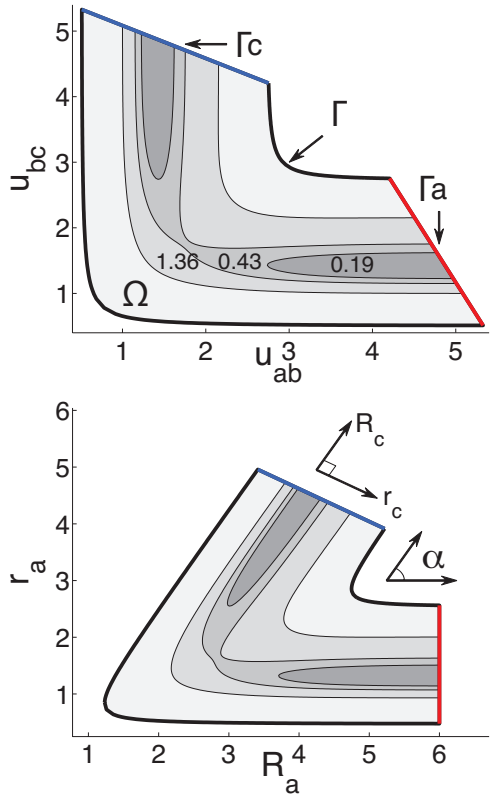

Figure 3.3: The domain for the symmetric, collinear H+H_2 →H_2+H reaction shown in bond coordinates (upper panel) and MSJ coordinates (lower panel). Distances in bohr. The reactant boundary, Γ_a, is shown in red, and the product boundary, Γ_c, in blue. The skew angle, α, is also shown. Some energy contours (in eV) of the HHH PES are shown in both figures; the zero of energy corresponds to H+$H_2(r = r_e)$.

3.3.2 Finite Element Solution

In the case of reactive scattering we solve the same formulation of Schrödinger's equation with the reactive scattering boundary conditions. The problem we would like to solve can be written as

$$\left[-\nabla^2 + 2m(V-E)\right]\Psi = 0 \text{ on } \Omega \tag{3.23}$$

and

$$\Psi = \Psi^{\Gamma} \text{ on } \Gamma, \tag{3.24}$$

where Ψ_Γ is given in Eq. (2.14).

In the previous section we developed the weak formulation of this problem. Because the wave function is exactly zero along the boundary for a bound state wave function we had $b(\xi, \Psi_\Gamma) = 0$. Instead we can substitute the reactive scattering boundary conditions for Ψ_Γ from Eq. (2.14) into Eq. (3.15). This gives

$$\begin{aligned}
\sum_i C_i\, a(\Phi_j, \Phi_i) &= b(\Phi_j, \Psi_\Gamma) \\
&= b(\Phi_j, \Psi_{\Gamma_a}) + b(\Phi_j, \Psi_{\Gamma_c}) \\
&= b(\Phi_j, f^*_{\mathrm{v}_a}) + b(\Phi_j, \sum_{\mathrm{v}_a{}'=0}^{\mathcal{N}_a} f_{\mathrm{v}_a{}'} S_{\mathrm{v}_a{}',\mathrm{v}_a}) + b(\Phi_j, \sum_{\mathrm{v}_c{}'=0}^{N_c} f_{\mathrm{v}_c{}'}\, S_{\mathrm{v}_c{}',\mathrm{v}_a}) \\
&= b(\Phi_j, f^*_{\mathrm{v}_a}) + \sum_{\mathrm{v}_a{}'=0}^{\mathcal{N}_a} S_{\mathrm{v}_a{}',\mathrm{v}_a}\, b(\Phi_j, f_{\mathrm{v}_a{}'}) + \sum_{\mathrm{v}_c{}'=0}^{\mathcal{N}_c} S_{\mathrm{v}_c{}',\mathrm{v}_a}\, b(\Phi_j, f_{\mathrm{v}_c{}'})
\end{aligned} \tag{3.25}$$

where Γ_a, and Γ_c channels are the asymptotic reactive scattering boundary conditions for the reactant and product channels. These can be written as

$$\Psi_{\Gamma_a} = f^*_{\mathrm{v}_a}(\bar{R}_a, \bar{r}_a) + \sum_{\mathrm{v}_a{}'=0}^{\mathcal{N}_a} f_{\mathrm{v}_a{}'}(\bar{R}_a, \bar{r}_a)\, S_{\mathrm{v}_a{}',\mathrm{v}_a}$$

and

$$\Psi_{\Gamma_c} = \sum_{\mathrm{v}_c'=0}^{\mathcal{N}_c} f_{\mathrm{v}_c'}(\bar{R}_c, \bar{r}_c)\, S_{\mathrm{v}_c',\mathrm{v}_a}.$$

Equation (3.25) can be recast as the matrix equation

$$\mathbf{A}\,\mathbf{C} = \mathbf{b} + \mathbf{B}_a\mathbf{S}_a + \mathbf{B}_c\mathbf{S}_c. \tag{3.26}$$

From Eq. (3.17) $\mathbf{A}$ is the $N \times N$ bilinear matrix, with elements $A_{ij} = a(\Phi_j, \Phi_i)$, $\mathbf{C}$ is a $N \times 1$ column vector containing the expansion coefficients at each of the nodes, [from Eq. (3.10)], $\mathbf{b}$ is a $N \times 1$ column vector with elements $(\mathbf{b})_j = b(\Phi_j, f^*_{\mathrm{v}_a})$, $\mathbf{B}_\gamma$ is an $N \times N_\gamma$ matrix with elements $(\mathbf{B}_\gamma)_{j\mathrm{v}_{\gamma'}} = b(\Phi_j, f_{\mathrm{v}_{\gamma'}})$. Here, N_γ is the number of vibrational levels included in the γ arrangement. Thus, in terms of the maximum vibrational levels $\mathcal{N}_a$ and $\mathcal{N}_c$ defined in Eq. (2.14), we have $N_\gamma = \mathcal{N}_\gamma + 1$. Finally, $\mathbf{S}_\gamma$ is an $N_\gamma \times 1$ column vector containing the inelastic, $\gamma = a$, and reactive, $\gamma = c$, scattering amplitudes corresponding to an incoming wave in arrangement a in state $\mathrm{v}{=}\mathrm{v}_a$.

To solve for $\mathbf{C}$, $\mathbf{S}_a$ and $\mathbf{S}_c$ simultaneously we create a single vector of unknowns by concatenating $\mathbf{C}$, $\mathbf{S}_a$ and $\mathbf{S}_c$. This vector satisfies the linear equation

$$\begin{bmatrix} \mathbf{A} & -\mathbf{B}_a & -\mathbf{B}_c \end{bmatrix} \begin{bmatrix} \mathbf{C} \\ \mathbf{S}_a \\ \mathbf{S}_c \end{bmatrix} = \mathbf{b} \tag{3.27}$$

This is a set of N equations in $N + N_a + N_c$ unknowns, and is hence underdetermined. We can remove this indeterminacy by introducing explicity the boundary conditions contained in Eqs. (2.14). These relate the wave function at all points along the

boundaries Γ_a and Γ_c to expressions containing the $\mathbf{S}_\gamma$ vectors. Let N_{Γ_a} and N_{Γ_c} be the number of nodes along Γ_a and Γ_c, respectively. The terms along the reactant boundary Γ_a from Eq. (2.14) can be written compactly as

$$\begin{bmatrix} \mathbf{I}_a & \mathbf{F}_a & \mathbf{0_a} \end{bmatrix} \begin{bmatrix} \mathbf{C} \\ \mathbf{S}_a \\ \mathbf{S}_c \end{bmatrix} = \mathbf{f} \tag{3.28}$$

Here $\mathbf{I}_a$ is a unit-like matrix of dimension $N_{\Gamma_a} \times N$. The row index of $\mathbf{I}_a$ corresponds to the N_{Γ_a} nodes which lie on Γ_a while the column index corresponds to all the nodes. All elements of $\mathbf{I}_a$ are zero except for the columns which correspond to nodes which lie on the boundary Γ_a.

For the $N_{\Gamma_a} \times N_a$ matrix $\mathbf{F}_a$ the row index corresponds to the nodes which lie on Γ_a while the column index corresponds to the vibrational states of the diatomic moiety in the reactant arrangement.The elements of $\mathbf{F}_a$ are

$$(\mathbf{F}_a)_{i\mathrm{v}_{a'}} = f_{\mathrm{v}_{a'}}(\bar{R}_{ai}, \bar{r}_{ai}) = k_{\mathrm{v}_{a'}}^{-1/2} \exp(ik_{\mathrm{v}_{a'}}\bar{R}_{ai})\, \chi_{\mathrm{v}_{a'}}(\bar{r}_{ai}).$$

Also, $\mathbf{0}$ designates an $N_a \times N_c$ nul matrix. The elements of the $N_a \times 1$ vector $\mathbf{f}$ on the r.h.s. of Eq. (3.28) are

$$(\mathbf{f})_i = k_{\mathrm{v}_a}^{-1/2} \exp(-ik_{\mathrm{v}_a}\bar{R}_{ai})\, \chi_{\mathrm{v}_a}(\bar{r}_{ai}).$$

We can similarly express the boundary conditions along Γ_c as

$$\begin{bmatrix} \mathbf{I}_c & \mathbf{0}^T & \mathbf{F}_c \end{bmatrix} \begin{bmatrix} \mathbf{C} \\ \mathbf{S}_a \\ \mathbf{S}_c \end{bmatrix} = \mathbf{0}_c \tag{3.29}$$

Here $\mathbf{I}_c$ is a unit-like matrix of dimension $N_{\Gamma_c} \times N$, defined similarly to $\mathbf{I}_a$ except that the non-zero elements correspond to nodes which lie on the boundary Γ_c. The $N_{\Gamma_c} \times N_c$ matrix $\mathbf{F}_c$ is similar to $\mathbf{F}_a$ except that the row index corresponds to the N_{Γ_c} nodes which lie on Γ_c while the column index corresponds to the vibrational states of the diatomic moiety in the *product* arrangement. Thus the elements of $\mathbf{F}_c$ are

$$(\mathbf{F}_c)_{i\mathrm{v}_{c'}} = f_{\mathrm{v}_{c'}}(\bar{R}_{ci}, \bar{r}_{ci}) = k_{\mathrm{v}_{c'}}^{-1/2} \exp(ik_{\mathrm{v}_{c'}}\bar{R}_{ci})\, \chi_{\mathrm{v}_{c'}}(\bar{r}_{ci}).$$

Equations (3.27), (3.28) and (3.29) can be combined as

$$\begin{bmatrix} \mathbf{A} & -\mathbf{B}_a & -\mathbf{B}_c \\ \mathbf{I}_a & -\mathbf{F}_a & \mathbf{0} \\ \mathbf{I}_c & \mathbf{0}^T & -\mathbf{F}_c \end{bmatrix} \begin{bmatrix} \mathbf{C} \\ \mathbf{S}_a \\ \mathbf{S}_c \end{bmatrix} = \begin{bmatrix} \mathbf{b} \\ \mathbf{f} \\ \mathbf{0}_c \end{bmatrix}. \tag{3.30}$$

This is a set of $(N+N_{\Gamma_a}+N_{\Gamma_c})$ equations in $(N+N_a+N_c)$ unknowns. Provided that the number of nodes along the boundaries are greater than or equal to the number of energetically accessible BC and AB vibrational states, this set of equations is overdetermined. In practice we ensure that $N_a + N_c = N_{\Gamma_a} + N_{\Gamma_c}$ by using every vibrational state state on both boundaries, where there is one vibrational state on each boundary for each nodal point on that boundary.

The additional equations reflect a linear dependency, because the coefficients of the basis functions along the Γ_a and Γ_c boundaries are constrained by Eq. (3.25) to be a linear combination of a smaller number of vibrational functions multiplied by incoming or outgoing waves. Consequently, Eq. (3.30) will have a unique solution, yielding, in one shot, both the scattering wave function as well as one column of the inelastic and reactive S-matrix.

If we include as many vibrational levels as points on the boundary, then Eq. (3.30) becomes uniquely determined, with the number of unknowns equal to the number of equations. This can be achieved easily by the addition of "closed" (energetically inaccessible) vibrational states. The 1D FE calculation of the vibrational functions returns one vibrational state per boundary point, so this is feasible. Since the size of the calculation depends on the size of the much larger $\mathbf{A}$ matrix in Eq. (3.30), inclusion of energetically closed states does not slow down the calculation. We also find no loss in numerical stability after including the energetically closed states because the exponential term in Eq. (2.15) is real valued and very small for these closed states. Accordingly, for well-defined domains the scattering amplitudes for energetically closed states are exactly zero.

Furthermore, we can add additional columns to the r.h.s. of Eq. (3.30) corresponding to different choices of the initially populated vibrational level v_a. Solving this larger system allows the determination of multiple columns of, or even the full, S-matrix without a significant increase in computational overhead.

3.3.3 Boundary Integrals

In this section we describe the procedure for evaluating the boundary integrals that appear in Eq. (3.25). Making use of Eq. (3.8) to expand these integrals, we have

$$b(\Phi_j, f_{\mathrm{v}_\gamma}) = \int_{\Gamma_\gamma} \Phi_j \; \hat{n} \cdot \nabla f_{\mathrm{v}_\gamma}, \tag{3.31}$$

where $\gamma \equiv a/c$ for the reactant/product boundary. Since the normal derivative is perpendicular to the boundary, $\hat{n} \cdot \nabla = \partial/\partial R_\gamma$. Substituting this partial derivative for the gradient in Eq. (3.31) and using the definition of f_{v_γ} in Eq. (2.15), we find

$$b(\Phi_j, f_{\mathrm{v}_\gamma}) = \int \Phi_j(R, r) \frac{\partial}{\partial R_\gamma} \left[k_{\mathrm{v}_\gamma}^{-1/2} \exp(i k_{\mathrm{v}_\gamma} \bar{R}_\gamma) \, \chi_{\mathrm{v}_\gamma}(\bar{r}_\gamma) \right] dr_\gamma, \tag{3.32}$$

where we have replaced the integral over Γ_γ with an integral over r_γ because R_γ is constant along the Γ_γ boundary. Since $f_{\mathrm{v}\gamma}$ is defined in standard Jacobi coordinates, we can use the definition of the MSJ coordinates, Eq. (2.3), to evaluate the derivatives occurring in Eq. (3.32), obtaining

$$b(\Phi_j, \, f_{\mathrm{v}_\gamma}) = \frac{1}{\lambda_\gamma} \, {k_{\mathrm{v}_\gamma}}^{1/2} \exp(i k_{\mathrm{v}_\gamma} \bar{R}_\gamma) \int \Phi_j(R, r) \, \chi_{\mathrm{v}_\gamma}(\bar{r}_\gamma) \, dr_\gamma. \tag{3.33}$$

Changing to an integral over $\bar{r}_\gamma$ [Eq. (2.3)] adds another factor of $1/\lambda_\gamma$

$$b(\Phi_j, f_{\mathrm{v}_\gamma}) = \frac{1}{{\lambda_\gamma}^2} \, {k_{\mathrm{v}_\gamma}}^{1/2} \exp(i k_{\mathrm{v}_\gamma} \bar{R}_\gamma) \int \Phi_j(\bar{R}, \bar{r}) \, \chi_{\mathrm{v}_\gamma}(\bar{r}_\gamma) \, d\bar{r}_\gamma, \tag{3.34}$$

where we have expressed the basis functions in terms of the unscaled Jacobi coordinates. The integration follows the $\gamma = a$ or $\gamma = c$ boundary. The only non-vanishing integrals are those which include nodes that are unity at one of the nodes along the boundary. As can be seen in Fig. 3.2, in this 1D projection, there is one basis function per node along the boundary. For $P = 2$ these 1D basis functions span either one or two triangles. We can write the 1D projections as follows

$$\Phi_j(\bar{R}_\gamma, \bar{r}_\gamma) = \Phi_j^\Gamma(\bar{r}_\gamma) = \sum_{k=1}^{n_j^\Gamma} \phi_{jk}^\Gamma(\bar{r}_\gamma), \tag{3.35}$$

where n_j^Γ is either 1 or 2.

We use a similar 1D, $P = 2$ FE method to obtain the vibrational wave functions along either γ_a or γ_c, which are solutions to Eq. (2.13). Thus

$$\chi_{\mathrm{v}_\gamma}(\bar{r}_\gamma) \approx \sum_{k=1}^{N_\gamma} g_{\mathrm{v}k}\, \Phi_k^\Gamma(\bar{r}_\gamma). \tag{3.36}$$

Here the $g_{\mathrm{v}l}$ coefficients are just the values of the χ_v vibrational function at each node (either vertex or midpoint) along the boundary. Consequently, the boundary integrals are

$$b(\Phi_j, f_{\mathrm{v}_\gamma}) = \tfrac{1}{\lambda_\gamma{}^2}\, {k_{\mathrm{v}_\gamma}}^{1/2} \exp(ik_{\mathrm{v}_\gamma}\bar{R}_\gamma) \textstyle\sum_{k=1}^{n_k^\Gamma} g_{\mathrm{v}k} \int \Phi_j^\Gamma(\bar{r}_\gamma)\, \Phi_k^\Gamma(\bar{r}_\gamma)\, d\bar{r}_\gamma \tag{3.37}$$

$$= \tfrac{1}{\lambda_\gamma{}^2}\, {k_{\mathrm{v}_\gamma}}^{1/2} \exp(ik_{\mathrm{v}_\gamma}\bar{R}_\gamma)\, (\mathbf{O}^\Gamma\, \mathbf{G})_{j\mathrm{v}}, \tag{3.38}$$

where the the $(j, \mathrm{v}_\alpha + 1)^{th}$ element of the $N_\gamma \times N_\gamma$ matrix $\mathbf{G}$ is the value of the vibrational function $\chi_{\mathrm{v}_\gamma}(\bar{r}_\gamma)$ at node j along the boundary and $\mathbf{O}^\Gamma$ is the $N_\gamma \times N_\gamma$ boundary overlap matrix, [the 1D counterpart to $\mathbf{O}$, in Eq. (3.21)]. The matrix $\mathbf{O}^\Gamma$ is also used in the 1D FE approximation to the vibrational functions themselves in Eq. (2.13). In practice the wave functions and the boundary integrals are computed at the same time, and then stored.

3.3.4 Comparison with Earlier FE Implementation

In previous applications of the FE method to reactive scattering, [18,111–118] the boundary conditions are fixed to a pure vibrational state. That is, the wave function along the reactant boundary is fixed to specified values of v_a=$\mathrm{v}_c = 0$. $N_a + N_c$ linearly independent pairs of such artificial boundary conditions are used to generate standing waves in the scattering region. These standing waves and

their directional derivatives normal to the reactant and product boundaries are then projected into the set of vibrational boundary functions. Askar [18] gives a relationship between these projections and the $(N_a + N_c) \times (N_a + N_c)$ S-matrix.

A complexity in the numerical solution of scattering problems is that the behavior of the wave function on the boundary is not known in advance. In Section 3.3.2, we have shown how a FE solution of the Schrödinger Equation can be extended to include determination of both the value of the wave function at each grid point and the column of the S matrix corresponding to incoming flux in vibrational level v.

It is conceptually simpler to impose in advance a particular form for the wave function on Γ_a and Γ_c and then solve the Schrödinger's Equation. For example, we could require that the wave function vanish on Γ_c and, on Γ_a, be equal to a constant multiple of a particular $\chi_{\mathrm{v}}(r)$ vibrational wave function. We could impose a set of such initial conditions, sufficient in size to generate a set of linearly independent solutions to Schrödinger's Equation. Then, we could chose a linear combination of these independent solutions to satisfy the physical scattering boundary conditions. From this linear combination, we can determine the S matrix, as in the propagator (finite-difference) based solution of the time-idependent scattering equations [98]. In this Section we present an alternative, concise discussion of this procedure, which was introduced by Askar *et al.,* [18] and used in subsequent FE treatments [111–118].

We assume that the boundaries Γ_a and Γ_c are located sufficiently far into the reactant and product arrangements that the three body term in the PES vanishes, Eq. (2.11). Then, in analogy with Eq. (2.14), along the boundaries Γ_a and Γ_c any

solution to Schrödinger's Equation, i.e. $\Xi(R,r)$, will be a linear combination of the energetically open BC or AB vibrational states, namely

$$\lim_{\{R_a,r_a\}\to\Gamma_a} \Xi(R,r) = \sum_{\mathrm{v}=0}^{\mathcal{N}_a} t_{\mathrm{v}_a}(\bar{R}_a)\chi_{\mathrm{v}_a}(\bar{r}_a) \tag{3.39}$$

and

$$\lim_{\{R_c,r_c\}\to\Gamma_c} \Xi(R,r) = \sum_{\mathrm{v}'=0}^{\mathcal{N}_c} t_{\mathrm{v}'_c}(\bar{R}_c)\chi_{\mathrm{v}'_c}(\bar{r}_c). \tag{3.40}$$

For simplicity, we can replace these two equations by a single equation

$$\lim_{\{R,r\}\to\Gamma} \Xi(R,r) = \sum_{\mathrm{v}=1}^{N_\mathrm{v}} t_{\mathrm{v}}(\bar{R})\chi_{\mathrm{v}}(\bar{r}). \tag{3.41}$$

Here we use a single index v, with the understanding that the limit is evaluated on either the reactant or product boundaries and that $1 \le m \le N_a$ refers to the vibrational levels of the BC moiety and $N_a + 1 \le m \le N_\mathrm{v}$ refers to the vibrational levels of the AB moiety. As before N_v is the total number of open vibrational levels in both the reactant and product arrangements.

There will exist in general $2N_\mathrm{v}$ linearly independent solutions of Schrödinger's equation. Of these, only N_v will have the proper exponentially decreasing dependence on R as the distance becomes small. Let us designate the behavior on the boundaries Γ_a and Γ_c of this set of N_v linearly-independent solutions as the square matrix $\boldsymbol{\Xi}_\Gamma(r)$ of size $N_\mathrm{v} \times N_\mathrm{v}$. Each row corresponds to the index v in Eq. (3.41) while each column corresponds to a particular linearly-independent solution. In matrix notation, Eq. (3.41) is

$$\lim_{\{R,r\}\to\Gamma} \boldsymbol{\Xi} \equiv \boldsymbol{\Xi}(r)|_\Gamma = \boldsymbol{\chi}(\bar{r})\mathbf{T}(\bar{R}). \tag{3.42}$$

Here $\mathbf{T}$ is a square $N_\mathrm{v} \times N_\mathrm{v}$ matrix each column of which corresponds to the coefficients defined in Eq. (3.41). Since $\bar{R}_a$ (or $\bar{R}_c$) have fixed values along the boundaries Γ_a (Γ_c), the $\mathbf{T}$ matrix is a set of constants. Also $\boldsymbol{\chi}(r)$ is a diagonal $N_\mathrm{v} \times N_\mathrm{v}$ matrix with elements (note that these diagonal elements are functions, rather than numbers)

$$[\boldsymbol{\chi}(\bar{r})]_{mn} = \delta_{mn}\chi_m(\bar{r}). \tag{3.43}$$

Again, we understand that the first N_a rows of matrix Equation (3.42) correspond to the behavior on the reactant boundary Γ_a while rows $N_a + 1, \ldots, N_\mathrm{v}$ correspond to the behavior on the product boundary.

Askar *et al.* [18] and subsequent practitioners [111–118] preselect a set of linearly independent solutions by a particular choice of the matrix $\mathbf{T}$ that is real and non-singular with elements either 0 or ± 1 and with real eigenvalues. Each column of $\mathbf{T}$ corresponds to a particular preselected choice of boundary conditions.

The normal derivative on the boundaries Γ_a and Γ_c is proportional to either $\partial/\partial\bar{R}_a$ or $\partial/\partial\bar{R}_c$. Since the vibrational functions χ depend only on r_a or r_c, the normal derivative of the set of linearly-independent solutions is [from Eq. (3.39)]

$$\lim_{\{R_a, r_a\}\to\Gamma_a} \hat{n}\cdot\nabla\Xi(R,r) = \sum_{\mathrm{v}=0}^{\mathcal{N}_a} \frac{dt_{\mathrm{v}_a}(\bar{R}_a)}{d\bar{R}_a}\chi_{\mathrm{v}_a}(r_a), \tag{3.44}$$

and, similarly along Γ_c. Combining the two boundaries, in matrix notation we have

$$\lim_{\{R,r\}\to\Gamma} \hat{n}\cdot\nabla\boldsymbol{\Xi} \equiv \boldsymbol{\Xi}'(r)|_\Gamma = \boldsymbol{\chi}(\bar{r})\mathbf{T}'(\bar{R}), \tag{3.45}$$

where $\mathbf{T}'$ is a real matrix of constants corresponding to the derivatives, evaluated on the boundaries, of the $t_{\rm v}(\bar{R})$ functions of Eq. (3.41).

If, as suggested by Askar and co-workers, [18] each column of the $\mathbf{T}$ matrix is limited to one (or two) entries, then the corresponding column of the $\mathbf{T}'$ matrix will be limited to the same number of entries. Thus, the summation over v in Eq. (3.44) will be limited to one (or two) terms. Unfortunately, one can obtain the non-zero entries of the $\mathbf{T}'$ matrix only by a complete FE solution of Schrödinger's Equation.

The physical scattering boundary conditions of Eq. (2.14) can be written compactly as

$$\lim_{R,r\to\Gamma} \mathbf{\Psi}(\bar{r},\bar{R}) \equiv \mathbf{\Psi}(r)|_\Gamma = \boldsymbol{\chi}(\bar{r}) \left(\mathbf{h}^{(-)} + \mathbf{h}^{(+)}\mathbf{S}\right), \tag{3.46}$$

where $\mathbf{h}^{(\pm 1)}$ are diagonal matrices with elements

$$h^{(\pm)}_{mn} = \delta_{mn} k_m^{-1/2} \exp(\pm i k_m \bar{R}_a),\ 1 \le m \le N_a$$

and

$$h^{(\pm)}_{m'n} = \delta_{m'n} k_{m'}^{-1/2} \exp(\pm i k_{m'} \bar{R}_c),\ N_a + 1 \le m' \le N_{\rm v}.$$

This corresponds to a diagonal matrix $\boldsymbol{\chi}(\bar{r})\mathbf{h}^{(-)}$ with incoming waves in each channel [remember that $\boldsymbol{\chi}$ is diagonal, see Eq. (3.43)] along with a full matrix corresponding to outgoing waves in all (inelastic plus reactive) channels. Similarly, the normal derivative of $\mathbf{\Psi}(r,R)$ on the boundaries Γ_a and Γ_c is

$$\hat{n}\cdot\nabla\mathbf{\Psi}|_\Gamma \equiv \mathbf{\Psi}'(r)|_\Gamma = i\boldsymbol{\chi}(r)\mathbf{k}\left(-\mathbf{h}^{(-)} + \mathbf{h}^{(+)}\mathbf{S}\right), \tag{3.47}$$

where $\mathbf{k}$ is the diagonal matrix of wave vectors.

As discussed above, each column of the $\mathbf{T}$ matrix defines a particular, but arbitrary, behavior of the solution to Schrödinger's Equation along the boundary, with the values of the corresponding normal derivatives given by the matrix $\mathbf{T}'$. The corresponding set of linearly independent solutions along the boundary is given by the $N_{\mathrm{v}} \times N_{\mathrm{v}}$ matrix $\boldsymbol{\Xi}(r)_{\Gamma}$. One can construct a linear transformation of $\boldsymbol{\Xi}(R, r)$ to obtain a set of solutions which correspond to the desired scattering boundary conditions on Γ, namely (where we have, for convenience, suppressed the dependence on r),

$$\boldsymbol{\Xi}_{\Gamma}\, \mathbf{X} = \boldsymbol{\Psi}_{\Gamma}.$$

From Eq. (3.46) this is equivalent to

$$\boldsymbol{\chi}\mathbf{T}\, \mathbf{X} = \boldsymbol{\chi}\left(\mathbf{h}^{(-)} + \mathbf{h}^{(+)}\mathbf{S}\right), \tag{3.48}$$

and, for the normal derivative

$$\boldsymbol{\chi}\mathbf{T}'\, \mathbf{X} = i\boldsymbol{\chi}\mathbf{k}\left(-\mathbf{h}^{(-)} + \mathbf{h}^{(+)}\mathbf{S}\right).$$

We can eliminate the common premultiplication by $\boldsymbol{\chi}$ from both equations, to obtain

$$\mathbf{T}\, \mathbf{X} = \mathbf{h}^{(-)} + \mathbf{h}^{(+)}\mathbf{S}, \tag{3.49}$$

and

$$\mathbf{T}'\, \mathbf{X} = i\mathbf{k}\left(-\mathbf{h}^{(-)} + \mathbf{h}^{(+)}\mathbf{S}\right). \tag{3.50}$$

Then, exactly as in the standard finite-difference time-independent formulation of inelastic and reactive scattering, elimination of the matrix $\mathbf{X}$ will allow us to obtain

the S matrix by solution of the following set of linear equations [98]

$$\left[(\mathbf{T})^{-1} - i(\mathbf{T}')^{-1}\mathbf{k}\right]\mathbf{h}^{(+)}\mathbf{S} = -\left[(\mathbf{T})^{-1} + i(\mathbf{T}')^{-1}\mathbf{k}\right]\mathbf{h}^{(-)}.$$

The method of Askar *et al.* [18] requires N_v decompositions of an $N \times N$ matrix, followed by solution of an $N_\mathrm{v} \times N_\mathrm{v}$ matrix equation. In our method, we need to decompose one $(N + N_\mathrm{v}) \times (N + N_\mathrm{v})$ matrix and then back substitute for each column of the S matrix that is desired. Since $N >> N_\mathrm{v}$, the two methods are computationally equivalent if the full S matrix is desired. Our method is N_v times faster if only one column is desired.

3.3.5 MATLAB Code

As mentioned in the Introduction, we have written a MATLAB based code to implement FE solution of the collinear reactive scattering problem. The source code and user's guide are available online at http://www2.chem.umd.edu/groups/alexander/FEM. All calculations were carried out with MATLAB 2013B running on a 2009 vintage MacPro with a dual-processor, 4 core (per processor) Xeon W3520 (Nehalem) CPU with a 2.66 GHz clock speed. The machine contained 16GB of 1066 MHz DD3 RAM with a 256K L2 cache (per core) and an 8 MB L3 cache (per processor).

We use MATLAB's symbolic capability to determine the values of the integrals which underly the elements of the **T**, **V** and **O** matrices [Eqs. (3.20), (3.22) and (3.21)]. We find values identical to those reported by Askar and co-workers [18]. Also, by exploiting MATLAB's implicit vectorization capabilities, we can compute all elements of these matrices in a single command without explicitly looping over

nodes or triangles.

3.3.6 Test Calculations

To verify our algorithm for determination of a single column of the S-matrix and to test our MATLAB script, we calculated reactive transition probabilities for the H+H_2, F+H_2 and F + HCl reactions, using, respectively, the collinear potential energy surface of Mielke *et al.* [124], the Muckerman V PES [125] and Deskevich's F+HCl surface [126]. The calculated reactive transition probabilities for the H+H_2 system, shown in Fig. 3.4, are in excellent agreement with earlier finite-difference calculations of Bondi and Connor [127], based on the older Porter-Karplus [128] and Liu-Siegbahn-Truhlar-Horowitz [129, 130] PES's.

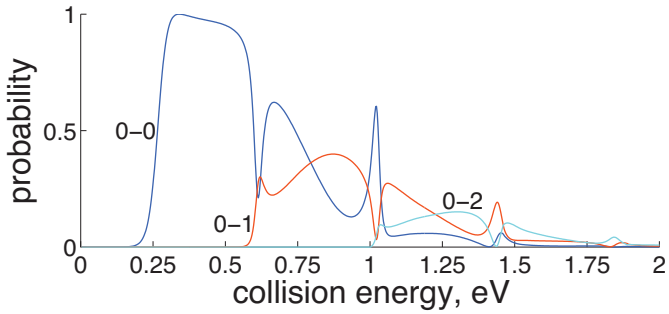

Figure 3.4: Reaction probabilities for H+H_2(v_a=0)→H_2(v_c=0,1,2)+H as a function of collision energy based on the PES of Mielke *et al.* [124]. The mesh used to calculate these data contained 1900 nodes, to achieve an accuracy of 0.1 percent. This figure illustrates the results of calculations at 1300 energies and required a total time of less than 20 seconds ($\simeq$1.5 ms per energy).

The scattering probabilities of the F+H_2 system, shown in Fig. 3.5 system

agree well with earlier finite-difference [131] and finite-element calculations [112], both of which use the Muckerman V PES. The scattering probabilities of the F+HCl system are shown in Fig. 3.6.

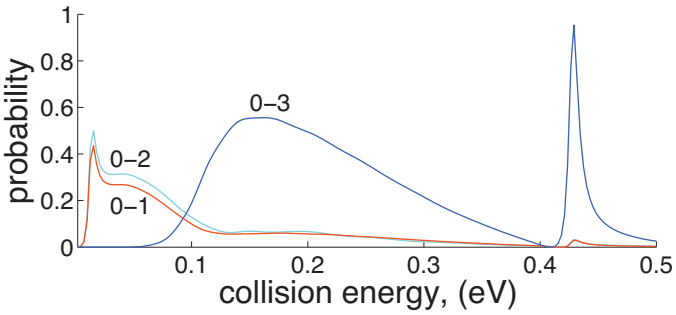

Figure 3.5: Reaction probabilities for the F+H_2(v_a=0)→HF(v_c=1,2,3)+H reaction as a function of collision energy based on the Muckerman V PES [125]. The $v_a = 0 \rightarrow v_c$=1 probability has been multiplied by a factor of 100. The mesh used to calculate these data contained 11,059 nodes. This figure illustrates the results of calculations at 601 energies ($\sim$ 10 ms per energy).

3.3.7 Timing, Parallelization and Error

Matrix calculations in MATLAB are simple to invoke and make use of highly optimized kernels, which, at least on computers containing multi-core Intel processors, exploit the parallelism built into in Intel's MKL library. In addition, crucial to the present application, MATLAB's matrix operations check for and make use of sparseness, automatically and transparently [132]. The slowest step in the present application is solution of the linear equations (3.30). For this we use MATLAB's powerful matrix division (backslash) super-operator, which uses the Unsymmetrical

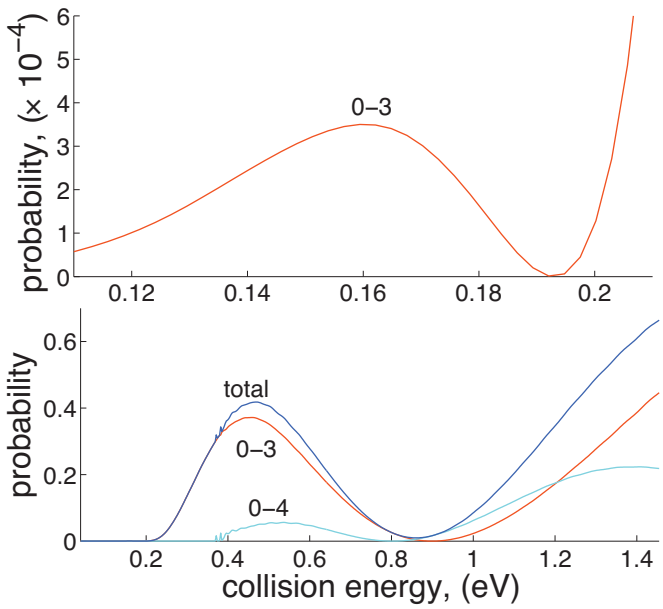

Figure 3.6: Reaction probabilities for the F+HCl(v_a=0)→HF(v_c=3,4)+Cl reaction as a function of total based on the Deskevich PES [126]. The mesh used to calculate these data contained 12,320 nodes. This figure encompasses a grid of 521 energies. The total computation time required was less than one minute.

MultiFrontal method developed at the University of Florida [133]. Solution proceeds through LU decomposition in the case of a square matrix or through QR decomposition in the case of a rectangular matrix (which corresponds to an overdetermined solution).

As mentioned earlier, one great advantage of the FE approach is the sparseness of the resulting matrices. The left panel in Fig. 3.7 shows the fractional number of non-zero elements in the **T**, **O**, and **V** matrices, as a function of the number of nodes N. For mesh sizes on the order of 1000–10,000 (Figs. 3.4–3.6), we see that the fraction of non-zero elements is between 0.001 and 0.01. Consequently,

the expected computation time for an LU decomposition should scale much more favorably than $\mathcal{O}(N^3)$ [132]. Work in the communications field suggests that at large N the timing for sparse-matrix-vector operations should scale as $\mathcal{O}(N \log N)$ [134]. Since MATLAB's backslash operator exploits sparsity, transparently, [133] we find, as shown in the right panel in Fig. 3.7, that our actual timings may be consistent with this scaling but there seems to be an upward trend suggesting an $N^{3/2}$ scaling. The timing of the MultiFrontal MATLAB's backslash operator depends on the shape of the triangulated domain. Optimal timing is achieved for rectangular meshes with one dimension much larger than the other. The irregular domains used in the reactive scattering calculations do not fit this description, which can explain the fact that we do not see an exact $N \log N$ relationship for the timing of the solution to the sparse linear system.

It is important to note that the largest contribution to numerical error in the FE calculation is the number of nodes used in the triangulation. The error also depends on the order of the Galerkin polynomials used in the calculation as well as the minimum angle of all triangles in the mesh. However, the error in the calculation will converge most rapidly by simply increasing the number of nodal points used in the triangulation of the domain. We also note the existence of error in the representation of the boundary conditions. In the statement of the boundary conditions we assumed the gradient of the potential energy in the R_γ direction is zero, i.e. the atom is a free particle. In practice we define the boundary to the reactive system at some large, finite value of R_γ, and the gradient of the potential is not exactly zero. To reduce the numerical and modeling errors in these calculations we increase first

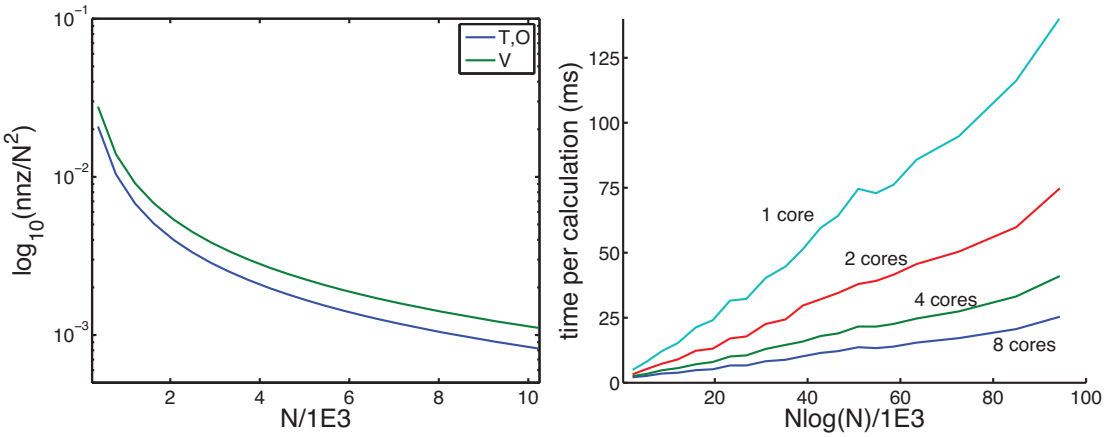

Figure 3.7: (Left panel) The fractional number of non-zero elements as a function of the number of nodes N for the **T**, **O** matrices (blue) and **V** matrix (green) [Eqs. (3.20), (3.21) and (3.22)]. (Right panel) The effective run time per energy, as a function of $N\log(N)$ and of the number of parallel cores.

R_γ then the number of nodes in the calculation until the probabilities are stationary with respect to each of these variables.

In addition to sparsity, the computational overhead of an LU decomposition can be reduced by minimization of the overall bandwidth of the matrices. As mentioned earlier, to triangulate the domain Ω we used the MATLAB scripts of Persson [135]. This minimizes the bandwidth of the **A** matrix [Eq. (3.17)]. However, we obtain the S-matrix as well as the scattering wave function by solution of a set of linear equations containing the full matrix on the LHS of Eq. (3.30) of which **A** is only one component. The additional components of this matrix disrupt, to a small extent, the compactness of the structure. However, we found that further invoking, within MATLAB, the Cuthill-McKeee algorithm [136] to reduce the bandwidth of

the this full matrix led to only an insignificant reduction in computation time.

Additionally, MATLAB can be parallelized, via MATLAB's Parallel Computing Toolbox (PCT). Calculations at individual energies can be sent to different cores. This is done totally transparently, by replacing the MATLAB loop command `FOR` by the command `PARFOR`. Using 8 cores, we have found up to a factor of 5 speed-up using the PCT as shown in Fig. 3.7. Typically, the calculations summarized in Figs. 3.4, 3.5 and 3.6 require on the order of 10–100 milliseconds per energy.

The MATLAB software that accompanies this work is intended to be simple, general and accessible. We have not included any advanced FE techniques such as, for example, hp-adaptivity (adaptively changing the size of the mesh or the polynomial order of the basis functions), multi-grid methods, or hierarchical basis functions. However, we have achieved a dramatic reduction in overall computation time by exploiting MATLAB's built-in sparse matrix capabilities and vectorized syntax (no explicit loops over nodal indices). Additional optimization could be achieved, as suggested by Askar *et al.*, [18] by using the scattering solution at one energy to speed up the calculation at the next energy, as, for example, by matrix preconditioning. However, this would be incompatible with our use of the PCT to distribute calculations at different energies to separate cores. For the relatively small systems studied in this work (less than 5e4 nodal points), we believe the speedup from parallelization greatly outweighs any possible gains from this preconditioning. For problems that require many more nodal points, however, using the solution at one energy to speed the matrix decomposition at the next energy may alleviate the computational effort to solve Eq. (3.30).

3.3.8 Automatic Mesh Generation

Included in the provided suite of MATLAB subroutines is an automatic mesh generator which extends the `distmesh2d` triangulation algorithm of Persson and Strang [135, 137]. The automated mesh generation depends only on the potential energy surface for a given A+BC system. Our routine exploits the fact that the potential surfaces of A+BC systems are generally similar i.e. exponentially repulsive walls for small values of R_a or r_a and a plateau in the region corresponding to triatomic dissociation.

We parameterize the domain of the reactive scattering with four parameters, the asymptotic distances, R_a and R_c, and two potential values, one along the exponential wall and one along the separated atoms plateau. These four values are used to construct the domain as shown in the right panel of Fig. 3.3, and the user only supplies a MATLAB script for the potential energy surface.

The most important considerations for a 'good triangulation' for reactive scattering problems are i) at the boundaries which define the repulsive wall and triatomic dissociation regions the potential must be sufficiently large that the scattering wave function is effectively zero, ii) there are enough nodal points to accurately describe any rapidly oscillating behavior in the scattering wave function and iii) the asymptotic values of R_a and R_c are large enough that $\partial V(R_\alpha, r_\alpha)/\partial R_\alpha$=0 at the boundary of each arrangement.

We have found this automatic triangulation subroutine to be extremely robust and effective. Meeting the three criteria can be more or less difficult depending on

the potential surface itself. We have had success with both analytic potential functions and interpolation of *ab initio* data. This subroutine is independent of the form of the potential in the reactive region and accordingly insensitive to local extrema (barriers, dispersion wells, etc). This routine produces meshes that can be used for high collision energies, assuming the first and second criteria are met. At high collision energies or for large masses, where the local de Broglie wavelength is small, finer meshes will be required. More detail about the this automatic mesh generation can be found in the user's manual that accompanies the provided software [119].

3.3.9 Probability Density and its Vector Current

The FE calculation generates the wave function directly. Squaring this gives the reactive and inelastic probability density. From the wave function, we can calculate the probability current density field [Eq. (3.64)]. Fig 3.8 shows plots of the probability density for the H+H_2 and F+H_2 reactions at various energies.

For H+H_2 the first two of these energies are just below and above the zero-point corrected barrier to reaction (see Fig. 3.4; the barrier height itself, E_a=0.4274 eV, is considerably lower), and the third, at higher energy. For the F+H_2 reaction, the energies depicted correspond to below the onset of the HF(v=3) channel, at the point where this probability is minimized, and at at the point where this probability is maximized.

For H+H_2 at the first and third of the energies displayed, and for F+H_2 at all

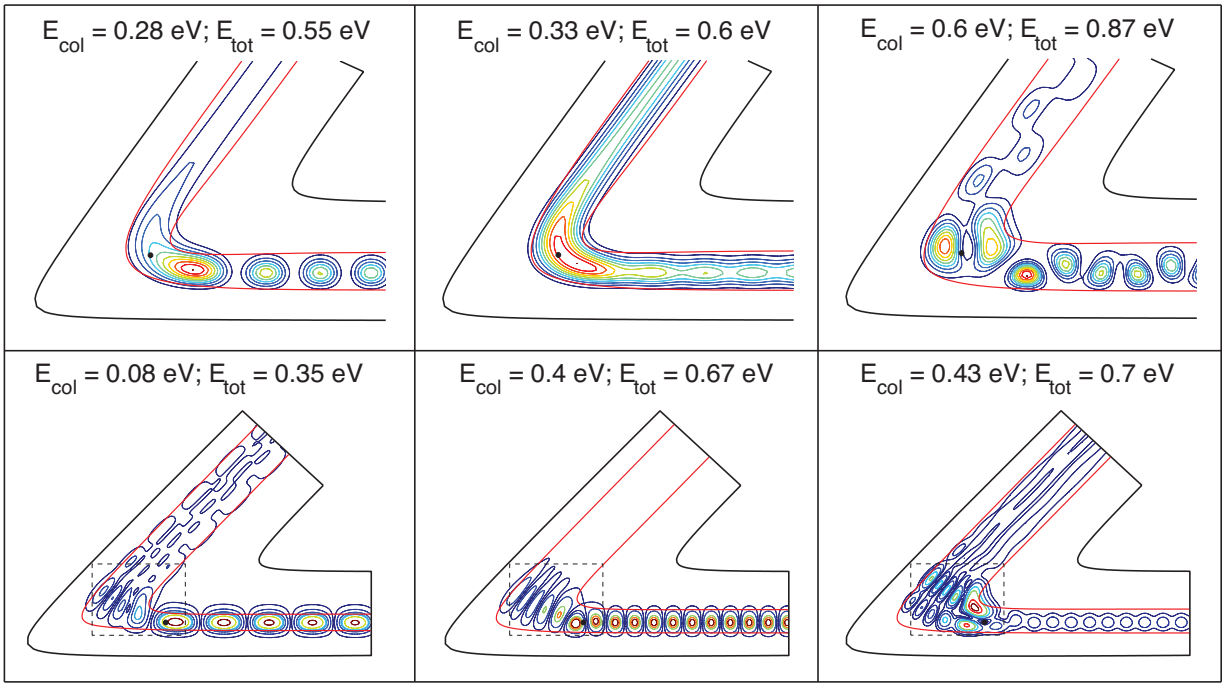

-

Figure 3.8: Probability densities for the H+H_2 (upper panels) and F+H_2 (lower panels). The red curves delimits the classically allowed region. The position of the barrier is marked by a black dot. The dashed box in the lower panels encloses the region plotted in Fig. 3.10.

the energies displayed, the total probability of reaction (summed over the energetically accessible product vibrational levels) is less than unity (see Figs. 3.4 and 3.5). Thus, as one might have anticipated, the square of the probability density in the reactant arrangement shows substantial evidence of interference between the incoming and inelastically scattered waves. For F+H_2 the dominant product channel corresponds to HF in v=3. We see in the lower panels of Fig. 3.8 that the v=3 character (three nodes along the HF vibrational coordinate r_c) is established immediately once

the product arrangement is accessed, so that the vibrational nonadiabaticity in the reaction [H_2(v=0)→HF(v=3)] develops promptly.

Also, we see in Fig. 3.5 a near vanishing of the reactive probability for the F+HCl reaction at $E_{col} \approx 0.4$ eV. In Fig. 3.8 we see that although the wave function does extend over the barrier at this energy, it does not extend at all into the product arrangement. There is total reflection at this energy.

Plots of reactive scattering wave functions for H+H_2 have been given earlier by Wyatt and co-workers [22, 24] and for F+H_2 by Jaquet [89, 112]. Although these plots are eye-opening, far more insight is given by the probability current density field. Some years ago, Kuppermann and his group (Bowman, Adams, Truhlar) explored [21, 88] similar probability current density fields for the H+H_2 reaction (based on an earlier PES), but this work was not published. Wyatt and co-workers used a time-dependent simulation to determine a probability current density field for the H+H_2 reaction and a time-independent method for the F+H_2 reaction. [22,23,89] Alexander, Manolopoulos and co-workers have presented comparable probability current density fields for molecular photodissociation processes [25, 91–94].

For the H+H_2 reaction Fig. 3.9 illustrates the probability current density field at three total energies. The larger the magnitude of an arrow, the greater the quantum probability that the reaction will pass through that location. These vector fields provides the same picture as a macrocanonical (mono-energetic) ensemble of classical trajectories, but with the addition of quantum interference and tunneling.

At energies below the height of the barrier, the H+H_2 probability current density field does not follow the minimum energy reaction path, but cuts the corner.

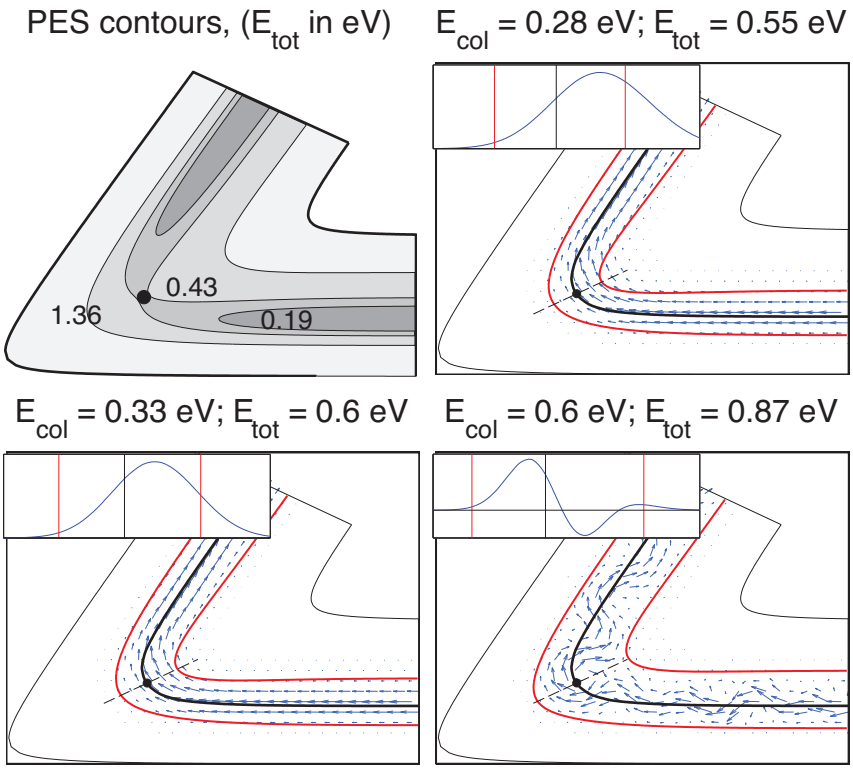

Figure 3.9: Probability current density fields for the H+H_2 reaction. In this inset, the classically forbidden region is delineated by the vertical red lines and the position of the barrier, by the vertical black line. The location of the barrier is shown by the black dot. The thick black line marks the minimum energy path. The inset figure shows the probability current projected along the dashed line which lies perpendicular to the reaction path and intersects the transition state.

This feature has been explored before, [138–140] by determination of the path along which the imaginary component of the integrated classical action is smallest (the classical action acquires an imaginary component because the momentum is imaginary whenever the path traverses a classically forbidden region). This one picture

(the upper right hand panel of Fig. 3.9) presents, in our opinion, a vivid and immediate illustration of this [88]. We note that once the energy becomes greater than the barrier height, so that passage over the minimum energy path becomes classically allowed, very little probability current extends into the classically forbidden region, even for this most quantum of chemical reactions. In a semiclassical picture reaction at energies below the barrier can be attributed to a single (or dominant) trajectory which evolves in complex phase space [141]. In the quantum picture the probability current density field extends over a large region in coordinate space,

We see also at the higher energies the appearance of a vortex or whirlpool [89] in the probability density field. In some regions this leads to the appearance of a net flux in the backward direction (product→reactant). This is the quantum fingerprint, in two dimensions, of barrier "recrossing", a phenomenon that has been often discussed in the collision dynamics literature [142]. Recrossing and tunneling are made more apparent by projecting the probability current density field onto a line perpendicular to the transition state. Bowman and Kupperman [88] name this projection the "current density profile." These profiles are shown in insets in the three panels of Fig. 3.9. The topology of the H_3 PES results, at higher energy, in reaction on the inside of the transition state with significant recrossing on the outside.

Similar images of probability current density fields for the F+H_2 and F+HCl reactions are shown in Figs. 3.10 and 3.11. For F+H_2 we observe a persistent vortex inside the transition state. Curiously, the helicity of this vortex changes as the collision energy increases. As the collision energy rises from 0.407 eV to 0.409 eV,

the helicity of this vortex changes from counterclockwise to clockwise. At 0.408 eV the vorticity vanishes. This coincides with the vanishing (Fig. 3.5) of the total reaction probability at this energy. For F+H_2 there is little evidence of corner-cutting, even at low collision energy.

For the F+HCl reaction, we observe a strong, double vortex at all the collision energies shown. In this heavy-light-heavy reaction, the PES is characterized by a small skew angle [Eq. (2.7); for F+HCl $\alpha \approx 16^o$]. As might be expected, at low energy (especially below the barrier) most of the reaction occurs by corner-cutting. What is unexpected is the significant degree of recrossing (from products to reactants) even at this low energy. As in the case of F+H_2, the helicity of the vortices in the probability current density field reverses at the energy increases. Specifically, the reversal which occurs as E_{col} increases from 0.19 to 0.22 eV corresponds to the vanishing of the reaction probability at this energy seen in upper panel of Fig. 3.6.

3.3.10 Discussion

We have applied the finite element method to the relatively old problem of collinear atom-diatom reactive scattering with a novel treatment of the undetermined Dirichlet boundary conditions, i.e. the physical scattering boundary conditions, and our results agree well with published results.

We have developed a generalized suite of MATLAB scripts to handle any collinear atom diatom reactive system using the FE method for any polynomial order basis functions. The implicit parallelization and vectorization of the MATLAB code

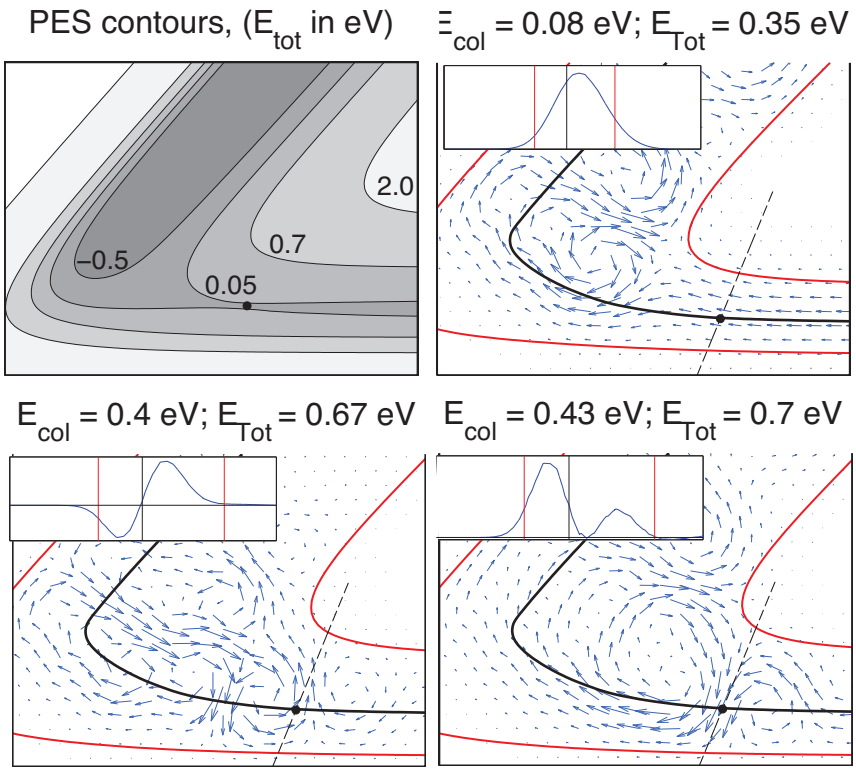

Figure 3.10: Contour plots of the potential (upper left panel) and probability current density fields for the F+H_2 reaction at three collision energies. The inset figure shows the current projected onto the transition state – the "current density profile" (Ref. [88]). The reaction path is indicated by the heavy black line and the location of the barrier, by the black dot. The dashed black line displays the normal mode motion perpendicular to reaction at the barrier. In the inset plot, the vertical red lines delimit the classically allowed region, while the vertical black line indicates the position of the barrier.

allows scattering probabilities for thousands of collision energies to be computed in a matter of minutes even on a small laptop. The major computational effort is

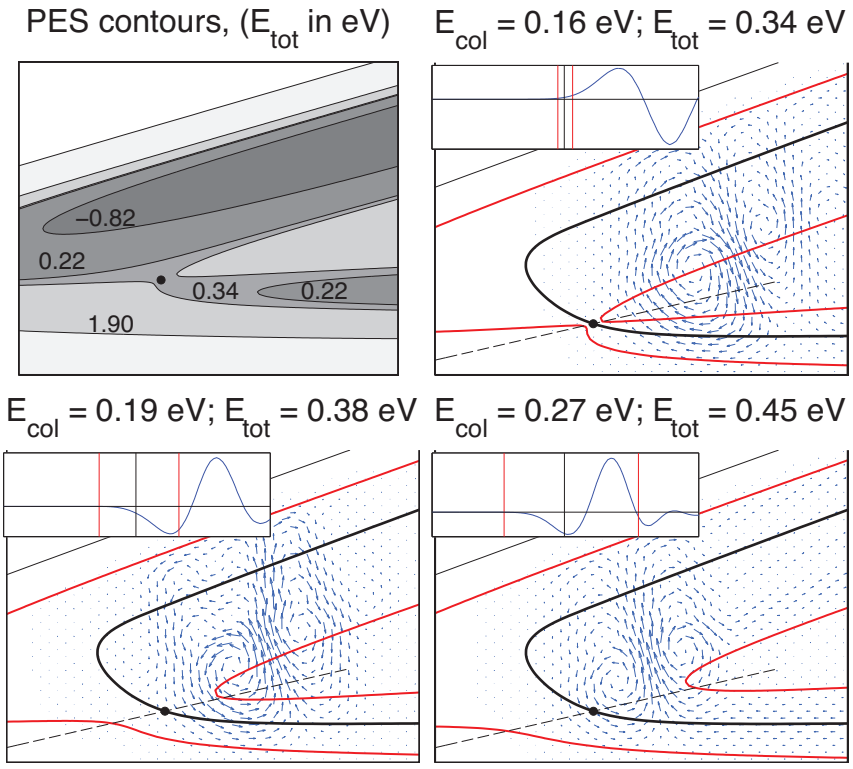

Figure 3.11: Contour plots of the potential (upper left panel) and probability current density fields for the F+HCl reaction at three total energies. The inset figure shows the current projected onto the transition state – the "current density profile" (Ref. [88]). The reaction path is indicated by the heavy black line and the location of the barrier, by the black dot. The dashed black line displays the normal mode motion perpendicular to reaction at the barrier. In the inset plot, the vertical red lines delimit the classically allowed region, while the vertical black line indicates the position of the barrier.

solving the sparse linear system of Eq. (3.30) (sparse LU factorization), which we have shown scales roughly as $N \log N$ for a mesh with N nodal points.

Our automatic triangulation routine uses a uniform nodal point density. We could expect better performance with potential adapted triangulations or from implementing an adaptive FE algorithm. We have experimented with meshes ranging from 500 to 150,000 nodal points. Typically 10,000-50,000 nodal points are required for convergence. Based on these results, we expect our approach can treat any collinear A+BC system efficiently (calculation times on the order of minutes) with perhaps the exception of extremely heavy atoms at high collision energies or extremely long range forces that would require dense meshes over larger areas. In both cases we expect dramatic improvement using non-uniform node distributions.

One particular advantage of the FE application is that the reactive scattering wave function is determined directly (time-independent propagation methods and time-dependent wave packet methods both require post-processing to obtain the wave function). As we have shown here the scattering wave function can be used to extend our intuition of the quantum features in chemical dynamics. The next section details the natural extension of this treatment of the scattering boundary conditions to collinear reactions on multiple potential energy surfaces. As we will show, the scattering wave function will be an invaluable tool for analyzing the dynamics of nonadiabatic reactions.

3.4 Collinear Nonadiabatic Scattering

In the previous section we described a time-independent, finite-element (FE) method to determine numerically the quantum scattering wave function for collinear,

atom-diatom reactions. In this section we provide a generalization to collinear reactions evolving on n-coupled electronic states.

As illustrative examples for reactions evolving on multiple potential surfaces we use the collinear $F(^2P) + HCl(v) \rightarrow HF(v') + Cl(^2P)$ and $F(^2P) + H_2(v) \rightarrow HF(v') + H$ reactions. With the scattering wave function in hand we can calculate the probability current density field for each electronic state and its divergence. We can use the divergence of the probability current density field – which we will call the nonadiabatic divergence – to pinpoint the location and extent of nonadiabaticity during the collision.

This section is organized as follows: first we extend our FE approach for collinear atom-diatom reactions to systems that evolve on coupled potential surfaces. Next we show a straight forward application of this method to the $F(^2P) + HCl(v)$ reaction, based on a new *ab initio* calculation of the PES's and coupling. We then detail how to modify the boundary conditions to analyze the reactive dynamics of the coupled $F(^2P)+H_2(v)$ reaction. Finally we give a brief discussion of these results and their implications.

3.4.1 FE Solution

To apply the FE method from Section 3.3, one uses the weak form of the Schrödinger equation. As in the previous Section, to obtain the weak form we premultiply by a test function and then integrate over the scattering domain, Ω. The wave function and test function are then replaced by, respectively, by an expansion

in finite elements and a single member of this expansion. We will continue to use piece-wise, Galerkin-type polynomials defined on the triangulation.

The extension to multiple electronic states is straightforward. The electronic state index η can be added to the expansion coefficients and the wave function must satisfy boundary conditions appropriate to multi-state scattering. From Eq.(2.22) we have

$$\lim_{R_\gamma \to \infty} \Psi(R_\gamma, r_\gamma) = \Psi_\Gamma(R_\gamma, r_\gamma) = \sum_\gamma^{a,c} \left[f_{\mathrm{v}_a}^{\eta\ *}(\bar{R}_a, \bar{r}_a)|\eta\rangle \delta_{a,\gamma} + \sum_{\eta'} \sum_{\mathrm{v}_{\gamma'}} S^{\eta',\eta}_{\mathrm{v}_{\gamma'},\mathrm{v}_a} f^{\eta'}_{\mathrm{v}_{\gamma'}}(\bar{R}_\gamma, \bar{r}_\gamma)\,|\eta'\rangle \right], \tag{3.51}$$

where $f^\eta_{\mathrm{v}_\gamma}$ is the asymptotic (A+BC or AB+C) wavefunction (the product of a plane wave multiplied by a vibrational wave function for the diatomic in electronic state η in arrangement γ as defined in Eq. (2.23).

Inelastic or reactive scattering can occur to any energetically open vibrational level associated with any electronic state. The S matrix is doubly-indexed in the electronic state, so that $S^{\eta',\eta}_{\mathrm{v}_{\gamma'},\mathrm{v}_a}$ is the amplitude for a transition from the BC vibrational state v_a in electronic state η to either the AB vibrational state $\mathrm{v_c}'$ in the ABC electronic state η' or BC vibrational state $\mathrm{v_a}'$ in the ABC electronic state η'.

For simplicity, we restrict the ensuing discussion to only two electronic states, which we designate $\eta = 1, 2$, and, further, assume that the system is initially in electronic state $|\eta = 1\rangle$. The following expressions, however, can be easily extended to an arbitrary number of states. Thus, Eq. (3.26) becomes

$$\left[\begin{bmatrix} \mathbf{T} & \boldsymbol{\emptyset} \\ \boldsymbol{\emptyset} & \mathbf{T} \end{bmatrix} - 2\mu \left(\begin{bmatrix} \mathbf{V}_{11} & \mathbf{V}_{12} \\ \mathbf{V}_{12} & \mathbf{V}_{22} \end{bmatrix} - E \begin{bmatrix} \mathbf{O} & \boldsymbol{\emptyset} \\ \boldsymbol{\emptyset} & \mathbf{O} \end{bmatrix} \right) \right] \begin{bmatrix} \mathbf{C}^1 \\ \mathbf{C}^2 \end{bmatrix}$$

$$= \begin{bmatrix} \mathbf{A}_{11} & \mathbf{A}_{12} \\ \mathbf{A}_{12} & \mathbf{A}_{22} \end{bmatrix} \begin{bmatrix} \mathbf{C}^1 \\ \mathbf{C}^2 \end{bmatrix} = \begin{bmatrix} \mathbf{b}^1 + \mathbf{B}_a^1 \mathbf{S}_a^{11} + \mathbf{B}_c^1 \mathbf{S}_c^{11} \\ \mathbf{B}_a^2 \mathbf{S}_a^{21} + \mathbf{B}_c^2 \mathbf{S}_c^{21} \end{bmatrix}. \tag{3.52}$$

The definition of the sub-matrices are the two-state generalization of those given in Eqs. (3.20-3.21). For example, $\mathbf{S}_{a(c)}^{21}$ refers to the the S-matrix for the inelastic (reactive) scattering out of electronic state $|1\rangle$ into electronic state $|2\rangle$. Also, $\boldsymbol{\emptyset}$ is a null matrix.

In imposing the boundary conditions of Eq. (3.51) we assume that incoming flux is restricted to a single electronic state η. For this to be correct, the coupling between different electronic states must vanish asymptotically, in all arrangements. In other words, we have

$$\lim_{R \to \infty} \mathbf{V}_{12} = 0. \tag{3.53}$$

As in the case of a single electronic-state calculation the scattering amplitudes are not known *a priori*. We can move these to the l.h.s. and include them in the vector of unknowns,

$$\begin{bmatrix} \mathbf{A_{11}} & \mathbf{A_{12}} & -\mathbf{B}_a^1 & -\mathbf{B}_c^1 & \boldsymbol{\emptyset} & \boldsymbol{\emptyset} \\ \mathbf{A_{12}} & \mathbf{A_{22}} & \boldsymbol{\emptyset} & \boldsymbol{\emptyset} & -\mathbf{B}_a{}^2 & -\mathbf{B}_c^2 \end{bmatrix} \begin{bmatrix} \mathbf{C}^1 \\ \mathbf{C}^2 \\ \mathbf{S}_a^1 \\ \mathbf{S}_c^1 \\ \mathbf{S}_a^2 \\ \mathbf{S}_c^2 \end{bmatrix} = \begin{bmatrix} \mathbf{b}^1 \\ \boldsymbol{\emptyset} \end{bmatrix}. \tag{3.54}$$

This set of equations is under-determined. We can use the boundary conditions

to extend this system of equations to be uniquely (exactly) determined

$$\begin{bmatrix} \mathbf{A}_{11} & \mathbf{A}_{12} & -\mathbf{B}_a^1 & -\mathbf{B}_c^1 & 0 & 0 \\ \mathbf{A}_{12} & \mathbf{A}_{22} & 0 & 0 & -\mathbf{B}_a^2 & -\mathbf{B}_c^2 \\ \mathbf{I}_a^1 & 0 & -\mathbf{F}_a^1 & 0 & 0 & 0 \\ \mathbf{I}_c^1 & 0 & 0 & -\mathbf{F}_c^1 & 0 & 0 \\ 0 & \mathbf{I}_a^2 & 0 & 0 & -\mathbf{F}_a^2 & 0 \\ 0 & \mathbf{I}_c^2 & 0 & 0 & 0 & -\mathbf{F}_c^2 \end{bmatrix} \begin{bmatrix} \mathbf{C}^1 \\ \mathbf{C}^2 \\ \mathbf{S}_a^1 \\ \mathbf{S}_c^1 \\ \mathbf{S}_a^2 \\ \mathbf{S}_c^2 \end{bmatrix} = \begin{bmatrix} \mathbf{b}^1 \\ 0 \\ \mathbf{f}^1 \\ 0 \\ 0 \\ 0 \end{bmatrix}, \tag{3.55}$$

where the elements of the $\mathbf{I}$, $\mathbf{f}$ and $\mathbf{F}$ matrices are defined in Section 3.3.2.

The solution of the matrix equation (3.55) will yield the scattering wave function and a single column of the S-matrix for a given total energy. The entire S-matrix can be determined in a single calculation by including all possible initial states in the r.h.s. as is shown in Eq. (3.56)

$$\begin{bmatrix} \mathbf{A}_{11} & \mathbf{A}_{12} & -\mathbf{B}_a^1 & -\mathbf{B}_c^1 & 0 & 0 \\ \mathbf{A}_{12} & \mathbf{A}_{22} & 0 & 0 & -\mathbf{B}_a^2 & -\mathbf{B}_c^2 \\ \mathbf{I}_a^1 & 0 & -\mathbf{F}_a^1 & 0 & 0 & 0 \\ \mathbf{I}_c^1 & 0 & 0 & -\mathbf{F}_c^1 & 0 & 0 \\ 0 & \mathbf{I}_a^2 & 0 & 0 & -\mathbf{F}_a^2 & 0 \\ 0 & \mathbf{I}_c^2 & 0 & 0 & 0 & -\mathbf{F}_c^2 \end{bmatrix} \begin{bmatrix} \mathbf{C}^1 \\ \mathbf{C}^2 \\ \mathbf{S}_a^1 \\ \mathbf{S}_c^1 \\ \mathbf{S}_a^2 \\ \mathbf{S}_c^2 \end{bmatrix} = \begin{bmatrix} \mathbf{B}_a^1 & 0 \\ 0 & \mathbf{B}_a^2 \\ \mathbf{F}_a^1 & 0 \\ 0 & 0 \\ 0 & \mathbf{F}_a^2 \\ 0 & 0 \end{bmatrix}. \tag{3.56}$$

This formalism is entirely general and can support any atom-diatom reaction evolving on any number of coupled electronic surfaces. Before we use this result to analyze the significance of nonadiabatic (spin-orbit) behavior in the F(^{2}P)+HCl and F(^{2}P)+H_2 reactions we first develop the potential energy surfaces that dictate the dynamics.

3.4.2 Basis Choice for Coupled Potential Surfaces

In this section we are interested in predicting the scattering dynamics of the nonadiabatic F+H_2 and F+HCl reactions. In the case of the F+HCl reaction the products and reactants are symmetric, i.e. the lone atom in in both reactant and product channels is a ^2P halogen (p^5 occupancy). Both halogens have non-negligible SO coupling which is the source of nonadiabaticity. In the case of F+H_2, this symmetry doesn't exist; the lone H atom in the product channel does not exhibit any SO coupling. As such, the transformation that diagonalizes the coupled potential in the product channel is not the same for these two reactions.

The nonadiabatic boundary conditions from Eq. (3.53) assume a diagonal form of the potential in all asymptotic channels. In this section we introduce the natural choices represent coupled, nonadiabatic potential energy surfaces. We will use these results to account for the possibility of potentials that are asymmetric with respect to this asymptotic diagonalization. This will provide a general framework for handling asymptotic boundary conditions for any nonadiabatic atom-diatom reaction.

3.4.2.1 Quasi-Diabatic Bases

Alexander, Manolopoulos and Werner [52] have presented a framework to describe the reactive encounter of a halogen atom with a closed-shell diatomic. There are six states in the so-called $\Lambda\Sigma$ basis, each labelled in the projection quantum numbers of the electronic orbital and spin angular momenta. We designate these in the shorthand notation $|\Sigma\rangle$, $|\bar{\Sigma}\rangle$, $|\Pi_1\rangle$, $|\bar{\Pi}_1\rangle$, $|\Pi_{-1}\rangle$, $|\bar{\Pi}_{-1}\rangle$, where Π and Σ refer to the

projection of the electronic orbital angular momentum and the absence or presence of an overbar designates a spin projection quantum number of +1/2 or –1/2. These six states form an "electrostatic" basis.

In these reactions nonadiabatic coupling is induced by the spin-orbit Hamiltonian or by the mixing between the nominally Σ and nominally $\Pi(A')$ states. The latter coupling vanishes in collinear geometry where a classic $\Sigma - \Pi$ conical intersection occurs. In the Cl+H_2 →HCl+H reaction, Sun, Zhang, and Alexander have shown [60] that the spin-orbit Hamiltonian is the primary source of electronic nonadiabaticity, not this latter mixing, which is small. Since, at least for the Cl+H_2 reaction the spin-orbit coupling varies little with triatomic angle, [143,144] investigation of the simpler collinear case will provide meaningful insight into the predominant mechanism for inelasticity in these halogen reactions.

In collinear geometry, the Σ and $\Pi_{\pm 1}$ states belong to different irreducible representations and hence form a natural diabatic basis, since the differing symmetries are independent of nuclear geometry (provided the molecule remains collinear). The matrix of the Hamiltonian blocks into two identical 2×2 matrices, coupling the two states with total (spin plus electronic orbital) projections +1/2, $|\Sigma\rangle$ and $|\bar{\Pi}_1\rangle$ (or, equivalently, the two states with total projection –1/2, $|\bar{\Sigma}\rangle$ and $|\Pi_{-1}\rangle$). The two states with total projection quantum number ±3/2 ($|\Pi_1\rangle$ and $|\bar{\Pi}_{-1}\rangle$ are not coupled to any other. Reactions on these two uncoupled potential energy surfaces can be treated with the single-state FE methodology from Section 3.3.

The spin-orbit operator will couple the two states with total projection +1/2 (or, equivalently, the two states with projection –1/2). We will hereafter refer to

the diabatic basis formed out of states corresponding to specified orientations of the electronic angular momentum as the Λ basis. The 2×2 matrix of the potential plus spin-orbit coupling is [62]

$$\mathbf{V}^{\Lambda}(Q) = \mathbf{V}_{el}(Q) + \mathbf{V}_{\mathrm{SO}}(Q) = \begin{bmatrix} V_{\Sigma}(Q) & 0 \\ 0 & V_{\Pi}(Q) \end{bmatrix} + \begin{bmatrix} 0 & -2^{1/2}B(Q) \\ -2^{1/2}B(Q) & B(Q) \end{bmatrix}, \tag{3.57}$$

where $B(Q)$ is the spin-orbit coupling matrix element, which depends on the nuclear coordinates Q.

Asymptotically, in the limit of large A–BC or AB–C separations, the V_{Σ} and V_{Π} potential energy surfaces are equal, and become the vibrational potentials of the BC or AB molecules. Also as $R \to \infty$ the spin-orbit coupling goes to the constant value appropriate to the isolated halogen. In this asymptotic limit, the 2×2 Hamiltonian matrix of Eq. (3.59) can be diagonalized. The eigenvectors correspond to the two j_a (fine-structure) states ($j_a = 3/2$ and $j_a = 1/2$) with energies $V_{\Sigma} - B$ and $V_{\Sigma} + 2B$, respectively.

The asymptotic orthogonal transformation from the Λ basis to the j_a basis is,

$$\mathbf{D} = 3^{-1/2} \begin{bmatrix} 2^{1/2} & -1 \\ 1 & 2^{1/2} \end{bmatrix}. \tag{3.58}$$

The matrix of the potential energy in the j_a basis is

$$\mathbf{V}^{j_a} = \mathbf{D}^T \mathbf{V}^{\Lambda} \mathbf{D} = \begin{bmatrix} V_{3/2} & V_d \\ V_d & V_{1/2} \end{bmatrix} = \begin{bmatrix} V_s - B & V_d \\ V_d & V_s + 2B \end{bmatrix}, \tag{3.59}$$

where $V_s = (2V_{\Sigma} + V_{\Pi})/3$ and $V_d = 2^{1/2}(V_{\Sigma} - V_{\Pi})/3$. All the matrices except $\mathbf{D}$ are

functions of the nuclear coordinates, Q, which we have suppressed for simplicity.

The j_a states also constitute a quasi-diabatic basis, since the transformation from the Λ to the j_a basis is independent of the ABC geometry. For interactions of a halogen atom with a closed-shell diatomic molecule, the j_a basis is diagonal asymptotically, when the splitting between the Σ and Π PES's vanishes. If the A+BC Jacobi vector defines the z-axis, then the Σ and Π states correspond, respectively, to single and double occupancy of the $2p_z$ atomic orbital on the halogen.

As the partners approach, the electrostatic interactions for these two electron occupancies become increasingly different. Eventually, the splitting between the Σ and Π PES's becomes larger than the spin-orbit splitting. At this point the off-diagonal coupling in the j_a basis, which is proportional to $V_\Sigma - V_\Pi$, becomes larger than the off-diagonal coupling in the Λ basis, which is proportional to the spin-orbit term, B. At this point the best zeroth order description of the electronic state of the ABC system switches from the j_a to the Λ basis.

In a two-dimensional model this is a seam, defined by

$$|V_d| = 2^{1/2} B$$

or, equivalently,

$$|V_\Sigma - V_\Pi| = 3B. \tag{3.60}$$

Asymptotically, the halogen spin-orbit splitting is $3B$. As we shall see below, the spin-orbit coupling term can vary significantly over the PES. On the seam defined by Eq. (3.60), of which there can be more than one, the electrostatic splitting is equal in magnitude to the *local* spin-orbit splitting. This has long been thought to

be the locus of points at which nonadiabaticity is most probable, [145–147] although the usual interpretation is the comparison of the local electrostatic splitting with the *asymptotic* spin-orbit splitting.

3.4.2.2 Electronically Adiabatic Basis

Diagonalization of the Hamiltonian in either the Λ or j_a basis at each value of R and r defines the electronically adiabatic (or, for short, adiabatic) basis. In a basis of two states, diagonalization is equivalent to a planar rotation

$$\begin{bmatrix} a_1 \\ a_2 \end{bmatrix} = \begin{bmatrix} \cos\theta & -\sin\theta \\ \sin\theta & \cos\theta \end{bmatrix} \begin{bmatrix} d_1 \\ d_2 \end{bmatrix}, \tag{3.61}$$

where θ is the so-called diabatic mixing angle, whose value varies with Q.

For a two-state problem, with Hamiltonian matrix elements H_{11}, H_{22}, and H_{12}, the mixing angle is

$$\theta = \frac{1}{2}\tan^{-1}\left(\frac{2H_{12}}{H_{22}-H_{11}}\right).$$

Thus, from Eq. (3.59) we see that mixing angle in the j_a diabatic basis is

$$\theta_{j_a} = \frac{1}{2}\tan^{-1}\left(\frac{2V_d}{3B}\right) \approx \frac{1}{2}\tan^{-1}\left[\frac{V_\Sigma - V_\Pi}{\Delta E_{so}}\right]. \tag{3.62}$$

were ΔE_{so} is the halogen fine-structure splitting. Similarly, in the Λ diabatic basis, the mixing angle is

$$\theta_\Lambda = \frac{1}{2}\tan^{-1}\left(\frac{-2^{1/2}B}{V_\Pi - V_\Sigma + B}\right). \tag{3.63}$$

3.4.3 Time-Independent, Hydrodynamic Interpretation

Hirschfelder, [19, 20] Kuppermann, [21] and Wyatt, [22–24], have introduced the use of a time-independent, fluid-dynamics interpretation which uses the probability current density field, given here as

$$\mathbf{J} = \frac{-i\hbar}{2m}\left\{\Psi(Q)\boldsymbol{\nabla}\Psi^*(Q) - [\boldsymbol{\nabla}\Psi(Q)]\Psi^*(Q)\right\}. \tag{3.64}$$

This widespread expression for the probability current density field can be easily derived [26] from the flux operator of Miller, Schwartz, and Tromp [148, 149].

Implicit in this expression is (i) a dependence of the wave function on the electronic coordinates, q, and (ii) integration over these coordinates in evaluating the probability current density field as a function of just the nuclear coordinates, Q. Thus, Eq. (3.64) should be written formally as

$$\mathbf{J} = \frac{i\hbar}{2m}\int_q \left[\Psi^*(Q,q)\boldsymbol{\nabla}_Q\Psi(Q,q) - \Psi(Q,q)\boldsymbol{\nabla}_Q\Psi^*(Q,q)\right] dq. \tag{3.65}$$

Specifically, if we have two coupled electronic states, we expand the wave function in terms of two orthonormal diabatic states $|d_1\rangle$ and $|d_2\rangle$,

$$\Psi(Q,q) = \Psi^{d_1}(Q,q) + \Psi^{d_2}(Q,q) = \psi^{d_1}(Q)|d_1\rangle + \psi^{d_2}(Q)|d_2\rangle. \tag{3.66}$$

Substitution of this into Eq. (3.65) and integration over the electronic coordinates gives

$$\begin{aligned}
\mathbf{J}(Q) &= \frac{i\hbar}{2m}\sum_{i=1}^{2}\int_q \left[\Psi^{(i)*}(Q,q)\boldsymbol{\nabla}_Q\Psi^{(i)}(Q,q) - \Psi^{(i)}(Q,q)\boldsymbol{\nabla}_Q\Psi^{(i)*}(Q,q)\right] \\
&= \frac{i\hbar}{2m}\sum_{i=1}^{2}\left[\psi^{d_i*}(Q)\boldsymbol{\nabla}_Q\psi^{d_i}(Q) - \psi^{d_i}(Q)\boldsymbol{\nabla}_Q\psi^{d_i*}(Q)\right]
\end{aligned}$$

$$= \mathbf{J}^{d_1}(Q) + \mathbf{J}^{d_2}(Q). \tag{3.67}$$

The total probability current density is the sum of the probability current density associated with scattering on each of the diabatic states.

Typically, scattering calculations are carried out in a quasi-diabatic basis. However, the most physically meaningful quantity is the probability current density field in the electronically-adiabatic basis. This will be independent of whatever diabatic basis is chosen for the calculations.

To expand the wave function in the adiabatic basis we replace the right-hand side of Eq. (3.66) with

$$\begin{aligned}
\Psi(Q,q) &= \psi^{d_1}(Q)\left(\cos\theta|a_1\rangle - \sin\theta|a_2\rangle\right) + \psi^{d_2}(Q)\left(\sin\theta|a_1\rangle + \cos\theta|a_2\rangle\right) \\
&= \left[\cos\theta\psi^{d_1}(Q) - \sin\theta\psi^{d_2}(Q)\right]|a_1\rangle + \left[\sin\theta\psi^{d_1}(Q) + \cos\theta\psi^{d_2}(Q)\right]|a_2\rangle \\
&= \psi^{a_1}(Q)|a_1\rangle + \psi^{a_2}(Q)|a_2\rangle.
\end{aligned} \tag{3.68}$$

Here ψ^{a_1} and ψ^{a_2} are the (R,r) dependent components of the scattering wave function expressed in terms of the two electronically adiabatic states.

The probability current density field in the adiabatic basis is, in analogy to Eq. (3.67)

$$\begin{aligned}
\mathbf{J}(Q) &= \frac{i\hbar}{2m}\sum_{i=1}^{2}\left[\psi^{a_i*}(Q)\boldsymbol{\nabla}_Q\psi^{a_i}(Q) - \psi^{a_i}(Q)\boldsymbol{\nabla}_Q\psi^{a_i*}(Q)\right] \\
&= \mathbf{J}^{a_1}(Q) + \mathbf{J}^{a_2}(Q).
\end{aligned} \tag{3.69}$$

We evaluate this expression by replacing $\psi^{a_i*}(Q)$ by its representation [from the 2nd line of Eq. (3.68)] in terms of the scattering wave functions in the diabatic basis $\psi^{d_i*}(Q)$ and the mixing angle. Since the latter also depends on the nuclear

coordinates, the gradient operates on both $\psi^{d_i *}(Q)$ and $\cos\theta$ (or $\sin\theta$).

The reader can show that

$$\begin{aligned}\frac{-2mi}{\hbar}\mathbf{J}^{a_1}(Q) &= \cos\theta^2\left(\psi^{d_1*}\boldsymbol{\nabla}\psi^{d_1}-\psi^{d_1}\boldsymbol{\nabla}\psi^{d_1*}\right)+\sin\theta^2\left(\psi^{d_2*}\boldsymbol{\nabla}\psi^{d_2}-\psi^{d_2}\boldsymbol{\nabla}\psi^{d_2*}\right)\\ &+\cos\theta\,\sin\theta\left(\psi^{d_1*}\boldsymbol{\nabla}\psi^{d_2}-\psi^{d_1}\boldsymbol{\nabla}\psi^{d_2*}+\psi^{d_2*}\boldsymbol{\nabla}\psi^{d_1}-\psi^{d_2}\boldsymbol{\nabla}\psi^{d_1*}\right)\\ &+\left(\psi^{d_1*}\,\psi^{d_2}-\psi^{d_1}\,\psi^{d_2*}\right)\boldsymbol{\nabla}\theta \qquad (3.70)\end{aligned}$$

and

$$\begin{aligned}\frac{-2mi}{\hbar}\mathbf{J}^{a_2}(Q) &= \sin\theta^2\left(\psi^{d_1*}\boldsymbol{\nabla}\psi^{d_1}-\psi^{d_1}\boldsymbol{\nabla}\psi^{d_1*}\right)+\cos\theta^2\left(\psi^{d_2*}\boldsymbol{\nabla}\psi^{d_2}-\psi^{d_2}\boldsymbol{\nabla}\psi^{d_2*}\right)\\ &-\cos\theta\,\sin\theta\left(\psi^{d_1*}\boldsymbol{\nabla}\psi^{d_2}-\psi^{d_1}\boldsymbol{\nabla}\psi^{d_2*}+\psi^{d_2*}\boldsymbol{\nabla}\psi^{d_1}-\psi^{d_2}\boldsymbol{\nabla}\psi^{d_1*}\right)\\ &-\left(\psi^{d_1*}\,\psi^{d_2}-\psi^{d_1}\,\psi^{d_2*}\right)\boldsymbol{\nabla}\theta. \qquad (3.71)\end{aligned}$$

Summing these two equations [Eqs. (3.70) and (3.71)], we find

$$\mathbf{J}^{a_1}(Q)+\mathbf{J}^{a_2}(Q)=\mathbf{J}^{d_1}(Q)+\mathbf{J}^{d_2}(Q).$$

The total probability current density is independent of the electronic basis used to expand the scattering wave function, as we would expect.

The two vector fields $\mathbf{J}^{a_1}(Q)$ and $\mathbf{J}^{a_2}(Q)$ correspond to the flow of probability associated with the two electronically adiabatic states. The divergence of the probability current density fields associated with the electronically adiabatic states corresponds to the loss (or gain) of probability density associated with one or the other state. Since the scattering process does not create or destroy particles, a consequence of the equation of continuity [150] is that loss in one state coincides with gain in the the other,

$$\nabla\cdot\mathbf{J}^{a_1}(Q)=-\nabla\cdot\mathbf{J}^{a_2}(Q.$$

) Thus, regions of high nonadiabatic divergence indicate those places on the potential energy surface where nonadiabatic transitions are occurring [25, 26].

We turn now to a determination of the probability current density field and its divergence for two exemplary reactions: F+HCl→FH+Cl and F+H_2 →FH+H.

3.4.4 F+HCl→FH+Cl Reaction

In this hydrogen exchange reaction, a classic heavy-light-heavy system, there are two electronic states (one degenerate) which are energetically accessible in both the reactant and product arrangement. Because of the strong interaction between the quadrupole moment of the halogen atom and the dipole-moment of the hydrogen halide, the Σ and Π electronic states are significantly split in both the reactant and product channels. In both the reactant and product arrangements this dipole-quadrupole interaction causes the Π orientation to be attractive while the Σ orientation is correspondingly repulsive (especially in the product FH+Cl arrangement where both the atomic and molecular electrostatic moments are larger). However, the Σ orientation has a lower barrier. Thus, a conical intersection occurs in both arrangements.

Because of the sizable splitting between the Σ and Π states at long range, these conical intersections occur near the barrier. We therefore have the possibility of electronic nonadiabaticity in both the inelastic F(j_a)+HCl→F(j_a')+HCl and reactive F(j_a)+HCl→FH+Cl(j_c') channels.

3.4.4.1 Potential Energy Surface

In this section we use the recent collinear potential surface calculations from Klos [30] for the lowest two adiabatic (V_Σ and V_Π) potentials and the spin-orbit coupling constant, A, as function of the nuclear coordinates. We present the contour plots of these collinear potential surfaces in Figs.(3.12) and (3.13).

The transformation from the Λ to the j_a bases is independent of the ABC geometry. Thus the j_a basis is also a quasi-diabatic basis, which has the additional advantage of being diagonal asymptotically in both the reactant (F+HCl) and product (FH+Cl) arrangements.

In the numerical implementation we use a simple bi-cubic interpolation routine to calculate the potential energy surface at the nodal points in the triangulation. This removes any fit related errors and because we use high density of *ab initio* points we do not have any issues with nonconvergent calculations while using MATLAB's built-in interpolation routines. Finally, Table 3.2 lists the predicted parameters of the FHCl barriers.

3.4.4.2 Results: Scattering Dynamics

In Figures (3.15) and (3.16) show the scattering probabilities for nonreactive and reactive collisions of, respectively, F($j_a = 3/2$) and F($j_a = 1/2$) with HCl as a function of energy.

One can see (in the lower panels) the presence of Stueckelberg oscillations [153–156] in the nonreactive probabilities. In purely non-reactive systems, these are

Table 3.2: Parameters of the FHCl barrier in the Λ, j_a and adiabatic bases.[1]

State	$(u_{\mathrm{HF}}, u_{\mathrm{HCl}})$[2]	E_a[3]	ω_{TS}[4]	E_{zpt}[5]
Σ	(2.569, 2.525)	0.3275	0.1159	0.1995
Π	(2.432, 2.631)	0.7910	0.0628	0.6365
j_a=3/2	(2.455, 2.582)	0.4583	0.0667	0.3218
j_a=1/2	(2.434, 2.612)	0.6384	0.0630	0.4518
a_1	(2.569, 2.525)	0.3267	0.1156	0.2147
a_2	(2.432, 2.631)	0.7955	0.0628	0.6088

[1]Distances in bohr, energies and vibrational frequencies in eV.

[2]Geometry of the saddle point, in bond coordinates.

[3]Barrier height relative to F+HCl(r_e) at $R_a = 24$.

[4]Frequency of the non-reactive normal mode at the saddle point.

[5]Zero-point corrected barrier: $\mathrm{E}_{zpt} = \mathrm{E}_a + 1/2(\omega_{\mathrm{TS}} - \omega_{\mathrm{HCl}})$. Here, ω_{HCl} on the *ab initio* PES's is 0.3756 eV, slightly larger than the experimental value of 0.3708 eV.

[6]Ref. [152].

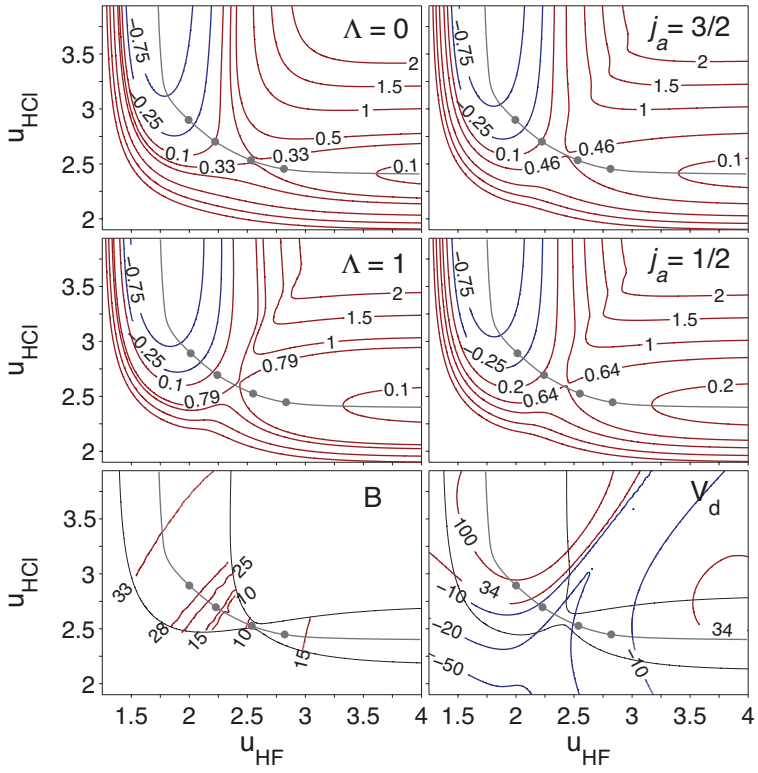

Figure 3.12: The FHCl PES's in the Λ and j_a diabatic bases. Distances in bohr and energies in eV in all panels except the spin-orbit coupling, B, and the electrostatic splitting, V_d, which are shown in meV. The zero of energy corresponds to F(Σ)+HCl(r_e) at $R_a = 24$. The F+HCl and FH+Cl asymptotes correspond to, respectively, the lower-right and upper-left valleys. Asymptotically, at distances considerably larger than shown here, in both arrangements the two diabatic PES's become identical ($V_\Sigma = V_\Pi$). Shown in grey is the minimum energy path (MEP) on the lowest adiabatic surface calculated using the method of Weinan *et al.* [151] The filled circles on the MEP are marker points to allow a comparison with the one-dimensional reaction path shown later in Fig. 3.14.

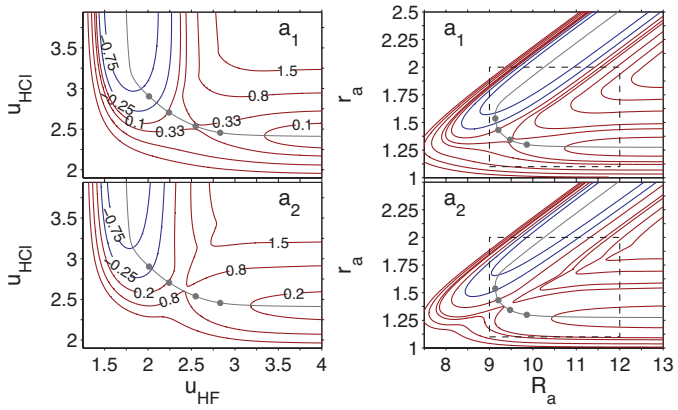

Figure 3.13: The FHCl PES's in the adiabatic basis in (left) bond coordinates and (right) in mass-scaled Jacobi coordinates. Distances in bohr and energies in eV. The potential contours in the right panels are identical to those on the left. The dashed box in the right panels show the area examined in more detail later in Fig. 3.17. The zero of energy corresponds to F(Σ)+HCl(r_e), at $R_a = 24$. Shown in grey is the minimum energy path (MEP) on the lowest adiabatic surface calculated using the method of Weinan *et al.* [151] The solid grey circles are marker points to allow a comparison with the one-dimensional reaction path shown later in Fig. 3.14.

due to interference between trajectories which undergo nonadiabatic ($j_a \rightarrow j_a \pm 1$) transitions as the particles approach and those, which recede after having bounced off the repulsive wall. Although the zero-point corrected barrier on the lower FHCl adiabatic PES is low (∼0.2 eV), the barrier up the first excited adiabatic PES is much higher, (∼0.6 eV). Thus, a significant fraction of the collisions are non-reactive for all values of the collision energies shown in Figs. (3.15) and (3.16). This leads to the pronounced oscillatory character in the non-reactive transition probabilities.

As can be seen in the upper panels of these two figures there is also a significant

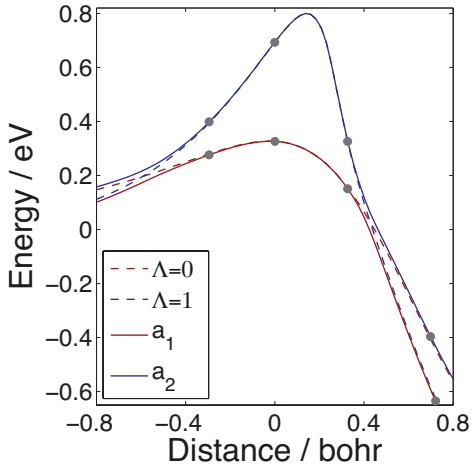

Figure 3.14: The FHCl potential energy surfaces along the minimum energy path (MEP) of the lower adiabat. The solid circles shown here are identical to the solid circles in Figs. 3.13 and 3.17 and thus provide a mapping of the 1D potential shown here onto the collinear PES's shown in these figures.

amount of nonadiabatic reactivity. As one might expect, reaction commences once the collision energy exceeds the zero-point corrected barrier on the lower PES (∼0.2 eV; see Tab. 3.2). Initially, Cl products are formed in the lower ($j_c = 3/2$) spin-orbit states. The upper spin-orbit state lies 0.11 eV higher, which explains the higher threshold for $j_c = 1/2$ products. We observe no evidence of oscillatory structure in the reactive products. There are no reflections corresponding to curve-crossing on the product side (Fig 3.14). Once the system proceeds through this crossing, there is no return. There is also nearly complete vibrational adiabaticity ($v_a{}' = v_a$) in the inelastically scattered products, and nearly complete vibrational specificity in the products ($v_c{}' = 3$).

More insight into the mechanism of nonadiabaticity is given by the divergence

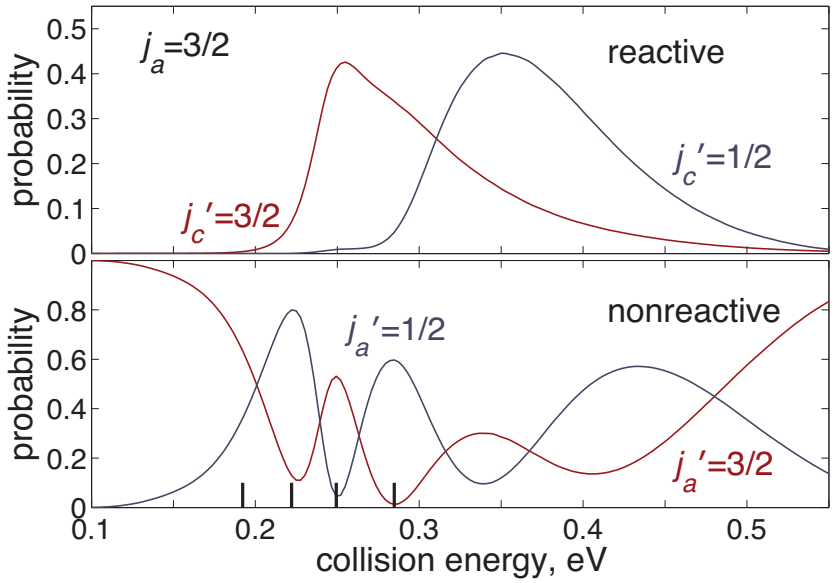

Figure 3.15: (Upper panel) Reactive F($j_a = 3/2$) + HCl($v_a = 0$) $\rightarrow$ HF($v_c' = 3$)+Cl(j_c') transition probabilities. (Lower Panel) Inelastic F($j_a = 3/2$) + HCl($v_a = 0$) $\rightarrow$ F(j_a') + HCl($v_a' = 0$) probabilities. The inelastic and reactive probabilities into other final vibrational levels are negligibly small. The thick black lines mark the energies probed in Fig. 3.17.

of the probability current density on the lower adiabatic state, $\nabla \cdot \mathbf{J}^{a_1}$ [where $\mathbf{J}^{a_1}$ is given by Eq. (3.70)]. Contour plots of the nonadiabatic divergence for this reaction are given in Fig. (3.17). As seen in rows 2–4, once the collision energy is high enough for reaction to occur ($E_{col} \geq E_{zpt}$ in Tab. 3.2), the region of strongest nonadiabatic divergence occurs in the product arrangement, delimited by the seams where $|V_\Sigma - V_\Pi| = 3B$ and centered on the seam where $V_\Sigma = V_\Pi$.

In all cases, the nonadiabatic divergence has both positive and negative lobes, evocative of wave crests and troughs, with a node located on the $V_\Sigma = V_\Pi$ seam.

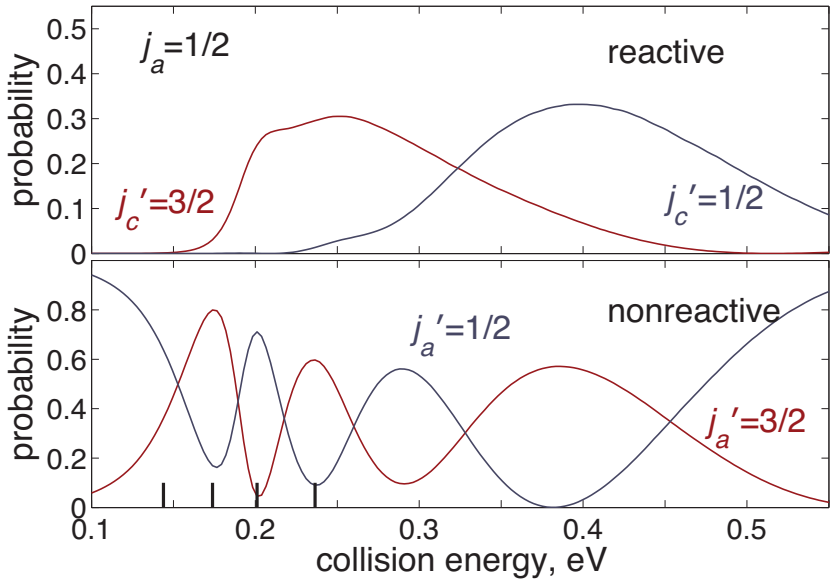

Figure 3.16: (Upper panel) Reactive F($j_a = 1/2$) + HCl($v_a = 0$) $\rightarrow$ HF($v_c' = 3$)+Cl(j_c') transition probabilities. (Lower Panel) Inelastic F($j_a = 1/2$) + HCl($v_a = 0$) $\rightarrow$ F(j_a') + HCl($v_a' = 0$) probabilities. The probabilities, both inelastic and reactive, into other vibrational levels are negligibly small. The thick black lines mark the energies probed in Fig. 3.17.

Figure 3.17 also shows a scale bar corresponding to the de Broglie wavelength of the F+HCl system. As we might have anticipated, we see that the range over which significant oscillations in nonadiabaticity occurs is roughly comparable to the de Broglie wavelength.

In the study on just the lowest electronically-adiabatic PES (Section 3.3):, at low energy the probability current density field indicated a substantial degree of corner cutting [138–140]. The bulk of the reaction takes a sharper turn than the MEP. Similarly, the contour plots of the nonadiabatic divergence in the exit

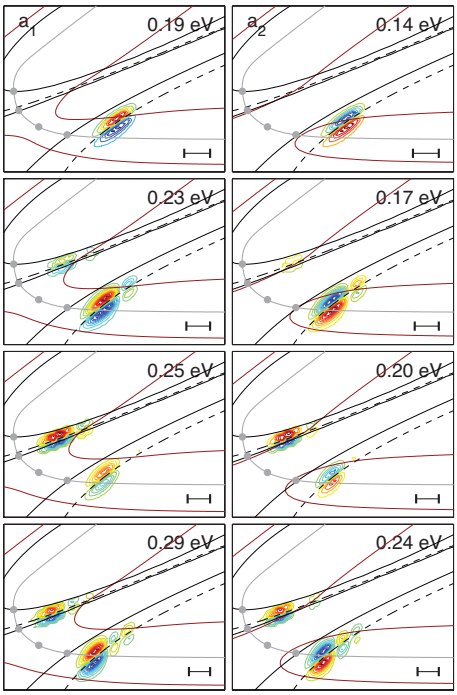

Figure 3.17: Divergence of the probability current density $\nabla \cdot \mathbf{J}^{a_1}$ associated with the lower adiabatic state, at several collision energies (left panels) for the reaction of F($j_a = 3/2$) (left panels) or F($j_a = 1/2$) (right panels) with HCl($v_a = 0$). Each row corresponds to a given total energy (the corresponding collision energies differ by the F-atom fine-structure splitting of 0.05 eV). The red contours in the left (right) panels delimit the classically forbidden region on the lower (upper) adiabatic PES. The solid and dashed black lines delineate, respectively, the seams where $|V_\Sigma - V_\Pi| = 3B$ and $V_\Sigma = V_\Pi$. The blue and red contours correspond to loss (gain) of current density associated with the lower (a_1) adiabatic state. The scale bar at the bottom right in each panel indicates the de Broglie wavelength at each collision energy.

channel show that the maximum electronic nonadiabaticy occurs inside the MEP. For nonadiabaticity occurring in the product arrangement the nodal structure of the nonadiabatic divergence is longitudal (parallel to the MEP).

Figure 3.17 reveals that in reactive encounters the incoming F atom moves adiabatically over the lower barrier (the barrier on the a_1 PES, regardless of its initial state, and behaves nonadiabatically only after it has crossed the barrier and moves through the region of curve-crossing on the FH+Cl side. For collision energies less than ∼0.6 eV (see Tab. 3.2), barrier crossing is possible only in the a_1 state. Thus, nonadiabaticity in the FH+Cl rearrangement is independent of which initial state is initially populated. Notice the sign of the divergence changes the reactant channel but is the same in the product channel when comparing the left and right panels of Fig. 3.17.

We also note that the relative minimum in the nonadiabatic, inelastic scattering probability in both the a_1 and a_2 states, at 0.25 eV and 0.20 eV respectfully, coincides with a significant reduction of the nonadiabatic divergence in the entrance channel as seen in the third row of Fig. 3.17.

Although a $\Sigma - \Pi$ curve crossing occurs also in the reactant arrangement (see Fig. 3.14), the degree of nonadiabaticity is much less. A quiver plot of the gradient of the mixing angle is shown in Fig. 3.18. The largest changes in the mixing angle occur beyond the barrier and are confined by the same set of contours where $|V_\Sigma - V_\Pi| = 3B$. In the reactant arrangement, the maximum nonadiabatic divergence is centered on the MEP and has both longitudinal and transverse characteristics.

The differing topography of the nodal patterns in the nonadiabatic divergence

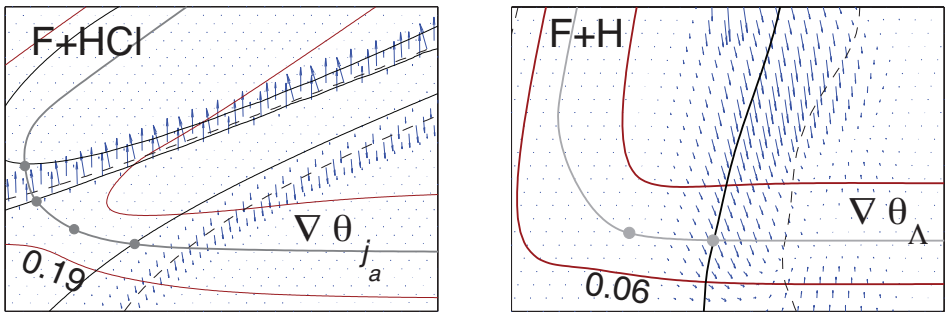

Figure 3.18: Quiver plot of the gradient of the mixing angle, θ [Eq. 3.61)], for the F+HCl (left) and F+H_2 (right) reactions. The red contours delimit the classically allowed region at the two collision energies indicated (eV). The solid and dashed black lines delineate, respectively, the seams where $|V_\Sigma - V_\Pi| = 3B$ and $V_\Sigma = V_\Pi$.

of the probability density suggests that the details of the electronic nonadiabaticity may vary with the degree of initial vibrational excitation of the HCl moiety.

We also observe that the change of sign of the nonadiabatic divergence in the entrance channel is to be expected: F atoms in the lower adiabatic state can undergo transitions to the upper state, with a loss of probability density out of the lower adiabatic state. Conversely, F atoms in the upper adiabatic state can undergo transitions to the lower, with a gain of probability in the lower state. Note that these two processes are reciprocal, despite the larger degeneracy of the lower state. This is because 50% of the $j_a = 3/2$ are uncoupled to the upper state, and hence evolve solely on the lower adiabatic PES.

Finally, the directionality of the gradient of the mixing angle, θ, shown in the quiver plot in the left panel of Fig. 3.18, offers a simple explanation of the difference

between the orientations of the waves in the nonadiabatic divergence in the reactant as compared to product arrangements. In the reactant channel the gradient of the mixing angle has a large vector component perpendicular to the MEP while in the product channel the vector field is predominantly parallel to the MEP.

3.4.5 $F+H_2 \rightarrow HF+H$

(Reactions with Mixed Boundary Conditions)

In this section we consider reactions that induce changes in electronic properties; i.e. reactions that involve different electronic structure in the reactant and product channels. Our model reaction in this section will be $F+H_2$. For this reaction the lone F atom in the entrance channel has non-zero spin-orbit coupling, whereas the lone H atom in the product channel does not exhibit this behavior. In this section we solve for the nonadiabatic dynamics of such a system using the FE approach outlined above.

The boundary conditions of Eq. 3.51 assume that the potential is asymptotically separable, $V_{ii}(R_\infty, r) = V_{ii}(r)$ and uncoupled, $V_{ij}(R_\infty, r) = 0$. As was the case for F+HCl and FH+Cl, for the $F+H_2$ arrangement, the j_a diabatic basis satisfies these criteria. However, in the FH+H product arrangement, the ground $^1\Sigma^+$ electronic state of HF lies far below the first excited Π state, [62] so that only the former is energetically accessible. The appropriate diabatic basis in the product arrangement is the Λ basis.

We can write the boundary condition in the reactant channel using the j_a basis

$$\Psi_{\Gamma_a}(R_a, r_a) = f_{\mathrm{v}_a}^{j_a *}(\bar{R}_a, \bar{r}_a)|j_a\rangle + \sum_{j_a'} \sum_{\mathrm{v}_{\gamma'}} S_{\mathrm{v}_{\gamma'}, \mathrm{v}_a}^{j_a', j_a} f_{\mathrm{v}_{\gamma'}}(\bar{R}_a, \bar{r}_a)\, |\mathrm{j}_a'\rangle \tag{3.72}$$

And we use the Λ basis in the product arrangement,

$$\Psi_{\Gamma_c}(R_c, r_c) = \sum_{\Lambda_c'} \sum_{\mathrm{v}_{\gamma'}} S_{\mathrm{v}_{\gamma'}, \mathrm{v}_a}^{\Lambda_c', \Lambda_c} f_{\mathrm{v}_{\gamma'}}(\bar{R}_c, \bar{r}_c)\, |\Lambda_c'\rangle, \tag{3.73}$$

where the electronic states are designated $|j_a\rangle$ in the reactant channel and $|\Lambda_c\rangle$ in the product channel.

We will solve the equations in the Λ diabatic basis. At the reactant boundary Γ_a, we can use the transformation between the two diabatic bases [Eq. (3.58)] to re-express the boundary conditions on Γ_a in terms of the Λ states. We have

$$\Psi_{\Gamma_a} = \sum_{\Lambda_a} f_{\mathrm{v}_a}^{j_a *} D_{j_a, \Lambda_a} |\Lambda_a\rangle + \sum_{\Lambda_a'} \sum_{j_a'} \sum_{\mathrm{v}_a'} f_{\mathrm{v}_a'}^{j_a'}\, S_{\mathrm{v}_a', \mathrm{v}_a}^{j_a', j_a} D_{j_a' \Lambda_a'} |\Lambda_a\rangle, \tag{3.74}$$

where $D_{j_a' \Lambda_a'}$ is the matrix element coupling j_a' and Λ_a'. Thus, for a single initial condition (F in a particular j_a state and H_2 in a particular vibrational level) the mixed-state equivalent of the one-column solution Eq. (3.30) is

$$\begin{bmatrix} \mathbf{A}_{11} & \mathbf{A}_{11} & -D_{11}\mathbf{B}_a^{3/2} & -D_{21}\mathbf{B}_a^{1/2} & -\mathbf{B}_c^{\Sigma} & 0 \\ \mathbf{A}_{12} & \mathbf{A}_{12} & -D_{12}\mathbf{B}_a^{3/2} & -D_{22}\mathbf{B}_a^{1/2} & 0 & -\mathbf{B}_c^{\Pi} \\ \mathbf{I}_a^{\Sigma} & 0 & -D_{11}\mathbf{F}_a^{3/2} & -D_{21}\mathbf{F}_a^{1/2} & 0 & 0 \\ 0 & \mathbf{I}_a^{\Pi} & -D_{12}\mathbf{F}_a^{3/2} & -D_{22}\mathbf{F}_a^{1/2} & 0 & 0 \\ \mathbf{I}_c^{\Sigma} & 0 & 0 & 0 & -\mathbf{F}_c^{\Sigma} & 0 \\ 0 & \mathbf{I}_c^{\Pi} & 0 & 0 & 0 & -\mathbf{F}_c^{\Pi} \end{bmatrix} \begin{bmatrix} \mathbf{C}^{\Sigma} \\ \mathbf{C}^{\Pi} \\ \mathbf{S}_a^{3/2} \\ \mathbf{S}_a^{1/2} \\ \mathbf{S}_c^{\Sigma} \\ \mathbf{S}_c^{\Pi} \end{bmatrix} = \begin{bmatrix} D_{11}\mathbf{b}^{3/2} \\ D_{12}\mathbf{b}^{3/2} \\ D_{11}\mathbf{f}^{3/2} \\ D_{12}\mathbf{f}^{3/2} \\ 0 \\ 0 \end{bmatrix}. \tag{3.75}$$

In order to write this in a more concise form, we have reordered the scattering amplitudes in the vector of unknowns from Eq. (3.56). Technically, the spin-orbit

Hamiltonian couples the Σ state with the $\bar{\Pi}$ (and, similarly, the $\bar{\Sigma}$ state with the Π state). For simplicity, we have suppressed the superscript bar. The solution to this system of equations yields the scattering wave function in the Λ basis, as well as the mixed-state reactive and nonreactive scattering amplitudes. Note that the transformation from the Λ basis to the j_a basis at the boundary Γ_a reduces the sparsity of the 2^{nd} and 3^{rd} columns of the matrix in Eq. (3.30), after introduction of the elements of the $\Lambda\Sigma \rightarrow j_a$ transformation matrix.

3.4.5.1 Potential Energy Surface

To investigate nonadiabaticity in the collinear F+H_2 reaction, we use the recent Li-Werner-Alexander-Lique (LWAL) FH_2 PESs [63]. Figure 3.19 displays contour plots of these PES's in both the j_a and Λ bases. A similar plot of the FH_2 PES's in the adiabatic basis, in both bond- and mass-scaled-Jacobi coordinates, is presented in Fig. 3.20. The corresponding one-dimensional plot of the energies along the MEP is shown in Fig. 3.21. At the barrier, the energy of the Π state is so high, that the lowest electronically adiabatic state is indistinguishable from the energy of the Σ state. We used the same asymptotic value of the spin-orbit constant in the reactant channel as in the F+HCl simulations: $B_{\mathrm{F}} = 0.01607$ eV.

3.4.5.2 Two-State Scattering with Mixed Boundary Conditions

Figures 3.22 and 3.23 show the scattering probabilities for nonreactive and reactive collisions of, respectively, F($j_a = 3/2$) and F($j_a = 1/2$) with H_2.

Figure 3.24 is a contour plot of the divergence of the probability current density field on the lower adiabatic state, $\nabla \cdot \mathbf{J}^{a_1}$. Because the Π surface is energetically inaccessible in the exit channel, nonadiabaticity in the F+H_2 reaction occurs only in the reactant arrangement, largely confined to regions of configuration space between the seams where $|V_\Sigma - V_\Pi| = 3B$ and $V_\Sigma = V_\Pi$.

Unlike the F+HCl reaction, we see that the nonadiabatic, inelastic scattering probabilities (the probabilities for fine-structure changing F(j_a)+H_2 collisions) drop to nearly zero at two energies. As one might have anticipated, we see (rows 2 and 4 in Fig. 3.24) that the nonadiabatic divergence almost completely vanishes at these energies. In contrast, for the F+HCl reaction the nonadiabatic, inelastic transition probabilities never quite reach zero so that the nonadiabatic divergence in the reactant channel never quite vanishes.

The sign of the nonadiabatic divergence in the reactant channel of the F+H_2 reactions is again opposite for the initial states a_1 and a_2, as can be seen by comparing the columns of Fig. 3.24. This is the identical to the F+HCl reaction. We see the location of the nonadiabatic divergence is the same for both initial states, however the direction of the nonadiabatic divergence is not. At the total energy represented by the third row of plots in Fig. 3.24 the largest nonadiabatic divergence occurs, which corresponds to maximal nonadiabatic, inelastic probability (Figs. 3.22 and 3.23).

From the right panel of Fig. 3.18 we can see that for F+H_2 the gradient of the mixing angle, θ, is confined to the reactant channel. This is expected from the repulsive behavior of the upper state. Once the Σ and Π states become separated

by an amount much larger than the $3B$ ($\sim$ 0.05 eV for the F atom), there is no more mixing. We also note that the direction of the vector field is about 45° relative to the direction of the reaction path. Consequently, there is no preferred sense (longitudinal or transverse) in the wave character of the nonadiabatic divergence.

3.4.6 Discussion

In this section we have extended the FEM time-independent treatment of collinear reactive scattering from Section 3.3 to reactions involving coupled potential surfaces. We solve the electronically coupled Schrödinger equation in a diabatic basis. This can be transformed easily on the boundary, to allow treatment of atom+diatom systems in which different diabatic bases correspond to the asymptotically uncoupled basis in the two arrangements.

The FEM method yields the scattering wave function directly, without post processing. By transforming the scattering wave function into an electronically adiabatic basis, we can obtain the adiabatic probability current density. In the fluid dynamic picture of quantum scattering, the divergence of this vector field shows unambiguously where, and over what range, nonadiabaticity occurs. This is the first two-dimensional extension of simpler one-dimensional models [67, 68, 157, 158] of nonadiabaticity in reaction dynamics.

In applications to the F+HCl→FH+Cl and F+H_2 →FH+H reactions, we observe that the nonadiabatic divergence displays pronounced oscillatory behavior, extending over a range similar to the de Broglie wavelength of the reacting partners.

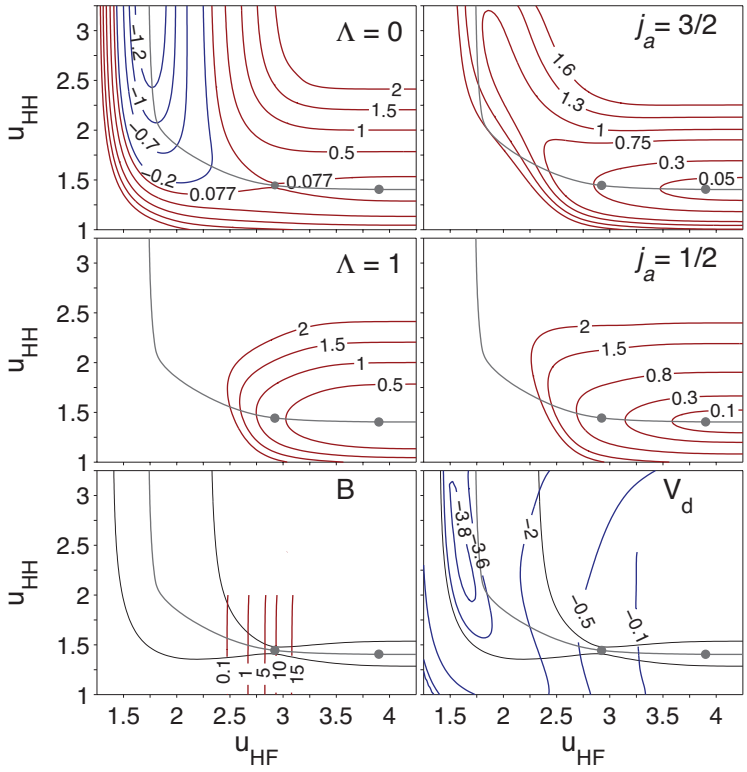

Figure 3.19: Contour plots of the Li-Werner-Alexander-Lique (LWAL) [63] FH_2 PESs in both the Λ and j_a bases. The units here are eV, except for B, which is shown in meV. The zero of energy corresponds to $F(\Sigma)+H_2(r_e)$, $R_a = 10.5$. Asymptotically, at distances considerably larger than shown here, the two diabatic PES's become identical, $V_\Sigma = V_\Pi$ for large R_a and R_c. Shown in grey is the minimum energy path (MEP) on the lowest adiabatic surface calculated using the method of Weinan *et al.* [151] The solid grey circles are marker points to allow a comparison with the one-dimensional reaction path shown later in Fig. 3.21.

These divergence waves occur where the off-diagonal coupling in the electrostatic and spin-orbit diabatic basis is equal. Nonadiabaticity has long been thought [145–147]

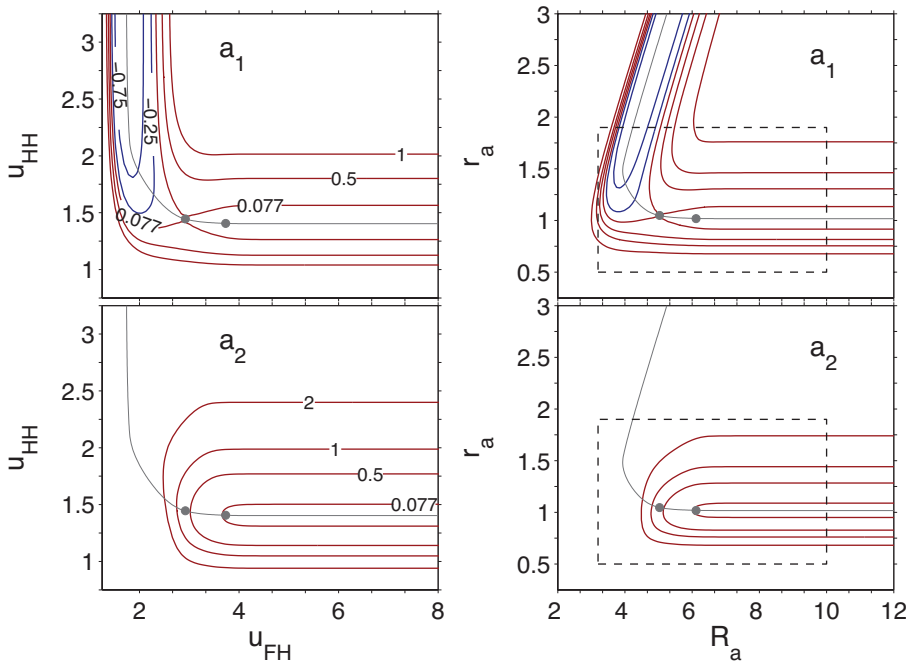

Figure 3.20: The FH_2 PES's in the adiabatic basis in bond coordinates (left panels) and in mass-scaled Jacobi coordinates (right panels); distances in bohr and energies in eV. The contour values on the right panels are identical to those on the left. The dashed box shows the area examined in Fig. 3.24. The zero of energy corresponds to $F(\Sigma)+H_2(r_e)$, $R_a = 10.5$. The light gray line corresponds to the minimum energy path calculated using the method of Weinan *et al.* [151] The solid grey circles are marker points to allow a comparison with the one-dimensional reaction path shown in Fig. 3.21.

to be most pronounced on this seam. For the F+HCl reaction we observed that the predominant nonadiabaticity in the formation of reactive products occurs in a region well inside the minimum energy path, in a manifestation of corner-cutting in this heavy-light-heavy reaction.

Comparing the nature of nonadiabaticity in the F+HCl and $F+H_2$ reactions

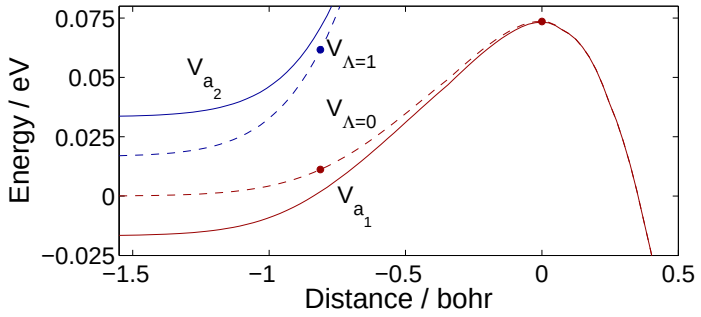

Figure 3.21: The LWAL FH_2 PESs along the minimum energy path on the lower adiabatic surface, in the region of the barrier. The solid circles correspond to the points marked solid circles in the collinear contour plots presented in Figs. 3.19, 3.20 and 3.24.

we observe a qualitative similarity in the nonadiabatic divergence. In these reactions we observe an expected behavior, namely the divergence intensifies at energies corresponding to relative maxima in nonadiabatic transitions (inelastic and reactive) and is diminished at energies corresponding to relative minima in the nonadiabatic scattering probabilities.

In a recent paper [159] Guo *et al.*, investigated the state-to-state dynamics of the F+HCl system using a 3D time-dependent study on solely the ground state potential energy surface (PES) of Deskevich [126]. These authors speculated that electronic nonadiabaticity could contribute to the observed disagreement between the predictions of the calculations and experiment [160]. Here we have shown, albeit in reduced dimensionality, that nonadiabaticity in the F+HCl reaction can be significant, and vary with collision energy. We believe that nonadiabaticity will be similarly important in the F+HCl reaction in full dimensionality.

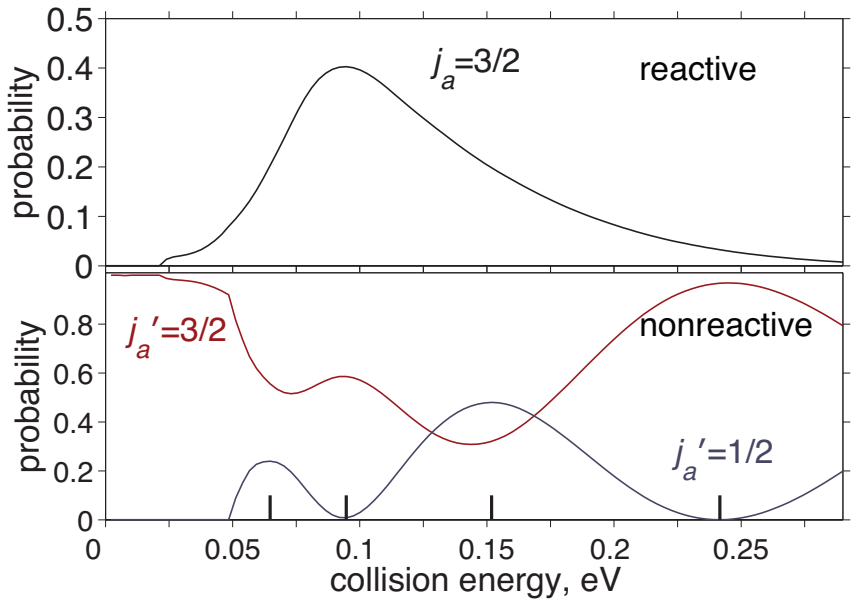

Figure 3.22: (Upper panel) Probability of reactive F(j_a = 3/2) + H_2(v_a = 0) → HF(v_c' = 3)+H scattering. HF products are formed only in the lower (Λ = 0) electronic state. (Lower Panel) Probability of inelastic F(j_a = 3/2) + H_2(v_a = 0) → F(j_a') + H_2(v_a' = 0) scattering. Note: Probabilities of reactive or inelastic scattering to other vibrational levels are negligibly small. The thick black lines mark the energies probed in Fig. 3.24.

Tully and his collaborators have developed a suite of powerful quasi-classical surface-hopping methods, that have permitted the simulation of collision dynamics in complex systems where multiple PES's are coupled together [15, 66–71]. The initial work on these methods was guided by a number of one-dimensional models. We believe that the two-dimensional snapshots presented here increase our ability to unravel the details of electronic nonadiabaticity in chemical reactions. As such, the examples presented here, or similar studies on other exemplary systems, will provide

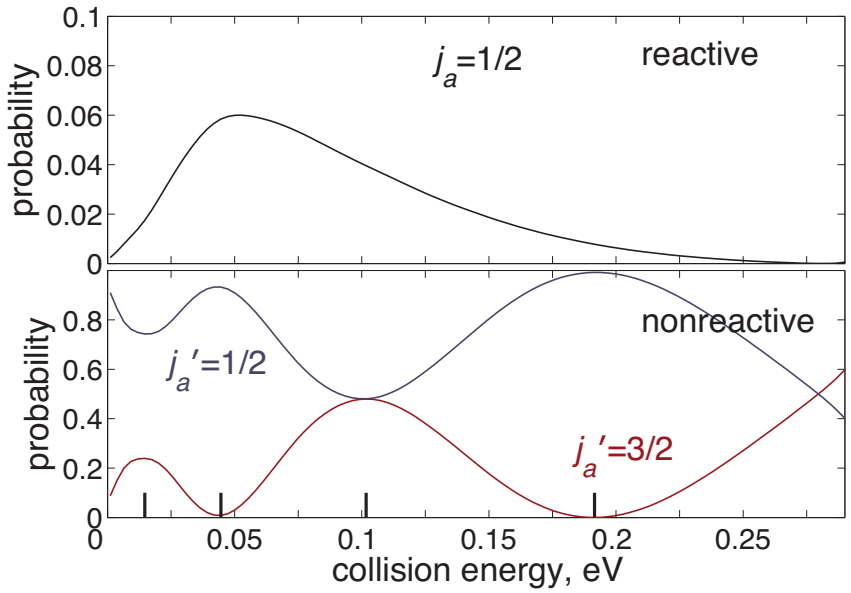

Figure 3.23: (Upper panel) Probability of reactive F(j_a = 1/2) + H_2(v_a = 0) → HF(v_c' = 3)+H scattering. HF products are formed only in the lower (Λ = 0) electronic state. (Lower Panel) Probability of inelastic F(j_a = 1/2) + H_2(v_a = 0) → F(j_a') + H_2(v_a' = 0) scattering. Note: Probabilities of reactive or inelastic scattering to other vibrational levels are negligibly small. The thick black lines mark the energies probed in Fig. 3.24.

far more stringent testbeds for the development and calibration of sophisticated trajectory-based methods.

Two-dimensional calculations are not the state of the art in reactive scattering. Extension of the FEM method to 3D scattering, even in the J = 0 limit, will be computationally difficult, due to the large size of the matrices. More standard time-independent methods for reactive scattering involving a single [6] or multiple potential energy surfaces [62] are based on propagation of the ratio of the derivative of the scattering wave function to the wave function itself (the so-called log-derivative).

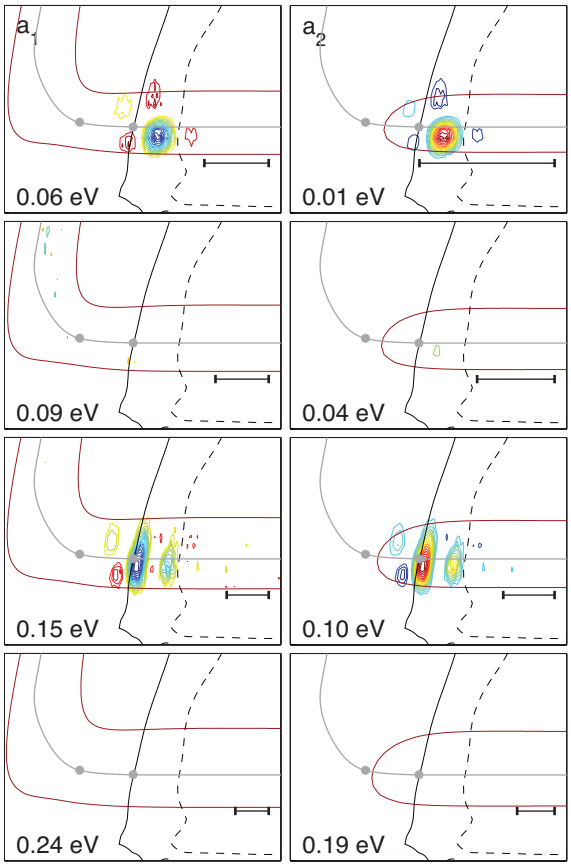

Figure 3.24: Divergence of the F(j_a) + H_2($v_a = 0$) probability current density field on the lower adiabatic surface, $\nabla \cdot \mathbf{J}^{a_1}$, for a range of collision energies and for $j_a = 3/2$ (left) and $j_a = 1/2$ (right). The red curves in the left (right) panels delimit the classically allowed regions on the lower (upper) adiabatic potential. The solid and dashed black lines delineate, respectively, the seams where $|V_\Sigma - V_\Pi| = 3B$ and $V_\Sigma = V_\Pi$. The blue and red contours correspond to loss (gain) of current density associated with the lower (a_1) adiabatic state. The two panels in each row correspond to the same total energy. The region of the PES depicted corresponds to the dashed rectangles in Fig. 3.20.

Once the S matrix has been determined, at the end of the propagation, one could back-propagate to extract the wave function, and, from this, the current density field and, in the case of scattering on multiple PES's, the vector divergence. This is now routine in time-dependent inelastic scattering [161]. However, no generalized software exists to perform these fully 3D nonadiabatic calculations. Notwithstanding, these collinear calculations provide unique, and hitherto unseen, insight into nonadiabaticity in reactive collisions.

3.5 Ultracold Nonadiabatic Reactions: Li+CaH

3.5.1 Introduction

There is recently much interest to efficiently produce cold and ultra-cold molecules [162, 163]. The field of low temperature chemistry offers increased control over the quantum state of the reactants and collision energy resolution. The cold regime also allows for precise single-molecule spectroscopy [164] and control over chemical reactions using external fields or trapping cold molecules in optical lattices [165] and magnetic traps [166]. Optical lattices are a promising tool for realizations of quantum information objectives, i.e. quantum computers and simulators.

The magnetic trapping and co-trapping of cold atoms and molecules are tools for precise studies of collision dynamics and measurements that can reveal new physics [167]. Stark deceleration has been used successfully to slow down supersonic beams of polar molecules such as OH [168, 169] and ND_3 [170]. Sub-kelvin reac-

tions have also been studied by exploiting the Zeeman effect. The Zeeman effect is exploited using curved magnetic quadrupole guides to merge a beam molecules with a magnetic moment, such as metastable Ne, with another beam of molecules to investigate resonances in the ultra-cold reaction regime [171–173].

Reaction kinetics in the low kelvin regime have also been studied by the so-called CRESU technique (cinétique de réaction en éclement supersonique uniforme, or reaction kinetics in uniform supersonic flow). Sims and coworkers [64] have recently used this technique to determine the F+H_2 reaction rate from 11 K to 295K. These measurements, which are below the 800K reaction barrier, confirmed that the reaction rate in the low temperature regime is driven by quantum tunneling effects.

Recently, a slow beam of CaH($X^2\Sigma^+$) molecules has been realized by two-stage cell buffer gas method [174,175]. A similar method has been used to prepare a source of slow CaF molecules [166]. Beams of slow moving molecules can be used as a source for loading molecular traps. In this study we are interested in the feasibility of using these techniques to cool trapped CaH molecules to sub-kelvin temperatures via controlled interactions with a beam of cold Li atoms.

The theoretical plausibility of using cold Li atoms for sympathetic cooling of CaH molecules in a spin-polarized state has been demonstrated in scattering calculations [176]. The calculations on the spin-polarized Li-CaH triplet surface show a favorable ratio of elastic to inelastic collisions, which predicts minimal collision induced loses. Tscherbul *et al.* claim that extending the CaH interatomic distance does not lead to the reaction on the triplet surface, on the other hand, the singlet surface may lead to the following exothermic reaction with exothermicity of 0.67

eV:

$$\mathrm{Li}(^2\mathrm{S}) \quad + \quad \mathrm{CaH}(^2\Sigma^+) \rightarrow \mathrm{Ca}(^1\mathrm{S}) + \mathrm{LiH}(^1\Sigma^+). \tag{3.76}$$

Low temperature collisions on the endothermic triplet surface should not lead to reaction. The possibility of spin-orbit coupling between triplet and singlet surfaces that would lead to depolarizing the high spin state and cause a loss in sympathetic cooling process remains an open questions. Therefore, in this work, we present reduced dimensionality finite element method (2D-FEM) studies of collisions between Li and CaH on the triplet (S=1) potential energy surface with coupled by the spin-orbit term to the barrierless singlet (S=0) surface. To perform these scattering calculations we first calculate new potential surfaces including the singlet and triplet surfaces as well as the spin-orbit coupling term from first-principle configuration interaction calculations.

3.5.2 *ab initio* Potential Surfaces

In this study we are interested in the interaction between Li(^{2}S) atom and the CaH molecule in the ground electronic $X^2\Sigma^+$ state. In our *ab initio* approach to calculate the $S = 0$ (singlet), $S = 1$ (triplet) potential energy surfaces and the spin-orbit coupling between these surfaces we used the state-averaged complete active space configurational self-consistent field (SA-CASSCF) method to obtain reference orbitals for subsequent internally contracted multi-reference configuration interaction calculations including explicitly single and double excitations (*ic*-MRCISD).

The Davidson correction was applied to account for effects of higher excitations in an approximate manner. The Ca atom was described by all-electron correlation consistent quadruple-zeta basis set (vQZ), the Li atom by augmented, correlation consistent quadruple-zeta (aug-cc-pVQZ) and hydrogen by aug-cc-pVTZ basis sets.

The reference wave function for the MCSCF calculations were obtained from the restricted Hartree-Fock calculations (RHF) for the high-spin case. The first step of the CASSCF calculations was to perform state-averaged calculations for the singlet and triplet states. The active space in the CASSCF calculation was composed of 13 orbitals in A' representation and 3 orbitals of A'' representation of the C_s symmetry group. The first four A' and one A'' orbitals were kept frozen with an additional four A' and one A'' correlated but kept doubly occupied.

Using the MRCI density matrices for the $S = 0$ and $S = 1$ Li-H-Ca electronic states we calculated spin-orbit coupling matrix elements between the two surfaces. The potentials and spin-orbit matrix element were calculated for geometry described by two bond coordinates, u_{LiH} and u_{HCa} and $\angle$ Li-H-Ca bond angle. We calculated the potential surfaces and the coupling term for the $\angle$ Li-H-Ca bond angle of 160 degrees andon a grid of interatomic distance from 1.4 to 24 a_0 for u_{LiH} and from 1.8 to 24 a_0 for u_{HCa}.

Figure 3.25 shows the contour plots of the potential energy surfaces and spin-orbit constant in the interaction region for each fixed value of θ. In Fig. 3.26 we show the potential energy surfaces along the minimum energy path along the triplet surface for $\theta = 160$. Lastly, we provide the descriptive parameters of each potential surface in Table 3.5.2.

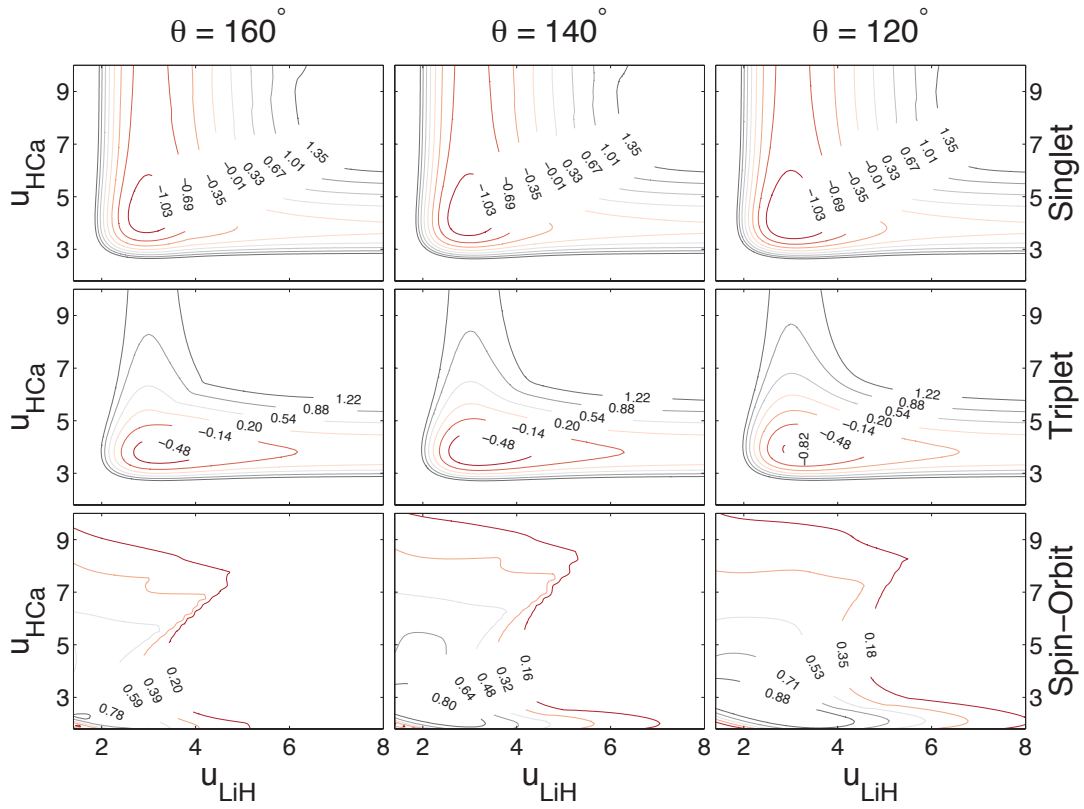

Figure 3.25: Potential contours of the Li+CaH reaction for the singlet surface in eV (top), triplet surface in eV (middle) and spin-orbit matrix element in meV (bottom) as a function of bond coordinates for three fixed collision angles $\theta = 120°, 140°, 160°$.

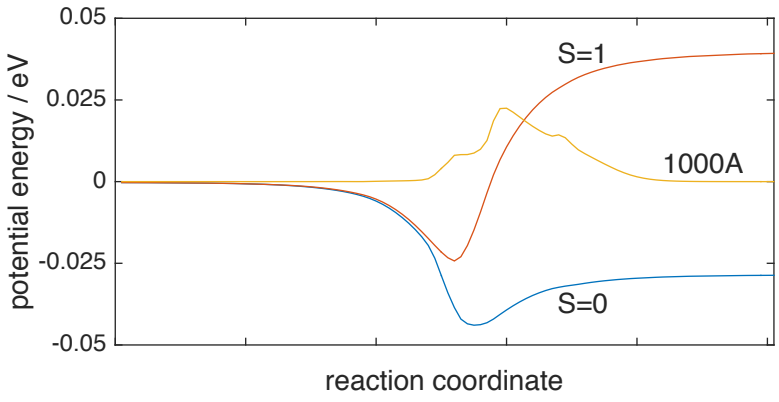

Figure 3.26: Potential surfaces of the Li+CaH reaction for the singlet and triplet surface in eV and spin-orbit matrix element in meV along the minimum energy path for $\theta = 160^{\circ}$ (from Weinan's method [151]).

3.5.3 Results and Discussion

We use the reactive scattering software developed in this Chapter to simulate the nonadiabatic reaction dynamics of Li+CaH coupled singlet and triplet potential surfaces. Specifically we are interested in the possible quenching of the by spin-orbit

Table 3.3: Minimum geometries for the singlet and triplet surfaces of Li+CaH. Values given in bohr and eV.

	θ	U_{LiH}	U_{HCa}	V_{min}
singlet	120	2.99	4.19	-1.37
	140	2.99	4.23	-1.27
	160	2.99	4.40	-1.24
triplet	120	3.19	3.90	-0.91
	140	3.19	3.82	-0.78
	160	3.22	3.82	-0.66

induced nonadiabatic transitions. The singlet and triplet surfaces are coupled by the spin-orbit operator, namely,

$$\mathbf{V}(Q) = \mathbf{V}_{el}(Q) + \mathbf{V}_{\mathrm{SO}}(Q) = \begin{bmatrix} V_{S=0}(Q) & 0 \\ 0 & V_{S=1}(Q) \end{bmatrix} + \begin{bmatrix} 0 & B(Q) \\ B(Q) & 0 \end{bmatrix}. \quad (3.77)$$

The spin-orbit constant, B, vanishes asymptotically in both the reactant and product channels. Accordingly, we can use the same potential basis in both reactant and product channels as we did in the case of F+HCl in Section 3.4.4. In Fig. 3.27 we provide the results of the scattering simulations at low collision energies.

From Fig. 3.27 we can see there is essentially zero spin-orbit induced nonadiabatic reaction probability. The probabilities do vary some as a function of the bond angle and therefore one expects the full three dimensional scattering calculations

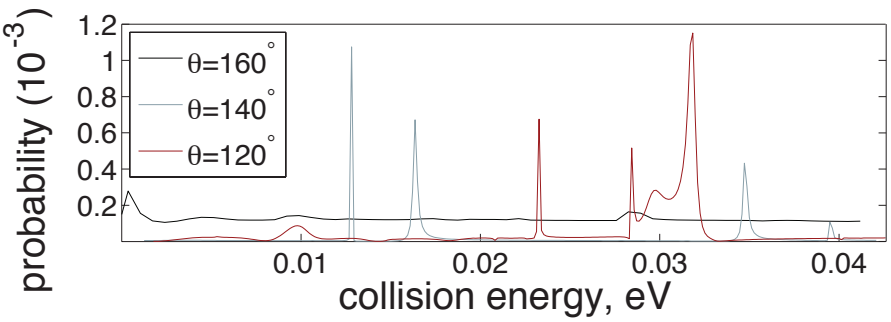

Figure 3.27: Nonadiabatic reactive scattering probabilities summed over all final states for triplet Li(^2S)+CaH($^2\Sigma$) $\rightarrow$ Ca(^1S)+LiH($^1\Sigma$) as a function of angle. Note: the results for $\theta = 160°$ are increased by a factor of 100.

would accordingly vary from these results qualitatively. However, the magnitude of these results is so small that it is unlikely that the inclusion of rotational dynamics will dramatically increase the probability of nonadiabatic transitions induced by spin-orbit couplings.

Nonadiabatic transitions are most probable when the off-diagonal elements of the coupling potential are on the order of magnitude of the difference between the diagonal potential surfaces. Based on the new *ab initio* potential surfaces presented in this work, we have found that the spin-orbit coupling never satisfies this requirement. Our scattering calculations, albeit in reduced dimensionality, have shown that for collision energies relevant in ultra-cold cooling methods, the spin-orbit induced transitions are negligibly small. This emboldens the claim made by Tscherbul and coworkers [176] that lithium atoms are very promising collision partners to produce ultra cold CaH molecules.

Chapter 4: Representation of Reactive Potential Surfaces

4.1 Overview

In this Chapter we describe some aspects of the potential energy surfaces required for the study of nonadiabaticity in atom-diatom reactions. We refer the reader elsewhere for an introduction to *ab initio* electronic structure calculations [3–5, 73, 177, 179]. In particular, we will introduce the use of a time-reversal-invariant basis for reactive scattering. We also discuss the results of our recent potential energy calculations for the $O(^3P)$+H_2 system.

As discussed in the preceding chapters, to model accurately the reaction dynamics of open-shell systems we require multiple, coupled potential energy surfaces. To simplify the treatment of the dynamics we need to take advantage of all possible symmetries in the representation of the electronic Hamiltonian. In this chapter we show how exploiting time-reversal [180] symmetry can achieve a significant blocking of the matrix of the Hamiltonian. We apply this simplification to a set of new, accurate potential energy surfaces for the $O(^3P)$ +H_2 reaction including electronic diabatic and spin-orbit couplings.

4.2 A(^{2}P)+BC

Consider the collision of an atom in a ^2P electronic state with a closed-shell diatomic. Asymptotically, the electronic angular momentum $L = 1$ and the spin $S = 1/2$. and there are 6 electronic states (two values of m_s and three values of m_l). We will use the $|\Lambda\Sigma\rangle$ basis of Alexander and co-workers, [62] namely $|\Sigma\rangle$, $|\bar{\Sigma}\rangle$, $|\Pi_1\rangle$, $|\bar{\Pi}_1\rangle$, $|\Pi_{-1}\rangle$ and $|\bar{\Pi}_{-1}\rangle$], where

$$|\Sigma\rangle \equiv |l = 1, m_l = 0\rangle|s = 1/2, m_s = 1/2\rangle$$

which can be simplified as

$$|\Sigma\rangle \equiv |0\rangle|1/2\rangle$$

and so forth, for example,

$$|\bar{\Pi}_1\rangle = |1\rangle|-1/2\rangle.$$

In this definite-m representation (so-called because the projection of the electronic angular momentum is a good quantum number), the matrices of the electronic Hamiltonian given by Alexander [62]

$$\mathbf{H}_{el}^{\Lambda\Sigma} = \left[\begin{array}{c|cccccc} & \Sigma & \bar{\Sigma} & \Pi_1 & \bar{\Pi}_1 & \Pi_{-1} & \bar{\Pi}_{-1} \\ \hline \Sigma & V_\Sigma & 0 & -V_1 & 0 & V_1 & 0 \\ \bar{\Sigma} & 0 & V_\Sigma & 0 & -V_1 & 0 & V_1 \\ \Pi_1 & -V_1 & 0 & V_\Pi & 0 & V_2 & 0 \\ \bar{\Pi}_1 & 0 & -V_1 & 0 & V_\Pi & 0 & V_2 \\ \Pi_{-1} & V_1 & 0 & V_2 & 0 & V_\Pi & 0 \\ \bar{\Pi}_{-1} & 0 & V_1 & 0 & V_2 & 0 & V_\Pi \end{array}\right].$$

It is also possible to use a basis in which Cartesian representation of the Π states (Π_x and Π_y are used. For a triatomic system, with a plane of symmetry, there will be no coupling between the Π_y state, which is antisymmetric with respect to reflection in this plane, and the Π_x and Σ states, which are symmetric with respect to this same reflection. The elements of the electronic Hamiltonian in this basis are the product of standard electronic structure codes (for example MOLPRO [3]). We have $V_\Sigma = V_{zz}$, $V_\Pi = (V_{xx} + V_{yy})/2$, $V_2 = (V_{yy} - V_{xx})/2$ and $V_1 = V_{xz}/\sqrt{2}$. Here, each term is a function of the three internal coordinates of the triatomic system.

The spin-orbit Hamiltonian is also given by Alexander [62]

$$\mathbf{H}_{so}^{\Lambda\Sigma} = \left[\begin{array}{c|cccccc} & \Sigma & \bar{\Sigma} & \Pi_1 & \bar{\Pi}_1 & \Pi_{-1} & \bar{\Pi}_{-1} \\ \hline \Sigma & 0 & 0 & 0 & -\sqrt{2}B & 0 & 0 \\ \bar{\Sigma} & 0 & 0 & 0 & 0 & -\sqrt{2}B & 0 \\ \Pi_1 & 0 & 0 & -A & 0 & 0 & 0 \\ \bar{\Pi}_1 & -\sqrt{2}B & 0 & 0 & A & 0 & 0 \\ \Pi_{-1} & 0 & -\sqrt{2}B & 0 & 0 & A & 0 \\ \bar{\Pi}_{-1} & 0 & 0 & 0 & 0 & 0 & -A \end{array}\right],$$

where A and B are defined in [Ref. [62]]. In the following section we show how the total Hamiltonian for this system (a coupled 6×6 system) can be block-diagonalized in a basis of states – the so-called Kramers states – in which the time-reversal operator $\hat{\boldsymbol{\theta}}$ is diagonal.

4.2.1 Kramers States

The Kramers states are those that diagonalize the time-reversal operator $\hat{\boldsymbol{\theta}}$ (which commutes with the Hamiltonian). Knowing the action of the time-reversal invariant operator, from Brink [180],

$$\hat{\boldsymbol{\theta}}|jm\rangle = (-1)^{j-m}|j-m\rangle,$$

where j can be either l or s, we can construct the matrix of $\hat{\boldsymbol{\theta}}$. This operator acts simultaneously in both the three-dimensional coordinate space and in the spin space, so that

$$\hat{\boldsymbol{\theta}} \equiv \hat{\boldsymbol{\theta}}_l \hat{\boldsymbol{\theta}}_s.$$

It is easy to compute the matrix of $\hat{\boldsymbol{\theta}}$ in the $|\Lambda\Sigma\rangle$ basis. We find that the full matrix of $\hat{\boldsymbol{\theta}}$ is

$$\theta^{\boldsymbol{\Lambda\Sigma}} = \left[\begin{array}{c|cccccc} & \Sigma & \bar{\Sigma} & \Pi_1 & \bar{\Pi}_1 & \Pi_{-1} & \bar{\Pi}_{-1} \\ \hline \Sigma & 0 & 1 & 0 & 0 & 0 & 0 \\ \bar{\Sigma} & -1 & 0 & 0 & 0 & 0 & 0 \\ \Pi_1 & 0 & 0 & 0 & 0 & 0 & -1 \\ \bar{\Pi}_1 & 0 & 0 & 0 & 0 & 1 & 0 \\ \Pi_{-1} & 0 & 0 & 0 & -1 & 0 & 0 \\ \bar{\Pi}_{-1} & 0 & 0 & 1 & 0 & 0 & 0 \end{array}\right].$$

As a result, in the $|\Lambda\Sigma\rangle$ basis the matrix of the time-reversal operator is "anti-unitary" so that $\hat{\boldsymbol{\theta}}^2 = -\mathbf{I}$. Diagonalization gives six eigenvectors

$$|\Sigma^{(\varepsilon)}\rangle = 2^{-1/2}\left(|\Sigma\rangle + i\varepsilon|\bar{\Sigma}\rangle\right),$$

$$|\Pi_{1/2}^{(\varepsilon)}\rangle = 2^{-1/2}\left(|\Pi_{-1}\rangle - i\varepsilon|\bar{\Pi}_{1}\rangle\right)$$

and

$$|\Pi_{3/2}^{(\varepsilon)}\rangle = 2^{-1/2}\left(|\Pi_{1}\rangle - i\varepsilon|\bar{\Pi}_{-1}\rangle\right),$$

where $\varepsilon = \pm 1$. The subscript refers to the z-component of the total angular momentum $m_j = m_l + m_s$. We will denote these eigenfunctions as Kramers states (or Kramers doublets, although the word "doublet" designates the triple two-fold degeneracy, not the multiplicity). The index ε is related to the eigenvalue of $\hat{\boldsymbol{\theta}}$, namely

$$\hat{\boldsymbol{\theta}}|\Lambda^{(\varepsilon)}\rangle = i\varepsilon|\Lambda^{(\varepsilon)}\rangle.$$

Note that the definition of the Kramers states in Ref. [62] is incorrect, specifically Eq. (27). The correct definitions of the Kramers Π states involve linear combinations of $|\Pi_\lambda\rangle$ and $|\bar{\Pi}_{-\lambda}\rangle$. Specifically, the Kramers states $|\Pi_{1/2}^{\pm}\rangle$ are complex linear combinations of the two states with $\omega = \lambda + \sigma = \pm 1/2$ while the $|\Pi_{3/2}^{\pm}\rangle$ states are complex linear combinations of the two states with $\omega = \lambda + \sigma = \pm 3/2$.

In the Kramers basis, the matrices of both the potential and the spin-orbit Hamiltonian separate into 3×3 blocks. We find

$$\mathbf{H}_{el}^{(\varepsilon)}(R,\theta) = \begin{vmatrix} \mathbf{H}_{el}^{(+)} & \mathbf{0} \\ \mathbf{0} & \mathbf{H}_{el}^{(-)}, \end{vmatrix}$$

where

$$\mathbf{H}_{el}^{(+)}(R,\theta) = \left|\begin{array}{c|ccc} & \Sigma^{(+)} & \Pi_{1/2}^{(+)} & \Pi_{3/2}^{(+)} \\ \hline \Sigma^{(+)} & V_\Sigma & V_1 & -V_1 \\ \Pi_{1/2}^{(+)} & V_1 & V_\Pi & V_2 \\ \Pi_{3/2}^{(+)} & -V_1 & V_2 & V_\Pi \end{array}\right|,$$

and $\mathbf{H}_{el}^{(-)} = \mathbf{H}_{el}^{(+)}$. For the spin-orbit Hamiltonian, we find

$$\mathbf{H}_{so}^{(\varepsilon)}(R,\theta) = \begin{vmatrix} \mathbf{H}_{so}^{(+)} & \mathbf{0} \\ \mathbf{0} & \mathbf{H}_{so}^{(-)}, \end{vmatrix}$$

where

$$\mathbf{H}_{so}^{(+)}(R,\theta) = \begin{array}{c|ccc} & \Sigma^{(+)} & \Pi_{1/2}^{(+)} & \Pi_{3/2}^{(+)} \\ \hline \Sigma^{(+)} & 0 & i2^{1/2}B & 0 \\ \Pi_{1/2}^{(+)} & -i2^{1/2}B & A & 0 \\ \Pi_{3/2}^{(+)} & 0 & 0 & -A \end{array}$$

and $\mathbf{H}_{so}^{(-)}(R,\theta) = \mathbf{H}_{so}^{(+)}(R,\theta)^{\dagger}$.

4.2.2 Collinear Geometry

In collinear geometry, $A = B$ and $V_1 = V_2 = 0$. The matrix of the full Hamiltonian (electrostatic plus spin-orbit) is then, in the Kramers basis

$$\mathbf{H}_{\mathrm{K}}^{(\pm)}(R,\theta) = \begin{array}{c|ccc} & \Sigma^{(\pm)} & \Pi_{1/2}^{(\pm)} & \Pi_{3/2}^{(\pm)} \\ \hline \Sigma^{(\pm)} & V_\Sigma & \pm i2^{1/2}A & 0 \\ \Pi_{1/2}^{(\pm)} & \mp i2^{1/2}A & V_\Pi + A & 0 \\ \Pi_{3/2}^{(\pm)} & 0 & 0 & V_\Pi - A \end{array} . \tag{4.1}$$

In the limit where $V_\Sigma = V_\Pi$, the three eigenvalues are $V_\Pi - A$ (doubly degenerate) and $V_\Pi + 2A$, with eigenvectors (column ordered).

$$\begin{array}{c|ccc} E & V_\Pi - A & V_\Pi - A & V_\Pi + 2A \\ \hline C_\Sigma & 0 & \left(\frac{2}{3}\right)^{1/2} i & \left(\frac{1}{3}\right)^{1/2} i \\ C_{\Pi_{1/2}} & 0 & -\left(\frac{1}{3}\right)^{1/2} & \left(\frac{2}{3}\right)^{1/2} \\ C_{\Pi_{3/2}} & 1 & 0 & 0 \end{array} . \tag{4.2}$$

We shall refer to the 3×3 matrix of coefficients in this equation as $\mathbf{C}$.

One of the Π states is not coupled to the other two states. This is equivalent (in the Kramers basis) to the $\Pi_{3/2}$ and $\Pi_{-3/2}$ states in the $\Lambda\Sigma$ basis used in [62]. The only mixing is between the $\Pi_{\pm 1/2}$ and the $\Sigma_{\pm 1/2}$ states (in the $\Lambda\Sigma$ basis or between the $\Sigma^{(\varepsilon)}$ and $\Pi^{(\varepsilon)}_{1/2}$ states (in the Kramers basis).

For a ^2P atom with a p^5 electron occupancy, A is positive, so the state with $E = V_\Pi - A$ will be the lower and that state with $E = V_\Pi + 2A$, the upper. We shall designate these as "j_a" states, and label them as $|j_a \Omega\rangle$. Here Ω is the projection quantum number of the total (electronic orbital plus spin) angular momentum of the atom. We have $|\frac{3}{2}\frac{3}{2}\rangle$, $|\frac{3}{2}\frac{1}{2}\rangle$, and $|\frac{1}{2}\frac{1}{2}\rangle$. Note that the $|\frac{3}{2}\frac{3}{2}\rangle$ state is identical to the $|\Pi_{3/2}\rangle$ state.

4.2.3 Comparison with Previous Work

In the 6-state $\Lambda\Sigma$ basis, in collinear geometry the matrix of the potential is diagonal [see Eq. (20) of [62]]. The matrix of the spin-orbit coupling [Eq. (25) of [62]] consists of two 2×2 blocks and two singleton blocks. The matrix of $\hat{H}_{el} + \hat{H}_{so}$ is then

$$\mathbf{H} = \left[\begin{array}{c|cccccc} & \Sigma & \bar{\Pi}_1 & \bar{\Pi}_{-1} & \bar{\Sigma} & \Pi_{-1} & \Pi_1 \\ \hline \Sigma & V_\Sigma & -2^{1/2}A & 0 & 0 & 0 & 0 \\ \bar{\Pi}_1 & -2^{1/2}A & V_\Pi + A & 0 & 0 & 0 & 0 \\ \bar{\Pi}_{-1} & 0 & 0 & V_\Pi - A & 0 & 0 & 0 \\ \bar{\Sigma} & 0 & 0 & 0 & V_\Sigma & -2^{1/2}A & 0 \\ \Pi_{-1} & 0 & 0 & 0 & -2^{1/2}A & V_\Pi + A & 0 \\ \Pi_1 & 0 & 0 & 0 & 0 & 0 & V_\Pi - A \end{array}\right] .$$

In collinear geometry, the matrix of the Hamiltonian is block-diagonal in both the $\Lambda\Sigma$ and Kramers bases. In bent (non-collinear) geometry, however, only the Kramers states achieve this block diagonalization. The results presented here differ from [62] and are consistent with an alternative derivation of the Kramers basis for the A(^2P)+BC system [181].

4.2.4 Scattering Calculations

4.2.4.1 Two Possible Diabatic Bases

To describe scattering in the presence of multiple electronic states, we use a basis obtained by multiplying a wave function ψ, which is a function of the nuclear coordinates, by an electronic state function. For these we can use either the Kramers or j_a states. Note: the j_a basis is used previously to treat the nonadiabatic scattering of F+HCl in Section 3.4.4. If we neglect the $\Omega = 3/2$ state, which is not coupled to

the other two, then the transformation between the Kramers and j_a states is

$$\begin{bmatrix} j_a = 1/2 \\ \\ j_a = 3/2 \end{bmatrix} = \mathbf{D}^\dagger \begin{bmatrix} \Sigma \\ \\ \Pi_{1/2} \end{bmatrix}. \tag{4.3}$$

More compactly, we can write this equation as

$$|\mathbf{j_a}\rangle = \mathbf{D}^\dagger |\mathbf{\Lambda}\rangle \tag{4.4}$$

or, equivalently

$$|\mathbf{\Lambda}\rangle = \mathbf{D}|\mathbf{j_a}\rangle, \tag{4.5}$$

where $|\mathbf{j_a}\rangle$ and $|\mathbf{\Lambda}\rangle$ are 2×1 column vectors. Here we use $\mathbf{\Lambda}$ to designate the Kramers states with $\Lambda = 1$ and $\Lambda = 2$ corresponding, respectively, to the Σ state and Π_{-1} states.

The matrix $\mathbf{D}$ diagonalizes the upper 2×2 block of Eq. (4.1) in the limit that $V_\Sigma = V_\Pi$, namely

$$\mathbf{D}^\dagger \begin{bmatrix} V & \mp i 2^{1/2} A \\ \\ \pm i 2^{1/2} A & V + A \end{bmatrix} \mathbf{D} = \begin{bmatrix} V - A & 0 \\ \\ 0 & V + 2A \end{bmatrix}$$

from Eq. (4.2). Note that the matrix is column ordered, i.e.

$$\mathbf{D} = 3^{-1/2} \begin{bmatrix} 2^{1/2} i & i \\ \\ -1 & 2^{1/2} \end{bmatrix}. \tag{4.6}$$

Since in the Kramers basis the matrix of the Hamiltonian is block-diagonal in ε, and independent of this index (to within a sign difference), we can neglect ε.

Formally, then, we can write the Hamiltonian as

$$\hat{H}(Q) = \sum_{\Lambda} \sum_{\Lambda'} |\Lambda\rangle H^{(K)}_{\Lambda\Lambda'}(Q) \langle\Lambda'|, \tag{4.7}$$

where $\Lambda = 1, 2, 3$ designates the three Kramers states $|\Sigma\rangle$, $|\Pi_{-1}\rangle$ and $|\Pi_1\rangle$, and $H_{\Lambda\Lambda'}(Q)$ is the 3×3 matrix given in Eq. (4.1). Here we use the single variable Q to represent the nuclear coordinates $\{R, r\}$. Since the Π_1 state is uncoupled from the first two, a scattering calculation on the reaction of a halogen atom can be decoupled into two steps: (a) a single-state calculation based on a potential energy surface $V_\Pi - A$ [the (3,3) element of the H matrix of Eq. (4.1)], and a two-state calculation based on the expansion of Eq. (4.7) in which the summations are restricted to $|\Sigma\rangle$ and $|\Pi_{-1}\rangle$.

Alternatively, we can work in the j_a basis, in which case we write the Hamiltonian as

$$\hat{H}(Q) = \sum_{j_a} \sum_{j_a'} |j_a\rangle H^{(j)}_{j_a j_a'}(Q) \langle j_a'|. \tag{4.8}$$

4.2.4.2 S Matrix

The S matrix we then obtain will be indexed in the labels of whichever of the two diabatic bases we use. In the mixed halogen reactions (X+HY→XH+Y) we should use the j_a basis, since, asymptotically, the Hamiltonian is diagonal in this representation. However, in reactions of a halogen with H_2, the Hamiltonian is diagonal in the j_a basis in the reactant arrangement but diagonal in the Kramers basis in the product arrangement. Since V_Π and V_Σ differ dramatically in this region, it makes more sense to solve the scattering problem in the Kramers basis. However, on the reactant boundary, we then need to transform the S matrix from the Kramers to j_a basis.

If a scattering calculation is done in the Kramers basis, then we can expand the S-matrix formally similarly to Eq. (4.7), namely

$$\hat{S} = \sum_{\Lambda} \sum_{\Lambda'} |\Lambda\rangle S^{(K)}(\Lambda, \Lambda') \langle \Lambda'|. \tag{4.9}$$

Thus the S-matrix element for a transition between a state j_a in the reactant (X+H_2) to a state XH+H in the product arrangement is

$$S(j_a, \Lambda'') = \sum_{\Lambda} \langle j_a|\Lambda\rangle S^{(K)}(\Lambda, \Lambda''). \tag{4.10}$$

Similarly, the S-matrix element for a nonreactive transition between states j_a and j'_a both in the reactant arrangement is

$$S(j_a, j'_a) = \sum_{\Lambda} \sum \Lambda' \langle j_a|\Lambda\rangle S^{(K)}(\Lambda, \Lambda') \langle \Lambda'|j'_a\rangle.$$

Here $\langle j_a|\Lambda\rangle$ is an element of the $\mathbf{D}^\dagger$ matrix and $\langle \Lambda|j_a\rangle$ is an element of the $\mathbf{D}$ matrix. Note that this 2×2 transformation of the S matrix is diagonal in the vibrational index. In the reactant arrangement, the H_2 vibrational wave function is independent of the electronic state of the halogen atom. In the product arrangement, only the Σ state exists at low to moderate energies, so $S^{(K)}(1,2) = S^{(K)}(2,2) = 0$

4.2.4.3 Adiabatic Basis

It is also possible to define the electronically adiabatic states which result from by diagonalizing the (complex, hermitian) $\mathbf{H}$ matrix of Eq. (4.1) at each point on the PES. We shall refer to these states as $|a_1\rangle$ and $|a_2\rangle$, where the indices "1" and "2" designate the lower and upper of the electronically adiabatic states. The scattering on the $j_a = 3/2$ PES is unaffected. n either diabatic basis (Kramers or j_a), the

transformation into the adiabatic basis can be written in terms of a mixing angle which varies over the PES.

4.2.4.4 Kramers Basis

An orthogonal rotation in two dimensions can be described in terms of single angle θ. In the Kramers basis, this mixing angle is chosen to diagonalize the upper-left 2×2 matrix in Eq. (4.1). We can diagonalize Eq. (4.1) using the transformation $\mathbf{R}_K \mathbf{H}_K^+ \mathbf{R}_K^\dagger$, where

$$\mathbf{R}_K = \begin{bmatrix} \cos\theta_K & -\sin\theta_K \\ \sin\theta_K & \cos\theta_K \end{bmatrix} \tag{4.11}$$

and

$$\theta_{\mathrm{K}}(Q) = \frac{1}{2}\tan^{-1}\left[\frac{2^{3/2}A(Q)}{V_\Sigma(Q) - [V_\Pi(Q) - A(Q)]}\right], \tag{4.12}$$

which is a function of the coordinates R and r. The 2×2 unitary transformation (the complex analogue of the 2×2 rotation) is

$$\mathbf{C}_{\mathrm{K}} = \begin{bmatrix} i\cos\theta_{\mathrm{K}} & \sin\theta_{\mathrm{K}} \\ -i\sin\theta_{\mathrm{K}} & \cos\theta_{\mathrm{K}} \end{bmatrix}. \tag{4.13}$$

The mixing angle and, consequently, the orthogonal transformation $\mathbf{C}$ are functions of the nuclear coordinates Q.

In Eq. (4.13) we are ordering the eigenvectors by column, so that, in matrix notation

$$|\mathbf{a}\rangle = \mathbf{C}_{\mathrm{K}}^\dagger |\mathbf{\Lambda}\rangle, \tag{4.14}$$

where $|\mathbf{a}\rangle$ and $|\mathbf{\Lambda}\rangle$ are the 2×1 column vectors

$$|a_1\rangle = C_{11}^*|\Sigma\rangle + C_{21}^*|\Pi_{1/2}\rangle$$

and

$$|a_2\rangle = C_{12}^*|\Sigma\rangle + C_{22}^*|\Pi_{1/2}\rangle.$$

More specifically,

$$\mathbf{C}_\mathrm{K}^\dagger \begin{bmatrix} V_\Sigma & \pm i2^{1/2}A \\ \mp i2^{1/2}A & V_\Pi + A \end{bmatrix} \mathbf{C}_\mathrm{K} = \begin{bmatrix} E_l & 0 \\ 0 & E_u \end{bmatrix}$$

and

$$\begin{bmatrix} |a_1\rangle \\ |a_2\rangle \end{bmatrix} = \mathbf{C}_\mathrm{K}^\dagger \begin{bmatrix} |\Sigma\rangle \\ \left|\Pi_{1/2}\right\rangle \end{bmatrix}$$

The inverse transformation is

$$|\mathbf{\Lambda}\rangle = \mathbf{C}_\mathrm{K}|\mathbf{a}\rangle. \tag{4.15}$$

Asymptotically $V_\Pi = V_\Sigma$, so that the mixing angle becomes

$$\theta_\infty \equiv \lim_{R\to\infty} \theta_\mathrm{K} = \frac{1}{2}\tan^{-1}(2^{3/2}) \approx 0.1959\pi \tag{4.16}$$

This angle is in the first quadrant and we have

$$\cos\theta_\infty = (1/3)^{1/2} \text{ and } \sin\theta_\infty = (2/3)^{1/2} \tag{4.17}$$

Asymptotically the adiabatic states become the j_a states from Eq. (4.13)

$$\lim_{R\to\infty} \mathbf{C}_\mathrm{K} = \mathbf{D}.$$

Because the spin-orbit constant A is a positive number, the numerator in Eq. (4.12)] will be positive. When $V_\Sigma > V_\Pi + A$, the denominator is Eq. (4.12) will

also be positive, so that 2θ will lie in the first quadrant of $0 \leq \theta_{\rm K} \leq \pi/4$. When $V_\Sigma < V_\Pi + A$, the denominator will be negative, so that 2θ will lie in the second quadrant, and $\pi/4 \leq \theta_{\rm K} \leq \pi/2$. These considerations will provide a check on the numerical calculation of $\theta_{\rm K}$.

4.2.4.5 j_a Basis

The Hamiltonian in the j_a basis is obtained by transformation of the Hamiltonian in the Kramers basis $\mathbf{H}_K$[Eq. (4.1)] by the matrix $\mathbf{D}$ defined in Eq. (4.6). We have

$$\mathbf{H}_{j_a} = \mathbf{D}\mathbf{H}_{\rm K}{}^{(\pm)}\mathbf{D}^\dagger = \left[\begin{array}{c|ccc} & \frac{3}{2}\frac{3}{2} & \frac{3}{2}\frac{1}{2} & \frac{1}{2}\frac{1}{2} \\ \hline \frac{3}{2}\frac{3}{2} & V_\Pi - A & 0 & 0 \\ \frac{3}{2}\frac{1}{2} & 0 & \frac{1}{3}(V_\Pi + 2V_\Sigma) - A & \frac{2^{1/2}}{3}(V_\Sigma - V_\Pi) \\ \frac{1}{2}\frac{1}{2} & 0 & \frac{2^{1/2}}{3}(V_\Sigma - V_\Pi) & \frac{1}{3}(2V_\Pi + V_\Sigma) + 2A \end{array}\right]. \tag{4.18}$$

This real matrix can be diagonalized by the transformation using Eq. 4.11. The mixing angle in the j_a basis is thus

$$\theta_{j_a}(Q) = \frac{1}{2}\tan^{-1}\left[\frac{2^{3/2}(V_\Sigma - V_\Pi)}{V_\Sigma - V_\Pi - 9A}\right]. \tag{4.19}$$

The transformation between the j_a and adiabatic states is

$$|\mathbf{a}\rangle = \mathbf{R}^\dagger|\mathbf{j_a}\rangle.$$

For use later, we can invert this transformation, obtaining

$$|\mathbf{j_a}\rangle = \left(\mathbf{R}^\dagger\right)^{-1}|\mathbf{a}\rangle = \mathbf{R}|\mathbf{a}\rangle. \tag{4.20}$$

4.2.5 Mixed Halogen X+HY→XH+Y Reaction

This diagonalizing transformation from Kramers to the j_a bases is independent of the magnitude of the spin-orbit constant. Thus, for mixed halogen reactions, where both the reactant and product arrangements correspond to a ^2P atom plus a closed-shell diatomic molecule, the same Kramers $\rightarrow j_a$ transformation will be valid at both the reactant and product asymptotes. The appropriate diabatic basis is the j_a states, in which the Hamiltonian is diagonal in both the asymptotic reactant and product arrangements.

Note that this result is independent of the $\pm$ index (the time reversal symmetry) of the Kramers states. The matrix of $\hat{H}$ is purely real. Consequently, as we mentioned in the preceding subsection, it can be diagonalized by a (real) orthogonal transformation.

4.2.6 Reaction of Halogen Atom with H_2

In X+H_2 →XH+H reactions, in the product channel V_Π is very high and not equal to V_Σ. Thus, the Hamiltonian in the j_a basis [Eq. (4.18)] is not diagonal in the asymptotic product channel. However, since the spin-orbit coupling A goes to zero in the product channel (if one neglects the coupling between the two Π states, at very high energy), the Hamiltonian is diagonal in the Kramers basis. Thus, for X+H_2 →XH+H reactions, it is most appropriate to expand the wave function in terms of the Kramers states. Then, we use Eq. (4.10) to transform the S matrix into a mixed representation (j_a states for the X+H_2 asymptote and Kramers states

for the XH+H asymptote).

4.3 A(^{3}P)+B_2

We now consider the collision of an atom in a ^3P electronic state with a closed-shell diatomic, and example being O(^3P)+H_2 →OH+H. In the reactant asymptote are nine degenerate electronic states. To determine the form of the potential in the ΛΣ or Kramers basis we will first need to determine the transformation from a Cartesian basis (which is the usual basis for *ab initio* calculations) to the ΛΣ basis.

We assume that the molecule lies in the xz plane, so that p_x and p_z belong to the A' irreducible representation in C_s symmetry and the p_y orbital is out of plane and belongs to the A'' representation. For p^4 electron occupancy we identify a determinant by its two *half-filled* orbitals. Any p^4 determinants with a single p_y electron will therefore have A'' symmetry. These nine states are given below, with their respective symmetry, spin projection and Slater determinant.

$q(p^4)$	symmetry	M_S	Slater determinant
$\bar{x}\bar{z}$	A'	1	$\lvert p_x p_y \bar{p}_y p_z \rvert$
$\bar{y}\bar{z}$	A''	1	$\lvert p_x \bar{p}_x p_y p_z \rvert$
$\bar{x}\bar{y}$	A''	1	$\lvert p_x p_y p_z \bar{p}_z \rvert$
$x\bar{z}$	A'	0	$2^{-1/2}(\lvert \bar{p}_x p_y \bar{p}_y p_z \rvert + \lvert p_x p_y \bar{p}_y \bar{p}_z \rvert)$
$y\bar{z}$	A''	0	$2^{-1/2}(\lvert p_x \bar{p}_x \bar{p}_y p_z \rvert + \lvert p_x \bar{p}_x p_y \bar{p}_z \rvert)$
$x\bar{y}$	A''	0	$2^{-1/2}(\lvert \bar{p}_x p_y p_z \bar{p}_z \rvert + \lvert p_x \bar{p}_y p_z \bar{p}_z \rvert)$
xz	A'	-1	$\lvert \bar{p}_x p_y \bar{p}_y \bar{p}_z \rvert$
yz	A''	-1	$\lvert p_x \bar{p}_x \bar{p}_y \bar{p}_z \rvert$
xy	A''	-1	$\lvert \bar{p}_x \bar{p}_y p_z \bar{p}_z \rvert$

We can write down the Cartesian equivalents of the $\Lambda\Sigma$ states using the relationship between the definite-M and Cartesian orbitals, namely

$$p_{\pm 1} = \mp 2^{-1/2}[p_x \pm i p_y],$$

and

$$p_0 = p_z.$$

The transformation matrix between the $\Lambda\Sigma$ and Cartesian bases is block diagonal with respect to M_S, i.e.

$$\mathbf{T} = \begin{bmatrix} \tilde{\mathbf{T}} & 0 & 0 \\ 0 & \tilde{\mathbf{T}} & 0 \\ 0 & 0 & \tilde{\mathbf{T}} \end{bmatrix},$$

where

$$\tilde{\mathbf{T}} = \frac{1}{\sqrt{2}} \left(\begin{array}{c|ccc} M_L & \Pi_x & \Pi_y & \Sigma \\ \hline 1 & -1 & -i & 0 \\ 0 & 0 & 0 & 1 \\ -1 & 1 & -i & 0 \end{array} \right).$$

In the Cartesian basis, the matrix of the Hamiltonian is (a) diagonal in M_S, (since the choice of the z axis is arbitrary) and (b) with no coupling between the two states of A'' reflection symmetry and the single state of A' reflection symmetry. Thus the Hamiltonian matrix will be, for a p^4 electron occupancy,

$$\mathbf{H}_{el}^{(xyz)} = \left(\begin{array}{c|ccc} q & \Pi_x & \Pi_y & \Sigma \\ \hline xz & V_{\Pi_x} & 0 & 0 \\ yz & 0 & V_{\Pi_y} & V_1 \\ xy & 0 & V_1 & V_\Sigma \end{array} \right).$$

The electronic Hamiltonian is also block diagonal in the $\Lambda\Sigma$ basis. Using the $\tilde{\mathbf{T}}$ matrix, the electronic Hamiltonian in the $\Lambda\Sigma$ basis can be written as

$$\mathbf{H}_{el}^{(\Lambda\Sigma)} = \tilde{\mathbf{T}}\mathbf{H}_{el}^{(xyz)}\tilde{\mathbf{T}}^\dagger = \left(\begin{array}{c|ccc} M_L & 1 & 0 & -1 \\ \hline 1 & V_\Pi & -iV_1/\sqrt{2} & V_2 \\ 0 & iV_1/\sqrt{2} & V_\Sigma & iV_1/\sqrt{2} \\ -1 & V_2 & -iV_1/\sqrt{2} & V_\Pi \end{array} \right),$$

where $V_\Pi = (V_{\Pi_x} + V_{\Pi_y})/2$ and $V_2 = (V_{\Pi_x} - V_{\Pi_y})/2$.

We designate V_1 the coupling between the two states of A'' symmetry. Note that V_1 vanishes in linear geometry.

$$\lim_{\theta=0,\pi} V_1 = 0.$$

Thus in collinear geometry we have

$$\mathbf{H}_{el}^{(xyz)} = \left(\begin{array}{c|ccc} q & \Pi_x & \Pi_y & \Sigma \\ \hline xz & V_{\Pi_x} & 0 & 0 \\ yz & 0 & V_{\Pi_y} & 0 \\ xy & 0 & 0 & V_{\Sigma} \end{array}\right)$$

and

$$\mathbf{H}_{el}^{(\Lambda\Sigma)} = \left(\begin{array}{c|ccc} M_L & 1 & 0 & -1 \\ \hline 1 & V_{\Pi} & 0 & 0 \\ 0 & 0 & V_{\Sigma} & 0 \\ -1 & 0 & 0 & V_{\Pi} \end{array}\right).$$

4.3.1 Spin-Orbit Hamiltonian

The $|\Lambda\Sigma\rangle$ states are labelled by M_L and M_S. We'll call the total projection quantum number $\Omega = M_L + M_S$. The spin-orbit Hamiltonian is diagonal in Ω. The matrix of $\hat{H}_{SO}$ depends on two, coordinate-dependent terms A and B (as in the ^2P case

$$\mathbf{H}_{SO}^{(\Omega=0)} = \left(\begin{array}{cc|ccc} & M_L & 1 & 0 & -1 \\ M_L & M_S & -1 & 0 & 1 \\ \hline 1 & -1 & A & -2^{1/2}B & 0 \\ 0 & 0 & -2^{1/2}B & 0 & -2^{1/2}B \\ -1 & 1 & 0 & -2^{1/2}B & A \end{array}\right),$$

$$\mathbf{H}_{SO}^{(\Omega=\pm1)} = \left(\begin{array}{cc|cc} & M_L & \pm1 & 0 \\ M_L & M_S & 0 & \pm1 \\ \hline \pm1 & 0 & 0 & -2^{1/2}B \\ 0 & \pm1 & -2^{1/2}B & 0 \end{array}\right),$$

and

$$\mathbf{H}_{SO}^{(\Omega=\pm2)} = \left(\begin{array}{cc|c} & M_L & \pm1 \\ M_L & M_S & \pm1 \\ \hline \pm1 & \pm1 & -A \end{array}\right),$$

where

$$A \equiv \langle {}^3\Pi_x | L_z S_z | {}^3\Pi_y \rangle,$$

and

$$B \equiv \langle {}^3\Pi_y | L_y S_y | {}^3\Sigma \rangle.$$

The full 9×9 matrix of $\hat{H}_{SO}$ in the $\Lambda\Sigma$ basis can be written as follows (we suppress the lower triangle for simplicity)

$$\mathbf{H}_{SO}^{(\Lambda\Sigma)} = \left(\begin{array}{cc|ccc|ccc|ccc}
 & M_L & 1 & 0 & -1 & 1 & 0 & -1 & 1 & 0 & -1 \\
M_L & M_S & -1 & -1 & -1 & 0 & 0 & 0 & 1 & 1 & 1 \\
\hline
1 & -1 & A & 0 & 0 & 0 & -2^{1/2}B & 0 & 0 & 0 & 0 \\
0 & -1 & & 0 & 0 & 0 & 0 & -2^{1/2}B & 0 & 0 & 0 \\
-1 & -1 & & & -A & 0 & 0 & 0 & 0 & 0 & 0 \\
\hline
1 & 0 & & & & 0 & 0 & 0 & 0 & -2^{1/2}B & 0 \\
0 & 0 & & & & & 0 & 0 & 0 & 0 & -2^{1/2}B \\
-1 & 0 & & & & & & 0 & 0 & 0 & 0 \\
\hline
1 & 1 & & & & & & & -A & 0 & 0 \\
0 & 1 & & & & & & & & 0 & 0 \\
-1 & 1 & & & & & & & & & A
\end{array}\right).$$

4.3.2 Cartesian Coordinates

Transforming the spin-orbit matrix to the Cartesian basis we have

$$\mathbf{H}_{SO}^{(xzy)} = \mathbf{Z}\mathbf{T}\mathbf{H}_{SO}^{(\Lambda\Sigma)}\mathbf{T}^{\dagger}\mathbf{Z}^{T},$$

where $\mathbf{Z}$ takes into account the mixing between the two states with A'' symmetry. The $\mathbf{Z}$ matrix is block diagonal with respect to M_S, with each 3×3 block defined

as

$$\mathbf{Z}^{(M_S)} = \left(\begin{array}{c|ccc} & \Pi_x & \Pi_y & \Sigma \\ \hline 1A' & 1 & 0 & 0 \\ 1A'' & 0 & \cos\theta & \sin\theta \\ 2A'' & 0 & -\sin\theta & \cos\theta \end{array}\right),$$

here θ is the mixing angle between the two states of A'' symmetry. We can write the spin-orbit matrix in the Cartesian basis in terms of two 3×3 matrices

$$\mathbf{H}_{SO}^{(xzy)} = \left(\begin{array}{c|ccc} M_S & -1 & 0 & 1 \\ \hline -1 & \mathbf{A} & \mathbf{B} & 0 \\ 0 & \mathbf{B}^\dagger & 0 & \mathbf{B} \\ 1 & 0 & \mathbf{B}^\dagger & \mathbf{A}^\dagger \end{array}\right), \tag{4.21}$$

where

$$\mathbf{A} = \left(\begin{array}{c|ccc} & 1A' & 1A'' & 2A'' \\ \hline 1A' & 0 & Ai\cos\theta & -Ai\sin\theta \\ 1A'' & -Ai\cos\theta & 0 & 0 \\ 2A'' & Ai\sin\theta & 0 & 0 \end{array}\right)$$

and

$$\mathbf{B} = \left(\begin{array}{c|ccc} & 1A' & 1A'' & 2A'' \\ \hline 1A' & 0 & B\sin\theta & B\cos\theta \\ 1A'' & -B\sin\theta & 0 & -Bi \\ 2A'' & -B\cos\theta & Bi & 0 \end{array}\right).$$

This gives us an alternative method to determine the mixing angle from the *ab initio* calculations. Note that the mixing angle, θ, also vanishes in linear geometry, i.e.

$$\lim_{\theta=0,\pi} \theta = 0.$$

The elements of the spin-orbit operator are quite easily determined in the $\Lambda\Sigma$ basis. Transformation to the Cartesian basis provides checks for accuracy and consistency for the many non-zero *ab initio* $\mathbf{H}_{SO}$ elements.

4.3.3 Kramers Basis

Using the results from the preceding sections one can now write down the total Hamiltonian for the ^3P system. This total electronic Hamiltonian couples all 9 $\Lambda\Sigma$ states. In this section we introduce a Kramers basis, to simplify substantially the representation of the ^3P Hamiltonian.

As defined above, the matrix elements of the time reversal operator, θ_Λ, depends on the values of Λ and Σ and not on the actual occupation. In the $\Lambda\Sigma$ basis the time-reversal operator for a ^3P system is

$$\boldsymbol{\theta}_{\Lambda}^{(\Lambda\Sigma)} = \left(\begin{array}{cc|ccc|ccc|ccc} & M_L & 1 & 0 & -1 & 1 & 0 & -1 & 1 & 0 & -1 \\ M_L & M_S & -1 & -1 & -1 & 0 & 0 & 0 & 1 & 1 & 1 \\ \hline 1 & -1 & 0 & 0 & 0 & 0 & 0 & 0 & 0 & 0 & 1 \\ 0 & -1 & 0 & 0 & 0 & 0 & 0 & 0 & 0 & -1 & 0 \\ -1 & -1 & 0 & 0 & 0 & 0 & 0 & 0 & 1 & 0 & 0 \\ \hline 1 & 0 & 0 & 0 & 0 & 0 & 0 & -1 & 0 & 0 & 0 \\ 0 & 0 & 0 & 0 & 0 & 0 & 1 & 0 & 0 & 0 & 0 \\ -1 & 0 & 0 & 0 & 0 & -1 & 0 & 0 & 0 & 0 & 0 \\ \hline 1 & 1 & 0 & 0 & 1 & 0 & 0 & 0 & 0 & 0 & 0 \\ 0 & 1 & 0 & -1 & 0 & 0 & 0 & 0 & 0 & 0 & 0 \\ -1 & 1 & 1 & 0 & 0 & 0 & 0 & 0 & 0 & 0 & 0 \end{array}\right).$$

Diagonalizing this matrix gives 4 "doublets" and a "singlet", the so-called Kramers states, namely

Kramers state	$\Lambda\Sigma$ state	eigenvalue
$\|1,1^{\pm}\rangle$	$2^{-1/2}(\|-1,-1\rangle \mp \|1,1\rangle)$	± 1
$\|1,-1^{\pm}\rangle$	$2^{-1/2}(\|1,-1\rangle \mp \|-1,1\rangle)$	± 1
$\|1,0^{\pm}\rangle$	$2^{-1/2}(\|1,0\rangle \pm \|-1,0\rangle)$	± 1
$\|0,1^{\pm}\rangle$	$2^{-1/2}(\|0,-1\rangle \pm \|0,1\rangle)$	± 1
$\|0,0^{+}\rangle$	$\|0,0\rangle$	1

.

These doublets are the pairs $|m_l, m_s\rangle \pm |-m_l, -m_s\rangle$. After transformation to this Kramers basis, the total Hamiltonian separates into two blocks: a 5×5, $\mathbf{H}^{(+)}$, and a 4×4, $\mathbf{H}^{(-)}$,

$$\mathbf{H}_K(R,\theta) = \left| \begin{array}{cc} \mathbf{H}^{(+)} & \mathbf{0} \\ \mathbf{0} & \mathbf{H}^{(-)} \end{array} \right|$$

$$\mathbf{H}^{(+)} = \left(\begin{array}{c|ccccc} & |1,0^-\rangle & |0,1^-\rangle & |1,1^+\rangle & |1,-1^+\rangle & |0,0^+\rangle \\ \hline \langle 1,0^-| & V_{\Pi_y} & -B\sqrt{2} & -iB\sin\theta & iB\sin\theta & -iV_1 \\ \langle 0,1^-| & -B\sqrt{2} & V_\Sigma & V_d & V_d & 0 \\ \langle 1,1^+| & iB\sin\theta & -V_d & V_\Pi - A\cos\theta & V_2 & B(\cos\theta - 1) \\ \langle 1,-1^+| & -iB\sin\theta & -V_d & V_2 & V_\Pi + A & -B(\cos\theta + 1) \\ \langle 0,0^+| & iV_1 & 0 & B(\cos\theta - 1) & -B(\cos\theta + 1) & V_\Sigma \end{array} \right)$$

and

$$\mathbf{H}^{(-)} = \left(\begin{array}{c|cccc} & |1,0^+\rangle & |0,1^+\rangle & |1,1^-\rangle & |1,-1^-\rangle \\ \hline \langle 1,0^+| & V_{\Pi_x} & \sqrt{2}B\cos\theta & iB\sin\theta & iB\sin\theta \\ \langle 0,1^+| & \sqrt{2}B\cos\theta & V_\Sigma & V_d & V_d \\ \langle 1,1^-| & -iB\sin\theta & -V_d & V_\Pi - A\cos\theta & V_2 \\ \langle 1,-1^-| & iB\sin\theta & -V_d & V_2 & V_\Pi + A\cos\theta \end{array} \right)$$

where $V_d = i(V_1 + A\sin\theta)/\sqrt{2}$.

The sub-matrices of the Hamiltonian in the Kramers basis further reduce in

collinear geometry to

$$\mathbf{H}_{col}^{(+)} = \left(\begin{array}{c|ccccc} & |0,1^+\rangle & |1,0^+\rangle & |1,1^+\rangle & |1,-1^+\rangle & |0,0^+\rangle \\ \hline \langle 0,1^+| & V_\Sigma & -2^{1/2}B & 0 & 0 & 0 \\ \langle 1,0^+| & -2^{1/2}B & V_\Pi & 0 & 0 & 0 \\ \langle 1,1^+| & 0 & 0 & V_\Pi - A & 0 & 0 \\ \langle 1,-1^+| & 0 & 0 & 0 & V_\Pi + A & -2B \\ \langle 0,0^+| & 0 & 0 & 0 & -2B & V_\Sigma \end{array}\right),$$

and

$$\mathbf{H}_{col}^{(-)} = \left(\begin{array}{c|cccc} & |0,1^-\rangle & |1,0^-\rangle & |1,1^-\rangle & |1,-1^-\rangle \\ \hline \langle 0,1^-| & V_\Pi & 2^{1/2}B & 0 & 0 \\ \langle 1,0^-| & 2^{1/2}B & V_\Sigma & 0 & 0 \\ \langle 1,1^-| & 0 & 0 & V_\Pi - A & 0 \\ \langle 1,-1^-| & 0 & 0 & 0 & V_\Pi + A \end{array}\right).$$

In the following section we use the Kramers basis to study the potential surfaces of the O(^3P)+H$_2$($^1\Sigma_g^+$). Specifically, we analyze the magnitude of the nonadiabatic contributions.

4.4 O(^3P)+H$_2$($^1\Sigma_g^+$)

Much work has been done to study the many potential energy surfaces involved with the O(^3P,^1D,^1S)+H$_2$($^1\Sigma_g^+$) system [182, 183] and the adiabatic [184] and nonadiabatic dynamics of this reaction. This reaction has long been of interest in the field of chemical dynamics [182–188]. In this section we present new, chemically accurate, potential surfaces for the O(^3P)+H$_2$($^1\Sigma_g^+$) reaction and calculations

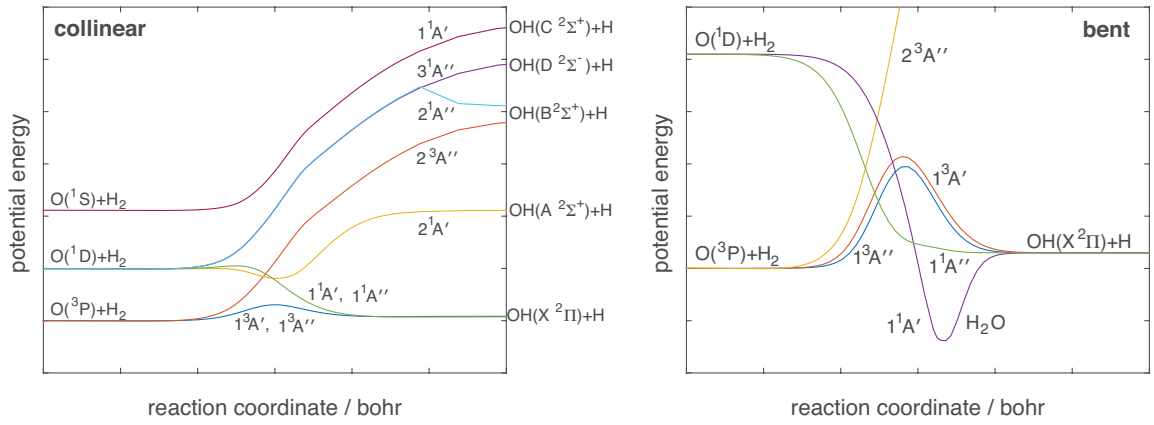

Figure 4.1: Schematic of the nine potential surfaces of the $O(^3P,^1D,^1S)+H_2$ reaction along the minimum energy path in (left) collinear and (right) slightly bent geometries. These potential curves are generated from MRCI calculations at the *avtz* level, with the exception of the attractive ^1D curves in the right panel, which are modeled by a simple sum of two Gaussian terms.

of the spin-orbit constants to aid in the future study of nonadiabatic effects in this reaction.

Figure 4.1 provides a semi-quantitative picture of the electronic states of the $O(^3P,^1D,^1S)+H_2$ reaction along the minimum energy reaction path and in collinear and slightly bent geometries.

Nonadiabatic transitions will be important only when two coupled potential surfaces lie close in energy. We see from Fig. 4.1 that this coupling will be significant over a sizable portion of the coordinate space accessed during the reaction. The couplings considered here are the mixing between two states of the same total symmetry (diabatic coupling, which we have designated V_1) or the spin-orbit interactions. Regardless of the basis used to describe the electronic structure, transitions

between electronic states are most probable when the coupling between the two states is comparable in magnitude to of the separation of the states.

In the reactant channel, diabatic coupling exists between the two ^3P states with A'' symmetry and between both sets of ^1D states, i.e. the pair of singlet states with A' symmetry and the set of three singlet states with A'' symmetry. In the collinear interaction region diabatic coupling exists at relatively high energies between the $2^3A''$ and $1^1A''$ states as well as between the $1^3A'$ and $1^1A'$ states. In bent geometries, the $^1A'$ and $^1A''$ states become very attractive (forming the deep H_2O well). Hoffmann and Schatz have shown the singlet states cross the triplet states just before barrier to reaction [189]. The dynamic implications of the diabatic coupling between the singlet and triplet states with A' and A'' symmetry just before barrier and into the product regions have been well studied [182, 189–191].

We also consider transitions between the potential surfaces induced by the spin-orbit coupling in this system. The spin-orbit matrix elements are non-zero between any pair of potential surfaces for which $\Delta\Omega = 0$ ($\Delta m_s + \Delta m_l = 0$). Furthermore, because all the states with the same symmetry are coupled by diabatic coupling the exact form of the spin-orbit matrix element is dense. If we consider reactions starting on the lowest ^3P potential surfaces, we can see in Fig. 4.1 that the spin-orbit coupling will be relevant throughout the reaction.

Specifically, the spin-orbit operator couples the ^3P states in all geometries as shown by Eq. 4.21. All ^1D states have $M_S = 0$. As such, these singlet states are not coupled to one another. However, spin-orbit coupling does mix these with both the ^3P and ^1S states. The magnitude of the spin-orbit matrix elements varies

throughout the space accessed by the reaction. Also, the size of the spin-orbit coupling is affected by the degree of adiabatic→diabatic mixing (θ) between states of the same symmetry, which also varies across the reaction geometry. More attentions should be devoted to the importance of spin-orbit coupling in reactions of ^3P atoms.

Full quantum scattering including spin-orbit and diabatic coupling in reactions between O(^3P,^1D,^1S)+H_2 will be a difficult computation challenge. There are a total of 15 possible projections (9 for ^3P, 5 for ^1D and 1 for ^1S), 6 states with A' symmetry and 9 with A'' symmetry. The complete description of this system will involve 15×15 Hamiltonian, in just the electronic space. Some states will be at energies high enough that they will not be relevant at thermal or hyper thermal energies. These states can then be eliminated, leading to some reduction in complexity.

In the next subsection, to study the significance of nonadiabaticity on the O+H_2 reaction we report on the lowest potential energy surfaces in the reactant channel up to and just over the barrier. In addition, over the same region, we have determined the spin-orbit coupling terms and the adiabatic→diabatic mixing angle.

This work is organized as follows: in the first of the following subsections we describe new *ab initio* calculations, with plots and comparisons with previous work on these potential energy surfaces. Finally, we discuss, in light of these calculations, the importance of the spin-orbit and diabatic coupling terms, and offer, in conclusion, some insight into the nonadiabatic dynamics of the family of O(^3P,^1D,^1S)+H_2 reactions.

4.4.1 *Ab initio* Calculations

In this section we present electronic structure calculations of a new set of the lowest $^3A'$ and two lowest $^3A''$ potential energy surfaces using the explicitly correlated variant [192–194] of the internally contracted multi-reference configuration-interaction method [195–197] with single and double excitations with the addition of the Davidson correction [198] (MRCISD-F12+Q) for the $O(^3P)+H_2(^1\Sigma_g^+)$ reaction. We use Dunning's triple-zeta, augmented correlation-consistent triple-zeta basis set, (aug-cc-pvtz) [199] coupled with generated JKFIT/MP2FIT density fitting basis which in conjunction with the F12 method given above, is close in accuracy to the complete basis set limit. The interaction energies are calculated by subtracting from the total energy at given geometry the asymptotic total energy of the oxygen and hydrogen molecule separated in collinear geometry by 40 a_0. The optimized interatomic H_2 distance for the asymptotic limit was 1.4017 a_0.

The calculations are done in C_s symmetry. The energies of the triply degenerate $O(^3P)$ atom will split upon the interaction with the hydrogen molecule to one energy corresponding to the wavefunction of the A' symmetry and two energies corresponding to wavefunctions of the A'' symmetry. The reference wavefunction for the subsequent MRCISD-F12+Q calculations is obtained from the complete active space self-consistent field (CASSCF) calculations used with state-averaging of two $^3A''$ and one $^3A'$ with equal weights. The eight correlated electrons were distributed in full valence active space composed of six orbitals, in which 5 were of A' and one of A'' symmetry. One additional orbital of the A' symmetry, the 1s(O) orbital, has

been kept as a frozen core orbital in the subsequent MRCISD-F12+Q calculations. The energies from the two-state MRCISD-F12+Q calculations performed for the A'' symmetry where chosen with a rotated reference (`energd4` variable in MOLPRO program). For calculations on the F+H_2 reaction this gave somewhat larger cluster corrections and gave better results by Werner *et al.* [200]

We used the quasi-diabatization DDR procedure of Werner and coworkers [144, 201] implemented in the MOLPRO code to obtain the diabatic PESs and diabatic coupling V_1 along with the mixing angle θ for the two states of the A'' symmetry which couple as the molecule bends out of collinear geometry. As described above, there is a seam of diabatic surface crossings (CI) between $^3\Sigma$ and $^3\Pi$ states at collinear geometries ($\theta = 0^\circ$ and $\theta = 180^\circ$, in which case, the adiabatic and diabatic orbitals coincide). The two-state quasi-diabatization procedure requires a set of reference orbitals for a geometry where the diabatic and adiabatic orbitals are identical. Here, we choose our reference orbitals to be these collinear orbitals $\theta = 180^\circ$.

During the calculations we save the CASSCF and MRCISD-F12 density matrices and orbitals for the determination of the geometry dependence of the full matrix in the triplet state of the spin-orbit (SO) coupling [202]. The transformed SO matrix elements can be used in the scattering calculations in the Kramers basis.

All calculations were performed on the angular grid, in reactant Jacobi coordinates, delimited by $\theta = 180^\circ$ and $\theta = 90^\circ$ with a step of 5° and on a radial grid of about 8K points in the range $R = [2 - 12] \times r = [0.9 - 4.5]$.

4.4.2 ^3P Potential Surfaces

We label the three lowest $O(^3P)H_2(^1\Sigma_g^+)$ diabatic states of triplet multiplicity Σ, Π_x, Π_y, which refer to the following p^4 occupancies, $|p_x p_y p_z \bar{p}_z|$, $|p_x p_y \bar{p}_y p_z|$ and $|p_x \bar{p}_x p_y p_z|$, respectively. The transformation between these diabatic states and the adiabatic states ($1A''$, $1A'$ and $2A''$) is described in the previous section. Figure 4.2 shows one-dimensional cuts of the potential energy surfaces corresponding to these diabatic states at a variety of angles in the reactant region for fixed $r_{HH} = 1.40$ bohr.

In collinear geometries, O+H_2 exhibits $C_{\infty v}$ symmetry, which has two irreducible representations Σ and Π. The diabatic states Π_x and Π_y map to the irreducible group Π and the diabatic Σ maps to the Σ irreducible group in collinear geometries. At long range the interaction between the quadrupole moment of the oxygen atom and the quadrupole moment of the hydrogen molecule significantly lowers the Σ state relative to the two Π states. Figure 4.3 shows the two adiabatic potentials ($1A'$ and $2A''$) and the spin-orbit constants in collinear geometry.

At short range, however, and into the product channel the Σ surface is purely repulsive, while the two Π states are reactive. This gives rise to a seam of crossings between the two diabatic surfaces in the reactant region of the potential. For the geometries shown in Fig. 4.2 this seam is depicted by a dashed line.

Figure 4.4 shows the mixing angle between the two states with A'' symmetry as well as the nonadiabatic coupling terms for a variety of angles with fixed $r_{HH} = 1.40$ bohr. This figure also indicates the geometries where complete (50:50) mixing

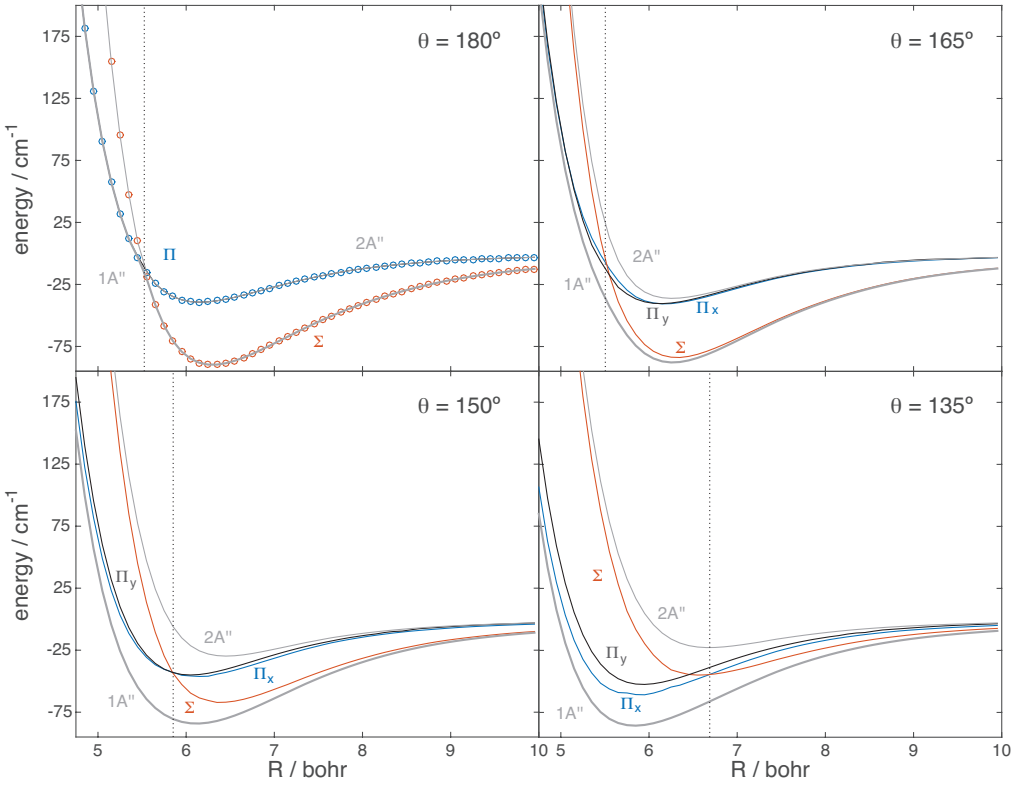

Figure 4.2: Potential curves of O(^3P)+H_2 in the reactant region for fixed r_{HH} = 1.40 bohr. The vertical dashed line indicates the location of the diabatic surface crossing. We suppress the label for the uncoupled adiabatic, $1A'$. In collinear geometry this uncoupled adiabatic potential is equivalent to the Π potential surface. In all other geometries, the uncoupled adiabatic potential is equivalent to the Π_y surface.

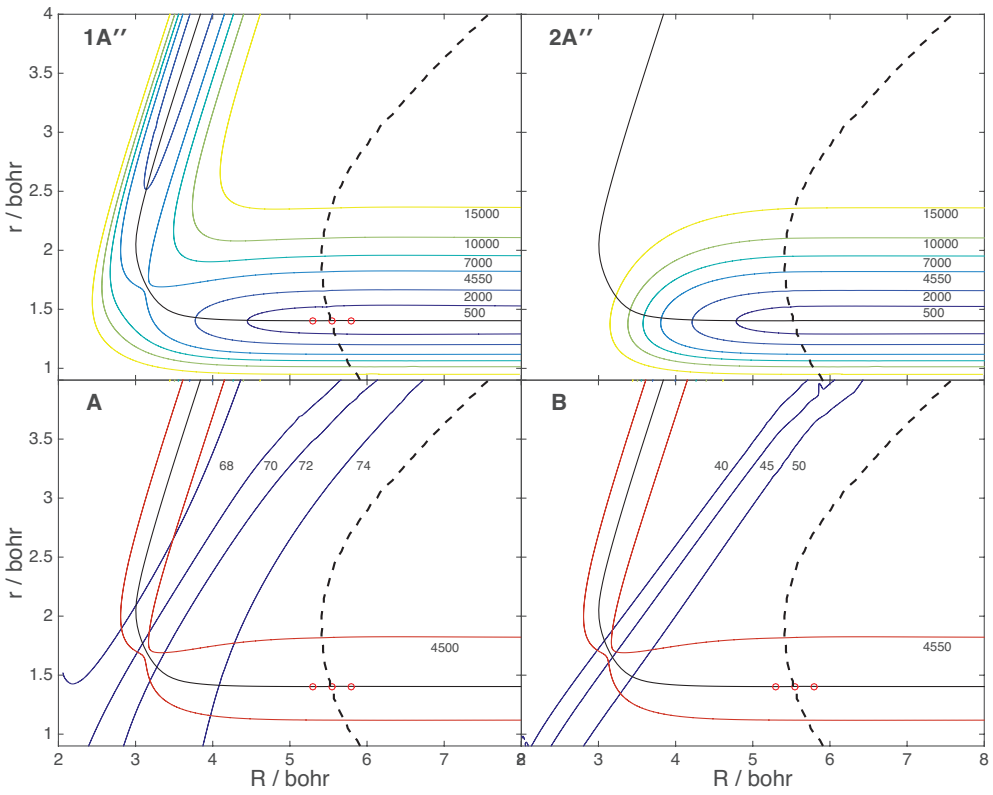

Figure 4.3: The lowest adiabatic potential curves and spin orbit constant in collinear geometries in terms of the Jacobi coordinates (R, r). Energies given in cm^{-1}. The solid black line denotes the minimum energy path along the $1A'$ surface. The dashed black line is an approximation to the seam of diabatic surface crossing. The red contour line in is generated from the lower adiabatic surface to give a sense of the reaction channel. The red circle correspond to the geometries sampled in Fig. 4.6.

between the two states occurs, which is the case at the crossing seam shown in Fig. 4.2. At these geometries the value of the nonadiabatic coupling terms, both diabatic coupling and spin-orbit coupling, is indicated with a vertical dashed line in Fig. 4.4.

Figure 4.5 shows the magnitude of the lowest adiabatic potential surfaces ($1A'$ and $1A''$) as a function of the Jacobi angle, θ, with the other Jacobi coordinates fixed to the global barrier geometry, namely (R, r) = [3.15 bohr, 1.68 bohr]. Figure 4.5 also shows the values of the two spin-orbit constants for these same geometries. The states are split by about 13000 cm^{-1} at the global barrier (collinear geometry), while the spin-orbit constants are A =75 cm^{-1} and B =53 cm^{-1} at this geometry, which is very small by comparison.

Nonadiabatic transitions are most probable when the coupling between the potential surfaces is on the order of the energetic difference between the potential surfaces of interest, which occurs, in the case of the $O(^3P)$+H_2 reaction, along the seam of diabatic surface crossing. To illustrate this Fig. 4.6 shows the value of the adiabatic and diabatic potential surfaces as well as the value of the coupling terms at points along the minimum energy path just before, near and just after the seam of diabatic surface crossing.

4.4.3 Discussion

The experimental study of the $O(^3P)$+H_2 reaction is a nontrivial endeavor as it requires nearly exact state specificity of the reactant oxygen atom. This is because the $O(^1D)$+H_2 reaction proceeds along a barrierless trajectory through the

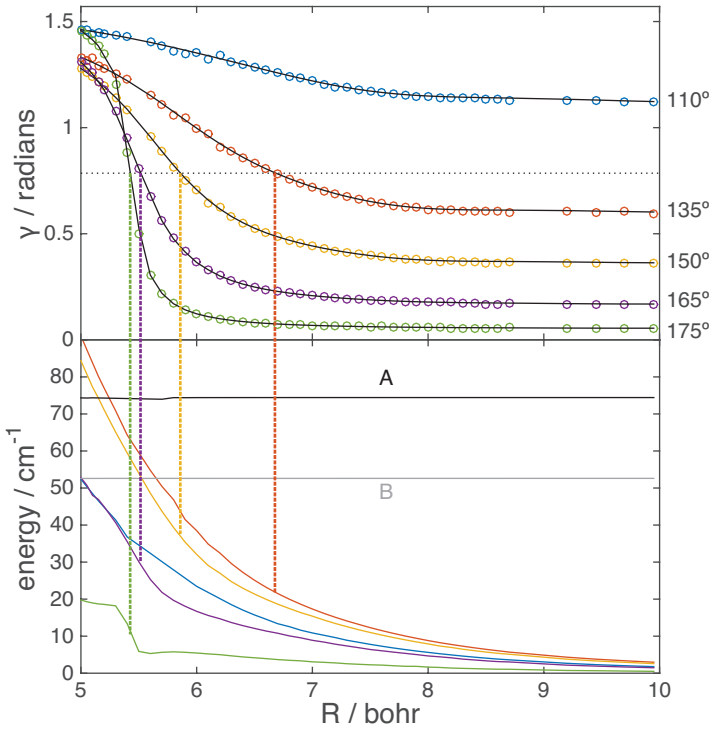

Figure 4.4: (top) Mixing angle, θ, between the two states with A'' symmetry for O(^3P)+H_2 in reactant region for fixed $r_{HH} = 1.40$ bohr. The horizontal dashed line is set at $\theta = \pi/4$, which indicates the geometers of even mixing between the states, i.e. the geometries of the diabatic potential surface crossings in Fig. 4.2. The circles are the outputs of the *ab initio* calculations and the black lines are the values extracted from the spin-orbit constants. (bottom) Diabatic coupling terms shown in color at various angles and spin-orbit terms for the O(^3P)+H_2 reaction with fixed $r_{HH} = 1.40$ bohr. The colors used in the bottom panel are consistent with the coloring scheme for various angles in the top panel. The vertical dashed lines between the panels are used to indicate the value of the nonadiabatic coupling terms at the geometries of diabatic potential surface crossing for each angle.

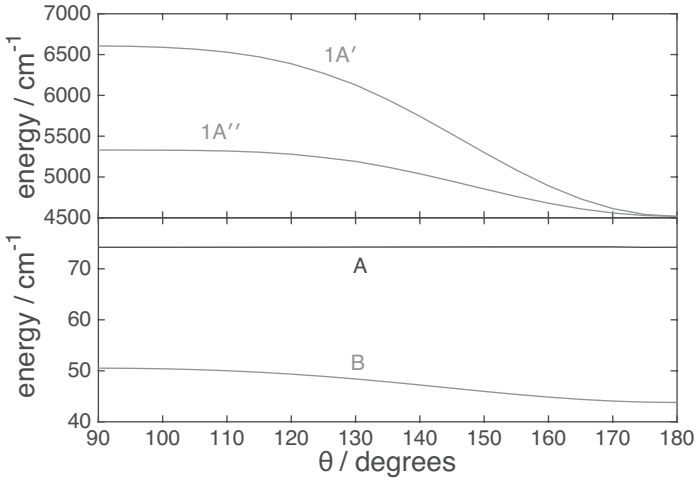

Figure 4.5: The lowest adiabatic potential curves and spin orbit constant as a function of the Jacobi angle, θ, with the other two coordinates fixed at the geometry of the global barrier, i.e. ($R = 3.15$ bohr, $r = 1.68$ bohr).

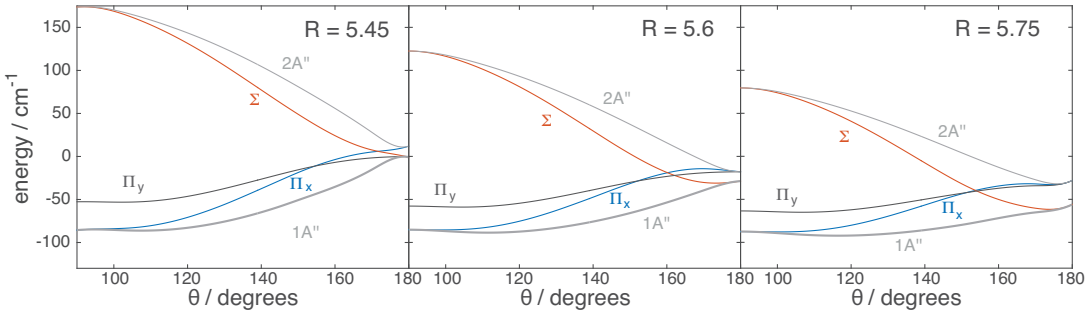

Figure 4.6: (top) The adiabatic and diabatic potential curves and (bottom) spin orbit constants, A and B, diabatic coupling potential V_1, and difference potentials as a function of the Jacobi angle, θ, with the other two coordinates fixed at the geometry (R , $r = 1.4$ bohr), where R is given in each panel. The difference potentials are defined as $V_{11} = |V_{1A'} - V_{1A''}|$, $V_{12} = |V_{1A'} - V_{2A''}|$, and $V_{A''} = |V_{1A''} - V_{2A''}|$. These geometries are shown in Fig. 4.3.

very deep water well (see Fig. 4.1). Accordingly, at an equal collision energy the ^1D reaction will be 6 orders of magnitude more likely than the triplet reactions [203,204]. Even singlet contaminations of 1 ppm will render the results meaningless. Very recent experiments have achieved, for the first time, state-to-state resolution of both the fine-structure and the Lambda-doublet of the OH product for reactive collisions of O(^3P)+D_2 [205]. However, these experiments are in disagreement with the leading [206]. In this context we are interested in refining our understanding of the importance of nonadiabatic transitions for the O(^3P)+H_2 reactions.

For 'low energy' reactions ($E_{col} < 5000$ cm^{-1} that start on the O(^3P) surfaces nonadiabatic coupling can induce, as the collision proceeds transitions to the lowest two ^1D potential surfaces or between any of the 3 ^3P potential surfaces. Transitions to the singlet surface can be induced by the diabatic or spin-orbit coupling and are most probable just below the barrier in bent geometries (right panel of Fig. 4.1) and deep into the reactant region. Diabatic coupling and spin-orbit coupling will induce transitions between the 3 ^3P potential surfaces. In this study we have provided new, chemically accurate potential surfaces of the lowest three triplet surfaces to analyze importance of nonadiabatic transitions between the triplet surfaces and will extend this analysis to the singlet surfaces in ongoing work.

Transitions between the triplet surfaces are most likely along near the seam of diabatic surface crossings (Fig. 4.6). The reaction barrier occurs in collinear geometry ($E_b = 4523.5$ cm^{-1} in this study, comparable to the estimate of from Rogers *et al.* E_b 4616.8 cm^{-1}). In collinear geometries the diabatic coupling vanishes. The spin-orbit matrix elements which couple the $1A'$ and $1A''$ surfaces (Eq. 4.21) are

roughly constant in the reactant region up to and over the barrier to reaction. As can be seen in Fig. 4.6 the spin-orbit matrix elements are equal to their asymptotic values along the seam of diabatic surface crossing. Thus we can expect transitions induced by the spin-orbit coupling to be significant in these geometries.

Analysis of the mixing angle as a function of the Jacobi angle is shown in Fig. 4.4 along the mixing angle for each angle analyzed. The dashed-horizontal line is used to indicate the location where the diabatic potential surfaces cross at each angle (this occurs when $\theta = \pi/4$). As can be seen in the lower panel of Fig. 4.4 the spin-orbit matrix elements are essentially constant, with insignificant angular anisotropy, along the reactant portion of the minimum energy path up to the diabatic surface crossing. Though the magnitude of the diabatic coupling shows significant variation at the diabatic surface crossing, it will still play a role in the nonadiabaticity in these geometries, albeit to a lesser degree than transitions induced by the the spin-orbit coupling, which is larger in magnitude.

The mixing angle shown in Fig. 4.4 was determined directly by the quasi-diabatization procedure in MOLPRO [3]. These values are shown by the colored circles in the top panel. The mixing angle can also be extracted from the spin-orbit matrix elements in bent geometries, by following Eq. 4.21. We observe that the values of the mixing angle calculated from the spin-orbit matrix elements are smoother than the values that come directly from MOLPRO. These two methods agree well in all studied geometries up to the barrier to reaction. At the barrier, the $2A''$ surface is about 11000 cm^{-1} higher in energy than the $1A'$ surface. Furthermore, in these geometries the attractive ^1D PES approaches and crosses the ^3P potential

surfaces. The diabatic mixing near the barrier to reaction, therefore, is not described by a single angle but by two angles: one for the mixing between the $1^1A'$ and $1^3A'$ states, and another for the mixing between the $1^1A''$ and $1^3A''$ states. This change in the nature of the diabatic mixing is seen in the disagreement between the values of the mixing angle near the barrier extracted from (a) the quasi-diabatization procedure or (b) the calculated spin-orbit matrix elements.

Finally Fig. 4.3 shows the potential surface cuts and coupling terms as a function of the Jacobi angle with (R, r) fixed to the geometries shown by the red circles in Fig. 4.6 which correspond to just before, near, and just after the diabatic surface crossing along the minimum energy path in collinear geometry. Because the spin-orbit matrix elements are comparable in magnitude to the splitting between the two lowest triplet surfaces, spin-orbit coupling will induce transitions between these states for all geometries shown. The diabatic coupling, however, is largest in magnitude at $\theta = 130°$. At that geometry, the diabatic coupling is much smaller than the separation between the two states with A'' symmetry. Thus, we can anticipate that the diabatic coupling will make a much smaller contribution to nonadiabatic transitions than the spin-orbit coupling.

4.4.4 Conclusion

In this study we have described new, accurate potential energy surfaces, as well as spin-orbit and diabatic coupling matrix elements in the reactant region and near the barrier for the experimentally challenging $O(^3P) + H_2$ reaction. From the

work presented here we have shown that the spin-orbit coupling can be expected to induce nonadiabatic transitions in all geometries along the seam of diabatic surface crossing and near the barrier between the lowest two adiabatic states. The diabatic coupling, on the other hand, will play at best only a secondary role in the nonadiabatic dynamics at all the geometries considered. Furthermore, the variation of the spin-orbit coupling is mild and one can accurately capture the coupling using the asymptotic value within the reactant channel.

As mentioned earlier in this chapter it is also essential to consider, in more detail than we have done here, the ^1D PES/s. In bent geometries, singlet states of A' and A'' reflection symmetry cross the $1^3A'$ and $1^3A''$ states near the barrier to reaction. Based, on the present results for the triplet PES's we expect the spin-orbit coupling to lead to significant nonadiabatic dynamics between the lowest triplet and singlet potential surfaces. Note that there will be no diabatic coupling between singlet and triplet states because their total spin differs. The diabatic coupling within the singlet and between the triplet states will be affected, but this will be only a second-order change due to a coupling term which is considerably smaller than the dominant spin-orbit coupling. The $^1D - ^3P$ coupling will be the subject of a future study.

Chapter 5: A Comparison of *ab initio* and Density Functional Potential Energy Surfaces

5.1 Overview

Electronic structure calculations from *ab initio* based quantum chemistry principles, like those considered in the previous chapters, are difficult to prepare and can be very computationally demanding. The computational efficiency of density-functional theory (DFT) makes it an appealing option to calculate the electronic structure of molecules. Using DFT to model intermolecular complexes, one must account for weak dispersion forces for a complete representation of the electronic environment. The standard test of DFT functionals is to benchmark them against a set of molecules with well-known properties, usually closed-shell molecules in their ground states. These benchmarks do not typically include long-range, dispersion interactions. Whether or not DFT methods can systematically describe van der Waals complexes involving open-shell molecules, or molecules in electronically excited states, is not well known.

Recently, Ershova *et al.* asked if the interaction between the open-shell NO

radical and a rare-gas atom could be described by DFT methods [28]. Their study, which tested a set of functionals with different long-range corrections, produced a high quality description of the ground electronic state, $X^2\Pi$. However, none of the tested functionals could accurately describe the NO-Ar system in the first excited electronic state, $A^2\Sigma^+$. Here we rigorously test new DFT calculations with novel long range, dispersion corrections for the ArNO ground state. These results are in very good agreement with results from PESs calculated from the more computationally-intensive CCSD(T) method for this system. Ershova's question about how well DFT can model the electronically-excited state of this moiety remains an open one.

The inelastic dynamics of open-shell diatomics with noble gases, such as the collisions of NO and Ar, have been well studied theoretically and experimentally [207–219]. The Ar+NO system has been a focus of interference studies in differential cross sections [220] and sophisticated experimental measurements that are capable of resolving the Λ-doublet fine structure [221]. These fine-structure results were confirmed by state-of-the-art scattering calculations based on Alexander's CCSD(T) surface [222]. The Ar–NO system has also been used to study the angular momentum orientation of the NO molecule after collisions with Ar atoms [223]. Furthermore, there is a long history to the refinement of the two PESs required to describe the ground state of Ar–NO($X^2\Pi$) [207–210, 224]. This wealth of experimental and theoretical knowledge of the system make it suitable as a benchmark for the new dispersion-corrected DFT calculations.

A post-Hartree-Fock scheme with corrections for dispersion interactions (UHFBR-XDM) developed by Johnson and Becke [225] has produced a new set of PESs for the ground state Ar–NO($X^2\Pi$) system. To add dispersion interactions to the UHFBR energies, Johnson applied the exchange-hole dipole moment (XDM) dispersion model [226] using the exact Hartree-Fock exchange-hole. Hartree-Fock with Becke-Roussel dynamical correlation [227] and the XDM dispersion correction has timings similar to standard Hartree-Fock, which are much faster than than the CCSD(T) calculations. These UHFBR-XDM PESs are qualitatively and quantitatively very similar to earlier CCSD(T) calculations [209, 210] and the more recent RCCSD(T) PESs by Cybulski *et al* [224].

To test the new UHFBR-XDM PESs against known experimental cross sections we perform fully-quantum, close-coupling scattering calculations of the integral sections at collision energies of 442 cm^{-1} and 1774 cm^{-1}, and differential cross sections at a collision energy of 530 cm^{-1}. These UHFBR-XDM potentials show the promise of using DFT with dispersion corrections to describe the physical properties of small intermolecular complexes, even for open-shell systems.

5.2 Potential Energy Surfaces

We use the *unscaled* Jacobi coordinates, (R, r, θ), to describe the triatomic system where we define $\theta = 0$ as the collinear approach Ar-NO and the NO bond length is fixed at $r_e = 1.15077$ Å. Note: here we suppress the $\bar{R}$ notation of earlier chapters. Due to the reflection symmetry in the triatomic plane, the approach of a

structureless atom to a diatomic in a $^2\Pi$ state gives rise to two PESs, A' and A''. The A' and A'' ground states PESs were generated from self-consistent Hartree-Fock calculations, performed using the basis-set-free NUMOL program [228]. Dynamical correlation and dispersion effects were included in a post-HF manner [225] using the Becke-Roussel correlation functional [227] and the exact-exchange formulation of the XDM dispersion model [226]. The two parameters in the XDM damping function were assigned values of $a_1 = 0.75$ and $a_2 = 1.39$ Å. This approach gives a mean absolute error of 2 cm^{-1} for the binding energies of the noble-gas pairs consisting of He, Ne, and Ar atoms [229]. Note that XDM-corrected potential-energy surfaces for larger molecules can easily be generated with Gaussian, or any electronic structure program capable of writing a wavefunction file, using the postg program [230, 231].

As can be seen in Figs. 5.1-5.3, the PESs calculated using UHFBR-XDM and CCSD(T) are qualitatively very similar. In Figure 5.3 we show the half-sum and half-difference potentials used in the dynamic calculations, defined as follows:

$$V_{sum}\,(R,\theta) = \frac{1}{2}[V_{A''}(R,\theta) + V_{A'}(R,\theta)] = \sum_{l=0}^{l_{max}} V_{l0}(R) d^l_{00}(\theta), \tag{5.1}$$

$$V_{dif}\,(R,\theta) = \frac{1}{2}[V_{A''}(R,\theta) - V_{A'}(R,\theta)] = \sum_{l=2}^{l_{max}} V_{l2}(R) d^l_{20}(\theta), \tag{5.2}$$

where $d^l_{m0}(\theta)$ denotes the reduced Wigner rotation matrix elements. Here we use $l_{max} = 10$.

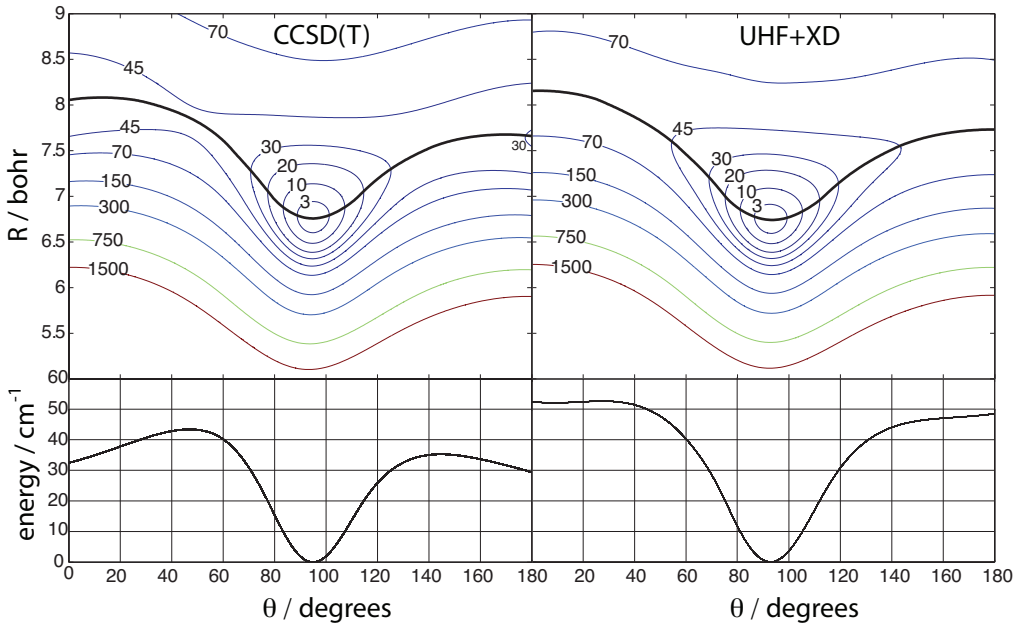

Figure 5.1: (upper) Contour plot of the A' PES. (lower) The minimum energy profiles of the A' PES as a function of θ. The contours are labeled in cm^{-1} relative to the minimum of the potential (for CCSD(T), D_e=116.6 cm^{-1} and for UHFBR-XDM, D_e=124.8 cm^{-1}).

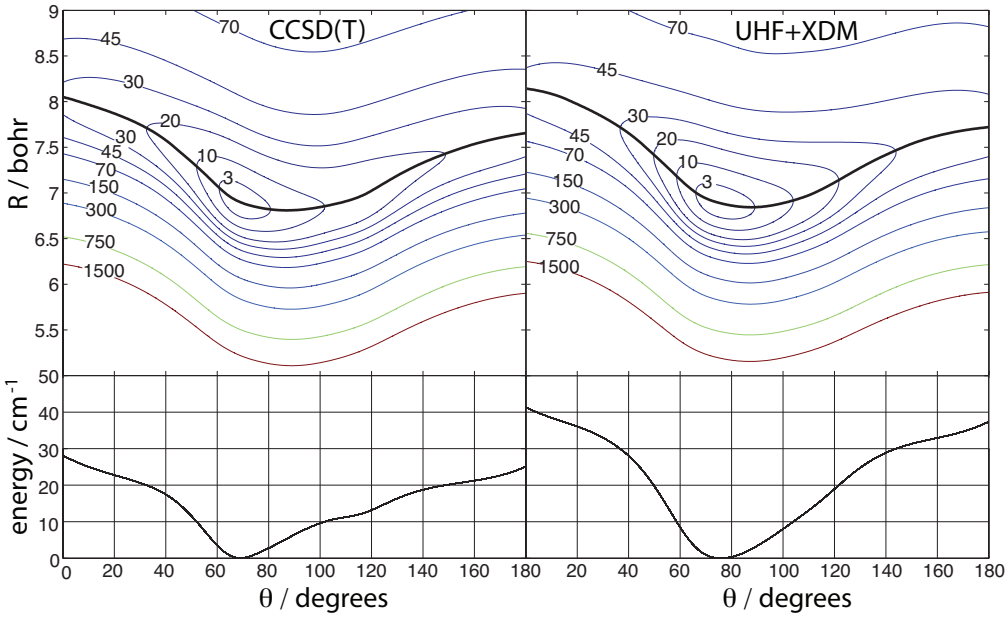

Figure 5.2: (upper) Contour plot of the A'' PES. (lower) The minimum energy profiles of the A'' PES as a function of θ. The contours are labeled in cm^{-1} relative to the minimum of the potential (for CCSD(T), D_e=112.3 cm^{-1} and for UHFBR-XDM, D_e=113.7 cm^{-1}).

The wells in the A' and A'' surfaces, as predicted by UHFBR-XDM calculations are all slightly deeper than those from CCSD(T) calculations. The UHFBR-XDM calculations also predict a lower half-sum potential relative to the CCSD(T) calculations. The right panel of Fig. 5.3 shows the half-difference potential as predicted by UHFBR-XDM calculations is in good agreement with the CCSD(T) potentials, though the UHFBR-XDM half-difference potential is slightly broader and higher than the corresponding CCSD(T) PES.

Table 5.1 compares the minimum geometry, (R_e, r_e, θ_e), and minimum energy,

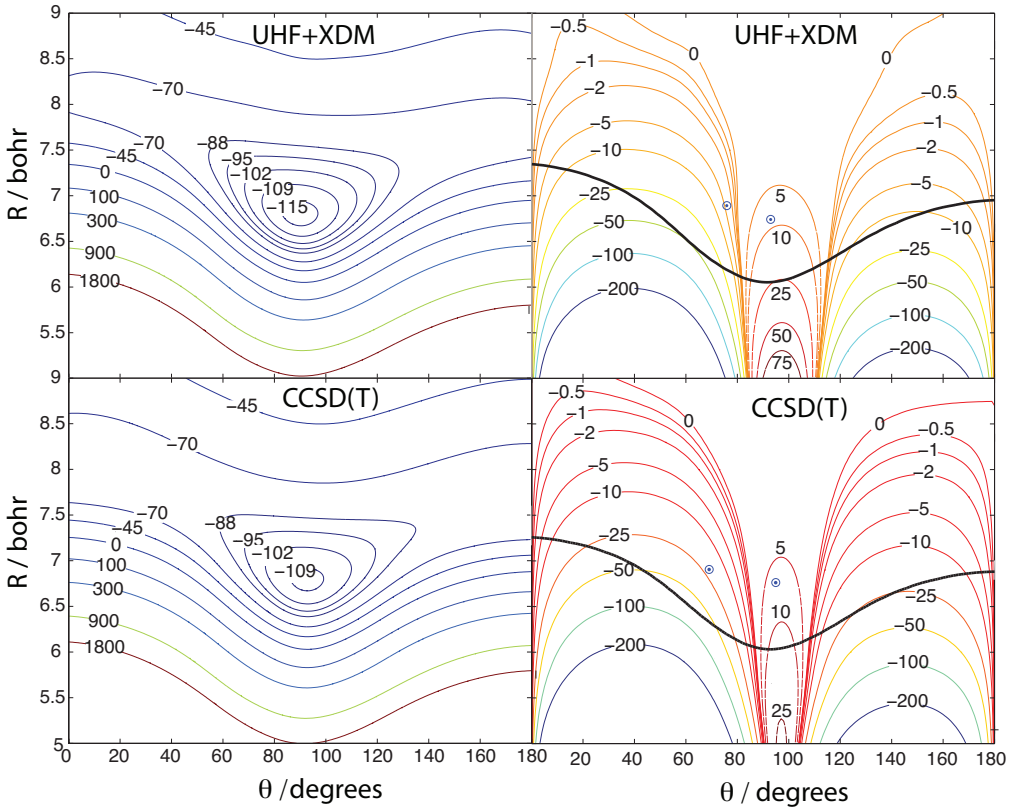

Figure 5.3: (left) $V_{sum}(R,\theta)$ (right) $V_{dif}(R,\theta)$. The thick black curve in the right panels indicates the beginning of the repulsive wall, where $V_{sum}(R,\theta) = 0$. The blue circles indicate the minimum geometries of $V_{A'}$ and $V_{A''}$. The minimum of V_{sum} for UHFBR-XDM and CCSD(T) are -116 cm^{-1} and -110.5 cm^{-1}, respectively.

D_e, for both of the Ar–NO PESs as predicted by the UHFBR-XDM method, Alexander's CCSD(T) PESs [209, 210], Alexander's coupled electron pair method (CEPA) calculations [207] and Cybulski's RCCSD(T) PESs [224]. The UHFBR-XDM values are in good agreement with both coupled-cluster methods. The A' well depth predicted by UHFBR-XDM is about 7% and 4% deeper than the CCSD(T) and RCCSD(T) predictions, respectively. The well depths of the A'' adiabatic PES are

quite similar for all listed methods except CEPA, which is much shallower.

Table 5.1: Minimum geometry (R_e, θ_e) in bohr and degrees and minimum energy, D_e, in cm^{-1} for the Ar–NO($X^2\Pi$) A' and A'' PESs calculated with different methods.

Method	$R_e(A')$	$\theta_e(A')$	$D_e(A')$	$R_e(A'')$	$\theta_e(A'')$	$D_e(A'')$
UHFBR-XDM[1]	6.74	92.9	124.8	6.89	75.9	113.7
CCSD(T)[2]	6.76	94.9	116.6	6.90	69.1	112.3
CEPA[3]	6.99	94.1	77.9	7.09	73.1	79.1
RCCSD(T)[4]	6.75	94.9	120.3	6.90	71.1	115.0

The CCSD(T) PESs based on Alexander's calculations [209] have been reproduced to ensure consistency in the comparisons with the new UHFBR-XDM calculations. As in the case of the UHFBR-XDM calculations, the CCSD(T) PESs were calculated with the NO bond length fixed at 1.15077 Å.

5.3 Bound States

In this section we briefly describe the parameters needed to converge the bound state wave functions and obtain rotational constants for the triatomic complex. The formal expressions for the wave functions of the Ar–NO complex have been developed previously [209, 211].

The bound states of Ar–NO($X^2\Pi$) were calculated using the HIBRIDON quantum chemistry package [161]. The radial part of the wave function was represented

by an equidistant distribution of Gaussian basis functions [232]. The fine-structure rotational channels of the $^2\Pi$ NO molecule were defined by the rotational constant of $B = 1.69611$ cm^{-1} and the spin-orbit constant of $A_{SO} = 123.1393$ cm^{-1}, with the reduced mass of the Ar–NO complex set to 17.135 a.m.u.

Each rotational level splits into two Λ-doublets where the Λ-doubling parameters are $p = 0.0117$ cm^{-1} and $q = 6.7 \times 10^{-4}$ cm^{-1}. In order converge the bound state for values of the total angular momentum in the range J =0.5-6.5, the NO rotational basis included channels up to $j_{max} = 18$. These predictions of the bound-state energies of the Ar–NO complex are in good agreement with the CCSD(T) calculations, as can be seen in Table 5.2 and Fig. 5.4.

We also calculated the bound-state energies within the coupled states (CS) approximation, which ignores the Coriolis coupling. For these CS calculations we used the same parameters and separately performed calculations for all possible values of the body-fixed frame projection quantum number, P, of the total angular momentum, $\vec{J}$. These CS calculations were used to identify the P quantum number for the close-coupling bound-state energies shown in Table 5.2.

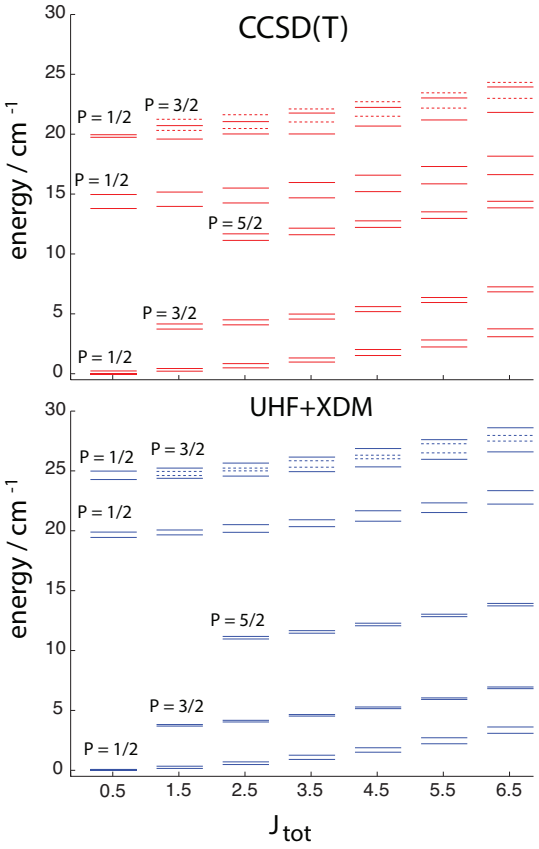

Figure 5.4: Relative positions of the lowest bend-stretch states of the Ar–NO complex. Only the positive parity states are shown. The states are labeled with the nominal value of P, which corresponds to the projection of the total angular momentum, J, onto the Ar–NO bond axis, R. The dependence of the energy of the states is shown as a function of total angular momentum. The dashed levels correspond to the first excited state with $P = 3/2$ to help distinguish these states from the second excited states with $P = 1/2$.

The bound state predictions using the UHFBR-XDM PESs are lower in energy relative to those calculated using the CCSD(T) potentials. This is consistent with the deeper wells in both the $V_{A'}$ and $V_{A''}$ UHFBR-XDM PESs. The predicted disso-

Table 5.2: Lowest bound state energies of Ar+NO in cm^{-1}.

	CCSD(T)				UHFBR-XDM		
P	$J = 1/2$	$J = 3/2$	$J = 5/2$	P	$J = 1/2$	$J = 3/2$	$J = 5/2$
1/2	-83.157	-82.973	-82.660	1/2	-86.990	-86.819	-86.511
1/2	-82.948	-82.720	-82.345	1/2	-86.896	-86.651	-86.267
3/2		-79.436	-79.090	3/2		-83.295	-82.946
3/2		-79.015	-78.669	3/2		-83.160	-82.811
5/2			-72.040	5/2			-76.018
5/2			-71.491	5/2			-75.806
1/2	-69.371	-69.196	-68.903	1/2	-67.518	-67.353	-67.072
1/2	-68.205	-68.002	-67.665	1/2	-67.106	-66.881	-66.513
1/2	-63.523	-63.442	-63.284	1/2	-62.704	-62.609	-62.397
1/2	-63.120	-62.942	-62.630	3/2		-62.349	-62.027
3/2		-62.480	-62.054	3/2		-62.043	-61.698
3/2		-61.919	-61.549	1/2	-61.992	-61.739	-61.340
1/2	-56.701	-56.562	-56.331	3/2		-57.314	-57.013
3/2		-56.331	-56.061	3/2		-56.355	-56.050
1/2	-55.276	-55.056	-55.038	1/2	-53.920	-53.743	-53.448
3/2		-55.372	-54.698	1/2	-53.694	-53.507	-53.316
5/2			-52.516	5/2			-53.195
5/2			-51.672	5/2			-52.569
1/2	-50.742	-50.554	-50.239	5/2			-48.803
1/2	-48.527	-48.335	-48.014	5/2			-48.029

ciation energy, D_0, of the lowest bound state of the Ar–NO complex from Johnson's PES is closer in energy to the experimental value of D_0 than from the CCSD(T) calculations, as can be seen in Table 5.3. The dissociation energy predicted by the UHFBR-XDM PES is very close to both the RCCSD(T) results of Cybulski *et al.* [224] and the experimental value of Tsuji *et al.* [213].

Table 5.3: Spectroscopic data, in cm^{-1}, for the Ar–NO complex.

	D_0	$\omega_{stretch}$[1]	ω_{bend}[2]
UHFBR-XDM	87.0	24.3	3.7
CCSD(T)	83.2	19.7	3.7
RCCSD(T)	86.7[3]	–	–
Experiment	87.8[4]	40[5]	

The bound state parities, as predicted by UHFBR-XDM and CCSD(T) calculations, are shown in Fig. 5.5. The lowest bound state of the Ar–NO complex should have positive parity and the next lowest bound states have the same parities as those predicted by the CCSD(T) calculations [211]. The UHFBR-XDM PESs incorrectly predict that the lowest bound state will have negative parity. Table 5.4 shows that the incorrect assignment of the bound-state parities leads to qualitatively incorrect predictions for transition energies out of several of the lowest bound states of the Ar–NO complex, i.e. negative energies. The slight differences between V_{dif} from the UHFBR-XDM and CCSD(T) calculations may give rise to this discrepancy in the parity of the bound states.

The rotational constants for the Ar–NO complex as predicted from both the CCSD(T) and UHFBR-XDM potentials are in good agreement with the CCSD(T) predictions and experimental values of Wen *et al.* [219] These rotational constants

Table 5.4: Transition energies in cm^{-1} for several pure rotational transitions in the Ar–NO complex. *See Fig. 5.5 for the explanation of state labeling*

Transistion	Exp.[1]	CCSD(T)[2]	UHFBR-XDM[2]
$J = 1/2, o(-) \rightarrow J = 1/2, o(+)$	0.020	0.023	-0.024
$J = 1/2, o(-) \rightarrow J = 3/2, o(+)$	0.035	0.003	0.055
$J = 3/2, o(-) \rightarrow J = 1/2, o(+)$	0.014	0.052	-0.099
$J = 3/2, o(-) \rightarrow J = 3/2, o(+)$	0.029	0.032	-0.020
$J = 3/2, o(+) \rightarrow J = 3/2, e(-)$	0.226	0.256	0.163
$J = 3/2, o(+) \rightarrow J = 5/2, o(-)$	0.574	0.589	0.578
$J = 3/2, e(+) \rightarrow J = 5/2, e(-)$	0.123	0.099	0.116

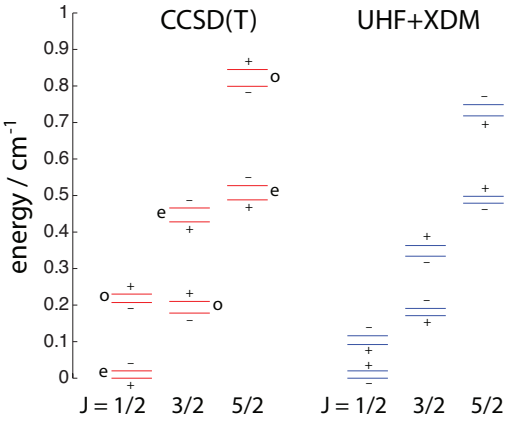

Figure 5.5: Relative positions of the lowest bend-stretch states of the Ar–NO complex with $P = 1/2$. The zero of energies are -83.16 cm^{-1} and -87.00 cm^{-1} for the CCSD(T) and UHFBR-XDM predictions respectively. The + and − labels indicate the total parity of each state. The e/o labeling is a shorthand for determining allowed transitions and is consistent with Ref. [211]

are shown in Table 5.5. The rotational constants were found with the following fit:

$$E_{\nu,J,P} = E_{\nu,P} + B_{\nu,P0}J(J+1) + a(J+\frac{1}{2}), \tag{5.3}$$

where $B_{\nu,P0}$ is the rotational constant listed in Table 5.5.

Table 5.5: Rotational constants, $B_{\nu,P0}$, in cm^{-1}.

Band[1]	Exp.[2]	CCSD(T)[3]	UHFBR-XDM[3]
A	0.0680	0.0686	0.0691
B	0.0683	0.0688	0.0695
B1	0.0681	0.0680	0.0688
C	0.0632	0.0627	0.0647
D1	0.0738	0.0638	0.0642
E	0.0653	0.0657	0.0656
D	0.0681	0.0584	0.0634
F	0.0691	0.0664	0.0661
G	0.0625	0.0631	0.0458
H	0.0665	0.0590	0.0575

We also present predictions of the bound-state calculations using both potentials within Close-Coupling (CC), Centrifugal Decoupled (CD) and Adiabatic Bender (AB) approaches, shown in Table 5.6. The predictions of the relative energies of the lowest bound states by UHFBR-XDM and CCSD(T) calculations are in good agreement. At higher energies the relative spacing between states is not consistent, which reflects the subtle differences between the UHFBR-XDM and CCSD(T) PESs, including the deeper UHFBR-XDM wells. The CD and AB energies from UHFBR-XDM are in good agreement with CCSD(T) as is shown in Table 5.6. With the exception of the bound state parities, these results are in very good agreement with those from Alexander's CCSD(T) PESs [209, 210].

Table 5.6: Relative energies in cm^{-1} of the lowest bound states of the Ar–NO complex.

				CC[1]		CC		CD[2]		AB[3]	
J[4]	P[5]	n[6]	ν_s[7]	π[8]$= 1$	$\pi = 1$	$\pi = -1$	$\pi = -1$				
				CCSD(T)	XDM	CCSD(T)	XDM	CCSD(T)	XDM	CCSD(T)	XDM
$\frac{1}{2}$	$\frac{1}{2}$	1	0	0	0.020	0.020	0	0	0	0	0
		2	0	0.230	0.920	0.207	0.116	0.192	0.051	0.090	0.051
		3	0	13.79	19.47	13.80	19.50	13.78	19.46	13.54	18.21
		4	0	14.96	19.91	14.96	19.88	14.94	19.85	16.11	20.00
		1	1	19.74	24.30	19.55	24.30	19.64	24.27	20.10	24.97
		2	1	19.96	25.01	20.14	25.01	20.02	24.97	23.18	26.65
$\frac{3}{2}$	$\frac{1}{2}$	1	0	0.210	0.171	0.178	0.191	0.210	0.212	0.209	0.212
		2	0	0.428	0.363	0.466	0.334	0.403	0.264	0.298	0.261
		3	0	13.97	19.68	13.97	19.62	13.97	19.66	13.73	18.42
		4	0	15.16	20.01	15.17	20.15	15.12	20.05	16.31	20.19
		1	1	19.59	24.40	19.86	24.38	19.83	24.47	20.27	25.15
		2	1	20.71	25.26	20.66	25.23	20.20	25.16	23.37	26.84

5.4 Adiabatic Bender States

The UHFBR-XDM adiabatic bender potentials, shown in Fig. 5.6, are very similar to those based on CCSD(T) calculations. However, the UHFBR-XDM $P = 1/2$, $n = 1, 2$ adiabatic bender potentials do not have the same strongly avoided crossing as do the equivalent CCSD(T) potentials. This is related to the anisotropy of the $V_{A'}$ PES from the linear to T-shaped geometry. As can be seen in lower panels of Fig. 5.1, there is an increasing barrier from $\theta = 0°$ to $\theta = 90°$ in the CCSD(T) PES, whereas the UHFBR-XDM PES has a very small barrier in

this region. Accordingly, the lowest two CCSD(T) adiabatic bender potentials have a much stronger avoided crossing. The $P = 1/2, 3/2$, $n = 1, 2$ bender potentials are predicted to be about 5 cm^{-1} lower in the UHFBR-XDM calculations, while the $P = 1/2$, $n = 3, 4$ bender potentials are predicted to be at about the same energy with both methods.

The CCSD(T) and UHFBR-XDM predictions of the distribution function, $\rho_{Pn}(R, \theta)$, which shows the probability of finding the Ar atom for given values of R and θ, is shown in Figs. 5.6 and 5.7 . In general, the distribution functions predicted by UHFBR-XDM and CCSD(T) calculations are in good agreement. However, the UHFBR-XDM calculations tend to predict more localized distribution functions than those predicted by CCSD(T) calculations, which reflects the incorrect anisotropy of the UHFBR-XDM potential energy surfaces.

5.5 Scattering Calculations

Initial and final state resolved differential cross section calculations with collision energy of $E_{col} = 530$ cm^{-1} for the UHFBR-XDM and CCSD(T) potentials are shown in Figure 5.8 for spin-orbit conserving collisions and Fig. 5.9 for spin-orbit changing collisions. We show the DCS for both parity-conserving and parity-changing transitions to compare with the recent experiment of Eyles *et al* [220]. The theoretical cross sections were averaged over a Gaussian distribution of angles with a FWHM = 8°. We scale the theoretical DCSs such that the integral of the

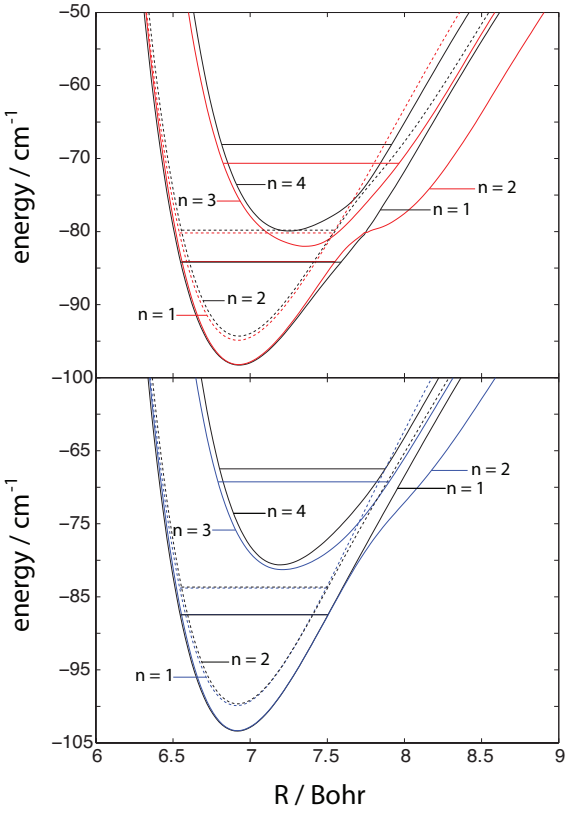

Figure 5.6: Adiabatic bender potential energy curves for the Ar–NO complex. The solid and dashed curves correspond to $P = 1/2$ and $P = 3/2$, respectively. The states are labeled with by the value of n, which correspond to the n^{th}-eigenvector of the $W(R)$ matrix for a given value of P. The horizontal lines correspond to the lowest vibrational level for each adiabatic bender potential, *see Table 5.6*. Note: the $P = 1/2$, $n = 1$ and $n = 2$, as well as, $P = 3/2$, $n = 1$ and $n = 2$ vibrational energies are nearly indistinguishable graphically.

DCS matches experiment for both parity-conserving and parity-changing collisions.

The integral cross sections calculated for $E_{col} = 442$ cm^{-1} and $E_{col} = 1774$ cm^{-1}, are shown in Figs. 5.10 and 5.11, respectively. For scattering calculations at the highest collision energy of 1774 cm^{-1}, we used $j_{max} = 33$. The integral cross

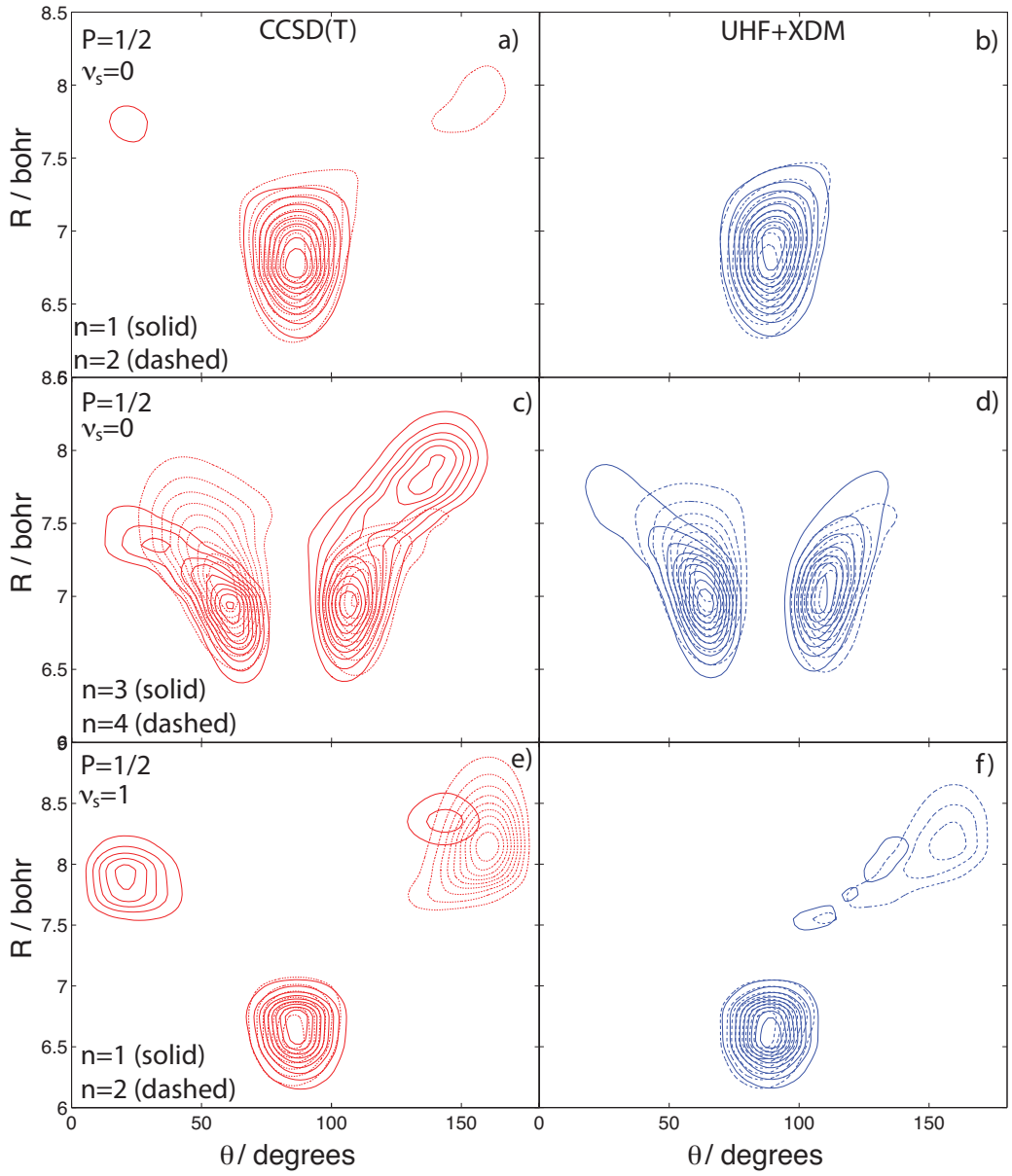

Figure 5.7: Plot of the distribution function, $\rho_{Pn}(R, \theta)$, describing the probability of finding Ar in the space described by Jacobi coordinates, R and θ with respect to the center of mass of NO for the $P = 1/2$ states.

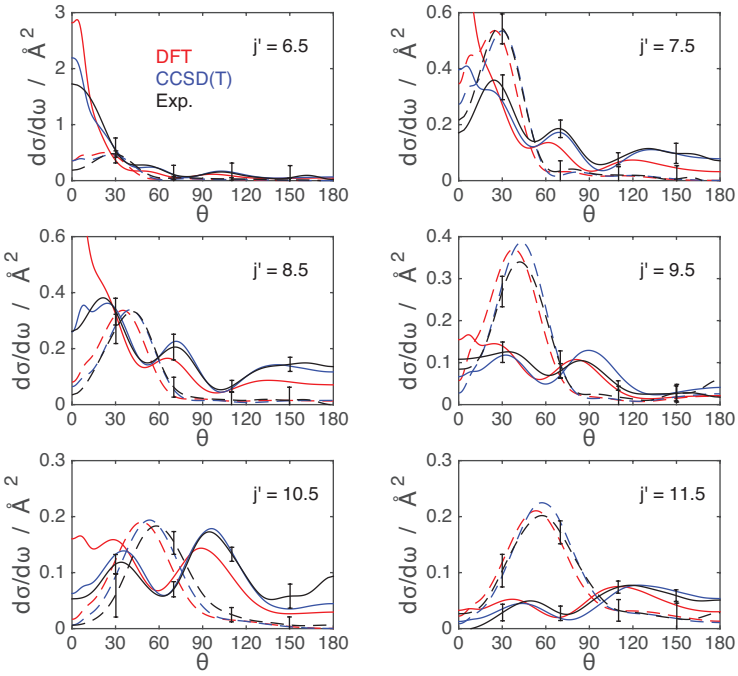

Figure 5.8: DCS for spin-orbit conserving transitions with collision energy E_{col} = 530 cm^{-1} from DFT (red) CCSD(T) (blue) and experimental results *et al* [220–222] (black) for the Ar+NO($^2\Pi_{1/2}$, $v = 0$, $j = 1/2, p = +1$) $\rightarrow$ Ar+NO($^2\Pi_{1/2}$, $v = 0$, $j = j', p = p'$). The overall parity of the state $p = \epsilon(-1)^{j-1/2}$ and $\epsilon = +1$ for e and $\epsilon = -1$ for f. Final states with positive parity (parity conserving) are shown with solid lines band those with overall negative parity (parity changing) are shown with dashed lines.

sections predicted by UHFBR-XDM and CCSD(T) at these two energies are in good agreement. The theoretical cross sections at E_{col} = 442 cm^{-1} were averaged over a Gaussian distribution of collisional energies with a FWHM = 10% of E_{col}. The calculations for E_{col} = 1774 cm^{-1} were found using a 4:1 relative population of

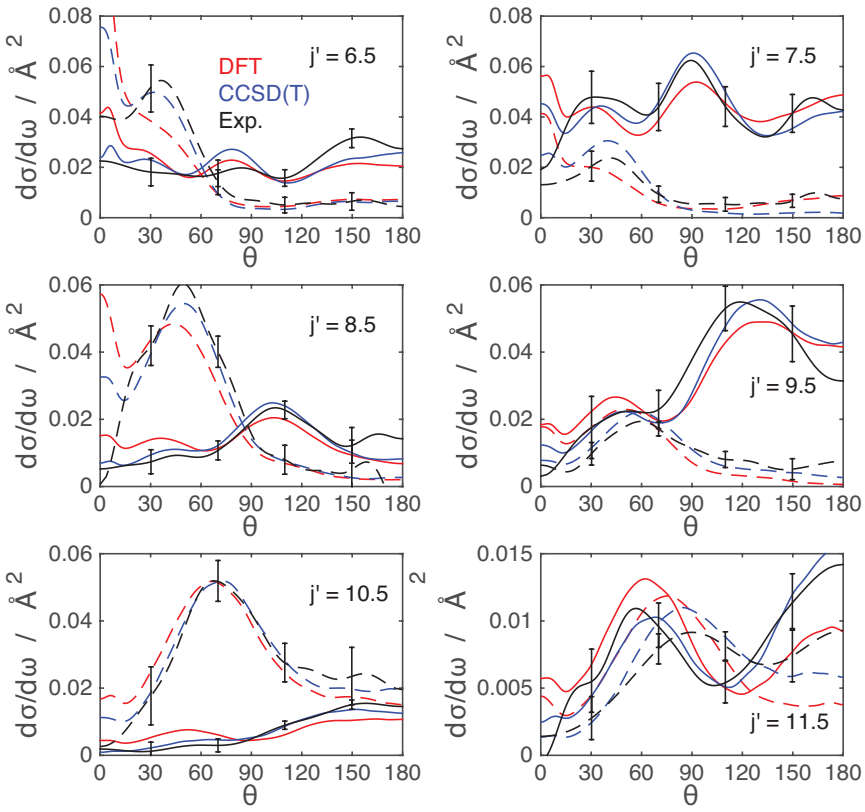

Figure 5.9: DCS for spin-orbit changing transitions with collision energy E_{col} = 530 cm^{-1} from DFT (red) CCSD(T) (blue) and experimental results*et al* [220–222] (black) for the Ar+NO($^2\Pi_{1/2}$, $v = 0$, $j = 1/2, p = +1$) $\rightarrow$ Ar+NO($^2\Pi_{3/2}$, $v = 0$, $j = j', p = p'$). The overall parity of the state $p = \epsilon(-1)^{j-1/2}$ and $\epsilon = +1$ for e and $\epsilon = -1$ for f. Final states with positive parity (parity conserving) are shown with solid lines band those with overall negative parity (parity changing) are shown with dashed lines.

the $j = 1/2$ and $j = 3/2$ rotational levels of the NO molecule to simulate thermal distribution of initial rotational states. To maintain a collisional energy of 1774

cm^{-1} the calculations for the $j = 3/2$ rotational level were performed at a total energy of 1779 cm^{-1}, as done previously [209].

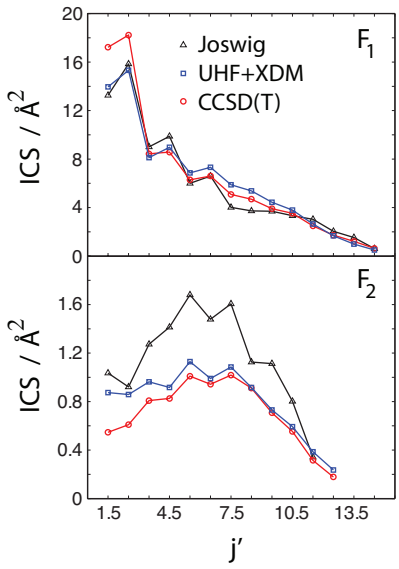

Figure 5.10: Integral cross sections with $E_{col} = 442$ cm^{-1}. (upper) SO-conserving, F_1, Ar+NO($^2\Pi_{1/2}$, $v = 0$, $j = 1/2, p = +1$) $\rightarrow$ Ar+NO($^2\Pi_{1/2}$, $v = 0$, $j = j', p = p'$) . (lower) SO-changing, F_2, Ar+NO($^2\Pi_{1/2}$, $v = 0$, $j = 1/2, p = +1$) $\rightarrow$ Ar+NO($^2\Pi_{3/2}$, $v = 0$, $j = j', p = p'$). The black triangles correspond to the Joswig experiments [215]. These cross sections are normalized such that the total cross section, F_1+F_2 , for both theoretical calculations and the experimental values are equal.

5.6 Discussion

In this chapter we showed the performance of the UHFBR-XDM potentials for the open-shell Ar–NO ground state system derived from the Becke-Johnson disper-

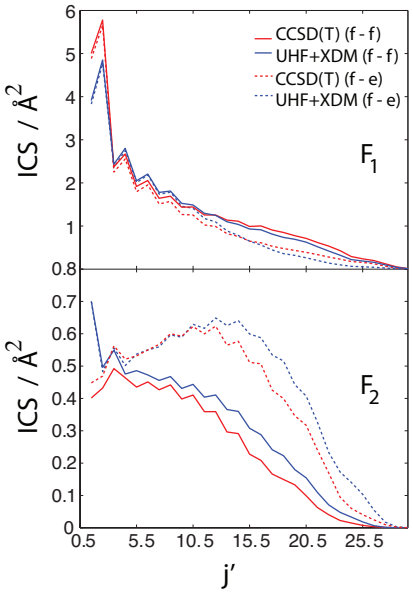

Figure 5.11: Integral cross sections with $E_{col} = 1774$ cm^{-1}. The cross sections are averaged over the initial e/f state and averaged over initial state population with a 4:1 ratio of the $j = 1/2$ and $j = 3/2$ rotational levels of the NO molecule. (upper) Cross section predictions for SO conserving transitions, $\omega = \omega' = 1/2$, F_1. (lower) Cross section predictions for SO changing transitions, $\omega = 1/2 \rightarrow \omega' = 3/2$, F_2.

sion correction formalism in the bound state and scattering calculations. The new potentials are compared to the previous ones based on the CCSD(T) Ar–NO potentials extrapolated to the basis set limit by Alexander [210] and newer RCCSD(T) PESs by Cybulski [224].

Johnson's new UHFBR-XDM potentials agree remarkably well with the CCSD(T) surfaces. The positions of minima are very similar, with the well being slightly more attractive in case of the UHFBR-XDM potentials, especially for the A' adiabatic

surface. The fact that the well depth is deeper by about 8 cm^{-1} for the A' adiabatic surface shifts the zero-point-corrected dissociation energy closer to the experimental value of Tsuji *et al.* [213] (Table 5.3). The agreement with CCSD(T) is promising if we keep in mind that the UHFBR-XDM model is by far the less computationally demanding method of the two.

The computational cost of computing the XDM dispersion is negligible relative to the HF calculation. Thus we have obtained accuracy close to CCSD(T) level with essentially the cost of HF. The UHFBR-XDM potentials (Figures 5.1 and5.1) exhibit somewhat different anisotropy in the vicinity of collinear arrangements of the atoms. Specifically near the collinear approaches, the UHFBR-XDM PESs are more repulsive and the A' adiabat is flatter in comparison to the CCSD(T) PES.

The diabatic surfaces, V_{sum} and V_{dif}, for both UHFBR-XDM and CCSD(T) are shown in Fig. 5.3. The UHFBR-XDM model predicts saddle points for collinear geometries, while the CCSD(T) exhibits small local minima. The general anisotropy is similar with the global minimum being in the T-shape geometry (near 90 degrees) showing the near-homonuclear character of the V_{sum} PES. In case of UHFBR-XDM, the difference potential calculations show a slightly wider repulsive region than the CCSD(T) diabat.

The dissociation energy predicted from UHFBR-XDM is in better agreement with both Cybulski's RCCSD(T) PESs and experiment as compared to the CCSD(T)

predictions. The UHFBR-XDM stretching frequency, $\omega_{stretch}$, shown in Table 5.3, is also slightly closer to experiment. While the theoretical frequencies are off by about 50%, one has to keep in mind that the experimental value can be ambiguous [233].

As shown in Fig. 5.5, the UHFBR-XDM PESs predict the incorrect parity of the bound-state wave functions. The incorrect assignment of the bound-state parities leads to qualitatively incorrect predictions of the transition energies out of the lowest bound states (Table 5.4). The source of this discrepancy between the UHFBR-XDM and CCSD(T) is not well understood and may serve as a target for improving future DFT surfaces for open-shell systems.

The Close-Coupling bound states were used to estimate the rotational constants of the Ar–NO complex using both potential models. The UHFBR-XDM PES results, shown in Table 5.5, are in very good agreement with both CCSD(T) and experimental results. In the Adiabatic Bender approximation (Fig. 5.6), the avoided crossing region in the UHFBR-XDM curves is slightly weaker than for the CCSD(T) curves. We also show ro-vibrational wave functions obtained from the Adiabatic Bender approximation in Figs. 5.6-5.7. The wave functions corresponding to the UHFBR-XDM potential are more localized due to the deeper well, but generally similar to those using CCSD(T).

From the scattering calculations we have obtained observables such as integral cross sections (ICSs) and differential cross sections (DCSs) using both potential models. We find very good agreement with the initial and final state resolved experiments of Eyles *et al* [220] for both UHFBF-XDM and CCSD(T) DCSs for spin-orbit conserving transitions (Fig. 5.8) and spin-orbit changing transitions (Fig. 5.11) at

E_{col} = 530 cm^{-1}. The theoretical cross sections tend to over-estimate the amount of backscattering and the DFT results universally predict more backscattering than the CCSD(T) results. However, the CCSD(T) results are consistent with Eyles [220] and the new DFT potential performs remarkably well when compared to experiment.

In Figure 5.10 the ICSs from the UHFBR-XDM and CCSD(T) calculations are compared with the experimental results of Joswig *et al.* [215] The total experimental ICS's are scaled to match the corresponding total theoretical cross sections. The total ICS is composed of transitions to both F1 and F2 spin-orbit manifolds,

$$ICS_{tot} = \sum_{j'} \sum_{i=1}^{2} \sigma(j', F_i').$$

As one can see, both UHFBR-XDM and CCSD(T) results reproduce experiment quite well in case of the SO-conserving transitions. The UHFBR-XDM potential gives better agreement with experiment for the lowest j' quantum numbers. The propensities in SO-changing transitions are well reproduced by both theoretical potentials, but the magnitude of the experimental cross sections is approximately twice as high as than those from calculations for j' up to 7.5. For a pure homo-nuclear PES only $\Delta j = even$ transitions are allowed. The near homo-nuclear character of the ArNO PESs angular anisotropy allows for all transitions but maintains a propensity for $\Delta j = even$ transitions. Both UHFBR-XDM and CCSD(T) ICS results show this $\Delta j = even$ propensity.

To probe the repulsive part of the UHFBR-XDM PESs we performed scat-

tering calculations of the ICSs at collision energy of 1774 cm^{-1} with respect to the $j = 1/2$ and $j = 3/2$ initial rotational states. The inelastic cross sections for spin-orbit manifold conserving and spin-orbit manifold changing transitions are shown in Figure 5.11. The $j = 3/2$ state was added with a weight of 0.2 to 0.8 of the $j = 1/2$ cross sections to simulate the thermal distribution of the rotational states of NO. The UHFBR-XDM cross sections are slightly smaller especially for the $j' = 1.5$ final rotational state, but for higher j' they are similar to CCSD(T). The repulsive wall is reproduced quite well and the agreement with experiment is almost as good as CCSD(T). One could use the low cost UHFBR-XDM method and extend the potential to include vibrational modes of the NO molecule to investigate the NO vibrational de-excitation upon collisions with Ar in future studies.

5.7 Conclusions

We report a comparison of the bound states and scattering results obtained on the new potential energy surfaces for the ground state Ar–NO($X^2\Pi$) system and those previously reported with Alexander's CCSD(T) PESs. The new UHFBR-XDM PESs are qualitatively and quantitatively similar to CCSD(T) calculations. The UHFBR-XDM V_{sum} PES is characterized by moderately deeper van der Waals well and a lower zero-order corrected dissociation energy, which is in better agreement with Cybulski's recent PES and experiment relative to previous Alexander's CCSD(T) results.

The anisotropy of the UHFBR-XDM surfaces does not agree with that of the CCSD(T) surfaces, especially in the vicinity of collinear geometries. Similarly, the anisotropies of the half-difference potential, V_{dif}, in the T-shape region are markedly different for these two surfaces. These facts may explain why the UHFBR-XDM potential predicts opposite parity splittings to those obtained with CCSD(T) PESs. One possible source of discrepancy between the XDM results and the reference CCSD(T) potential could be neglect of the three-body contribution to the dispersion energy, which will stabilize the collinear geometries. However, tests using the many-body generalization of the XDM model [234] indicate that this effect is not sufficiently large to account for the error and it is more likely due to the underlying dynamical correlation functional.

In the scattering calculations, the UHFBR-XDM PES performs very well compared to CCSD(T) and experiment, in spite of a pronounced preference for back scattering. The integral cross sections presented in this work agree fairly well with experiment, especially for the lowest rotational quantum numbers. The UHFBR-XDM scheme, as applied for the Ar-NO system, is in good agreement with both coupled-cluster methods and with experiments with the added benefit of great savings in computational time. The agreement between DFT, existing theory and experiment presented in this work is promising for the use of DFT with dispersion functionals to accurately model small, open-shell systems and serves as a benchmark for application of this method to larger molecular colliders.

Chapter 6: Conclusions and Future Directions

6.1 Conclusions

The underlying goal of the research presented was to investigate and visualize the quantum effects in nonadiabatic atom-diatom reactions. This work spanned two areas of reactive scattering theory, i) method development for simulating the quantum dynamics of the atom-diatom reactions (Chapters 2-3), and ii) the calculation, representation and modeling of the potential energy surfaces used in these dynamics simulations (Chapters 4-5 and Appendix A).

6.1.1 Reaction Dynamics

In the first part of this thesis we derived a novel extension of an existing finite-element based algorithm for simulating the time-independent quantum reactive scattering dynamics of atom-diatom reactions. We improved upon previous implementations of the finite-element approach to reactive scattering problems. In our approach we included the scattering amplitudes in the vector of unknowns to simultaneously solve directly for the scattering wave function *and* scattering amplitudes. The method of Askar [18] and later used by others [111–118] solves the

dynamical equations with multiple pairs of artificial, fixed boundary conditions. The scattering amplitudes are extracted by taking the linear combination of the artificial standing wave solutions that satisfies the time-independent formulation of Schrödinger equation. We showed that the speed-up expected from our method is on the order of the total number of open vibrational states in the reactant and product channels.

We rigorously tested our FE method and our results agreed with well known benchmark reactions including H+H_2, F+HCl and F+H_2 for all collision energies tested. Our was designed to be totally general, easy to use, freely available to the public and we have included a very thorough companion reference, which has been made available, alongside the source code, online [119].

Our interest in the quantum scattering dynamics of atom-diatom reactions was to better understand the nature of nonadiabatic transitions within reactive chemical systems. To this end, the FE scattering algorithm presented in the first half of Chapter 3 was extended to chemical reactions that evolve on multiple, coupled potential energy surfaces. With this coupled-surfaces algorithm in hand, we used the fluid-flow picture of the scattering wave-function as a tool to visualize nonadiabaticity in atom-diatom reactions.

To account for the fact that electronic occupancy of the scattering partners can change during the reaction, we derived a basis-independent generalization of the scattering boundary conditions. We then extended our MATLAB scattering software to handle reactions that evolve on multiple potentials. We provided the results for the nonadiabatic reactions of F+HCl, F+H_2 and Li+CaH on the lowest

set of coupled potential surfaces. Our results for these reactions included never before seen insights and visualizations of nonadiabatic dynamics for atom-diatom molecules.

Specifically, we showed that the flux of the current density as well as the mixing angle can shed light on the mechanisms of nonadiabatic behavior for this class of reactions. The flux in the current density allowed us to identify the locations of nonadiabatic behavior. The appearance of oscillations and nodal structures in the flux of the current density as well as the gradient of the mixing angle allowed us to discriminate between nonadiabatic transitions that are kinetically or vibrationally mediated. In summary, this work provided a new set of tools for understanding nonadiabaticity in atom-diatom reactions in reduced dimensionality.

6.1.2 Potential Surfaces

In the second half of this work we discussed various aspects of potential energy surfaces relevant for nonadiabatic atom-diatom reactions. In the first portion of Chapter 4, we derived the time-reversal invariant Kramers basis for the potential energy matrix for atom-diatom reactions of the type A(^2P) + BC and A(^3P) + B_2. For A(^2P) + BC reactions the derivation of the Kramers basis here provided corrections to a previous definition [62]. The Kramers basis was an ideal basis for reactive scattering calculations as it allowed us to minimize the number of states needed to fully describe the nonadiabatic coupling, which reduced the computational complexity of scattering dynamics simulations.

Also in Chapter 4 we presented a new set of highly accurate *ab initio* calculations for the $O(^3P) + H_2$ potential energy surfaces, diabatic coupling and spin-orbit matrix elements. We used the explicitly correlated variant of the internally contracted multi-reference configuration-interaction method with single and double excitations with the addition of the Davidson correction $MRCISD - F12 + Q$, which is known to be close in accuracy to the complete basis set limit. These new calculations estimated the barrier height of the $O(^3P) + H_2$ reaction on the lowest potential surface, $1A''$, to be 65.9 cm^{-1} lower than the previous calculations from Rogers and coworkers [182]. From these new potential surfaces we concluded that the nonadiabatic mixing terms, namely spin-orbit and diabatic mixing, must be included for an accurate account of the quantum dynamics of $O(^3P)$+H_2. We were also able to conclude that of these two nonadiabatic terms the spin-orbit coupling will be the dominant factor in nonadiabatic adiabatics. Furthmore, because it was shown that the spin-orbit coupling varies little with nuclear geometry, one can achieve accurate scattering results by assuming the spin-orbit coupling matrix elements are constant in the reactant channel.

The use of DFT for modeling the potential surfaces of small open-shell chemicals systems, i.e. systems with long range effects) is not well studied. In Chapter 5 we compared a set of new potential energy surfaces for the Ar-NO ground state system computed calculated using DFT with previously published potentials based on *ab initio* principles. We have shown these DFT potentials exhibited qualitative and quantitative agreement with both *ab initio* potential surfaces and experiment.

The minimum geometries of the new UHFBR-XDM DFT potentials agreed

very well with previously published CCSD(T) results. The DFT surfaces predicted a slightly deeper van der Waals well (8 cm^{-1} lower) relative to the CCSD(T) surfaces. As a result, the bound state energies predicted using the DFT potentials are slightly lower in energy relative to those predicted from CCSD(T) surfaces. The lower energy DFT bound state predictions were in better agreement with experimental values than those from CCSD(T) predictions. The scattering predictions from the DFT surfaces also agreed very well with the CCSD(T) results and known experimental values for the wide range of energies studied. The results from this section were in such good agreement with the more accurate *ab initio* surfaces, and more importantly with experiment, that we concluded the computationally cheaper DFT potential surfaces show great promise to be used to model the long range forces in small open-shell systems.

6.2 Future Directions

6.2.1 Three-Dimensional Scattering Software

The work presented in Chapter 3 provides never before seen visualizations of nonadiabaticity dynamics in atom-diatom collisions. However, in its current state our scattering software can only handle collinear atom-diatom reactions. To be truly state-of-the-art this software would need to be extended to rotating atom-diatom reactions. We have made some progress towards this goal including three-dimensional bound state calculations and some very preliminary results for the three-dimensional scattering dynamics of the symmetrical $H+H_2$ reaction. However, there

is much work to do. A general software suite that can predict the nonadiabatic effects of rotating atom-diatom reactions evolving on n-coupled potential surfaces would be very exciting. A three dimensional algorithm would allow for the direct comparison with modern experiment and further our intuition of the nature of nonadiabaticity in chemical reactions.

6.2.2 Photodissociation Spectrum

Photodetachment, photofragmentation and photodissociation of negative ionic species has long been an important tool for probing the transition states of molecular species [235]. The general principle of a photodissociation study is to trap an anionic species, e.g. FH_2^-, and expose the system to a laser beam with enough energy to eject the extra electron. This induces the system, formerly trapped on the bound anionic surface, to relax to the lower energy, reactive surface. The FH_2^- system is especially amenable to this type of study because the center of the anionic bound state of lies in geometries very near the transition state of the neutral species. Once on the reactive $F+H_2$ surface the system proceeds to one of the three product channels. The spectra of the product distributions can be used to infer the barrier height and resonances in these spectra can be used to determine the normal mode frequencies of the transition state.

Extending the reactive scattering software developed in the first half to study atom-diatom interactions in full dimensionality would enable the prediction of nonadiabatic photodissociation spectrum. Using our FEM method, the computation of

the photodissociation spectrum would be straight-forward. From Neumark *et al.* the photodissociation spectrum, $P(E)$, is determined, theoretically using a Franck-Condon factor for the overlap between the scattering wave function and the bound state wave function [236]

$$P(E) = \sum_n |\langle \Psi_n(E) | \Psi_i \rangle|^2$$

where E is the collision energy of the reaction, n and i are the quantum numbers of the reactive products and anionic bound states, respectively. Our algorithm can easily compute these wave functions and using the sparse FEM matrix representation, these overlap integrals would be trivial to compute. There may be very interesting physics revealed in nonadiabatic photodetachment studies.

6.2.3 The Roaming Mechanism

Roaming in chemical reactions is a recently discovered 'third' pathway to molecular dissociation. The first pathway to dissociation, and the one studied most extensively in this work, is a reactive collision that advances through a saddle-point or transition state. The second pathway to dissociation can occur whenever the kinetic energy of the bound nuclei exceeds the dissociation energy; this can be thought of as 'pulling' on the bond until it breaks. The roaming pathway can be seen as a combination of these two pathways and leads to unexpected physics in molecular collisions. In the first pathway classical trajectories of reactive collisions are tightly clustered around the minimum energy path from reactants to products. Roaming pathways explore large parts of the configuration space and move back and forth

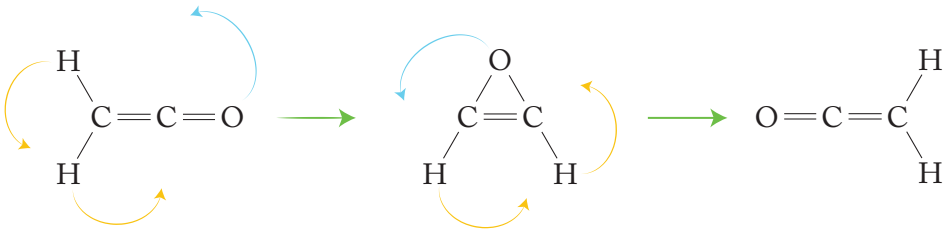

Figure 6.1: The isomerization mechanism for ketene.

between trajectories resembling bond breaking events and trajectories that resemble reactive collisions. The two dimensional model of the organic ketene molecule developed to study the 'roaming' of hydrogen atoms during isomerization is shown in Fig. 6.1.

Classical trajectory studies have shown that the isomerization of ketene can occur via roaming trajectories. The two dimensional model of ketene isomerization may be suitable to use in our reactive scattering software. The coupled motion of the hydrogen atoms, as shown in Fig. 6.1, will only accurately be described by quantum mechanics. It would be very interesting to adapt our reactive scattering code to study the quantum mechanical analogue of roaming in chemical reactions involving large organic molecules.

6.2.4 $O(^3P,^1D)+H_2$

Our calculations of the $O+H_2$ system were limited to the lowest ^3P potential surfaces. Based on our analysis of this system we expect the ^1D surfaces to play a significant role in the nonadiabatic dynamics. This study would require the calculation of the potential energy surfaces for the combined 14 surfaces (nine triplet

and 5 singlet). However, there are considerable technical difficulties that one would face to develop such a large potential surface, specifically the size of the active space required to converge calculations required when one includes the ^1D surface. With the resources available at the present time a calculation of this magnitude would requires months of computation. However, a study of the scattering dynamics of this system including a new, extended potential energy surface would be unprecedented and provide a complete picture of the nonadiabatic dynamics of O+H_2 for reactions.

6.2.5 Modeling Dispersion Forces with DFT Potentials

While, the DFT potential surfaces studied in Chapter 5 were much more affordable computationally than their CCSD(T) analogues, their predictions were not perfect. Specifically, the parity of the lowest bound states of the Ar-NO complex on the electronic ground state as predicted by DFT do not agree with CCSD(T) calculations or with experimental evidence. A systematic study of similar open-shell system would i) provide more evidence for the utility of DFT models to describe the long range dispersive interactions and ii) investigate the discrepancy of parity in the bound states calculations.

The Ar-NO van der Waals well arises from interactions between the dipole-moment of the NO molecule and an instantaneous dipole in the noble gas. Choosing a set of collision partners with varying polarizability would be a natural choice to investigate this discrepancy. Candidates for collision parters are other noble gases

such as neon, krypton and xenon, with polarizabilities in atomic units of 2.38 α_0, 16.47 α_0 and 29.67 α_0, respectively, as compared to 10.77 α_0 for argon [237].

Appendix A: Statistical Learning and Potential Energy Surfaces

A.1 Introduction

To model molecular collision dynamics requires fitting the underlying potential energy surfaces to some functional form. Depending on the application and the amount of available data points there exist a host of possible fitting procedures including least squares and moving least squares, splines and Morse-splines, three body expansions, Legendre expansions, interpolative routines such as Shepard interpolation, and trajectory based sampling, to name a few [238–242]. With each of these methods, one implicitly assumes the functional form of a given fitting method is valid for the system of interest. In this section we discuss the use of neural networks, a type of statistical learning algorithm, which can model an n-dimensional function to arbitrary accuracy, while remaining agnostic about the choice of functional form.

Neural networks, quite simply, are statistical tools based on nonlinear regression or classification. Because neural networks are very fast to evaluate and can model molecular PES's at precisions near the accuracy of the *ab initio* points, there has been increasing interest in their use in theoretical chemistry [243–254]. Neural networks are powerful and supported in popular programming languages [255].

The standard implementation of a neural network is the so-called multi-layer perceptron (MLP) neural network architecture. A network with MLP architecture has an input layer, one or more hidden layers, and an output layer. Each layer has a set of neurons and each neuron in a given layer is connected to every neuron in the following layer (called feed-forward) but to no other layers. MLP architectures have been successfully used to fit a range of PESs [243–254]. Furthermore, Witkoskie and Doren provide an in depth analysis of using neural networks with MLP architecture to fit potential energy surfaces [256].

Though popular, neural networks are powerful, they are not a magic bullet to the potential fitting problem. Common issues include i) training time and number of data points needed to accurately train the networks (especially relevant in high dimensional surfaces) and ii) overfitting, or training the network to be overly sensitive to noise in the tested sample, which reduces the interpolative power of the network, and iii) identifying an 'optimal' neural net, i.e. a network with the fewest number of layers, neurons and connections that achieves a desired accuracy. The first two introduce an art to use of neural networks, while the third can treated systematically.

In a recent study Wilamowski and coworkers [258] have shown that network architectures with connections to future layers are more flexible, more accurate and make it easier to identify optimal architectures. It is the goal of this work to develop efficient strategies for identifying optimal neural networks to model PES's using networks with connections to future layers.

The organization of this Appendix is as follows, first we introduce the formal-

ism of the feed-forward MLP network and show how, in their simplest form, neural networks reduce to simple linear regression. Next we discuss how the permutation-invariant input parameters developed by Guo and coworkers, [250,251] ensure spatial symmetry in neural networks. Motivated by Wilamowski's recent work we perform several numerical experiments to identify optimal network architectures for molecular PESs. Finally, we provide a brief discussion and conclusion based on our results. For assessment purposes, we focus on fitting the *ab initio* H_3 PES of Mielke [124] in 1 and 2 dimensions.

A.2 Neural Networks

Neural networks are multi-stage statistical models first developed to model the human brain. For the purpose of modeling PES's, neural networks serve as another non-linear fitting method. The form of a typical feed-forward neural network is an input layer followed by at least one hidden layer and finally followed by the output layer. In the case of PES modeling the input layer may be composed of the spatial coordinates themselves, or some transformation of these inputs, as in Guo's symmetrized polynomials [250]. The middle layers of the neural network are called 'hidden' because their features are derived by a series of non-linear transformations of the input data, and not directly observed in the data set. The output layer is typically a linear transformation of the last hidden layer. Figure A.1 shows the structure of a feed-forward neural network.

For a given set of inputs (spatial coordinates or transformed coordinates) and

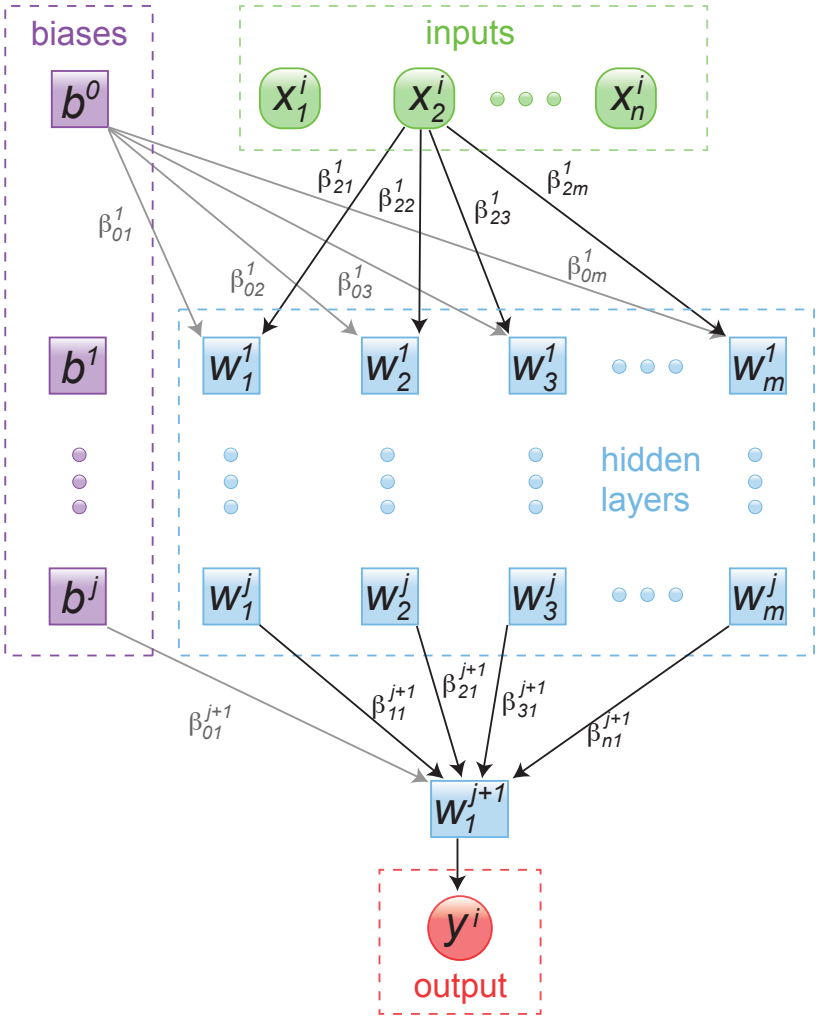

Figure A.1: Diagram of a feed-forward neural network with j hidden layers each made up of m neurons for a regression problem. Note: every node in a given layer is connected to every other node in the following layer, however, we omit many of these connections for clarity.

corresponding outputs (value of the PES) a neural network is acomplicated nonlinear function of many parameters. For a given set of parameters in the neural network we can use the root mean squared error (RMSE) to measure how well the network models the data,

$$R(\boldsymbol{\beta}) = \sum_k (N(\mathbf{x}^k, \boldsymbol{\beta}) - v^k)^2,$$

where $R(\boldsymbol{\beta})$ is the RMSE for the fit, N is the neural network function, $\mathbf{x}^k = [x_1^k, \ldots, x_n^k]^T$ is a set of the input parameters corresponding to the k^{th} geometry at which one wishes to evaluate the potential, v^k, and $\boldsymbol{\beta}$ is the set of all parameters in the fit. To optimize the fit of a given network, one searches for the global minimum $R(\boldsymbol{\beta})$. Here, we use MATLAB's neural network fitting toolbox [255] to build and optimize neural networks. We use MATLAB's implementation of the Levenberg-Marquadt algorithm for optimizing the non-linear parameters.

We now define the exact form of the neural network function, $N(\mathbf{x}^k, \boldsymbol{\beta})$. Each node in a given stage of the network takes a linear combination of the values from the previous stage and applies some 'activation function'. These activation functions mimic the neurons in the human brain. A typical activation function is the 'sigmoid' (hyperbolic tangent) function. The value of a given node in the network can be written as

$$w_j^{i+1} = \sigma_{i+1}\left(\beta_{0j}^i + \sum_{k=1}^{m_i} \beta_{kj}^i w_k^i\right),$$

where $\boldsymbol{\beta}^i$ is a matrix of size $(m_i + 1) \times (m_{i+1} + 1)$, with elements β_{jk}^i referring to the weight between the j^{th} node in the i^{th} layer and the k^{th} node in the $i + 1^{st}$ layer.

Note m_i is the number of nodes in the i^{th} layer excluding the bias node. In this work we will use a linear transfer function from the input and to output layers, and for all hidden layers we use a hyperbolic tangent transfer function, that is

$$\sigma_i(x) = \begin{cases} x & i = 1, j+1 \\ \tanh(x) & i \neq 1, j+1 \end{cases}$$

Note: the hyperbolic tangent function can be slow to evaluate numerically. MATLAB for example, uses the following implementation of the hyperbolic tangent sigmoid function,

$$\text{tansig}(n) = \frac{2}{1+\exp[-2n]} - 1,$$

which has been shown to speed up the training process [257].

We can write the value of the nodes in a given layer in matrix form as follows

$$w^{i+1} = \sigma\left(w^i \boldsymbol{\beta}^i\right)$$

where $w^i = [1, w_1^i, \ldots, w_m^i]$. For a system with j hidden layers, the output node, y, can thus be written in terms of the nodes of the last layer in the neural network

$$N(\mathbf{x}^k, \boldsymbol{\beta}) = y^k = w^{j+1}\boldsymbol{\beta}^{j+1}. \tag{A.1}$$

A.2.1 Single Hidden-Layer Feed-Forward Network

Here we consider a neural network composed of an input layer with n values, a single output node and one hidden layer with m nodes. For a given input point, $\mathbf{x}^k$, the output of this network can be written as

$$y^k = w^2\beta^2 = \sigma(w^1\boldsymbol{\beta}^1)\boldsymbol{\beta}^2, \tag{A.2}$$

where $\sigma(x)$ is applied element-wise. In this case the values $w^1 = [1, x_1^k, \ldots, x_n]$ is the set of input values, β^1 is a matrix of size $(n+1) \times (m+1)$ and β^2 is matrix of size $(m+1) \times 1$. Hence there are a total of $(m+1)(n+2)$ total parameters in this fit. To optimize this neural network, one applies the Levenberg-Marquadt algorithm using the derivative of the output function with respect to each fitting parameter to determine the gradient-descent step size.

If the transfer function is chosen as the linear function, the single-hidden layer network reduces to a linear regression, namely

$$y^k = w^1\boldsymbol{\beta}^1\boldsymbol{\beta}^2 = w^1\boldsymbol{\beta}^1\boldsymbol{\beta}^2 = w^1\boldsymbol{\beta}.$$

Thus, adding the sigmoid transfer functions in the neural network can be viewed as a non-linear generalization of the standard linear regression problem.

A.3 Identifying Ideal Neural Network Architectures for PES Fitting

The only neural network architecture considered up to this point have been single and multilayer perceptron (MLP). The MLP architecture is by far the most commonly used neural network because it lends itself quite naturally to programmatic handling. There are many studies on the applications of MLP networks applied to fitting molecular PESs [243–254].

In an MLP topology the output of every neuron in a given layer (and, typically an additional bias node) are connected to every neuron in the next layer. However, no connections are made to any other layers in the network. In this section we discuss neural network architectures where neurons in a given layer are connected to all future layers. Specifically, we consider two additional architectures, one that improves on the MLP architecture, the bridged multilayer perceptron (BMLP) which is an MLP topology with each neuron connected to all future neurons, and the fully connected cascade (FCC) topology, which is a BMLP network with a single neuron per layer. The three network architectures are shown in Figs. A.2-A.4.

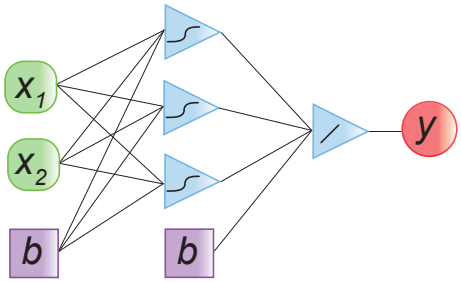

Figure A.2: MLP neural network architecture with 2 inputs, 4 neurons in 2 layers, 2 bias nodes, and 13 weights in a 2-3-1 architecture.

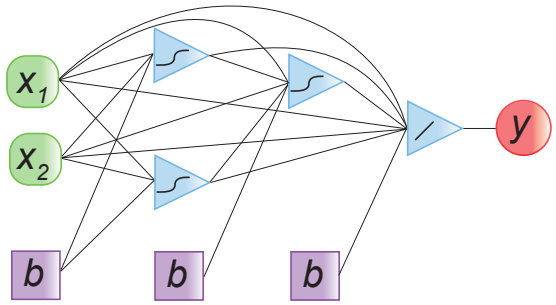

Figure A.3: BMLP neural network architecture with 2 inputs, 4 neurons in three layers, 3 bias nodes, and 16 weights in a 2-2-1-1 architecture.

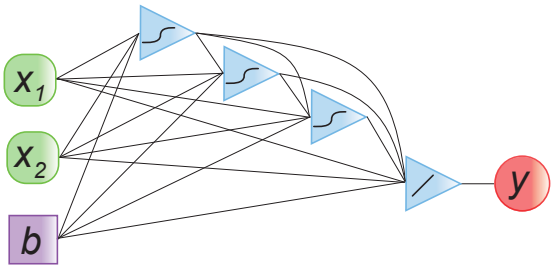

Figure A.4: FCC neural network architecture with 2 inputs, 4 neurons in four layers,1 bias node, and 18 weights in a 2-1-1-1-1 architecture.

A.3.1 Network Depth and Connectivity 1D

It is well known that across many applications deep networks, sometimes called deep-belief networks (DBN) perform better than shallow, broad networks with the same number of neurons [258, 259]. In this section we investigate the dependence of network performance on network depth using the RMSE of the network fit for a given PES as the metric for network performance.

For simplicity we start with fitting the one dimensional H_2 potential energy curve. The points used as training data in this section are generated from the H_3 PES

of Mielke and coworkers (which is a functional fit to quantum chemical calculations) [124]. Figure A.5 shows the results of a series of calculations assessing network fitting performance, as a function of architecture, number of neurons and number of layers in the network. We have used exclusively MATLAB's neural network fitting toolbox to train these neural networks [260]. In all cases we average 250 network fits trained using the Levenberg-Marquardt (LM) algorithm, using the mean-squared error to measure performance, with a maximum number of iterations set to 1E5. We use approximately 300 points in the range $r_{\mathrm{HH}} = [0.8 - 8]$ both as training data.

The FCC architectures have, by definition, the same number of neurons and layers. The (B)MLP architectures, in theory, have multiple possible configurations for a fixed number of neurons. When possible, we use evenly populated layers, for example a (B)MLP network with three layers and six neurons would use the 2-2-2-1 architecture (with one output neuron). In any case where there is ambiguity about the network structure we use the following architecture $n_1 \ldots n_1 - n_2 \ldots n_2 - 1$ (again with one output neuron) where $n_1 = \mathrm{floor}(n_{neurons}/n_{layers})$ and $n_2 = \mathrm{ceil}(n_{neurons}/n_{layers})$. For a/an (B)MLP architecture with 10 neurons and 4 layers we would have $n_1 = 2$ and $n_2 = 3$. The corresponding architecture would be 2-2-3-3-1. We have chosen this scheme for simplicity.

A.3.2 Fitting the Collinear H_3 PES with PIP Input Layer

A fitted potential for triatomic systems that involve spatial symmetries such as $A + A_2$, $B + A_2$, and $A + BA$ must account for these symmetries to avoid unnatural

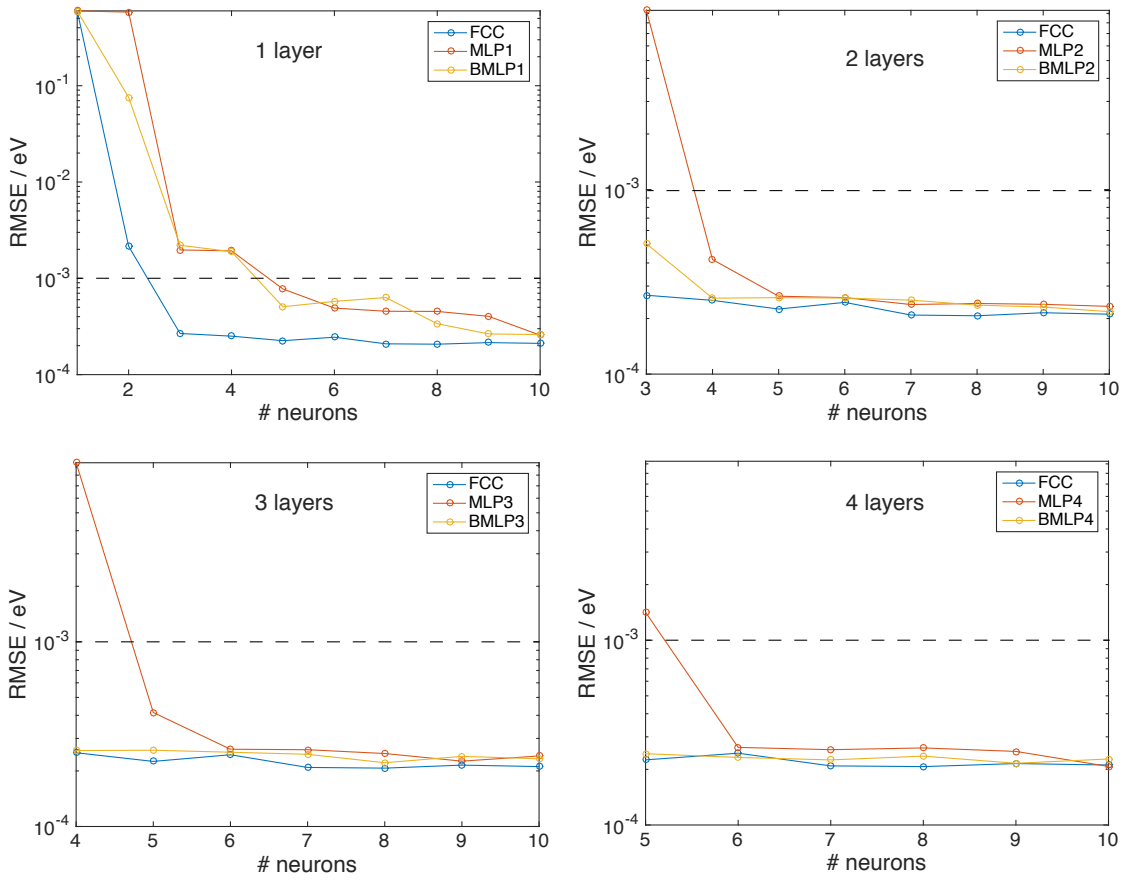

Figure A.5: RMSE performance of the FCC, MLP, and BMLP network architectures fitting the 1D H_2 potential as a function of the number of neurons. Shown is the optimal performance from a batch of 250 fits. Each panel denotes a different number of layers used in each architecture, (B)MLPN with N layers. Note: FCC architectures always have as many layers as they do neurons. The FCC results are identical in each panel. The output neuron of each network is not counted.

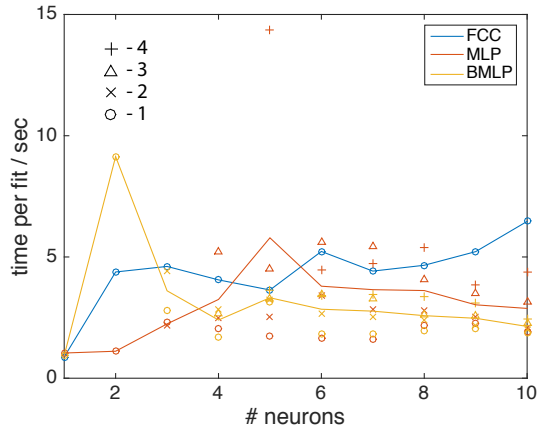

Figure A.6: Average time per fit for the FCC, MLP, and BMLP network architectures fitting the 1D H_2 potential curve as a function of the number of neurons. The markers denote the number of layers.

artifacts in dynamical calculations. In other words, the model that is fit to the *ab initio* data must be identical at any points of symmetry. Recently, Guo and coworkers [250,251] introduced the use of permutation-invariant polynomials (PIPs) to account for such symmetries in neural network models of reactive PES's.

Instead of using the spatial internuclear separation coordinates, r_{ij}, as inputs to the neural network, Guo and coworkers use the following symmetrized polynomial functions of the internuclear separation coordinates,

$$\mathbf{G} = \hat{\mathbf{S}} \prod_{i<j}^{N} p_{ij}^{l_{ij}}$$

where N is the number of atoms in the system, $\hat{\mathbf{S}}$ is the symmetrization operator, which contains projections for all possible intersystem symmetries, $p_{ij} = \log(r_{ij})$, and l_{ij} is the order of the monomial. From Ref. [250], these polynomials are given for an A_3 system as

$$G_1 = (p_{12} + p_{23} + p_{13})/3,$$

$$G_2 = (p_{12}p_{23} + p_{12}p_{13} + p_{13}p_{23})/3,$$

and

$$G_3 = p_{12}p_{23}p_{13}.$$

For an $B + A_2$ system, the PIPs can be written as

$$G_1 = (p_{13} + p_{23}))/2,$$

$$G_2 = p_{13}p_{23},$$

and

$$G_2 = p_{12}$$

These PIP models have been used successfully to model triatomic [250], tetraatomic [251] and molecule-surface [261] PES's. In this section we extend the use of these new architectures to fit the collinear H_3 PES. Figure A.7 shows the results of an experiment testing network fitting performance, as a function of architecture, number of neurons and number of layers in the network. Here, we use train each network a total of 50 times. We use approximately 1500 points in the range $r_{\mathrm{H1H2}} = [0.8 - 8]$ bohr, $r_{\mathrm{H2H3}} = [0.8 - 8]$ bohr as training data. Figure A.9 of a similar experiment to those shown in Fig. A.7, only in this case we use the PIP inputs for an A_3 system defined above.

A.3.3 Neural Networks and Multibody Expansions

The model derived by Guo and coworkers [250] discussed in the previous section naively fits a neural network to a set of training points in all coordinate space. To ensure an accurate fit, a dense grid of points must be sampled in the relevant regions of coordinate space. However, fitting the total electronic PES across all points in coordinate space does not take advantage of the simpler behavior of the reactive PES and one of the atoms separates.

For example the PES for the B+A_2 reaction can be written in a so-called multi-body expansion as

$$V(r_{BA_1}, r_{BA_2}, r_{A_1A_2}) = V^{(1)} + \sum_{i=BA_1,BA_2,A_1A_2} V^{(2)}(r_i) + V^{(3)}(r_{BA_1}, r_{BA_2}, r_{A_1A_2}),$$

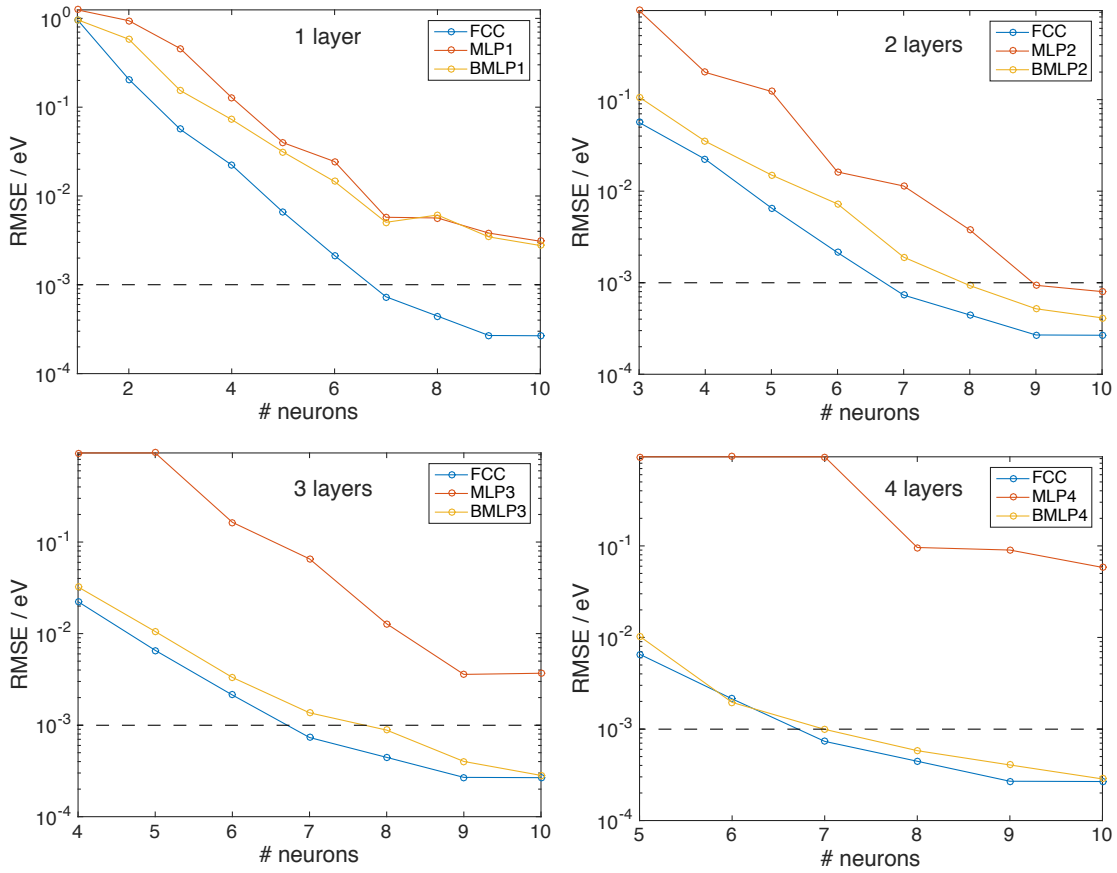

Figure A.7: RMSE performance of the FCC, MLP, and BMLP network architectures fitting the collinear H_3 PES as a function of the number of neurons. Shown is the optimal performance from a batch of 50 fits. Each panel denotes a different number of layers used in each architecture, (B)MLPN with N layers. Note: FCC architectures always have as many layers as they do neurons. The FCC results are identical in each panel. The output neuron of each network is not counted.

where the constant $V^{(1)}$ term is due from the additive energy of asymptotically separated atoms, the $V^{(2)}(r_i)$ terms are the asymptotic two-body potentials and $V^{(3)}$ is the interaction potential.

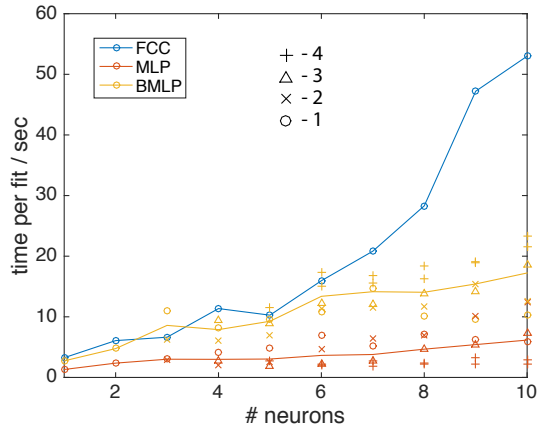

Figure A.8: Average time per fit for the FCC, MLP, and BMLP network architectures fitting the collinear H_3 PES as a function of the number of neurons. The markers denote the number of layers.

The interaction potential is exactly zero in any of the asymptotic regions of space,

$$\lim_{r_i \to \infty} V^{(3)}(r_{BA_1}, r_{BA_2}, r_{A_1A_2}) = 0$$

for any r_i. Because the three-body term vanishes asymptotically, training the neural network using points in these regions is unnecessary. The potential in the asymptotic channels is simply the diatomic term which can very easy be calculated and modeled with a 1-dimensional spline function or another neural network.

A.4 Discussion and Conclusions

Motivated by a recent study by Wilamowski and coworkers [258] we have attempted to determine some general guidelines for identifying optimal neural net-

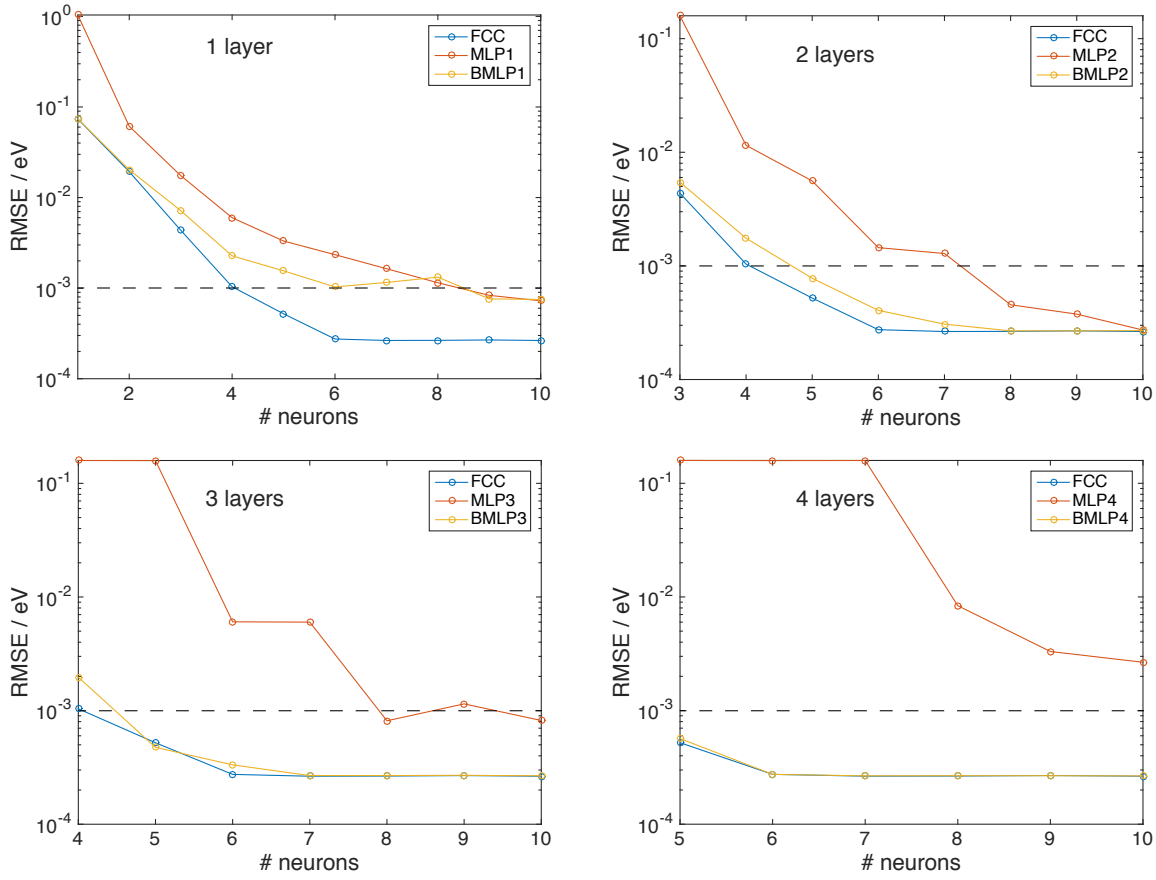

Figure A.9: RMSE performance of the FCC, MLP, and BMLP network architectures fitting the collinear (2D) H_3 PES as a function of the number of neurons. Shown is the optimal performance from a batch of 50 fits. Each panel denotes a different number of layers used in each architecture, (B)MLPN with N layers. Note: FCC architectures always have as many layers as they do neurons. The FCC results are identical in each panel. The output neuron of each network is not counted.

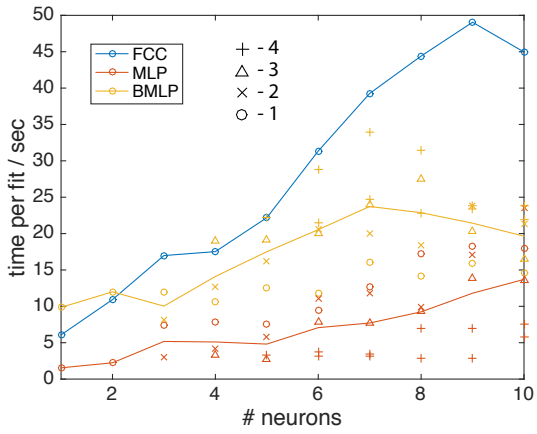

Figure A.10: Average time per fit for the FCC, MLP, and BMLP network architectures fitting the collinear H_3 PES as a function of the number of neurons. The markers denote the number of layers.

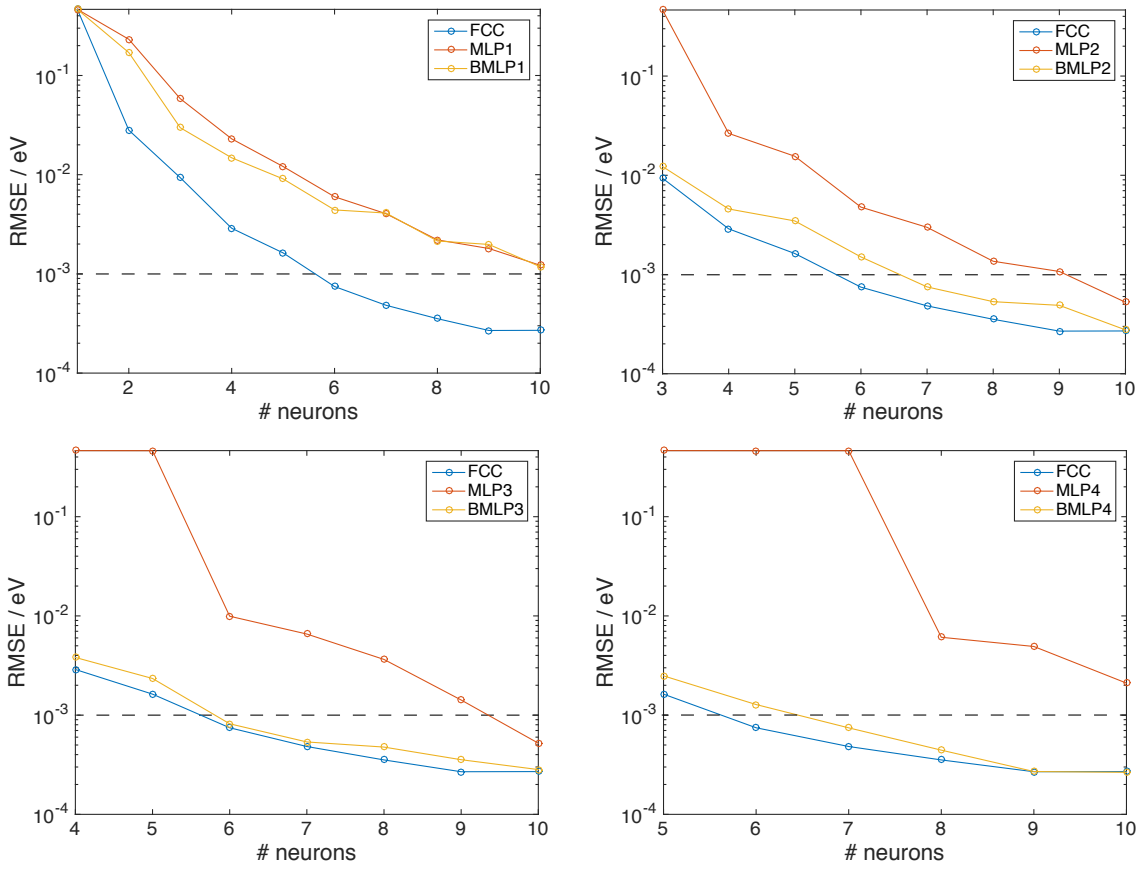

Figure A.11: RMSE performance of the FCC, MLP, and BMLP network architectures fitting the three-body term of the multi-body expansion for the collinear H_3 PES as a function of the number of neurons.

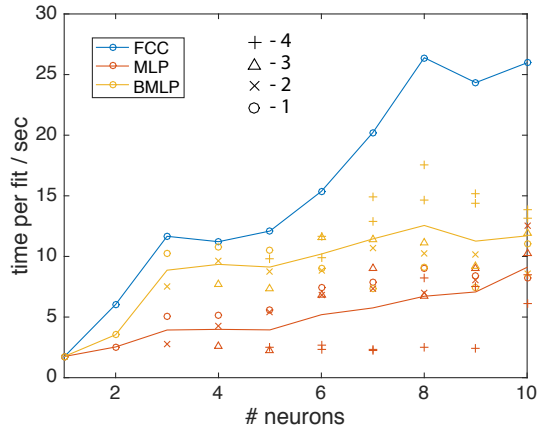

Figure A.12: Average time per fit for the FCC, MLP, and BMLP network architectures fitting the three-body term of the multi-body expansion for the collinear H_3 PES as a function of the number of neurons.

work topologies for fitting molecular PES's. According to Wilamowski, the ideal neural network is the network that achieves the desired error tolerance with the fewest neurons, a condition which provides maximum generalization capability, or, equivalently, minimizes overfitting.

From the network performance for fitting the 1D H_2 potential, shown in Fig. A.5, we can draw many conclusions. It is clear that the FCC architecture is superior in almost every experiment to the (B)MLP architectures for the same number of neurons for fitting the 1D H_2 potential curve. The 1-neuron, 1-layer fit in the top left panel of Fig, A.5 is anomolous. All toplogies share the same 1-1 configuration. We also see the accuracy of the network fits increase with both the number of neurons and the number of layers. The (B)MLP architectures become comparable

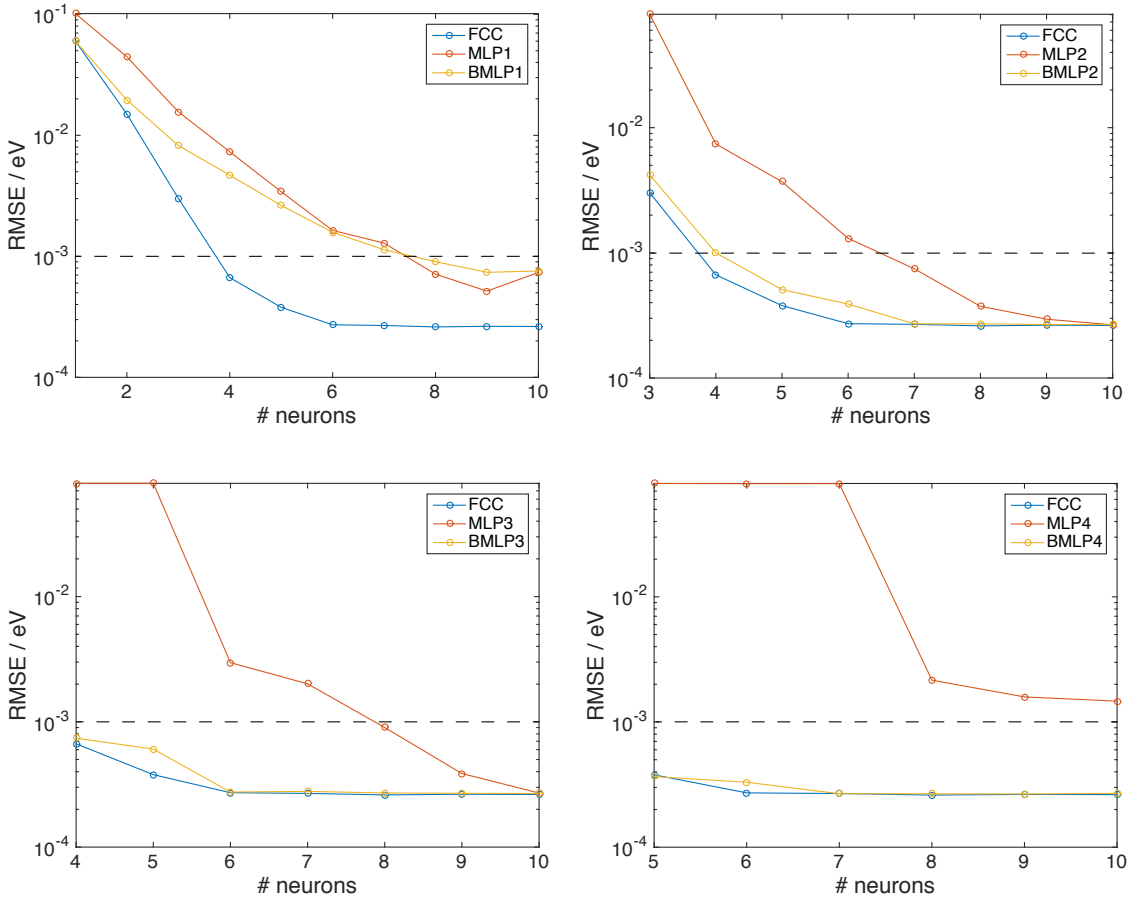

Figure A.13: RMSE performance of the FCC, MLP, and BMLP network architectures fitting the three-body term of the multi-body expansion for the collinear H_3 PES as a function of the number of neurons.

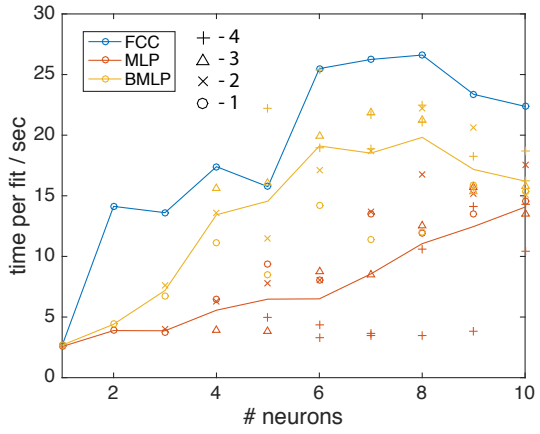

Figure A.14: Average time per fit for the FCC, MLP, and BMLP network architectures fitting the three-body term of the multi-body expansion for the collinear H_3 PES as a function of the number of neurons.

to the FCC networks as the number of layers increases. This is not unexpected; the BMLP architectures is identical to FCC and the MLP architecture is nearly identical to the FCC architecture when $n_{neurons} = n_{layers}$. We also see that the FCC architecture only requires three neurons, whereas the BMLP and MLP architectures require four neurons in two layers and six neurons in four layers, respectively, to achieve comparable results. These results are consistent with Wilamowski's findings for the N-parity problem [258].

Based on the time to train the networks for the 1D problem (Fig. A.6) we can see it takes more time to train FCC networks, on average, than either MLP or BMLP networks. This is reasonable, as FCC networks have more weights than their of the MLP and BMLP networks. From these results it seems the BMLP

architecture may be a decent compromise between accuracy and time to train. FCC networks may take more time to train, but their ideal architecture is easy to identify; simply increase the number of neurons until the desired accuracy is achieved.

The results of training neural networks to model the 2D H_2 potential points are shown in Figs. A.7-A.10. The 2D training results are less accurate than the 1D results (Fig. A.5) for a given network architecture. The 2D training also requires much more time to train per network. We used 1500 points to train the networks for the 2D problem and 300 training points for the 1D problem. This is not exceptional. The decrease in number of points per dimension explains the former, and the increase in total number of points explains the latter. Increasing the number of training data would increase the accuracy of the 2D networks, but we preferred shorter training times to overall accuracy.

We also notice that Guo's method of symmetrized PIP inputs is always more accurate than those networks trained without symmetrized inputs (Figs. A.7-A.10). The networks with PIP inputs are able to achieve a reasonable RMSE of < 1 meV with 6 neurons using the FCC architecture. Whereas 9 neurons are required if the PIP inputs are not used. Furthermore, we know networks with PIP inputs will not have any artificial dynamics with respect to lack of spatial symmetries. The timing of the two methods is comparable, and this is reasonable as both use the same number of training data.

In every experiment fitting neural networks to the collinear H_3 data we observe the same trend with respect to the three network topologies. FCC topologies always outperform the (B)MLP topologies. As in the 1D case, increasing the depth of the

network improves the fit of every topology. MLP topologies can be 'too deep' for a fixed number of neurons, and accordingly, can not be used at all as seen (see the lower panels of Figs. A.7 and A.9). In Fig. A.9, we see that after a second hidden layer is performed the BMLP topology is on par with FCC in terms of accuracy. Considering the relative timing in Figs. A.8 and A.10, i.e. FCC is always slower, BMLP topologies with 2 or more layers using PIP inputs are the preferred choice for these collinear PES's.

In Figs. A.11-A.14 we present the results of an experiment using the three topologies to fit the three-body term and adding back the one and two body terms. Using Figs. A.7 and A.9 as a reference we see the three-body fits with and without the PIP inputs are more accurate in every case. We also note that the fitting the three-body PES takes less time by almost a factor of two, which can be seen by comparing Fig. A.12 with Fig. A.8 and Fig. A.14 with Fig. A.10, respectively.

It is common to in the literature to find MLP architectures of 1–2 hidden layers with 5-10 neurons per layer to fit molecular PES's [248–251]. Based on these results, this choice of network architecture *may* work but is far from optimal. Wilamowski gives the rule of thumb: optimal networks are those with the highest performance per neuron [258]. We have seen in every study that the MLP topology are inferior to the BMLP and FCC topologies. As in Wilamowski's study, we have found that the most straightforward method to identifying the ideal network architecture is to use the FCC topology and increase the number of neurons until the desired error tolerance has been achieved.

We have confirmed Guo's [250] symmetrized input method drastically improves

the fit for a all architectures studied. We have also shown that using a multi-body expansion of a molecular PES can reduce the computational resources required to fit a neural network by up to a factor of two. These savings can be used to train more data leading to boosts in network accuracy. Based on these results, we show the optimal network topology for fitting molecular H_3 PES's is the FCC architecture with a symmetrized PIP input layer used to fit a multi-body expansion of the PES.

There are many aspects of using neural networks to fit PES's that are not addressed in this study. Specifically, future studies may target new training algorithms, such as Wilamowski's next-best-neuron algorithm, for improved speeds and accuracies in network fits. Adaptive and dynamic training algorithms, capable of pruning unimportant connections in the FCC architecture during the training process, may also lead to significant increase in performance.

Bibliography

[1] S. Datz and E. H. Taylor, J. Chem. Phys. **23**, 1211 (1955).

[2] M. Born and J. R. Oppenheimer, Ann. Phys. (Leipzig) **389**, 457 (1927).

[3] MOLPRO is a package of *ab initio* programs written by H.-J. Werner and P. J. Knowles, with contributions from R. D. Amos, A. Berning, D. L.Cooper, M. J. O. Deegan, A. J. Dobbyn, F. Eckert, C. Hampel, T. Leininger, R. Lindh, A. W. Lloyd, W. Meyer, M. E. Mura, A. Nicklaß, P. Palmieri, K. Peterson, R. Pitzer, P. Pulay, G. Rauhut, M. Schütz, H. Stoll, A. J. Stone and T. Thorsteinsson.

[4] M. J. Frisch, G. W. Trucks, J. R. Cheeseman, G. Scalmani, M. Caricato, H. P. Hratchian, X. Li, V. Barone, J. Bloino, G. Zheng, T. Vreven, J. A. Montgomery, Jr., G. A. Petersson, G. E. Scuseria, H. B. Schlegel, H. Nakatsuji, A. F. Izmaylov, R. L. Martin, J. L. Sonnenberg, J. E. Peralta, J. J. Heyd, E. Brothers, F. Ogliaro, M. Bearpark, M. A. Robb, B. Mennucci, K. N. Kudin, V. N. Staroverov, R. Kobayashi, J. Normand, A. Rendell, R. Gomperts, V. G. Zakrzewski, M. Hada, M. Ehara, K. Toyota, R. Fukuda, J. Hasegawa, M. Ishida, T. Nakajima, Y. Honda, O. Kitao and H. Nakai. Revision D.01, Gaussian Inc. Wallingford CT 2009.

[5] M. Schmidt, K. Baldridge, J. Boatz, S. Elbert, M. Gordon, J. Jensen, S. Koseki, N. Matsunaga, K. Nguyen, S. Su, J. Comput. Chem. **14**, 1347 (1993).

[6] D. Skouteris, J. F. Castillo, and D. E. Manolopoulos, Comput. Phys. Comm. **133**, 128 (2000).

[7] M. T. Cvitaš and S. C. Althorpe, J. Phys. A **113**, 4557 (2009).

[8] H.-D. Meyer, U. Manthe, and L. S. Cederbaum, Chem. Phys. Lett. **165**, 73 (1990).

[9] H.-D. Meyer, U. Manthe, and L. S. Cederbaum, J. Chem. Phys. **97**, 3199 (1992).

[10] S. C. Althorpe and J. O. Richardson, J. Chem. Phys. **134**, 054109 (2011).

[11] D. Bunker, Methods Comput. Phys. **10**, 287 (1971).

[12] D. L. Bunker and N. C. Blais, J. Chem. Phys. **41**, 2377 (1964).

[13] W. H. Miller, J. Chem. Phys. **61**, 1823 (1974).

[14] P. Y. Zhang, R. F. Lu, A. J. Zhang, T.-S. Chu, and K.-L. Han, J. Chem. Phys. **128**, 091103 (2008).

[15] J. C. Tully and R. K. Preston, J. Chem. Phys. **55**, 562 (1971).

[16] N. Makri and W. H. Miller, J. Chem. Phys. **87**, 5781 (1987).

[17] S. X. Wang and W. H. Miller, J. Chem. Phys. **109**, 7064 (1998).

[18] A. Askar, C. S. Cakmak, and H. A. Rabitz, Chem. Phys. **33**, 267 (1978).

[19] D. R. Dion, M. B. Milleur, and J. O. Hirschfelder, J. Chem. Phys. **52**, 3179 (1970).

[20] J. O. Hirschfelder and K. T. Tang, J. Chem. Phys. **64**, 760 (1976).

[21] A. Kuppermann, J. T. Adams, and D. G. Truhlar, in D. C. Kurepa and M. V. Cobic, eds., *VIII Int. Conf. Phys. Electron. At. Collisions*, Beograd, Yugoslavia (1973), pp. 149–150.

[22] E. A. McCullough and R. E. Wyatt, J. Chem. Phys. **54**, 3578 (1971).

[23] S. L. Latham, J. F. McNutt, R. E. Wyatt, and M. J. Redmon, J. Chem. Phys. **69**, 3746 (1978).

[24] E. Pollak, J. F. McNutt, and R. E. Wyatt, Chem. Phys. **70**, 207 (1982).

[25] D. E. Manolopoulos and M. H. Alexander, J. Chem. Phys. **97**, 2527 (1992).

[26] M. H. Alexander, J. Chem. Phys. **96**, 6672 (1992).

[27] M. D. Di Rosa, Eur. Phys. J. D **31**, 395 (2004).

[28] O. V. Ershova and N. A. Besley, J. Chem. Phys. **136**, 244313 (2012).

[29] M. Warehime and M. H. Alexander, J. Chem. Phys **141**, 024118 (2014).

[30] M. Warehime, J. Klos, and M. H. Alexander, J. Chem. Phys. **142**, 034108 (2015).

[31] M. Warehime, J. Klos, and M. H. Alexander, J. Chem. Phys. **142**, 024302 (2015).

[32] M. Nazeeruddin, F. De Angelis, F. S., A. Selloni, G. Viscardi, P. Liska, S. Ito, T. Bessho, and M. Gratzel, J. Am. Chem. Soc. **127**, 16835 (2005).

[33] S. Hammes-Schiffer and A. Soudackov, J. Phys. Chem. B **112**, 14108 (2008).

[34] S. Hammes-Schiffer, Acc. Chem. Res. **42**, 1881 (2009).

[35] S. Hahn and G. Stock, J. Phys. Chem. B **104**, 1146 (2000).

[36] A. Bayliss, B.J. Matkowsky, SIAM J. Appl. Math. **54**, 147 (1994).

[37] T. Taketsugu, A. Tajima, K. Ishii, and T. Hirano, Astrophys. J. **608**, 323 (2004).

[38] M. Costes, P. Halvick, K. Hickson, M. Daugey, and C. Naulin, Astrophys. J. **703**, 1179 (2009).

[39] L. M. Delves, Nucl. Phys. **9**, 391 (1959).

[40] D. W. Jepsen and J. O. Hirschfelder, J. Chem. Phys. **30**, 1032 (1959).

[41] F. T. Smith, J. Math. Phys. **3**, 735 (1962).

[42] J. Z. H. Zhang, *Theory and Application of Quantum Molecular Dynamics* (World Scientific, 1999).

[43] K. S. Sorbie and J. N. Murrell, Mol. Phys. **29**, 1387 (1975).

[44] J. N. Murrell, S. Carter, S. C. Farantos, P. Huxley, and A. J. C. Varandas, *Molecular Potential Energy Functions* (Wiley, Chichester, 1984).

[45] M. Baer, Chapter 4. In *Reactive Molecular Collisions* (CRC, Boca Raton, FL, 1985)

[46] H. Nakamura, Int. Rev. Phys. Chem. **10**, 123 (1991).

[47] D. R. Yarkony, Rev. Mod. Phys. **68**, 985 (1996).

[48] D. R. Yarkony, J. Phys. Chem. A **105**, 6277 (2001).

[49] G. A. Worth and L. S. Cederbaum, Annu. Rev. Phys. Chem. **55**, 127 (1994).

[50] B. Lepetit, J.-M. Launay, and M. Le Dourneuf, Chem. Phys. **106**, 103 (1986).

[51] B. Lepetit, J.-M. Launay, and M. Le Dourneuf, Chem. Phys. **106**, 111 (1986).

[52] M. H. Alexander, H.-J. Werner, and D. E. Manolopoulos, J. Chem. Phys. **113**, 11084 (1998).

[53] G. C. Schatz, J. Phys. Chem. **99**, 7522 (1995).

[54] G. C. Schatz, P. McCabe, and J. N. L. Connor, Faraday Discuss. **110**, 139 (1998).

[55] Y. Zhang, T. X. Xie, and K.-L. Han, J. Chem. Phys. **120**, 6000 (2004).

[56] K. Drukker and G. C. Schatz, J. Chem. Phys. **111**, 2451 (1999).

[57] V. Aquilanti, S. Cavalli, D. De Fazio, and A. Volpi, Int. J. Quantum Chem. **85**, 368 (2001).

[58] T.-S. Chu, Y. Zhang, and K.-L. Han, Int. Rev. Phys. Chem. **25**, 201 (2006).

[59] T.-S. Chu, K.-L. Han, and G. C. Schatz, J. Phys. Chem. A **111**, 8286 (2007).

[60] Z. Sun, D. H. Zhang, and M. H. Alexander, J. Chem. Phys. **132**, 034308 (2010).

[61] M. Gilibert and M. Baer, J. Phys. Chem. **98**, 12822 (1994).

[62] M. H. Alexander, D. E. Manolopoulos, and H.-J. Werner, J. Chem. Phys. **113**, 11084 (2000).

[63] F. Lique, G. L. Li, H.-J. Werner, and M. H. Alexander, J. Chem. Phys. **134**, 231101 (2011).

[64] M. Tizniti, S. D. L. Picard, F. Lique, C. Berteloite, A. Canosa, M. H. Alexander, and I. R. Sims, Nature Chem. **6**, 141 (2014).

[65] W. H. Miller and T. F. George, J. Chem. Phys. **56**, 5637 (1972).

[66] J. C. Tully, Chapter 5. In *Modern Theoretical Chemistry: Dynamics of Molecular Collisions, Ed* (Plenum Press, New York, 1976), pp. 217–268.

[67] J. C. Tully, J. Chem. Phys. **93**, 1061 (1990).

[68] W. H. Miller, Science **233**, 171 (1986).

[69] X. Sun, H. Wang, and W. H. Miller, J. Chem. Phys. **109**, 7064 (1998).

[70] M. F. Herman, Annu. Rev. Phys. Chem. **45**, 83 (1994).

[71] M. D. Hack and D. G. Truhlar, J. Phys. Chem. A **104**, 7917 (2000).

[72] A.W. Jasper, C. Zhu, S. Nangia and D. G. Truhlar, Faraday Discuss. **127**, 1-22 (2004).

[73] D. R. Yarkony, J. Phys. Chem. **100**, 18612 (1996).

[74] S. C. Althorpe and D. C. Clary, Annu. Rev. Phys. Chem. **54**, 493 (2003).

[75] W. Dong, C. Xiao, T. Wang, D. Dai, X. Yang, and D. H. Zhang, Science **327**, 1501 (2010).

[76] D. H. Zhang, M. Yang, S.-Y. Lee, and M. A. Collines, *First Principles Quantum Dynamical Study of Four-Atom Reactions* (World Scientific, Singapore, 2004), pp. 409–464.

[77] G. G. Balint-Kurti, Adv. Chem. Phys. **128**, 249 (2004).

[78] E. M. Goldfield and S. K. Gray, Adv. Chem. Phys. **136**, 1 (2007).

[79] M. T. Cvitaš and S. C. Althorpe, J. Chem. Phys. **134**, 024309 (2011).

[80] S. Liu, X. Xu, and D. H. Zhang, J. Chem. Phys. **136**, 144302 (2012).

[81] C. Xiao, X. Xu, S. Liu, T. Wang, W. Dong, T. Yang, Z. Sun, D. Dai, D. H. Zhang, and X. Yang, Science **333**, 440 (2011).

[82] S. Liu, J. Chen, Z. J. Zhang, and D. H. Zhang, J. Chem. Phys. **138**, 011101 (2013).

[83] I. W. M. Smith, *Kinetics and dynamics of elementary gas reactions* (Butterworths, London, 1980).

[84] J. I. Steinfeld, J. S. Francisco, and W. L. Hase, *Chemical kinetics and dynamics* (Prentice Hall, Englewood Cliffs, N. J., 1989).

[85] A. J. Alexander and R. N. Zare, J. Chem. Educ. **75**, 1105 (1998).

[86] A. Messiah, *Mécanique Quantique* (Dunod, Paris, 1965).

[87] D. R. Dion, M. B. Milleur, and J. O. Hirschfelder, J. Chem. Phys. **52**, 3179 (1970).

[88] J. M. Bowman, *Theoretical Studies of Electronically Adiabatic and Non-Adiabatic Chemical Reaction Dynamics*, Ph.D. Thesis, California Institute of Technology (1974).

[89] J. F. McNutt, R. E. Wyatt, and M. J. Redmon, J. Chem. Phys. **81**, 1704 (1984).

[90] M. H. Alexander, J. Chem. Phys. **95**, 8931 (1991).

[91] M. H. Alexander, C. Rist, and D. E. Manolopoulos, J. Chem. Phys. **97**, 4836 (1992).

[92] A. Vegiri and M. H. Alexander, J. Chem. Phys **101**, 4722 (1994).

[93] S. M. Miller and M. H. Alexander, J. Chem. Phys. **101**, 8663 (1994).

[94] S. M. Miller and M. H. Alexander, Chem. Phys. Lett. **232**, 451 (1995).

[95] G. Péoux, M. Monnerville, T. Duhoo, and B. Pouilly, J. Chem. Phys. **107**, 70 (1997).

[96] G. C. Schatz and A. Kuppermann, J. Chem. Phys. **65**, 4642 (1976).

[97] G. C. Schatz and A. Kuppermann, J. Chem. Phys. **65**, 4668 (1976).

[98] R. Walker and J. Light, Annu. Rev. Phys. Chem. **31**, 401 (1980).

[99] R. S. Friedman and M. J. Jamieson, Comput. Phys. Commun. **62**, 53 (1991).

[100] M. J. Jamieson and M. L. Du, Comput. Phys. Comm. **66**, 150 (1991).

[101] S. Larsson and V. Thomée, *Partial Differential Equation with Numerical Methods* (Springer, 2009).

[102] D. E. Manolopoulos, J. Chem. Phys. **85**, 6425 (1986).

[103] D. E. Manolopoulos, M. J. Jamieson, and A. D. Pradhan, J. Comput. Phys. **105**, 169 (1993).

[104] B. R. Johnson, J. Chem. Phys. **69**, 4678 (1978).

[105] F. D. Colavecchia, F. Mrugała, G. A. Parker, and R. T. Pack, J. Chem. Phys. **118**, 10387 (2003).

[106] J. Z. H. Zhang, S. Chu, and W. H. Miller, J. Chem. Phys. **88**, 6233 (1988).

[107] J. Z. H. Zhang and W. H. Miller, Chem. Phys. Lett. **153**, 465 (1988).

[108] J. Z. H. Zhang, J. Chem. Phys. **94**, 6047 (1991).

[109] R. Jaquet and U. Schnupf, Chem. Phys. **165**, 287 (1992).

[110] R. Jaquet and J. Gribkova, Theor. Chim. Acta **89**, 363 (1994).

[111] R. Jaquet, Theor. Chim. Acta **71**, 425 (1987).

[112] R. Jaquet, Chem. Phys. **118**, 17 (1987).

[113] J. Linderberg, S. B. Padkjaer, Y. Öhrn, and B. Vessal, J. Chem. Phys. **90**, 6254 (1989).

[114] V. Sethuraman and P. M. Hunt, J. Chem. Phys. **88**, 6938 (1988).

[115] A. Askar, J. Chem. Phys. **74**, 6133 (1981).

[116] R. Jaquet, A. Kumpf, and M. Heinen, J. Chem. Soc. Faraday T. **93**, 1027 (1997).

[117] F. V. Prudente and J. S. Neto, Chem. Phys. Lett. **309**, 471 (1999).

[118] M. N. Guimaraes and F. V. Prudente, Eur. Phys. J. D **64**, 287 (2011).

[119] M. Warehime and M. H. Alexander, `http://www2.chem.umd.edu/groups/alexander/FEM` (2014).

[120] G. Strang and G. J. Fix, *An Analysis of the Finite Element Method* (Prentice Hall, 1973).

[121] W. Kohn, Phys. Rev. **74**, 1763 (1948).

[122] J. A. Miller, R. J. Kee, and C. K. Westbrook, Annu. Rev. Phys. Chem. **41**, 345 (1990).

[123] P. Solin, K. Segeth, and I. Dolezel, *Higher-Order Finite Element Methods* (CRC Press, 2003).

[124] S. L. Mielke, D. W. Schwenke, G. C. Schatz, B. C. Garrett, and K. A. Peterson, J. Phys. Chem. A **113**, 4479 (2009).

[125] J. T. Muckerman, *Empty* (Academic Press, 1981), vol. 6A, pp. 1–77.

[126] M. P. Deskevich, M. Y. Hayes, K. Takahasi, R. T. Skodje, and D. J. Nesbitt, J. Chem. Phys. **124**, 224303 (2006).

[127] D. K. Bondi and J. N. L. Connor, J. Chem. Phys. **82**, 4383 (1985).

[128] R. N. Porter and M. Karplus, J. Chem. Phys. **40**, 1105 (1963).

[129] B. Liu and P. Siegbahn, J. Chem. Phys. **68**, 2457 (1978).

[130] D. G. Truhlar and C. J. Horowitz, J. Chem. Phys. **68**, 2466 (1978).

[131] G. C. Schatz, J. M. Bowman, and A. Kuppermann, J. Chem. Phys. **63**, 674 (1974).

[132] J. R. Gilbert, C. Moler, and R. Schreiber, SIAM J. Matrix Anal. A. **13**, 333 (1992).

[133] T. A. Davis, *UMFPACK: unsymmetric multifrontal sparse LU factorization package*, `http://www.cise.ufl.edu/research/sparse/umfpack/` (2011).

[134] J. R. Gilbert, C. Moler, and R. Schreiber, SIAM J. Matrix Anal. A. **13**, 333 (1992).

[135] P.-O. Persson and G. Strang, SIAM Rev. **46**, 329 (2004).

[136] E. Cuthill and J. McKee, in *Proc. 24th Nat. Conf. ACM* (1969), pp. 157–172.

[137] P.-O. Persson, *DistMesh – a simple mesh generator in MATLAB*, `http://persson.berkeley.edu/distmesh/` (2012).

[138] T. F. George and W. H. Miller, J. Chem. Phys. **57**, 2458 (1972).

[139] R. A. Marcus and M. E. Coltrin, J. Chem. Phys. **67**, 2609 (1977).

[140] R. T. Skodje, D. G. Truhlar, and B. C. Garrett, J. Chem. Phys. **77**, 5955 (1982).

[141] T. F. George and W. H. Miller, The J. Chem. Phys. **56**, 5722 (1972).

[142] J. Pu, J. Gao, and D. G. Truhlar, Chem. Rev. **106**, 3140 (2006).

[143] K. Stark and H.-J. Werner, J. Chem. Phys. **104**, 6515 (1996).

[144] G. Capecchi and H.-J. Werner, Phys. Chem. Chem. Phys. **6**, 4975 (2004).

[145] F. H. Mies, Phys. Rev. A **7**, 957 (1973).

[146] E. E. Nikitin, *Theory of elementary atomic and molecular processes in gases* (Clarendon Press, Oxford, UK, 1974).

[147] V. Aquilanti, R. Candori, D. Cappelletti, E. Luzzatti, and F. Pirani, Chem. Phys. **145**, 293 (1995).

[148] W. H. Miller, S. D. Schwartz, and J. W. Tromp, J. Chem. Phys. **79**, 4889 (1983).

[149] J. W. Tromp and W. H. Miller, Faraday Discuss. **84**, 441 (1987).

[150] M. L. Boas, *Mathematical Methods in the Physical Sciences* (John Wiley & Sons, Inc., New York, 2005), 3rd ed.

[151] E. Weinan, R. Weiqing, and E. Vanden-Eijnden, Chem. Phys. **126**, 164103 (2007).

[152] M. P. Deskevich, D. J. Nesbitt, and H.-J. Werner, J. Chem. Phys. **120**, 7281 (2004).

[153] E. C. G. Stueckelberg, Helv. Phys. Acta **5**, 369 (1932).

[154] V. K. Bykhovskii, E. E. Nikitin, and M. Y. Ovchinnikova, Sov. Phys. JETP **20**, 500 (1965).

[155] R. E. Olson and F. T. Smith, Phys. Rev. A. **3**, 1607 (1971).

[156] R. K. Preston, C. Sloane, and W. H. Miller, J. Chem. Phys. **60**, 4961 (1974).

[157] M. S. Child, Faraday Discuss. **53**, 18 (1972).

[158] M. S. Child, *Molecular Collision Theory* (Academic, New York, 1974).

[159] A. Li, H. Guo, Z. Sun, J. Kłos, and M. H. Alexander, Phys. Chem. Chem. Phys. **15**, 15347 (2013).

[160] A. M. Zolot and D. J. Nesbitt, J. Chem. Phys. **127**, 114319 (2007).

[161] HIBRIDON is a package of programs for the time-independent quantum treatment of inelastic collisions and photodissociation written by M. H. Alexander, D. Manolopoulos, H.-J. Werner, and B. Follmeg, with contributions by P. Vohralik, G. Corey, B. Johnson, T. Orlikowski, P. Valiron and J. Kłos.

[162] R. Krems, W. C. Stwalley, and B. Friedrich, eds., *Cold Molecules: Theory, Experiment, Applications* (CRC Press; Taylor & Francis Group, Boca Raton, London, New York, 2009).

[163] D. Patterson, J. Rasmussen, and J. M. Doyle, New J. of Phys. **11**, 055018 (2009).

[164] H. Loh, K. C. Cossel, M. C. Grau, K.-K. Ni, E. R. Meyer, J. L. Bohn, J. Ye, and E. A. Cornell, Science **342**, 1220 (2013).

[165] M. H. G. de Miranda, A. Chotia, B. Neyenhuis, D. Wang, G. Quéméner, S. Ospelkaus, J. L. Bohn, J. Ye, and D. S. Jin, Nature Physics **7**, 502 (2011).

[166] H.-I. Lu, I. Kozyryev, B. Hemmerling, J. Piskorski, and J. M. Doyle, Phys. Rev. Lett. **112**, 113006 (2014).

[167] J. J. Hudson, D. M. Kara, I. J. Smallman, B. E. Sauer, M. R. Tarbutt, and E. A. Hinds, Nature **473**, 493 (2011).

[168] S. Y. T. van de Meerakker, P. H. M. Smeets, N. Vanhaecke, R. T. Jongma, and G. Meijer, Phys. Rev. Lett. **94**, 023004 (2005).

[169] S. Y. T. van de Meerakker, P. H. M. Smeets, N. Vanhaecke, R. T. Jongma, and G. Meijer, Phys. Rev. Lett. **94**, 023004 (2005).

[170] H. L. Bethlem, F. M. H. Crompvoets, R. T. Jongma, S. Y. T. van de Meerakker, and G. Meijer, Phys. Rev. A **65**, 053416 (2002).

[171] A. Henson, S. Gersten, Y. Shagam, J. Narevicius, and E. Narevicius, Science **338**, 234 (2012).

[172] E. Lavert-Ofir, Y. Shagam, A. B. Henson, S. Gersten, J. Kłos, P. S. Żuchowski, J. Narevicius, and E. Narevicius, Nature Chem. **6**, 332 (2014).

[173] J. Jankunas, B. Bertsche, K. Jachymski, M. Hapka, and A. Osterwalder, J. Chem. Phys. accepted, http://arxiv.org/pdf/1405.0407.pdf (2014).

[174] H.-I. Lu, J. Rasmussen, M. J. Wright, D. Patterson, and J. M. Doyle, Phys. Chem. Chem. Phys. **13**, 18986 (2011).

[175] V. Singh, K. S. Harman, N. Tariq, M.-J. Lu, A. Ellis, M. J. Morrison, and J. D. Weinstein, Phys. Rev. Lett. **108**, 203201 (2012).

[176] T. V. Tscherbul, J. Kłos, and A. A. Buchachenko, Phys. Rev. A **84**, 040701 (2011).

[177] A. Szabo and N. S. Ostlund, *Modern Quantum Chemistry: Introduction to Advanced Electronic Structure Theory* (Dover Publications Inc, Mineola, New York, 1996).

[178] S. Drukker and G.C. Schatz, J. Phys. Chem. **111**, 2451 (1999).

[179] R. J. Bartlett, in D. R. Yarkony, ed., *Modern Electronic Structure, Part II* (World Scientific, Singapore, 1995), p. 1047.

[180] D. M. Brink and G. R. Satchler, *Angular Momentum* (Clarendon, Oxford, 1993), 3rd ed.

[181] T. A. Grinev, V. Tscherbul, A. A. Buchachenko, S. Cavalli, and V. Aquilanti, J. Phys. Chem. A **110**, 5458 (2006).

[182] S. Rogers, D. Wang, and A. Kuppermann, J. Phys. A **104**, 2308 (2000).

[183] J. Brandao, C. Mogo, and B. C. Silva, J. Chem. Phys. **121**, 8861 (2004).

[184] M. Gacesa and V. Kharchenko, J. Chem. Phys. **141**, 164324 (2014).

[185] D. C. Clary, J. N. L. Connor, and C. J. Edge, Chem. Phys. Lett. **68**, 154 (1979).

[186] R. E. Howard, A. D. Mclean, and W. A. Lester, J. Chem. Phys. **71**, 2412 (1979).

[187] T. Joseph, D. G. Truhlar, and B. C. Garrett, J. Chem. Phys. **88**, 6982 (1988).

[188] G. C. Schatz, A. Papaioannou, L. A. Pederson, L. B. Harding, T. Hollebeek, T. S. Ho, and H. A. Rabitz, J. Chem. Phys. **107**, 2340 (1997).

[189] M. R. Hoffmann and G. C. Schatz, J. Chem. Phys. **113**, 9456 (2000).

[190] T.-S. Chu, X. Zhang, and K.-L. Han, J. Chem. Phys. **122**, 214301 (2005).

[191] S. Y. Lin and H. Guo, J. Phys. Chem. A **113**, 4285 (2009).

[192] T. Shiozaki, G. Knizia, and H.-J. Werner, J. Chem. Phys. **134**, 034113 (2011).

[193] T. Shiozaki and H.-J. Werner, J. Chem. Phys. **134**, 184104 (2011).

[194] T. Shiozaki and H.-J. Werner, J. Chem. Phys. **111**, 607 (2013).

[195] H.-J. Werner and P. J. Knowles, J. Chem. Phys. **89**, 5803 (1988).

[196] P. J. Knowles and H.-J. Werner, Chem. Phys. Lett. **145**, 514 (1988).

[197] P. J. Knowles and H.-J. Werner, Theor. Chim. Acta **84**, 95 (1992).

[198] S. R. Langhoff and E. R. Davidson, Int. J. Quantum Chem. **8**, 61 (1974).

[199] T. H. Dunning, J. Chem. Phys. **90**, 1007 (1989).

[200] H.-J. Werner, M. Kállay, and J. Gauss, J. Chem. Phys. **128**, 034305 (2008)

[201] D. Simah, B. Hartke, and H.-J. Werner, J. Chem. Phys. **111**, 4523 (1999)

[202] A. Berning, M. Schweizer, H.-J. Werner, P. J. Knowles, and P. Palmieri, Mol. Phys. **98**, 1823 (2000).

[203] G. C. Schatz, J. Chem. Phys. **83**, 5677 (1985).

[204] S. Koppe, T. Laurent, P. D. Naik, H.-R. Volpi, J. Wolfrum, T. Arusi-Parpar, I. Bar, and S. Rosenwaks, Chem. Phys. Lett. **214**, 315 (2013).

[205] S.A. Lahankar, J.M. Zhang, K.G. McKendrick, T.K. Minton, Nature **5**, 546 (1993).

[206] M.H. Alexander, E.J. Rackham, D. E. Manolopoulos, J. Chem. Phys. **121**, 5221-5235 (2004).

[207] M. H. Alexander, J. Chem. Phys. **99**, 7725 (1993).

[208] G. C. Nielson, P. G. A., and R. T. Pack, J. Chem. Phys. **66**, 1396 (1977).

[209] M. H. Alexander, J. Chem. Phys. **111**, 7426 (1999).

[210] M. H. Alexander, J. Chem. Phys. **111**, 7435 (1999).

[211] P. D. A. Mills, C. M. Western, and B. J. Howard, J. Phys. Chem. **90**, 3331 (1986).

[212] P. D. A. Mills, C. M. Western, and B. J. Howard, J. Phys. Chem. **90**, 4961 (1986).

[213] K. Tsuji, K. Shibuya, and K. Obi, J. Chem. Phys. **100**, 5441 (1994).

[214] H. Kohguchi, T. Suzuki, and M. H. Alexander, Science **294**, 832 (2001).

[215] H. Joswig, A. P., and R. Schinke, J. Chem. Phys. **85**, 1904 (1986).

[216] M. S. Elioff and D. W. Chandler, J. Chem. Phys. **117**, 6455 (2002).

[217] T. Schmelz, P. Rosmus, and M. H. Alexander, Phys. Chem **98**, 1073 (1994).

[218] Y. Kim, J. Fleniken, H. Meyer, M. H. Alexander, and P. J. Dagdigian, J. Chem. Phys. **113**, 73 (2000).

[219] B. Wen, Y. Kim, H. Meyer, J. Kłos, and M. H. Alexander, Phys. Chem. A **112**, 9483 (2008).

[220] C. J. Eyles, M. Brouard, C.-H. Yang, J. Kłos, F. J. Aoiz, A. Gijsbertsen, A. E.Wiskerke, and S. Stolte, Nature Chemistry **3**, 597 (2011).

[221] C. J. Eyles, M. Brouard, H. Chadwick, B. Hornung, B. Nichols, C.-H. Yang, J. Kłos, F. J. Aoiz, A. Gijsbertsen, A. E. Wiskerke, *et al.*, Phys. Chem. Chem. Phys. **14**, 5403 (2012).

[222] C. J. Eyles, M. Brouard, H. Chadwick, F. J. Aoiz, J. Kłos, A. Gijsbertsen, X. Zhang, and S. Stolte, Phys. Chem. Chem. Phys. **14**, 5420 (2012).

[223] P. G. Jambrina, J. Kłos, F. J. Aoiz, and M. P. de Miranda, Phys. Chem. Chem. Phys. **14**, 9826 (2012).

[224] H. Cybulski and B. Fernández, J. Phys. Chem. A **66**, 7319 (2012).

[225] E. R. Johnson and A. D. Becke, J. Chem. Phys. **124**, 174104 (2006).

[226] J. Chem. Phys. A. D. Becke and E. R. Johnson, J. Chem. Phys. **127**, 154108 (2007).

[227] A. D. Becke, Intl. J. Quant. Chem. Symp. **52**, 625 (1994).

[228] A. D. Becke and R. M. Dickson, J. Chem. Phys. **92**, 3610 (1990).

[229] K. T. Tang and J. P. Toennies, J. Chem. Phys. **118**, 4976 (2003).

[230] A. Otero-de-la Roza and E. R. Johnson, J. Chem. Phys. **138**, 204109 (2013).

[231] *See http://gatsby.ucmerced.edu/wiki/.*

[232] I. P. Hamilton and J. C. Light, J. Chem. Phys. **84**, 306 (1986).

[233] J. Miller and W.-C. Cheng, J. Phys. Chem. **89**, 1647 (1985).

[234] A. Otero-de-la Roza and E. R. Johnson, J. Chem. Phys. **138**, 054103 (2013).

[235] R. B. Metz, A. Weaver, S. E. Bradforth, T. N. Kitsopoulos, and D. M. Neumark, J. Phys. Chem. **94**, 1377 (1990).

[236] D. E. Manolopoulos, K. Stark, H.-J. Werner, D. W. Arnold, S. E. Bradforth, and D. M. Neumark, Science **262**, 1852 (1993).

[237] J. Mitroy, M. S. Safronova, and C. W. Clark, J. Phys. B **43**, 1 (2010).

[238] G.G. Maisuradze, D.L. Thompson, A.F. Wagner, and M. Minkoff, J. Chem. Phys. **119**, 10002-10014 (2003).

[239] H. Koizumi, G.C. Schatz, and S.P. Walch, J. Chem. Phys. **95**, 4130 (1992).

[240] B.K. Taylor, and R.J. Hinde, J. Chem. Phys. **111**, 973 (1999).

[241] D.D. Shepard, A two dimensional interpolation function for irregularly spaced data. In *Proceedings of the 23rd National Conference ACM* (ACM Press, NY, 1968).

[242] R.H. Wood, E.M. Yezdimer, S. Sakane, J.A. Barriocanal, and D.J. Doren, J. Chem. Phys. **110**, 1329 (1999).

[243] B. T. Blank, B. S. D., A. W. Calhou, and D. J. Doren, J. Chem. Phys. **103**, 4129 (1995).

[244] F. V. Prudente, P. H. Acioli, and J. S. Neto, J. Chem. Phys. **109**, 8801 (1998).

[245] L. Sönke, A. Gross, and M. Scheffler, Chem. Phys. Lett. **395**, 210 (2004).

[246] S. Manzhos and T. Carrington, Jr., J. Chem. Phys. **125**, 084109 (2006).

[247] J. Behler and M. Parrinello, Phys. Rev. Lett. **98**, 146401 (2007).

[248] J. Behler, K. Reuter, and M. Scheffler, Phys. Rev. B. **77**, 115421 (2008).

[249] J. Behler, Phys. Chem. Chem. Phys. **12**, 17930 (2011).

[250] B. Jiang and H. Guo, J. Chem. Phys. **139**, 054112 (2013).

[251] J. Li, H. Guo, and B. Jiang, J. Chem. Phys. **139**, 204103 (2013).

[252] A. Li and H. Guo, J. Chem. Phys. **140**, 224313 (2014).

[253] J. Li and H. Guo, Phys. Chem. Chem. Phys. **16**, 6753 (2014).

[254] J. Li, J. Chen, D. H. Zhang, and H. Guo, J. Chem. Phys. **140**, 044327 (2014).

[255] M. H. Beale, M. T. Hagan, and H. B. Demuth, *Neural Network Toolbox^{TM} 7 User's Guide* (The MathWorks, Inc., Natick, MA, 2010).

[256] J.B. Witkoskie, and D.J. Doren, J. Chem. Theory Comput. **1**, 14 (2005).

[257] T.P. Vogl, J.K. Mangis, W.T. Zink, and D.L. Alkon, Biol. Cybern. **59**, 257 (1988).

[258] D. Hunter, H. Yu, M. S. Pukish, J. Kolbush, and B. M. Wilamowski, IEEE T. Ind. Inform. **8**, 228 (2012).

[259] J. Kamruzzaman, Y. Kumagai, and H. Hikita, IEICE T. Fund. Electr. **E76A**, 1877 (1993).

[260] The MathWorks, Inc., 24 Prime Park Way, Natick, MA, *MATLAB Version 2015a* (2015).

[261] B. Jiang and H. Guo, J. Chem. Phys. **141**, 034109 (2014).